



2017

Development Of A Scintillation Detector And The Influence On Clinical Imaging

Joseph Panetta

University of Pennsylvania, josephv@sas.upenn.edu

Follow this and additional works at: <https://repository.upenn.edu/edissertations>

 Part of the [Physics Commons](#)

Recommended Citation

Panetta, Joseph, "Development Of A Scintillation Detector And The Influence On Clinical Imaging" (2017). *Publicly Accessible Penn Dissertations*. 2512.

<https://repository.upenn.edu/edissertations/2512>

This paper is posted at ScholarlyCommons. <https://repository.upenn.edu/edissertations/2512>

For more information, please contact repository@pobox.upenn.edu.

Development Of A Scintillation Detector And The Influence On Clinical Imaging

Abstract

The detector is the functional unit within a Positron Emission Tomography (PET) scanner, serving to convert the energy of radiation emitted from a patient into positional information, and as such contributes significantly to the performance of the scanner. While modern whole-body scanners use detectors composed of very many (i.e., 20000-30000) small pixels, typically $\sim 4 \times 4 \times 20 \text{ mm}^3$ in size, several groups are actively investigating the performance of continuous crystals coupled to position sensitive photodetectors as an alternative detector design with a number of potential advantages, including improved spatial resolution and position sampling. This work in particular focuses on thick ($\geq 14 \text{ mm}$) continuous crystals in order to maintain the sensitivity of modern scanners. Excellent spatial resolution in continuous detectors that are thick, however, has proven difficult to achieve using simple positioning algorithms, leading to research in the field to improve performance. This thesis aims to investigate the effect of modifications to the scintillation light spread within the bulk of the scintillator to improve performance, focusing on the use of laser induced optical barriers (LIOBs) etched within thick continuous crystals, and furthermore aims to translate the effect on detector performance to scanner quantitation in patient studies.

The conventional continuous detector is first investigated by analyzing the various components of the detector as well as its limitations. It is seen that the performance of the detector is affected by a number of variables that either cannot be improved or may be improved only at the expense of greater complexity or computing time; these include the photodetector, the positioning algorithm, and Compton scatter in the detector. The performance of the detectors, however, is fundamentally determined by the light spread within the detector, and limited by the depth-dependence of the light spread and poor performance in the entrance region, motivating efforts to modify this aspect of the detector.

The feasibility and potential of LIOBs to fine-tune this light spread and improve these limitations is then studied using both experiments and simulations. The behavior of the LIOBs in response to optical light is investigated, and the opacity of the etchings is shown to be dependent on the parameters of the etching procedure. Thick crystals were also etched with LIOBs in their entrance region in a grid pattern in order to improve the resolution in the entrance region. Measurements show an overall improvement in spatial resolution: the resolution in the etched region of the crystals is slightly improved (e.g., $\sim 0.8 \text{ mm}$ for a 25 mm thick crystal), though in the unetched region, it is slightly degraded (e.g., $\sim 0.4 \text{ mm}$ for a 25 mm thick crystal). While the depth-dependence of the response of the crystal is decreased, the depth-of-interaction (DOI) performance is degraded as well. Simulation studies informed by these measurements show that the properties of the LIOBs strongly affect the performance of the crystal, and ultimately further illustrate that trade-offs in spatial resolution, position sampling, and DOI resolution are inherent in varying the light spread using LIOBs in this manner; these may be used as a guide for future experiments.

System Monte Carlo simulations were used to investigate the added benefit of improved detector spatial resolution and position sampling to the imaging performance of a whole-body scanner. These simulations compared the performance of scanners composed of conventional pixelated detectors to that of scanners using continuous crystals. Results showed that the improved performance (relative to that of 4-mm pixelated detectors) of continuous crystals with a 2-mm resolution, pertinent to both the etched 14 mm thick crystal studied as well as potential designs with the etched 25 mm thick crystal, increased the mean contrast recovery coefficient (CRC) of images by $\sim 22\%$ for 5.5 mm spheres.

Last, a set of experiments aimed to test the correspondence between quantification in phantom and patient images using a lesion embedding methodology, so that any improvements determined using phantom studies may be understood clinically. The results show that the average CRC values for lesions embedded in the lung and liver agree well with those for lesions embedded in the phantom for all lesion sizes. In addition, the relative changes in CRC resulting from application of post-filters on the subject and phantom images are consistent within measurement uncertainty. This study shows that the improvements in CRC resulting from improved spatial resolution, measured using phantom studies in the simulations, are representative of improvements in quantitative accuracy in patient studies.

While unmodified thick continuous detectors hold promise for both improved image quality and quantitation in whole-body imaging, excellent performance requires intensive hardware and computational solutions. Laser induced optical barriers offer the ability to modify the light spread within the scintillator to improve the intrinsic performance of the detector: while measurements with crystals etched with relatively transmissive etchings show a slight improvement in resolution, simulations show that the LIOBs may be fine-tuned to result in improved performance using relatively simple positioning algorithms. For systems in which DOI information is less important, and transverse resolution and sensitivity are paramount, etching thick detectors with this design, fine-tuned to the particular thickness of the crystal and application, is an interesting alternative to the standard detector design.

Degree Type

Dissertation

Degree Name

Doctor of Philosophy (PhD)

Graduate Group

Physics & Astronomy

First Advisor

Joel S. Karp

Keywords

Medical Imaging, PET, Scintillation Detector

Subject Categories

Physics

DEVELOPMENT OF A SCINTILLATION DETECTOR AND THE INFLUENCE ON
CLINICAL IMAGING

Joseph Vincent Panetta

A DISSERTATION

in

Physics and Astronomy

Presented to the Faculties of the University of Pennsylvania

in

Partial Fulfillment of the Requirements for the

Degree of Doctor of Philosophy

2017

Supervisor of Dissertation

Joel S. Karp, PhD

Professor of Radiologic Physics in Radiology, Department Of Radiology
Adjunct Professor, Department of Physics and Astronomy

Graduate Group Chairperson

Ravi K. Sheth, PhD

Professor, Department of Physics and Astronomy

Dissertation Committee

Joel S. Karp, Adjunct Professor, Department of Physics and Astronomy

Arjun G. Yodh, James M. Skinner Professor of Science, Department of Physics and Astronomy

Philip Nelson, Professor, Department of Physics and Astronomy

Larry Gladney, Edmund J. and Louise W. Kahn Professor for Faculty Excellence, Department of Physics
and Astronomy

Gary Bernstein, Reese W. Flower Professor, Department of Physics and Astronomy

DEVELOPMENT OF A SCINTILLATION DETECTOR AND THE INFLUENCE ON
CLINICAL IMAGING
COPYRIGHT

2017

Joseph Vincent Panetta

This work is licensed under the
Creative Commons Attribution-
NonCommercial-ShareAlike 3.0
License

ACKNOWLEDGMENT

I am eternally indebted to my parents for their encouragement throughout my education (St. Williams, the Prep, Penn, Penn, Penn), including my graduate years; their support has been unwavering and unconditional during this time and any achievements of mine stem from this. My family and friends additionally must be thanked for all they have done for me. Nikki deserves credit for putting up with me during these years; I thank her for her support. Special thanks goes to Molly, Charles, Cat, and Pep.

I thank Joel Karp for accepting me as his graduate student; for instructing me in my research, presentations, and papers; and for his patience throughout these years. He has done more than anyone else to guide the progress of my projects. Margaret has been very supportive and given me more of her time than she ever agreed to; her help in writing our paper and this thesis was incredible. Suleman has guided me in my work and eaten lunch with me since the beginning; both have been invaluable, though his role in the former is particularly invaluable to me and to the group in general, and he deserves a great deal of credit for his efforts in shaping the research during my time in the group. Last, the graduate students who came before me, Drs. Rony Wiener and Madhuri Kaul, must be thanked: Rony brought me into this lab and mentored me, while Madhuri showed me how to be a graduate student.

I have been with the Department of Physics and Astronomy at Penn for over a decade, and so would like to thank all of my classmates who helped shape my physics career and with whom I shared many late night homework sessions, as well as the professors at Penn who taught me everything I know about physics. I especially thank Prof. Nelson for accepting me as his TA for the last six years.

ABSTRACT
DEVELOPMENT OF A SCINTILLATION DETECTOR AND THE INFLUENCE ON
CLINICAL IMAGING

Joseph V. Panetta

Joel S. Karp

The detector is the functional unit within a Positron Emission Tomography (PET) scanner, serving to convert the energy of radiation emitted from a patient into positional information, and as such contributes significantly to the performance of the scanner. While modern whole-body scanners use detectors composed of very many (i.e., 20000-30000) small pixels, typically $\sim 4 \times 4 \times 20 \text{ mm}^3$ in size, several groups are actively investigating the performance of continuous crystals coupled to position sensitive photodetectors as an alternative detector design with a number of potential advantages, including improved spatial resolution and position sampling. This work in particular focuses on thick ($\geq 14 \text{ mm}$) continuous crystals in order to maintain the sensitivity of modern scanners. Excellent spatial resolution in continuous detectors that are thick, however, has proven difficult to achieve using simple positioning algorithms, leading to research in the field to improve performance. This thesis aims to investigate the effect of modifications to the scintillation light spread within the bulk of the scintillator to improve performance, focusing on the use of laser induced optical barriers (LIOBs) etched within thick continuous crystals, and furthermore aims to translate the effect on detector performance to scanner quantitation in patient studies.

The conventional continuous detector is first investigated by analyzing the various components of the detector as well as its limitations. It is seen that the performance of the detector is affected by a number of variables that either cannot be improved or may be improved only at the expense of greater complexity or computing time; these include the photodetector, the positioning algorithm, and Compton scatter in the detector. The performance of the detectors, however, is fundamentally determined by the light spread within the detector, and limited by the depth-dependence of the light spread and poor performance in the entrance region, motivating efforts to modify this aspect of the detector.

The feasibility and potential of LIOBs to fine-tune this light spread and improve these limitations is then studied using both experiments and simulations. The behavior of the LIOBs in response to optical light is investigated, and the opacity of the etchings is shown to be dependent on the parameters of the etching procedure. Thick crystals were also etched with LIOBs in their entrance region in a grid pattern in order to improve the resolution in the entrance region. Measurements show an overall improvement in spatial resolution: the resolution in the etched region of the crystals is slightly improved (e.g., $\sim 0.8 \text{ mm}$ for a 25 mm thick crystal), though in the unetched region, it is slightly degraded (e.g., $\sim 0.4 \text{ mm}$ for a 25 mm thick crystal). While the depth-dependence of the response of the crystal is decreased, the depth-of-interaction (DOI) performance is degraded as well. Simulation studies informed by these measurements show that the properties of the LIOBs strongly affect the performance of the crystal, and ultimately further illustrate that trade-offs in spatial resolution, position sampling, and DOI resolution are inherent in varying the light spread using LIOBs in this manner; these may be used as a guide for future experiments.

System Monte Carlo simulations were used to investigate the added benefit of improved detector spatial resolution and position sampling to the imaging performance of a whole-body scanner. These simulations compared the performance of scanners composed of conventional pixelated detectors to that of scanners using continuous crystals. Results showed that the improved performance (relative to that of 4-mm pixelated detectors) of continuous crystals with a 2-mm resolution, pertinent to both the etched 14mm thick crystal studied as well as potential designs with the etched 25mm thick crystal, increased the mean contrast recovery coefficient (CRC) of images by ~22% for 5.5mm spheres.

Last, a set of experiments aimed to test the correspondence between quantification in phantom and patient images using a lesion embedding methodology, so that any improvements determined using phantom studies may be understood clinically. The results show that the average CRC values for lesions embedded in the lung and liver agree well with those for lesions embedded in the phantom for all lesion sizes. In addition, the relative changes in CRC resulting from application of post-filters on the subject and phantom images are consistent within measurement uncertainty. This study shows that the improvements in CRC resulting from improved spatial resolution, measured using phantom studies in the simulations, are representative of improvements in quantitative accuracy in patient studies.

While unmodified thick continuous detectors hold promise for both improved image quality and quantitation in whole-body imaging, excellent performance requires intensive hardware and computational solutions. Laser induced optical barriers offer the ability to modify the light spread within the scintillator to improve the intrinsic performance of the detector: while measurements with crystals etched with relatively transmissive etchings show a slight improvement in resolution, simulations show that the LIOBs may be fine-tuned to result in improved performance using relatively simple positioning algorithms. For systems in which DOI information is less important, and transverse resolution and sensitivity are paramount, etching thick detectors with this design, fine-tuned to the particular thickness of the crystal and application, is an interesting alternative to the standard detector design.

TABLE OF CONTENTS

ABSTRACT	IV
LIST OF TABLES	X
LIST OF FIGURES	XI
LIST OF ACRONYMS.....	XVII
1 INTRODUCTION	1
1.1 Imaging.....	1
1.1.1 Medical Imaging: Foundations	1
1.1.2 Nuclear Imaging	2
1.2 Positron Emission Tomography	3
1.2.1 Clinical Utility	3
1.2.2 Radiotracers	5
1.2.3 Positron Decay and Annihilation	7
1.2.4 Signal Detection.....	9
1.2.5 Modern PET/CT Scanners	11
1.3. Image Quality in PET: Challenges in Scanner Design	12
1.3.1 Spatial Resolution	12
1.3.2 Signal-to-Noise Ratio.....	19
1.4 Image Reconstruction.....	22
1.4.1 Data Corrections	23
1.4.2 Impact of Image Reconstruction on Image Quality	23
1.5 Quantitation in PET	24
1.5.1 Metrics	25
1.5.2 Partial Volume Effect	27
1.5.3 Factors Affecting Quantitation.....	29
1.6. PET Detectors.....	30
1.6.1 Information Measured by Detector	30
1.6.2 Detector Components.....	31
1.6.3 Current Detector Designs.....	39
1.6.4 Continuous Detectors.....	41
2 THESIS	45
Outline of Thesis	46
3 PERFORMANCE OF CONTINUOUS DETECTORS.....	50

3.1 Introduction.....	50
3.1.1 Fundamental Limitations	51
3.1.2 Depth-of-interaction.....	55
3.1.3 Data Read-out	57
3.1.4 Positioning Algorithms	60
3.2 Experimental Set-up.....	66
3.2.1 Hardware.....	66
3.2.2 Electronics	68
3.2.3 Crystal Treatment	69
3.2.4 Data Collection	70
3.2.5 Testing Data Acquisition Count Rate	71
3.3 Simulations	73
3.3.1 Monte Carlo Simulations in PET	73
3.3.2 Validation of Detector Simulations.....	78
3.4 Continuous Crystal Light Spread.....	79
3.4.1 Impact of Light Spread	79
3.4.2 Head-on LRFs.....	82
3.5 Interactions at the Crystal Walls.....	83
3.5.1 Methods and Materials.....	86
3.5.2 Results.....	87
3.6 Impact of Photodetector	90
3.6.1 Methods and Materials.....	90
3.6.2 Results.....	91
3.7 Impact of Photodetector Read-out	93
3.7.1 Methods and Materials.....	94
3.7.2 Results.....	94
3.8 Impact of Positioning Algorithms.....	95
3.8.1 Methods and Materials.....	95
3.8.2 Results.....	98
3.9 Impact of Compton scatter.....	103
3.9.1 Methods and Materials.....	103
3.9.2 Results.....	103
3.10 Impact of DOI.....	104
3.10.1 Methods and Materials.....	104
3.10.2 Results.....	105
3.11 Discussion	109
3.12 Conclusions.....	115
 4 MODIFYING SCINTILLATION LIGHT SPREAD WITH LASER INDUCED OPTICAL BARRIERS	 117

4.1 Introduction.....	117
4.1.1 Improving the Performance of Continuous Systems.....	118
4.1.2 Fundamentals of Laser Etching.....	121
4.1.3 Laser-induced Optical Barriers	124
4.2 Optical Properties of LIOBs.....	126
4.2.1 Details on Laser Etching	126
4.2.2 Optical Measurements: Model	128
4.2.3 Optical Measurements: Samples	129
4.2.4 Optical Measurements: Apparatus	132
4.2.5 Optical Measurements: Experiments	133
4.2.6 Results.....	140
4.3 Position Measurements with Etched Continuous Crystals.....	146
4.3.1 Etched Crystal Designs	146
4.3.2 Comparison of Etched Crystals to Unetched Crystals: Single Layer of LIOBs.....	149
4.3.3 Light Spread in Etched Region	154
4.3.4 DOI Performance.....	156
4.3.5 Etched Region Coupled to MAPMT	157
4.3.6 Double Layer of LIOBs	158
4.3.7 Opacity of LIOBs Etched Within Thick Crystals	158
4.3.8 Position Sampling	159
4.3.9 Light Output.....	162
4.4 Simulations	162
4.4.1 Model.....	163
4.4.2 Methods and Materials.....	163
4.4.3 Simulations of Etched Crystals	164
4.4.4 Light Spread Caused by LIOBs	166
4.4.5 Varying Etching Parameters	167
4.5 Discussion	170
4.6 Conclusions.....	174
 5 SYSTEM SIMULATION STUDY OF THE IMPACT OF IMPROVED DETECTORS	 177
5.1 Introduction.....	177
5.1.1 System Simulations: EGS4	177
5.1.2 Image Reconstruction	179
5.2 Methods and Materials.....	181
5.2.1 Systems and Phantoms.....	181
5.2.2 Experiments	183
5.3 Results	188
5.4 Discussion	194
5.5 Conclusions.....	197

6 TRANSLATION OF PHANTOM-BASED QUANTITATION TO PATIENT QUANTITATION.....	198
6.1 Introduction.....	198
6.1.1 Connection between System Simulations and Clinical Scanners.....	199
6.1.2 Harmonization	200
6.1.3 Post-filters	205
6.1.4 Phantom Studies	206
6.2 Materials and Methods.....	210
6.2.1 Phantom Studies	210
6.2.2 Scanners and Reconstruction Algorithm.....	210
6.2.3 Lesion Embedding Technique	211
6.2.4 Clinical Metrics.....	215
6.2.5 Subject Studies.....	215
6.2.6 Effect of Post-filtering on Phantom and Subject Measurements.....	216
6.2.7 Harmonization of Scanners.....	217
6.3 Results	219
6.3.1 Measured vs. Embedded Spheres in Phantom	219
6.3.2 Embedded Spheres in Phantom vs. Subjects.....	222
6.3.3 Effect of Post-filtering on Phantom and Subject Measurements.....	223
6.3.4 Harmonization of Scanners.....	225
6.4 Discussion	226
6.5 Conclusions.....	234
THESIS SUMMARY AND CONCLUSIONS	236
BIBLIOGRAPHY	242

LIST OF TABLES

Table 1.1: Examples of radiotracers used for PET imaging, illustrating the wide variety of biologic activity that may be imaged.	6
Table 1.2: Properties of some of the scintillators used for PET.....	33
Table 3.1: Comparison of singles and coincidence rates for detector set-up.	73
Table 3.2: Fraction of photons detected by photodetector for photons directed toward each crystal surface at two depths and two transverse positions.	90
Table 3.3: Energy resolution of three crystals coupled to the SSPM as a function of temperature.	93
Table 4.1: Summary of LIOB parameters used for the cubes.....	131
Table 4.2: Reflectivity (R) for crystals etched using the lasers.	143
Table 4.3: Spatial resolution (mm) of the etched crystals averaged over a large central region of the crystal (12mm in each direction from the center).	154
Table 4.4: Ratio of PMT voltage through the etched region to the PMT voltage through the unetched region, for various thick etched crystals.	159
Table 4.5: Light output and energy resolution of various crystals.....	162
Table 6.1: Comparison of CRC_{mean} (top) and CRC_{max} (bottom) on the Ingenuity TF scanner for measured spheres and lesions embedded into the NEMA IQ phantom.	220
Table 6.2: Comparison of CRC_{mean} (top) and CRC_{max} (bottom) on the LaPET scanner for measured spheres and lesions embedded into the NEMA IQ phantom.	221
Table 6.3: Comparison of CRC_{mean} and CRC_{max} on the Ingenuity TF (top) and LaPET (bottom) scanners without post-filtering for lesions embedded in the phantom and lung and liver regions in the subjects.....	223
Table 6.4: Percent change ^a in CRC_{mean} and CRC_{max} on the Ingenuity TF scanner after application of various post-filters for lesions embedded in the phantom and lung and liver regions in the subjects.	225
Table 6.5: Percent differences ^a between CRC_{mean} on the Ingenuity TF and LaPET scanners for lesions embedded in the phantom and lung and liver regions in the subjects before and after harmonization.	229
Table 6.6: Percent differences ^a between CRC_{max} on the Ingenuity TF and LaPET scanners for lesions embedded in the phantom and lung and liver regions in the subjects before and after harmonization.	230

LIST OF FIGURES

Figure 1.1: Diagram illustrating true, scattered, and random coincidence events.....	8
Figure 1.2: Plot of attenuation coefficient vs. photon energy for LSO.	10
Figure 1.3: Logarithmic histogram of calculated Anger position along a transverse axis (i.e. x-direction), for events of a simulation in which a gamma beam was directed normal to a $50 \times 50 \times 25 \text{ mm}^3$ crystal surface.	14
Figure 1.4: Impact of discrete position sampling.	16
Figure 1.5: Energy of emitted positrons and effect on spatial resolution.	17
Figure 1.6: Parallax error and effect on spatial resolution.	19
Figure 1.7: Diagram of the partial volume effect.	28
Figure 1.8: Diagram depicting the improvement in the localization of events with TOF information (Source: [47]).	31
Figure 1.9: Photograph and diagram of the H8500 MAPMT, used throughout this work.	37
Figure 1.10: Diagram of various block detector designs; all current scanners use fully pixelated arrays read out by large PMTs or arrays of silicon photomultipliers.	40
Figure 1.11: PMT layout in detector module in LaPET scanner.	41
Figure 1.12: Diagram depicting current designs of the continuous detector, using small ($\sim 50 \times 50 \times 25 \text{ mm}^3$) blocks of scintillator coupled to a position sensitive photodetector.	43
Figure 3.1: Light spread within continuous scintillators.	51
Figure 3.2: Diagram depicting the LRF, defined as the light collected at a particular anode as a function of source position.	52
Figure 3.3: Diagram depicting Compton scatter within continuous (left) and pixelated (right) detectors.	55
Figure 3.4: Methods to measure DOI information during calibration of continuous detectors....	57
Figure 3.5: Diagram of row-column summing technique, by which the 64 anode signals are converted into 16 signals by summing along each orthogonal direction.	59
Figure 3.6: Diagram of various calibration schemes, in which data are collected using either point beams (depicted as points) or fan beams (depicted as lines) of gamma rays directed at the surface of the crystal at known, discrete positions.	59
Figure 3.7: Flood map of an array of uniformly spaced crystals showing pincushion artifacts near the center and barreling artifacts near the edges of the PMTs.	61
Figure 3.8: Schematic of apparatus designed to study continuous detectors.	67

Figure 3.9: Geometry of coincidence collimation.....	68
Figure 3.10: Schematic of the electronics set-up used for the measurements, in which the dynode signal of the MAPMT is operated in coincidence with the reference signal, and these signals are read out along with the individual 64 anodes.....	69
Figure 3.11: Model of interactions of photons within detector.....	76
Figure 3.12: Comparison of the LRFs resulting from the simulations and experimental measurements for the 25mm (left) and 14mm thick (right) crystals, and for both a central (top) and near-edge (bottom) row-column summed anode.....	78
Figure 3.13: LRFs for a single row-column summed anode and spatial resolution at various fixed depths for a 50x50x25mm ³ crystal and a 48x48x14mm ³ crystal.....	81
Figure 3.14: Positioning linearity for a 50x50x25mm ³ crystal for three fixed DOIs, showing the linearity in the central region of the crystal and monotonic change of the measured beam position with actual beam position.....	82
Figure 3.15: LRFs for a side-on and head-on scan for a 50x50x25mm ³ crystal.....	83
Figure 3.16: Diagram depicting the division of scintillation photons by direction.....	85
Figure 3.17: Diagram of scan positions for simulation studies of the information carried by photons directed toward the exit surface, entrance surface, and side surfaces of the crystal.....	87
Figure 3.18: Simulated LRFs and positioning histograms for photons emitted in various directions for a 50x50x25mm ³ crystal.....	89
Figure 3.19: LRFs for a central row-column summed anode, spatial resolution, and uncertainty for measurements using the 14mm thick crystal coupled to the SSPM.....	92
Figure 3.20: RMS noise of the SSPM as a function of temperature, showing that the RMS decreases with temperature.....	92
Figure 3.21: Comparison of spatial resolution using the NN algorithm with the 64-anode and row-column summed read-out schemes for: the 25mm thick crystal and H8500 (left), 14mm thick crystal and H8500 (middle), and 14mm thick crystal and SSPM at -35°C (right).	95
Figure 3.22: Gating on row-column summed anodes (red) for head-on (left) and side-on (right) scans.....	98
Figure 3.23: Diagram of gating schemes (left) and spatial resolution (right) for 50x50x25 mm ³ crystal at z=12mm for different gating strategies.....	99
Figure 3.24: Comparison of performance of the ML positioning algorithms.....	100
Figure 3.25: Comparison of NN positioning algorithms that do and do not incorporate the uncertainty of the LRFs, for z=4mm (left) and z=12mm (right) for the row-column summed read-out scheme.....	101

Figure 3.26: Comparison of NN algorithm, ML algorithm, and Cramer Rao bound for row-column summed (left) and 64-anode read-out schemes (right).....	102
Figure 3.27: Simulated spatial resolution for side-on (left) and head-on (right) configurations for the 50x50x25mm ³ crystal, with and without Compton scatter.	104
Figure 3.28: Histogram of the standard deviation of the 64 anode outputs for a head-on scan for a central beam position and a beam position near the edge of the detector.	107
Figure 3.29: Comparison of LRFs from side-on scans and head-on scans gated by the standard deviation of the anode signals.....	107
Figure 3.30: Spatial resolution (top) and positioning linearity (bottom) of side-on scans using side-on and head-on calibration data for three different DOI.	108
Figure 3.31: DOI information in continuous systems.	108
Figure 4.1: Various configurations of the scintillator and photodetector used to decode the light spread within the continuous scintillator.	120
Figure 4.2: Energy level diagram for Nd ³⁺ laser.	124
Figure 4.3: Diagram of etching procedure.	127
Figure 4.4: Model of the interaction of light with the LIOBs.	129
Figure 4.5: Etched LYSO cubes.	131
Figure 4.6: Experimental design to measure the optical properties of the LIOBs.	134
Figure 4.7: Diagram of the measurements of the profile of the directly transmitted light using the set-up diagrammed in Figure 4.6 B, in which the beam is transmitted through air, the unetched region of the crystals, and the etched region of the crystals.	136
Figure 4.8: Diagram of the simulation used to determine the fraction of diffusely transmitted light measured by the PMT.	138
Figure 4.9: Design to measure the reflectivity profile of the LIOBs.	139
Figure 4.10: Diagram of experiment to measure the behavior of the LIOBs as a function of vertical (left) and horizontal (right) position on the LIOB.....	140
Figure 4.11: Measurements of directly transmitted light for sample cubes with high and low reflectivity.....	141
Figure 4.12: Scatter plot of the fraction of transmitted light that is directly transmitted (f_s) vs. average reflectivity (R) for the various crystals.	142
Figure 4.13: Profiles of light reflected from the unetched and etched regions of the crystals for two crystals.	144

Figure 4.14: Normalized voltage of PMT as a function of horizontal position along etching length (top) and etching depth (bottom).	145
Figure 4.15: Diagram of the etched thick continuous crystals studied in this work.....	148
Figure 4.16: Diagram of the measurement to estimate the relative opacity of the LIOBs etched in the thick crystals: a beam of blue light is directed through the etched layer of the crystals and the output compared among the various crystals to determine the relative transmission through the crystals.	149
Figure 4.17: Photographs of etched and mechanically cut crystals.	151
Figure 4.18: Comparison of etched crystal to continuous crystal for the 25mm thick crystal (etched with 8mm deep LIOBs) (left) and the 14mm thick crystal (etched with 5mm deep LIOBs) (right).	152
Figure 4.19: Comparison of the 25mm thick etched crystal (etched with 8mm deep LIOBs) to continuous crystal (left) and mechanically cut crystal (right), using curves of spatial resolution (top) and LRFs for a central row-column summed anode (bottom), for three depths: within the etched region ($z=4\text{mm}/2\text{mm}$ for the 25mm/14mm thick crystals), within a middle region ($z=12\text{mm}/8\text{mm}$ for the 25mm/14mm thick crystals), and within a deep region ($z=20\text{mm}/12\text{mm}$ for the 25mm/14mm thick crystals).	153
Figure 4.20: LRFs and spatial resolution as a function of depth for the 14mm thick crystal etched with 5mm deep LIOBs (left) and the 25mm thick crystal etched with 8mm deep LIOBs (right).	155
Figure 4.21: DOI resolution of the 25mm thick crystal etched with a single layer of LIOBs. ...	156
Figure 4.22: Comparison of central row-column summed LRFs for the 25mm thick continuous crystal and the etched crystal (8mm deep LIOBs), with the etched region coupled to the MAPMT.	157
Figure 4.23: LRFs and spatial resolution for the 25mm thick crystal etched with a single layer and double layer of LIOBs.....	158
Figure 4.24: LRFs and positioning plots for etched crystals for side-on scans (fixed depths) and for a head-on scan.	161
Figure 4.25: Comparison of simulations to experimental measurements, showing LRFs for a central row-column summed anode for the 25mm and 14mm thick crystals etched with a single layer of LIOBs.....	165
Figure 4.26: Comparisons of simulated LRFs for a central row-column summed anode for a single and double layer of LIOBs etched into the 25mm thick continuous crystal.	166
Figure 4.27: Positioning histograms for photons directed toward the entrance surface, exit surface, and side surfaces of the etched and continuous crystals for two DOIs for the 25mm thick crystal.....	167
Figure 4.28: LRFs for the $50\times 50\times 25\text{-mm}^3$ crystal etched with LIOBs of varying opacity and depth.	169

Figure 4.29: Positioning linearity for the 50x50x25-mm ³ crystal etched with LIOBs of varying opacity and depth.	170
Figure 5.1: Diagram of model used in EGS4 system simulations.	180
Figure 5.2: Images of the simulated IEC phantom and point source simulation used to characterize the various scanners.	183
Figure 5.3: Diagram illustrating calculation in which a uniform sphere in a uniform background is blurred with a Gaussian PSF, and the CRC of the resulting blurred image is calculated using a VOI of diameter equal to the sphere diameter.	186
Figure 5.4: Central slice of the simulated IEC phantom for the 4-mm pixelated and continuous (1-mm pixelated) systems.	188
Figure 5.5: CRC _{mean} of the 4-mm pixelated system for three independent trials (left) and standard deviation of the measurements (right), showing the low uncertainty of the measurements made with the simulations.	189
Figure 5.6: CRC _{mean} for two spheres as a function of reconstruction iteration for the continuous system.	189
Figure 5.7: Point source resolution (left) and curves of CRC _{mean} (right) for the continuous system, reconstructed using various basis function grids and voxelized using 1-mm and 2-mm voxels.	190
Figure 5.8: Point source resolution as a function of radial source position (left) and CRC _{mean} as a function of sphere diameter (right) for the 4-mm pixelated system and the various continuous systems.	191
Figure 5.9: Percent difference between the CRC _{mean} measured in simulation for the 4-mm pixelated system when excluding and including object scatter (with scatter correction).	191
Figure 5.10: Comparison of CRC _{mean} curves measured using IEC phantom simulations and when calculating using the PSFs measured in the point source simulations.	192
Figure 5.11: PSFs for the various factors that affect system spatial resolution for the 4-mm pixelated system and the continuous system.	193
Figure 5.12: Point source resolution as a function of radial source position and CRC _{mean} as a function of sphere diameter for the 4-mm pixelated system and the various continuous systems after convolving all resolution effects.	194
Figure 6.1: Comparison of CRC resulting from phantom scans on the Philips Healthcare Vereos and from simulations of a 4-mm pixelated system; similar image reconstruction and data corrections are applied for each scanner.	200
Figure 6.2: NEMA image quality phantom used to quantify the performance of scanners.	203
Figure 6.3: Curves of CRC _{mean} and CRC _{max} versus sphere diameter for the NEMA IQ phantom scanned on the Ingenuity TF.	208

Figure 6.4: Comparison of (A) CRC_{mean} and (B) CRC_{max} values as a function of sphere size for NEMA IQ phantom data on the Siemens mCT and Philips Ingenuity TF scanners.	209
Figure 6.5: Curves of CRC_{max} collected for the Harmonization Initiative for several makes and models of PET scanners, before harmonization.	209
Figure 6.6: Average CRC_{mean} and CRC_{max} values for (a) 10-mm, (b) 17-mm, and (c) 28-mm lung and liver lesions for each of the patients on the Ingenuity TF.	221
Figure 6.7: Comparison of average (top) CRC_{mean} and (bottom) CRC_{max} values for 10-, 17-, and 28-mm lesions before and after application of various post-filters on the (left) Ingenuity TF and (right) LaPET scanners for the lesions embedded in the phantom and lung and liver regions in the subjects.	224
Figure 6.8: Comparison of CRC_{mean} , CRC_{peak} , and CRC_{max} values as a function of sphere diameter for phantoms on the Ingenuity TF and LaPET scanners (a) without harmonization and using (b) harmonization strategy 1 (6-mm Gaussian post-filter applied to the Ingenuity TF), (c) harmonization strategy 2 (4-mm Gaussian post-filter applied to the Ingenuity TF and LR deconvolution post-filter applied to LaPET), and (d) harmonization strategy 3 (2.5-mm ..	228

LIST OF ACRONYMS

CRC	– Contrast Recovery Coefficient
DOI	– Depth-of-interaction
EGS4	– Electron Gamma Shower 4
^{18}F -FDG	– ^{18}F -fluorodeoxyglucose
FWHM	– Full Width Half Maximum
FWTM	– Full Width Tenth Maximum
IEC	– Electrotechnical Commission
IQ	– Image Quality
LIOB	– Laser Induced Optical Barrier
LOR	– Line-of-response
LR	– Lucy-Richardson
LRF	– Light Response Function
LSO	– Cerium-doped Lutetium Oxyorthosilicate
LYSO	– Cerium-doped Lutetium Yttrium Oxyorthosilicate
MAPMT	– Multianode Photomultiplier Tube
MC	– Monte Carlo
ML	– Maximum Likelihood
MLEM	– Maximum Likelihood Expectation Maximization
NEMA	– National Electrical Manufacturers Association
NCI	– National Cancer Institute
NN	– Nearest Neighbor
OSEM	– Ordered Subsets Expectation Maximization
PDF	– Probability Distribution Function
PERCIST	– PET Response Criteria in Solid Tumors
PET	– Positron Emission Tomography
PMT	– Photomultiplier Tube
PSF	– Point Spread Function
PVE	– Partial Volume Effect
RECIST	– Response Evaluation Criteria in Solid Tumors
RMS	– Root Mean Square
ROI	– Region-of-interest
SiPM	– Silicon Photomultiplier
SNR	– Signal-to-noise ratio
SPECT	– Single Photon Emission Computed Tomography
SSPM	– Solid-state Photomultiplier
SUV	– Standardized Uptake Value
TOF	– Time-of-flight
VOI	– Volume-of-interest

CHAPTER 1

INTRODUCTION

1.1 Imaging

1.1.1 Medical Imaging: Foundations

An image is the representation of the mass and energy of some object or scene as a function of spatial position, and is the result of a transformation of the object in real space to an image in a transformed version of real space. The measurements needed to form an image ultimately involve the detection of some type of radiation (e.g., x-rays, gamma rays, sound) that is transported from the object to the imager; in the case of electromagnetic radiation, this detection is in turn fundamentally a result of the photoelectric interaction.

Medical imaging allows for the noninvasive assessment of a patient, but adds the additional constraints that the radiation being imaged must penetrate tissue, and that the practical ability to achieve such images as well as any dangers associated with the imaging must be weighed against the benefit of the imaging. The images that are produced are therefore evaluated technically to determine their utility, with common metrics including spatial resolution, contrast, linearity of response, and uniformity.

The usefulness of a medical imaging modality is based on the relation of the information obtained from the image to a clinical parameter of interest. The utility of the modality is often framed within the context of either detectability, the ability to reliably discern objects of interest within the image, or quantitative capability, the ability to

quantify metrics accurately based on the computed values at each point of the image. Therefore, improvements in a medical imaging device can be made by three general means: increasing the signal that creates the image, decreasing the noise inherent in the image, or improving the accuracy and precision of the object properties being imaged. The last is of particular concern for this thesis; while an ideal imaging system may be viewed mathematically as a (noiseless) linear, shift invariant system that maps points in real space to points in image space, real imaging systems deviate from this. These imperfections result in a number of problems for the system, including nonlinearities in response, finite resolution, and artifacts that all limit the capability of the imaging system [1-5].

1.1.2 Nuclear Imaging

Nuclear imaging is distinguished from most other forms of medical imaging in that it constitutes the subcategory of emission imaging, which aims to detect and image gamma radiation that originates within the subject. This is in contrast to transmission imaging (e.g., x-rays), in which gamma radiation outside the subject is directed through the body and detected. An important consequence is that although the form of the data collected by both systems is very similar, modeled roughly as line integrals of nonnegative functions, the two types of imaging provide different information. Specifically, while transmission imaging aims to measure the attenuation coefficient of the subject at the gamma energy of interest as a function of spatial position, emission imaging operates by measuring the source distribution within the subject, and treats attenuation as undesirable.

Nuclear imaging designed for whole-body imaging and imaging of large organs, such as the brain or heart, takes the form of either Single Photon Emission Computed Tomography (SPECT) or Positron Emission Tomography (PET). SPECT involves the imaging of tracers that emit single gamma photons of interest that are detected and localized using mechanical collimators, while PET involves the imaging of tracers that emit positrons, which annihilate with electrons in tissue to produce a pair of 511-keV photons that generally travel in opposite directions.

1.2 Positron Emission Tomography

Positron emission tomography begins with administration to a patient of a radiotracer with relevant physiologic characteristics. The spatial, and perhaps temporal, properties of the radiotracer distribution are then measured by the PET detector and a map of the radiotracer distribution is produced for clinical interpretation.

1.2.1 Clinical Utility

Nuclear medicine in general has grown in recent decades in the United States, as a result of advances in technology and radiopharmaceuticals, with the United States accounting for about half of nuclear medicine procedures worldwide. While most nuclear medicine procedures in the United States are SPECT scans, and mostly consist of nuclear cardiology and bone scintigraphy, there were ~1.5 million PET procedures each year, as of 2011. In particular, the advent of PET/CT, and more recently PET/MRI, has spurred its growth in popularity (>80% of PET facilities in the United States have PET/CT systems). Worldwide, nuclear medicine, which consists mostly of bone and thyroid scans, has increased overall, with PET in particular increasing in popularity. Additionally, while

costs of advanced imaging procedures have in general grown disproportionately compared to rising health costs, nuclear medicine procedures have been shown to be cost effective [6-9].

PET has become an established imaging modality for diagnosis, staging, recurrence detection, and therapeutic monitoring, particularly in oncology, which accounts for 90% of procedures, in addition to cardiology and neurology, which account for 4% each [10-16]. In all of these procedures, ^{18}F -fluorodeoxyglucose (^{18}F -FDG) is the most common radiotracer used, though there are other notable tracers used as well (Table 1.1). In addition to qualitative comparisons of tumor size and number, the quantitative ability of PET may be invoked in its clinical uses, by calculating some metric of interest related to tracer uptake. While standards exist to analyze tumors anatomically (e.g., World Health Organization (WHO) criteria, the Response Evaluation Criteria in Solid Tumors (RECIST)), PET therefore allows for the addition of quantitative information in clinical decisions, as reflected in the PET Response Criteria in Solid Tumors (PERCIST) standard [17].

As an example, PET has been proven to be very sensitive for the early detection and staging of lung cancer, with an overall sensitivity of >95% and a specificity of ~80%, limited by the accumulation of ^{18}F -FDG in nonmalignant areas. In particular, PET has an important use in preoperative staging, with the potential to result in potentially curative surgeries or to avoid potentially futile surgeries. PET similarly may be used for staging lymphomas and melanomas, and may additionally be used to monitor therapy for lymphomas, by indicating the potential for relapse or predicting progression-free survival. PET also holds an advantage over other imaging modalities in the detection and

staging of recurrent tumors in colorectal cancer and head and neck cancer, where changes in the tumor may be difficult to distinguish from the effects of treatment and changes in anatomy can affect the interpretation of anatomical images. Additionally, PET has found a use in nuclear cardiology, for which SPECT is still the most common modality, when absolute quantification is desired, or when detection of viable myocardium is important. The myriad uses for PET, which are based on the quantitative capability of the modality, highlight the importance of improved quantification. The clinical uses for PET are dependent on the accuracy and precision of the measurements, which in turn are a function of both the performance of the system, as well as the ability to extract information using proper quantification metrics [10-11, 18-19].

1.2.2 Radiotracers

The radiation distribution imaged by a PET scanner is administered using a radiotracer, which couples a compound used as a marker for natural biologic activity to a radioactive compound that can be imaged. While there are a number of β^+ emitting radiotracers, by far the most popular has been ^{18}F -fluorodeoxyglucose (FDG), because it acts as a natural analog to glucose but is not fully metabolized, and thus is trapped in tissue until radioactive decay; FDG has therefore found a key role in measuring metabolism, particularly in oncology. The utility of nuclear imaging is dependent on the radiotracers that they image. The ability to tag molecules that migrate into regions of biological interest with radioactivity, and the versatility of the molecules that may be tagged, give nuclear medicine its unique power to image biologic activity. Table 1.1 lists

some of the most widespread as well as new radiotracers and how they are used to image a wide range of biologic function [2, 20-31].

Table 1.1: Examples of radiotracers used for PET imaging, illustrating the wide variety of biologic activity that may be imaged.

Radioisotope	Radiotracer/ Administration	Half-life	Use
F-18	FDG Florbetapir FLT FMISO	110 min	Glucose metabolism Alzheimer's Disease Cell Proliferation Tumor hypoxia
C-11	11C-choline 11C-methionine 11C-acetate	20 min	Prostate cancer relapse Protein metabolism Lipid synthesis
Ga-68	Ga-DOTA Ga-PSMA	68 min	Somatostatin imaging PSMA targeting
Zr-89	Antibody	78 hr	Monoclonal antibody monitoring
Y-90	Radioembolization	64 hr	Liver therapy monitoring
Rb-82	Potassium analog	75 sec	Myocardial perfusion

1.2.3 Positron Decay and Annihilation

PET imaging relies on the production of positrons by the radiation administered to the patient. After decaying by β^+ emission, the positron will travel a short distance within the patient, ranging from tenths of a millimeter to several millimeters (< 1 ns in travel time), depending on its kinetic energy, as it loses this energy in collisions with atomic electrons within tissue. The positron will eventually annihilate with an electron; because the probability of annihilation increases as its speed decreases, this usually happens near to its stopping point. By conservation of linear momentum, annihilation usually results in the production of two coincident photons, each nearly 511 keV in energy (production of more than two photons is much less likely), which travel nearly opposite to one another; small deviations from this, usually within 1° , are the result of the nonzero linear momentum of the positron-electron pair immediately prior to annihilation.

The 511-keV photons that are produced may interact within the tissue by being absorbed or elastically scattering. Coincidence photons that are detected are therefore placed into one of three categories (Figure 1.1). The first are true coincidences that consist of two photons from the same annihilation event that do not interact with tissue; the second are scattered coincidences that result when one or both photons have scattered in the patient prior to detection, and the last are random coincidences that result when single photons from two different annihilation events are detected in coincidence. While true coincidences contain useful information that is desired in an image, random and scattered events do not and add bias to the image that may be removed using corrections, at the cost of increased noise. Because scattered photons deposit less energy in the photodetector, an energy gate is used after detection to reduce these events, particularly

those that scatter at large angles and that lose a large fraction of their energy, from the total set of events that are processed [4]. PET imaging requires detection of both coincidence photons to define a line-of-response (LOR) that connects the two 511-keV photon positions for image reconstruction. Each pair of coincident gammas therefore carries the information used to form an image, specifically regarding: the LOR along which the positron annihilation event occurs within the patient; the difference in the arrival times of the photons, known as the time-of-flight (TOF); and the energy of the photons that are detected by the scanner.

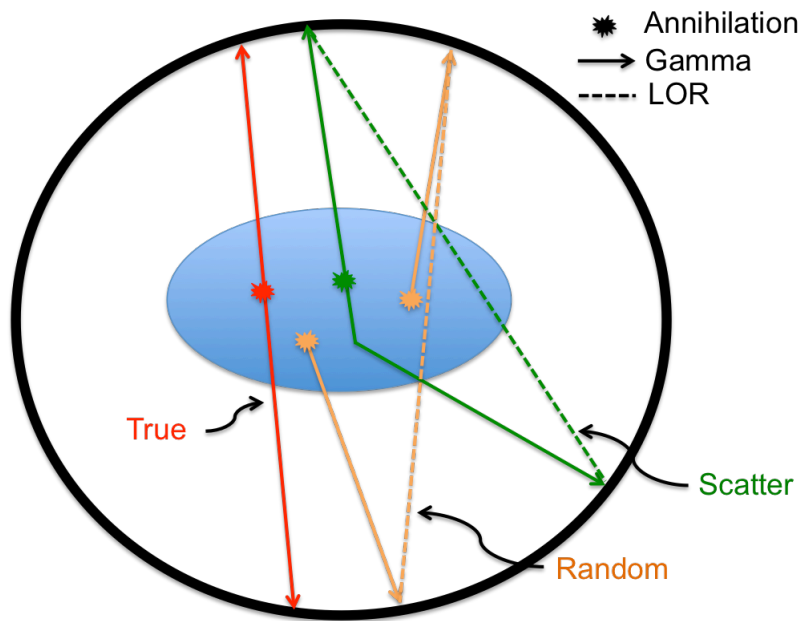


Figure 1.1: Diagram illustrating true, scattered, and random coincidence events.

1.2.4 Signal Detection

While the information of interest in PET imaging is the distribution of positrons that are emitted by the patient, these cannot be imaged directly. Instead, the signal that is detected is composed of the annihilation photons that are created by the positrons; information carried by these photons is then used to determine the positron distribution within the patient.

Annihilation Photon Detection

The emitted coincident photons must be detected by the PET scanner and further processed to determine positioning and timing information. Detection of the 511-keV photons in commercial scanners takes place using scintillators that convert the energy of the annihilation photons into scintillation photons that may be detected by a photodetector, which then converts the scintillation photons into electrical current. Importantly, scintillators and photodetectors both perform their conversion such that their output is proportional to the input energy. The photons involved in nuclear medicine may interact with the scintillator in essentially two different manners. The photons may undergo Compton scatter, by which they scatter off of free electrons, with the Klein-Nishina formula describing the scattering cross section as a function of scattering angle. Photons may also be totally absorbed by bound electrons through photoelectric absorption, leaving a photoelectron with most of the photon energy. Because all of the photon energy is deposited in the photoelectric interaction, and the energy is delivered in a single location, these interactions are more useful for PET imaging. Figure 1.2 shows the attenuation coefficients of LSO, which is a common scintillator in commercial PET

scanners that will be discussed later. Photoelectric interactions are more likely for lower energies and materials with higher atomic number; at 511 keV, Compton interactions are more prevalent, and play a large role in the performance of the detector.

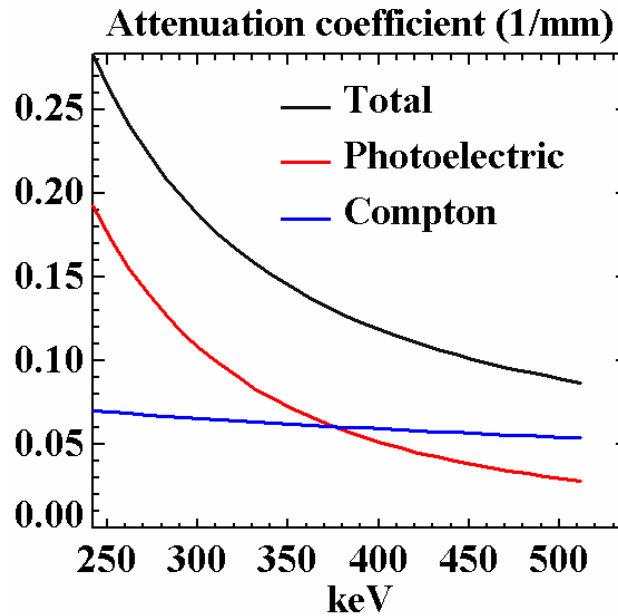


Figure 1.2: Plot of attenuation coefficient vs. photon energy for LSO. At 511 keV, Compton interactions are more likely than photoelectric interactions for this scintillator (Source: [32]).

Coincidence Detection

PET imaging uses timing information to differentiate coincidence events. Once an event is triggered in one detector, the electronics determine if another event has been registered within a fixed time difference from the first event; if so, the events are considered to be coincidence events, and are kept and further processed. A typical PET detector diameter is ~80-90cm with a 60cm field-of-view, so that detected photons may arrive at their opposing detectors as much as ~2ns apart from one another; because

detectors have a finite timing resolution, the measured timing distance τ is larger than this value. The total timing gate in a commercial PET scanner is typically given by $2*\tau = \sim 5\text{-}6\text{ns}$, to ensure that all true coincidences may be collected [33]. Recent developments in photon detection (e.g., on the Philips Vereos scanner [34]) or the use of faster scintillators (e.g., on the experimental LaPET scanner [35]) allow for shorter (4-ns) timing windows.

1.2.5 Modern PET/CT Scanners

The vast majority of clinical PET scanners are PET/CT scanners, in which the PET scanner and CT scanner are located next to one another (i.e., they are not concentric) and use a single bed, so that the two scans may be performed sequentially with the patient in the same position. This modality has the advantage that the PET image may be easily registered with the CT image, combining the metabolic information of PET with the anatomic information of CT; additionally, the CT scan serves as a relatively fast transmission scan for attenuation correction. The PET scanner is typically composed of several rings of detectors, with a patient bore $\sim 70\text{-}90\text{ cm}$, and an axial field-of-view $\sim 15\text{-}22\text{ cm}$, depending on the system; the CT scanner features a patient port similar in size to that of the PET scanners. Each ring of the PET scanner consists of dozens of detector modules, each of which is composed of scintillator pixels coupled to a photodetector (discussed later). Modern scanners operate exclusively in 3D mode, where the modules are not separated by septa axially and oblique LORs are collected, because of the vastly improved sensitivity. A typical whole-body PET/CT scan will last 15s-1min for the CT scan and 10-20 minutes for the PET scan.

Additionally, PET/MR scanners have been recently introduced into the clinical market, in which the MR scanner has replaced the CT scanner as the anatomical scanning modality. In these systems, the MR scanner is axially adjacent to the PET scanner, as in PET/CT scanners, or the PET scanner is located within the MR scanner, allowing for simultaneous acquisition of data. These systems hold a number of potential advantages, including:

1. The combination of the excellent soft tissue contrast of MR scanners with the metabolic information of PET scanners.
2. The elimination of the dose inherent in CT scanning.
3. The potential for simultaneous acquisition of the PET scan and MR scan, eliminating discrepancies caused by the delay between the long PET scan and the relatively quick CT scan.
4. The opportunity to use the unique information offered by MR scans, including functional information and dynamic (e.g., blood flow) [36].

1.3. Image Quality in PET: Challenges in Scanner Design

1.3.1 Spatial Resolution

Spatial resolution describes the ability of an imaging system to distinguish two objects from one another, or the smallest object that may be imaged clearly. A more rigorous definition for the resolution is the point spread function (PSF): the response of the imaging modality to an infinitesimally small source, approximated experimentally by a small drop of radiation. This response may be mathematically described in a number of different ways, though the most common is the full width at half maximum (FWHM),

defined to be the width of the PSF at one half of the maximum value, and the full width at tenth maximum (FWTM). While the most fundamental limit for resolution for any imaging modality is set by the wavelength of the light being imaged, there are a number of other factors that further limit the resolution for PET scanners [2-5]. The overall spatial resolution is often approximated by combining the various effects in quadrature [37].

Detector Resolution

For pixelated detector systems that consist of arrays of small crystals, the most important factor in the overall resolution of the scanner is the width of the crystal, which limits the intrinsic detector resolution at the center of the scanner to $\sim d/2$, where d is the width of the pixel; this resolution degrades away from the center, in part because of the geometry of the ring of detectors, as well as for other reasons discussed below. In current scanners, the pixel width is $\sim 4\text{mm}$, leading to an intrinsic resolution of $\sim 2\text{mm}$ at the center of the scanner. This resolution may only be achieved if the 511-keV photons only deposit their energy at one location in the detector; however, Compton scatter is an inevitable source of blurring, since it leads to the deposition of energy in more than one location. For most modern scanners, which typically employ Anger logic to position events, scattered events that deposit enough energy in the detector will be positioned by essentially averaging the positions of the primary and scattered interactions, weighted by the energy deposited, thereby mispositioning the coincidence event. Figure 1.3 shows the result of a simulation study in which a gamma beam was directed normal to and at the center of a $50 \times 50 \times 25\text{mm}^3$ detector, and an ideal Anger position along one transverse

dimension (i.e. the x-direction in the figure) calculated by averaging the positions of the interaction locations in the crystal (scattered and photoelectric), weighting by the energy deposited. While $\sim 60\%$ of incident 511-keV photons will Compton scatter in common clinical scintillators [38-39], most events are still positioned within 2mm of the center, so that Compton scatter primarily affects the tails of the point spread function, quantified by the FWTM. The effect of scatter on the PSF degrades contrast in images, and will limit the gains achieved by using smaller pixels, although simulation studies show that decreasing the size of the pixels from 4mm to smaller sizes results in an improvement in resolution, as measured by the FWHM [40].

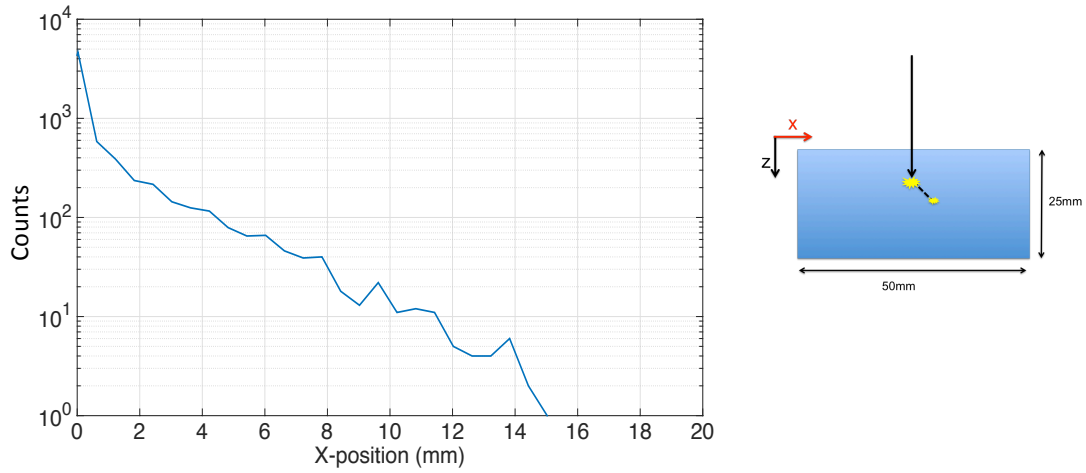


Figure 1.3: Logarithmic histogram (left) of calculated Anger position along a transverse axis (i.e. x-direction), for events of a simulation in which a gamma beam was directed normal to a $50 \times 50 \times 25 \text{ mm}^3$ crystal surface (right). Because most events are still positioned within 2mm, Compton scatter primarily affects the tails of the PSF.

Position sampling

According to the Shannon-Whittaker sampling theorem, a function may be faithfully represented if sampled at twice the bandwidth of the function. For PET, this translates to representing an image from the scanner by including enough LORs to sample the imaging space [41-42]; roughly, three samples for FWHM (empirically determined) are required to fully recover the resolution. For pixelated detectors, each LOR connects two pixels, so that the sampling density for a pixelated detector is determined by the pixel size. The pixel size therefore imposes additional limitations on the spatial resolution of the system than the intrinsic resolution discussed earlier. First, the maximum detector resolution of one half the pixel width cannot be achieved, even in the absence of other resolution degrading effects, because images may only be sampled in discrete increments of $d/2$ (Figure 1.4 left). Second, because the numbers of LORs that pass through an image voxel varies depending on the location and size of the voxel (Figure 1.4 right), the overall resolution of the system is degraded, depending on the crystal geometry; sensitivity corrections are performed during image reconstruction to correct for the variations in the density of LORs. Because the size of the basis function (voxels or blobs) may not be too small given the sampling density of the LORs, the position sampling also imposes a limit on the smallest size of the basis function that may be used, without introducing aliasing artifacts into the image [37, 41]. While early systems implemented a wobbling technique, by which the detector rings were shifted slightly to improve the sampling capability, this is no longer implemented in favor of simpler and faster scans in which the scanner is stationary. The sampling density may instead be improved for pixelated systems by decreasing the pixel size or adding

information regarding the depth at which the events interact, in order to increase the number of distinct LORs measured.

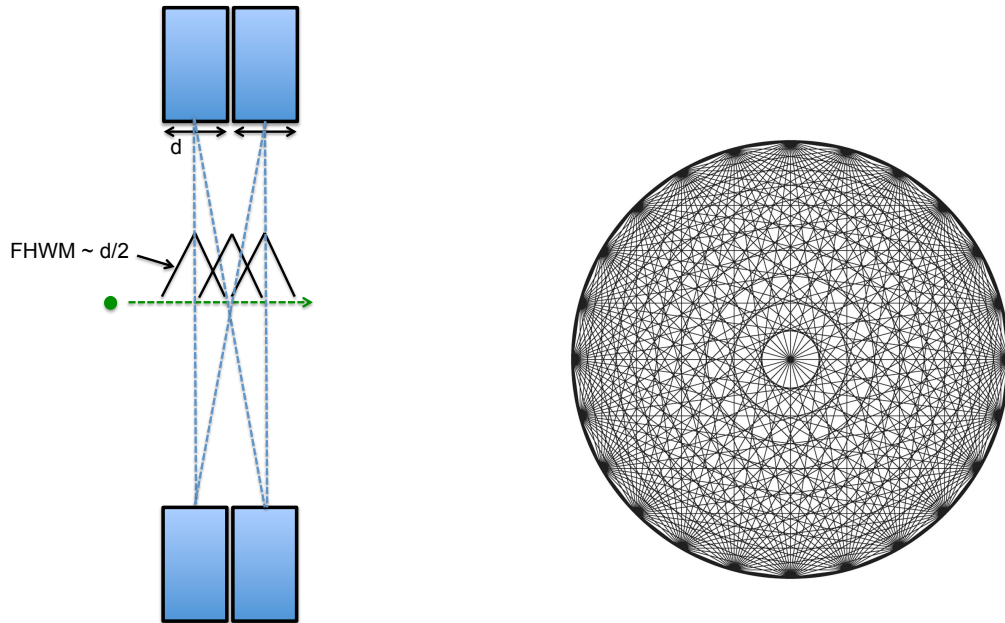


Figure 1.4: Impact of discrete position sampling. Left: Limited sampling prevents the scanner from achieving the maximum detector resolution at the center of the scanner. Right: Lines of response connecting the crystals (represented by dark spots at the perimeter) for a PET scanner; these lines sample the image space non-uniformly (Source: [37]).

Physics Limitations

There are two limitations imposed by the physics of positron annihilation on the resolution in PET scanners. The first is the positron range effect, which results from the non-zero kinetic energy of a positron after ejection from the nucleus. The positron therefore travels a short distance before annihilating with an electron, with the probability distribution of the distance traveled determined by the maximum kinetic energy of the

positron, which in turn is specific to the isotope; note that this distribution is not Gaussian (Figure 1.5). For a lower energy isotope such as ^{18}F , the effect of the positron range is relatively small, with a distribution of $\sim 0.1\text{mm}$ FWHM and $\sim 1.0\text{mm}$ FWTM; for a source such as ^{68}Ga , with a higher maximum kinetic energy, the positron range has a larger effect on the achievable resolution. The second limitation is acollinearity, which results from the nonzero momentum of the positrons before annihilation: conservation of momentum implies that the pair of 511-keV photons produced will be emitted at slightly less than 180° from one another. For ^{18}F , the distribution of the deviation from perfect collinearity is $\sim 0.2^\circ$ in FWHM, and has been found empirically to result in a blurring of

$$\text{FWHM} = 0.0044 \cdot R, \quad (1.1)$$

where R is the radius of the scanner [43-44]; for a typical scanner radius, the FWHM is $\sim 1.8\text{mm}$.

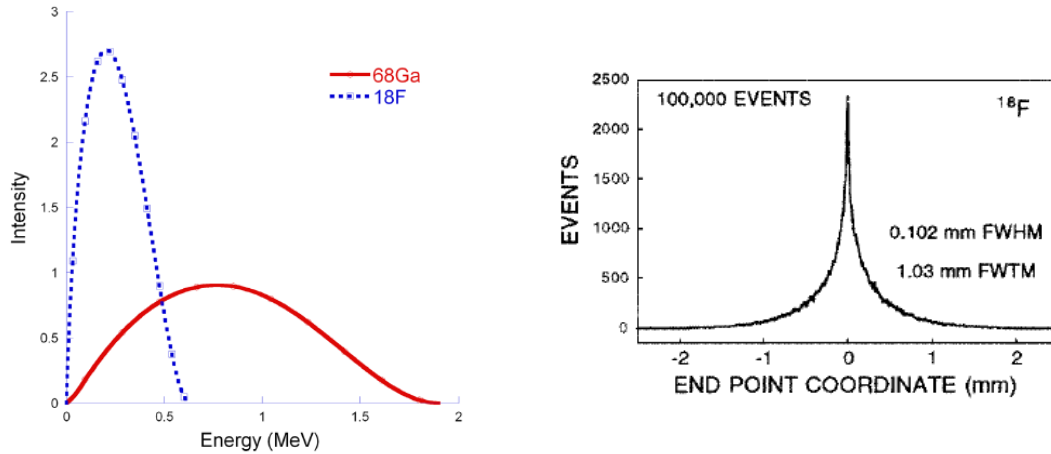


Figure 1.5: Energy of emitted positrons and effect on spatial resolution. Left: Histogram of positron energy after decay for two isotopes (Source: [44]). Right: Distribution of total distance traveled by ^{18}F positrons in water, leading to a spatial blurring (Source: [43]).

Depth-of-Interaction

Events that occur radially offset from the center of the detector will interact with pixels at an oblique angle, as depicted in Figure 1.6. Without knowledge of the depth at which the 511-keV photon interacts in the detector, known as the depth-of-interaction (DOI), the event is inaccurately assumed to have interacted at a fixed depth (i.e., front face of the detector), resulting in another source of uncertainty in the measured LOR, which is described by a Gaussian of width equal to

$$\text{FWHM} = \frac{12.5 r}{\sqrt{r^2 + R^2}}, [37] \quad (1.2)$$

with r equal to the radial offset and R the radius of the scanner.

The blurring that results from parallax therefore increases with radial distance and decreases as scanner radius increases. For a scanner with 4-mm pixels, the resolution can degrade by ~40% at 20cm from the center of the scanner (Figure 1.6 right) [45-46]. While this effect is large enough for small animal scanners (diameter ~10-20cm) that efforts are made to correct for it, no commercial whole-body scanner measures and corrects for this effect.

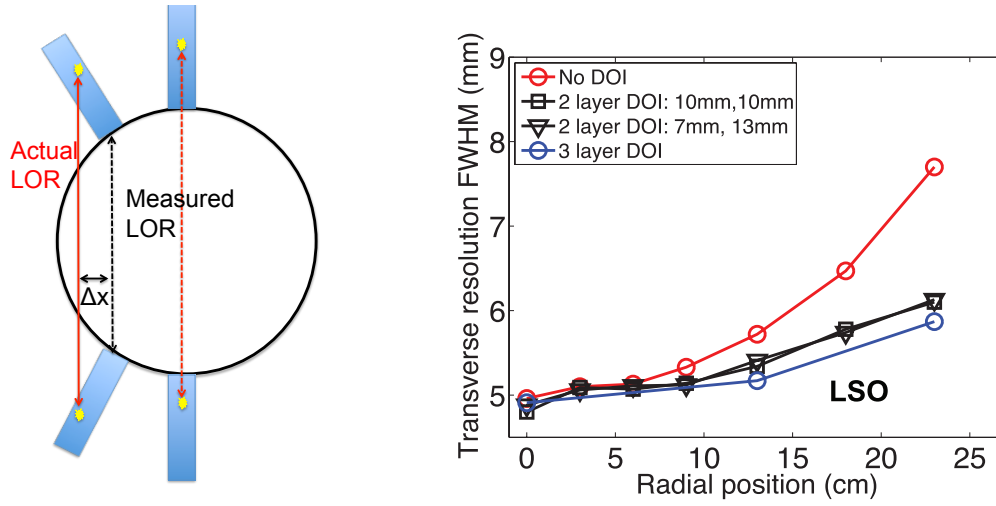


Figure 1.6: Parallax error and effect on spatial resolution. Left: Diagram depicting parallax error resulting from LORs radially offset from the center of scanners. Right: Simulation study, showing degradation of spatial resolution with radial distance (red curve) and improvement in resolution after correcting for DOI (Source: [46]).

Multiplexing

Scanners using block detectors typically employ more pixels than photodetectors, in order to reduce the complexity and cost in the electronic readout. The effect of this on resolution has not been quantified, but is close to a Gaussian of width equal to one third of the pixel width, depending on the geometry of the detector [37]. Scanners employing one-to-one coupling avoid this additional source of resolution loss [34].

1.3.2 Signal-to-Noise Ratio

Noise is another important aspect of an image, which may be quantified using metrics such as the signal-to-noise (SNR) ratio or contrast-to-noise ratio; noise may arise in different manners, including in the form of structured noise, resulting from imaging artifacts, or statistical noise, resulting from the Poisson nature of radioactive decay and

radiation detection, and the finite number of counts collected in an image. Focusing on one of these metrics, SNR is dependent on the number of true counts collected by the scanner, and may therefore be increased by collecting more events in total, or accepting a larger fraction of true events (i.e., excluding more scattered and random events). The SNR is therefore affected by a number of scanner parameters [2, 41].

Sensitivity

The sensitivity of the scanner describes the fraction of radioactive decays that occur that are detected by the scanner. This metric is the result of a geometrical and intrinsic component; the true count rate is given by:

$$R_{true} \sim \varepsilon^2 g,$$

where R_{true} is the count rate of true events, ε is the efficiency of the detectors, and g is the geometric efficiency of the scanner [41].

The geometric efficiency is a function of the geometry of the scanner, in particular its diameter and axial extent. One of the most recent research efforts in the field is therefore the development of a long axial field-of-view scanner, to be built with an axial field-of-view of 200cm (compared to ~18cm for typical clinical scanners), thereby potentially improving sensitivity by a factor of ~40 [45-46].

The intrinsic sensitivity of the scanner is a function of:

1. The absorption efficiency and thickness of the crystals (ε), which determines how likely an event that traverses a pixel will be detected: $\varepsilon = 1 - e^{-\mu T}$, where μ is the attenuation coefficient of the crystal and T is the thickness of the detector. Pixels in modern scanners are ~20mm in thickness.

2. The fraction of the detector modules that are composed of crystal (packing fraction).

At high count rates, the count rate of the system will also be affected by the dead time of the system, defined as the finite time after which the system detects an event during which it cannot process another event. The dead time is itself a function of the crystal (e.g., decay time of the scintillators) as well as the number of photomultipliers that share light from a scintillation pixel. Because of the finite dead time, the count rate depends on the activity being imaged as well.

The sensitivity of typical scanners is $\sim 7\text{-}10$ cps/kBq (measured using a thin line source near the center of the scanner); with a typical injected dose of ~ 600 MBq, $\sim 90\%$ of events removed by attenuation and a significant fraction of events removed by the energy gate, the count rate for a typical patient scan is $\sim 100\text{-}200$ kcps. A PET scanning procedure consists of several individual scans of different regions of the body, acquired by fixing the bed at a given position in the PET bore to acquire enough counts, and then translating the bed to the next position for the next acquisition. The count rate of the scanner allows scans at each bed position to be $\sim 1.5\text{-}3$ min to be clinically useful, with the total scanning procedure (all bed positions) summing to $\sim 10\text{-}20$ min [37, 47-49].

Energy Resolution

Gating on the energy of the detected events allows for scattered events to be rejected, decreasing the bias caused by scatter and improving the SNR of the image. A number of factors degrade the ability of the system to measure energy, including: the

statistics of the finite number of scintillation photons created and collected as well as the statistics associated with photoelectron production in photodetectors, noise associated with the photodetector, and nonuniformities in the luminosity and surfaces of the scintillation crystals. The finite energy resolution leads to a broadened energy spectrum, forcing a wide gate around the photopeak to capture the photoelectric events; typical values of energy resolution for modern scanners are 10-13% at 511 keV [41, 50], and typical energy gates are in the range of 440-650 keV.

1.4 Image Reconstruction

Reconstruction algorithms interpret the positioning and timing information provided by the detectors into an image, and are divided into two categories: analytic reconstruction algorithms and statistical reconstruction algorithms. Analytic algorithms view the data as deterministic and operate by backprojecting the measured LORs, which are assumed to be line integrals of data, to form an image; these offer the advantages of simplicity and computational speed. Iterative algorithms are capable of modeling the deviations from the assumption that the LORs are simple line integrals of data, including the spatial blurring brought about by the finite resolution of the scanner as well as statistical noise associated with the measurement procedure and physical effects. Solutions to reconstruction algorithms using these more complex models cannot be found analytically, however, requiring longer, iterative solutions that repeatedly update the image to better match the measured data [51]. Iterative algorithms are used almost exclusively in the clinic because of the improved signal-to-noise ratio and the capabilities of faster computers [4], and will be described in more detail in Chapter 5.

1.4.1 Data Corrections

In order to produce images that reflect the true distribution of activity within the patient, the data that are acquired on a PET scanner must be corrected for various effects related to the physics involved in the detection of annihilation radiation within a patient and to the design of the scanners. These include an attenuation correction, in order to correct for events that are absorbed as a function of LOR; a scatter correction, to correct for the 30-65% of emitted events that are scattered within the patient body; a correction for random coincidences; and a normalization correction, to correct for nonuniformities in the many scintillators and photodetectors involved in a PET scanner, as well as the geometrical nonuniformities in the LORs as a function of radial position [4, 33, 41]

1.4.2 Impact of Image Reconstruction on Image Quality

The trade-off between image spatial resolution and noise is also strongly dependent on the specific image reconstruction used. Analytic algorithms employ filters to control noise in the images; however, the choice of cutoff frequency introduces a trade-off between noise and spatial resolution, as with the common Hanning and Shepp-Logan filters that suppress high frequency noise. Iterative algorithms similarly show an inherent trade-off between resolution and noise: as the algorithms are iterated longer, the quantitative accuracy increases (until convergence is reached) at the cost of increased noise. Additionally, the models (e.g., modeling of positron range and attenuation, PSF modeling, the statistical model of photon detection) used in the algorithm as well as the post-filters applied afterwards strongly affect the resolution. Two common examples are the Gaussian smoothing post-filter, which is used to control noise but which necessarily

degrades resolution, and the increasingly common point spread function (PSF) modeling and deconvolution post-filters that improve resolution at the cost of increased noise and the potential for edge enhancement [52-59].

Incorporation of TOF information into the reconstruction additionally improves the SNR of an image, resulting in an effective increase in counts. The TOF resolution describes the precision with which this measurement is made, with one common metric being the FWHM of the timing histogram from a point source measurement. TOF resolution is affected most by the scintillator (especially the light output), the photodetector (noise inherent in photoelectron generation), and the detector configuration. Common current clinical scanners have a resolution of 500-650ps (compared to a maximum TOF difference for a 60cm field-of-view (FOV) of ~ 2 ns), while the Philips Vereos and the experimental LaPET scanners have a TOF resolution of <350 ps [34-35, 60].

1.5 Quantitation in PET

PET/CT has become an established imaging modality in part because of its quantitative ability. In the context of medical imaging, quantitation refers to the use of quantifiable aspects of an image in order to assess normalcy, the status of a disease or injury, or a change in such status. In order for an imaging modality to be sufficiently and usefully quantitative, it must produce images that are sufficiently accurate, precise, and clinically relevant; furthermore, these values (and the images from which they derive) must be properly acquired and interpreted. The quantitation of PET/CT relies on the relation between each voxel value and the concentration of radioactivity at that location,

which is related to some clinically relevant feature; for ^{18}F -FDG PET/CT, these voxel values are related to glucose metabolic rate. Furthermore, the clinical utility of this modality derives from the unique role that metabolic information plays (e.g. this is often a better indicator of response to therapy than anatomic information alone) [5].

1.5.1 Metrics

Interpretation of the data offered by PET/CT images is accomplished by calculating metrics at appropriate locations within the images. There are a number of such metrics that have become popular and have been studied for their utility: standardized uptake value (SUV), contrast recovery coefficient (CRC), metabolic tumor volume (MTV), total lesion glycolysis (TLG), and various textural features. These metrics ultimately find use in the clinic by connecting their values to clinically relevant features. Two of these metrics, SUV and CRC, are used in this thesis, and are discussed in more detail below.

SUV is the most popular metric used for PET/CT and is used as a normalized measure of counts/voxel/min (e.g., related to glucose concentration for ^{18}F -FDG studies) to help differentiate normal (SUV ~ 1) from abnormal tissue. While the use of SUV is well defined for ^{18}F -FDG, whose concentration is trapped in tissue and thus considered to be equilibrated after some time, for other tracers, these assumptions may not hold. It is generally defined as:

$$\text{SUV} = \frac{S}{kA}, \quad (1.3)$$

where S is the radioactivity concentration in a region or voxel, A is the decay-corrected activity injected into the patient, and k is a normalization constant [61]. Three popular

normalization constants are: body-weight (the most widely used), body surface area, and lean body mass. A number of options exist for computation of the radioactivity concentration as well, often involving drawing a region of interest (ROI) around the area or volume of the image to be quantified; note that when the ROI is three dimensional, it may be termed a volume-of-interest (VOI). The three most widely used metrics are: maximum SUV (SUV_{max}), defined as the maximum concentration of the voxels within the ROI; mean SUV (SUV_{mean}), defined as the average concentration within the ROI; and peak SUV (SUV_{peak}), defined as the mean concentration of a small volume within the ROI (e.g., a 1-cm³ spherical volume centered on the maximum voxel). There is no clear consensus regarding which metric is best for clinical assessment, as each has advantages: SUV_{max} is the easiest to implement (requiring no exact tumor delineation), is not prone to inter-observer variability, and does not suffer as much from the partial volume effect (described below); SUV_{mean} incorporates information from the entire tumor and is less susceptible to noise but is affected by the partial volume effect; and SUV_{peak} offers a compromise between the two. The usefulness and importance of accurate quantification of these metrics can be demonstrated by the SUV, for which a number of strategies have been devised to determine how best to use this metric, including PERCIST for oncologic imaging [61]. For example, SUV_{max} may be tracked to monitor treatment and to determine the likelihood for progression-free survival [62-66].

CRC has found use in phantom scans, in which a known distribution of radiation is measured, as a means to assess the degree to which a scanner faithfully reproduces contrast in an image. It is defined as:

$$CRC = \frac{\frac{S}{B_{local}} - 1}{A - 1}, \quad (1.4)$$

where S is the lesion uptake (activity concentration), B_{local} is average value of the local background, and A is the true activity ratio [67]. Note that with this definition, perfect contrast recovery corresponds to a CRC value of 1, while no recovery (i.e., the lesion is indistinguishable from background) corresponds to a value of 0.

In this work, S was chosen to be either the average voxel value within the lesion, calculated using a VOI of the same diameter as the lesion and centered over each lesion (for CRC_{mean}) or the maximum voxel value within the VOI (for CRC_{max}). Because CRC requires knowledge of the true contrast ratio, it is not typically used for patient studies. Nevertheless, both CRC and SUV are scaled estimates of lesion uptake, so CRC is often an appropriate surrogate for SUV.

1.5.2 Partial Volume Effect

The partial volume effect (PVE) is an inherent limitation in quantitation for PET scanners that encompasses two separate effects (Figure 1.7). The first results from the finite spatial resolution of the PET scanners: the blurring (convolution) caused by the finite resolution causes counts to spill out from a structure to the background and spill in from the background to the structure. The second effect is termed the tissue fraction effect and results from the finite sampling of the images that occurs when the images are displayed using voxels (voxelized): a given voxel at the edge of a structure will contain parts of the structure and parts of the background; because each voxel has only one value, the voxel will represent an average of the two regions. These effects act to degrade the contrast of the image and cause small objects to appear more spread out and dimmer.

PVE therefore affects both the qualitative appearance of lesions and the quantification of images (e.g., SUV_{mean} and SUV_{max}). PVE is a function of the spatial resolution of the system, the size and shape (surface area) of the ROI, the background, and the voxel size. Because PVE can cause severe discrepancies in the quantification of lesions and detectability [68-71], a number of correction algorithms have been devised to compensate for this effect [54, 57, 69, 72-73].

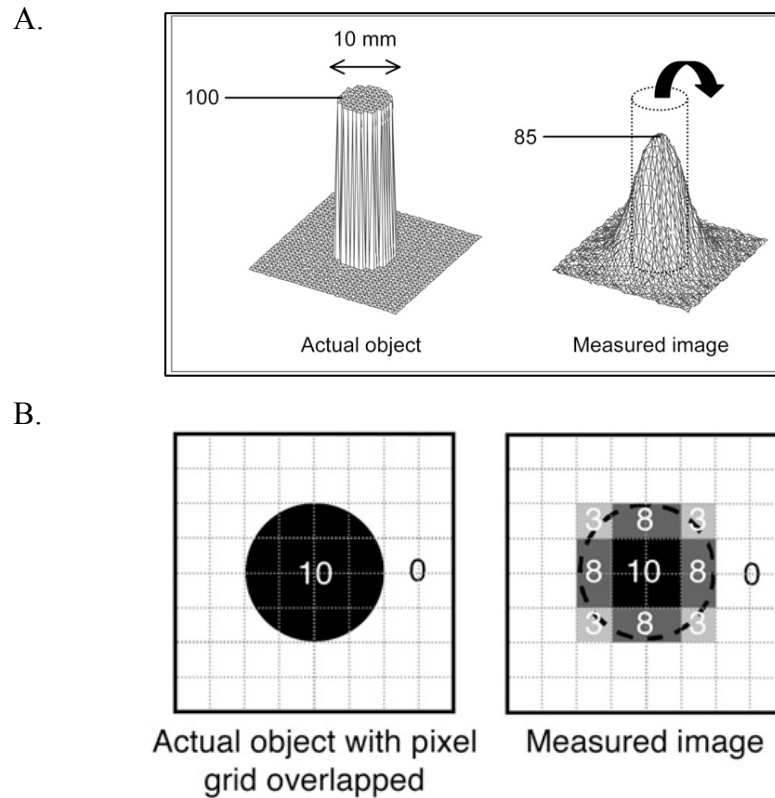


Figure 1.7: Diagram of the partial volume effect. A. Spill-over resulting from the finite spatial resolution that leads to counts within an ROI being placed in the background region. B. Tissue fraction effect resulting from voxelization of image, leading to voxels that are an average of the radioactive concentration in multiple regions (Source: [68]).

1.5.3 Factors Affecting Quantitation

Separate from PVE (i.e., spatial resolution and size/shape of ROI), a number of factors influence the ability to absolutely quantify images during clinical evaluation by introducing biases and degrading precision. Limitations in the quantitative performance of the scanner in turn affect both the clinical use of metrics, such as SUV, that are measured from an image, as well as the statistical power of a research study that uses quantitative information. These limiting factors can be broadly classified into a few categories [74-75].

1. Physiological factors related to the patient (e.g., the plasma glucose level at the time of scanning for ^{18}F -FDG PET/CT and the time interval between the FDG administration and scanning (uptake period)).
2. Technical factors related to the scanning (e.g., the method of attenuation correction, scan duration).
3. Errors in administration or scanning (e.g., improper scanner calibration).
4. TOF resolution, as improved resolution allows for faster convergence of the image reconstruction and therefore of metric quantification.
5. Image reconstruction factors, including:
 - A. Reconstruction algorithm: many different choices exist, including filtered backprojection and iterative algorithms with a number of different models, which each have different effects on quantitative accuracy.
 - B. The number of iterations for iterative algorithms: in general, as the numbers of iterations increases, the accuracy of the images increases, while the noise of

the images increases as well. In the clinic, reconstruction is stopped prior to full convergence in order to produce less noisy images.

C. Point spread function modeling: Iterative algorithms may model the effect of the finite resolution of the detector during reconstruction, generally improving accuracy at the cost of increased noise.

D. Post-reconstruction filter: As discussed previously, post-filters exist that may degrade resolution (and exacerbate the PVE) to smooth the image or may improve the resolution at the expense of noise.

1.6. PET Detectors

1.6.1 Information Measured by Detector

The detector serves to measure the information needed to localize the events; the output of the detector is information regarding the energy, position, and time-of-flight of the coincident photons:

1. Energy information is used in order to minimize the fraction of scattered and random events that are positioned.
2. The position that each photon event is used to determine the LOR.
3. Given the finite timing resolution of TOF PET/CT scanners, information regarding the difference in the arrival times of the two photons is also used to reject random events, and to further localize the event (Figure 1.8) and confine noise to a smaller region during back-projection in image reconstruction. The end result is an improvement in SNR, particularly for larger patients (for whom

attenuation is more likely and thus fewer photons are detected), as well as an improvement in the speed of image reconstruction convergence for iterative algorithms [33, 38, 47, 76-83].

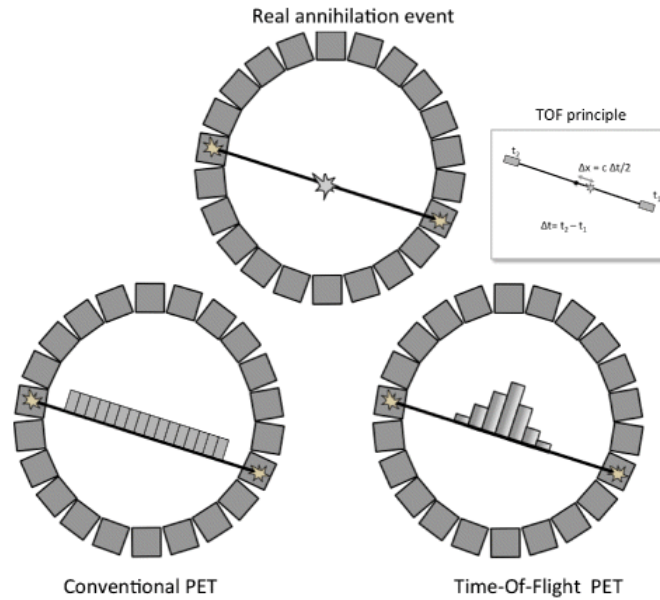


Figure 1.8: Diagram depicting the improvement in the localization of events with TOF information (Source: [47]). TOF information is used to improve the noise characteristics of an image.

1.6.2 Detector Components

Scintillators

A number of gamma detectors have been and continue to be investigated for PET, including semiconductors (e.g., CdTe and CZT), Liquid Xenon, and ceramics (e.g., GluGag); however, all modern detectors for whole-body PET are based on inorganic scintillators, and so the discussion will be focused on this technology. Scintillators

function in nuclear medicine imaging to convert the energy of gamma rays into light that is collected by a photodetector, and may be broadly classified as either organic or inorganic. Organic scintillators make up a large variety of scintillators, including liquid and plastic scintillators; however, because of their improved detection efficiency, all scintillators used for clinical scanners are inorganic, and the discussion henceforth will be limited to this type. For these scintillators, excited electrons result in three types of scintillation: 1. An electron excited from the valence band to the conduction band, leaving electron-hole pairs, may return to the valence band, resulting in fluorescence. 2. An excited electron forbidden from returning to the ground state absorbs thermal energy, resulting in phosphorescence, which generally has a longer wavelength and a longer characteristic decay time. 3. Quenching, in which a transfer of thermal energy from certain excited states to the ground state occurs without radiation and again with a long time constant, resulting in a decrease in conversion efficiency and long afterglow. Activator dopants are often added to these scintillators to create energy levels in the forbidden gap, in order to increase the efficiency of scintillation and allow the wavelength of the emitted photons to be in the visible range as the electrons return to the valence band [50].

The qualities that make up an ideal scintillator are: high sensitivity (high density), a high light output (to improve energy and timing resolution), a large fraction of incident photons converted to prompt fluorescence, scintillation light that is transparent to the scintillator (to avoid reabsorption) and compatible with the photodetector absorption spectrum, an output that is proportional to the energy of the incident photons over a wide range, short decay time (both to limit the coincidence window and to improve TOF

resolution), a refractive index close to that of glass (the photodetector encasing), as well as good properties for commercial manufacture (i.e., cost, availability, ease of manufacturing). No scintillator exists that maximizes performance in each category, requiring a trade-off in performance; some of the most common scintillators with relevant characteristics are shown in Table 1.2 [21, 47, 83-84].

Table 1.2: Properties of some of the scintillators used for PET.

Scintillator	Relative Light Output	Density (g/cm ³)	Decay Constant (ns)	Attenuation Length for 511 keV (mm)	Max Emission Wavelength (nm)
NaI (Tl) (Thalium-doped Sodium Iodide)	100 (~38000 ph/MeV)	3.67	230	23	410
BGO (Bismuth Germinate)	15	7.13	300	10.4	480
LYSO (Cerium-doped Lutetium Yttrium Oxyorthosilicate)	75	7.3	40	11.4	420
LaBr₃ (Lanthanum Bromide)	160	5.29	15	22.3	380
GSO (Gadolinium Oxyorthosilicate)	19	6.71	30-60	14.1	440

Cerium-doped Lutetium Oxyorthosilicate (LSO) was introduced in the 1990's, and Cerium-doped Yttrium Lutetium Oxyorthosilicate (LYSO) later; since then, the quality of their production has improved enough that they are the most common scintillators used in current clinical scanners, because of the good balance between high

light output, fast decay time, high density, and an emission spectrum that matches the absorption spectrum of common photodetectors well; additionally, its emission does not consist of components with a slower decay time. The performance of these two crystals is generally quite similar, with some studies indicating differences with regard to afterglow, and a slightly lower density for LYSO. These scintillators allowed for the implementation of TOF in modern PET scanners in the 2000's, because the fast scintillation time was paired with a high sensitivity, unlike any TOF scintillator until that point.

LYSO/LSO do exhibit a number of features that must be considered when using them. Both scintillators have an afterglow (phosphorescence) when exposed to radiation, resulting from charge trapping within the scintillator; this afterglow gradually decays with time and requires that the scintillators be shielded from outside light. At the low count rates typically encountered in the lab, this afterglow does not pose a problem, though baseline shifts have been reported at higher count rates. Additionally, because Lu^{3+} is naturally radioactive, these scintillators exhibit a natural background of ~ 300 cts/s/cc, though this does not exhibit a strong effect on the coincidence rate. The light output for these also exhibit a non-proportionality with respect to incident energy, driving their energy resolution to be slightly worse than that of GSO, despite a higher light output [4, 85-91].

Photodetectors

The photodetector converts the energy of the scintillation light into an electrical signal through the photoelectric effect. The SNR provided by a photodetector is a

function of dark (or thermal) noise in the detector as well as the quantum efficiency, defined as the number of electrons produced per incident photon, which determines the noise resulting from the statistical nature of photodetection. The quantum efficiency is determined by a number of factors, including light reflection at the protective glass covering a photodetector; the photocathode material, which determines the absorptive efficiency and reflectivity of the photocathode; and the thickness of the photocathode, which affects both the absorptive efficiency and the number of electrons that escape the cathode. The resolution allowed by the photodetector is a function of sampling width, determined by the sampling pitch of the detector, and the amount of signal averaging, determined by the detector aperture width. The sensitivity of the photodetector is wavelength-dependent and largely determined by the spectral response of the photocathode, which is a function of its composition. Last, another important metric is the pulse rise time resulting from scintillation pulses, determined by the quantum efficiency of the photodetector as well as the electron multiplication scheme. Through the years, photodetectors have evolved greatly in their method of operation, physical design, and performance; details on some of the important current photodetectors are given below [4, 57].

Photomultiplier Tube

The photomultiplier tube (PMT) has been the workhorse of nuclear medicine since its inception. Gains are typically ~ 4 -6 electrons per dynode, resulting in an amplification for 10 stages of $\sim 10^6$ - 10^7 . The maximum quantum efficiency for those typically used is ~ 25 -35%. Some of the advantages of PMTs include their reliability and low noise, with thermal emission of electrons orders of magnitude lower compared to the

current induced by a photoelectric event. Photocathode nonuniformities resulting from variations of photocathode thickness (especially in large area PMTs), result in nonuniform sensitivity, as well as nonuniform collection of photoelectrons at the first dynode depending across the photocathode area [4, 50].

Multianode PMT

Multianode PMTs (MAPMTs), or position sensitive PMTs, offer two benefits compared to PMTs: compact size, with a length of $\sim 12\text{mm}$ compared to the length of a PMT of $\sim 150\text{mm}$; and a grid of anodes that allows for positioning information (Figure 1.9). For the purposes of this thesis, this discussion will focus on the Hamamatsu H8500. A fundamental requirement of position sensitive PMTs is that the process of electron multiplication retains the spatial separation of the original electron cloud resulting from the photoelectric interaction. MAPMTs may be constructed using a number of techniques to do this, including the use of a fine mesh layer to channel the electrons from one dynode layer to the next; the H8500 uses 12 stages of metal channel dynodes that are arranged to channel electrons between layers. To retain the positional information at the anode, each anode is read out separately for the H8500. Recent models are compact, with an active area of $49.7\text{mm} \times 49.7\text{mm}$ (total area of $51.7\text{mm} \times 51.7\text{mm}$), arranged in an 8×8 grid of anodes (each $6\text{mm} \times 6\text{mm}$), and a $\sim 2\text{mm}$ thick window. The cross talk between the anodes is $\sim 1\%$, and the performance metrics for the H8500 (e.g., quantum efficiency, gain, timing, dark current) are comparable to standard PMTs. The gain of the anodes may vary by a factor of 3 within the array, because of both nonuniformities in the thickness of the photocathode and variations in the efficiency in collecting photoelectrons

as a function of emission position; this may be corrected to some extent using gain correction factors. Another disadvantage of some MAPMTs is the presence of nonlinearities near the edges of the detector, resulting in an unusable area that reduces the sensitivity of the detector [92-95]. The MAPMT was chosen for this work because its active area matched the size of the crystals studied in this work well and because of its favorable noise properties.

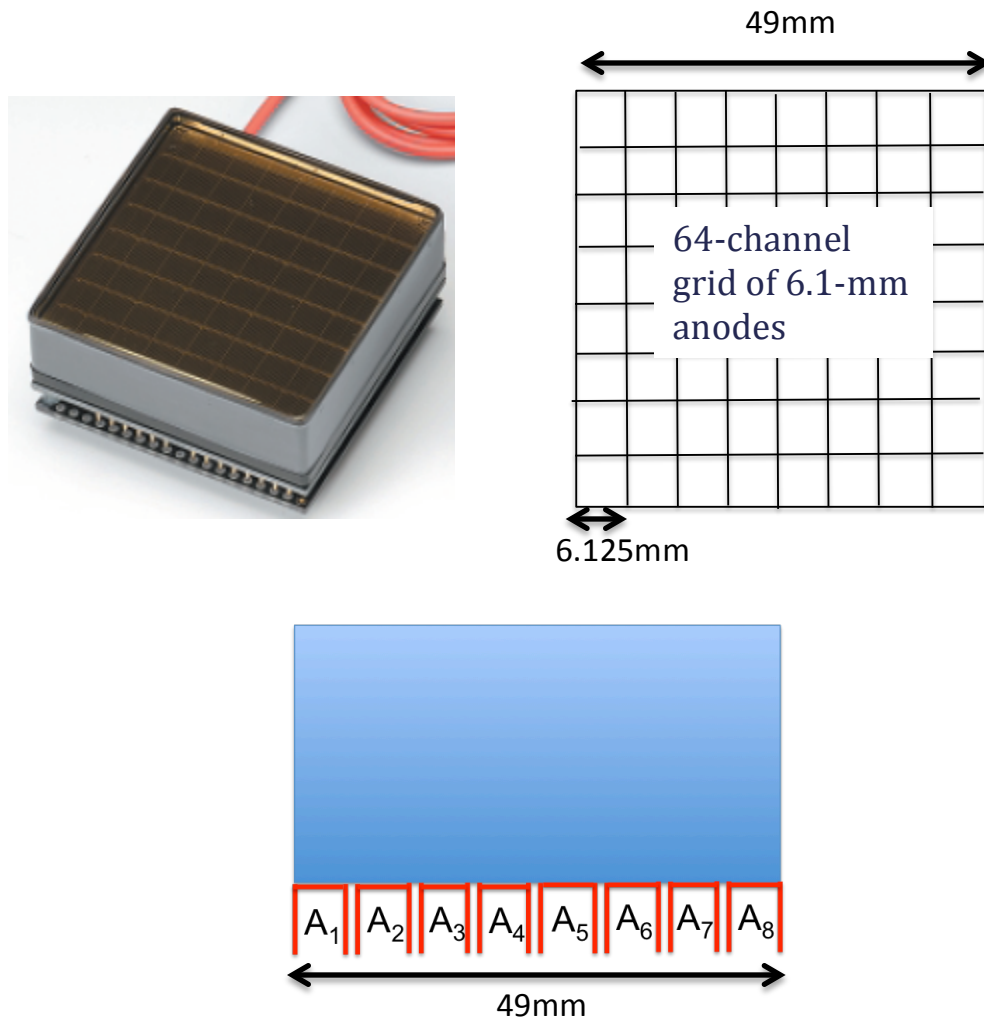


Figure 1.9: Photograph and diagram of the H8500 MAPMT, used throughout this work. Top Left: Photograph of Hamamatsu H8500 MAPMT. Top right: Diagram of the 64-anode layout. Bottom: Diagram of a continuous crystal coupled to the H8500 MAPMT, viewed from the side.

Silicon Photomultiplier

Silicon photomultipliers (SiPMs) detect radiation by using the junction between n-type and p-type silicon, created by doping, to create an electrical current when electron-hole pairs are formed after a photon deposits energy in the photodetector; an electrical field (generated by an applied bias voltage) increases this current. SiPMs used in scanners are designed as a 2D array of pixels ranging from 1-4mm, each divided into thousands of micropixels composed of avalanche photodiodes, which operate in Geiger mode. While each micropixel registers the same output after absorbing enough energy, the collection of many micropixels allows for the output to be linear with total absorbed energy. Since their introduction into the field a decade ago, research into their use has blossomed and produced detectors that offer a number of advantages: compactness, cheapness, insensitivity to magnetic fields (important for incorporation in a PET/MR scanner), high gain (up to 10^6), good timing performance (recent detectors have a timing resolution $<250\text{ps}$ when coupled to small scintillators), and a large quantum efficiency. This has led to the introduction of the Philips Digital Photon Counter, which is a fully digital detector, with electronics (e.g., the analog-to-digital converter) built into the readout chip [16]. Aside from less readout electronics, this detector offers the added advantages of an improved dark count rate and timing performance. The major disadvantages of SiPMs have been the dead area between the pixels, the temperature dependence of the performance, relatively large bias voltage required and the dark count rate, though in recent years the latter has decreased enough that they are used in clinical scanners with cooling [4, 38, 47, 37, 92, 96-99].

1.6.3 Current Detector Designs

The fundamental unit of the PET scanner is the detector, consisting of a scintillator, a photodetector, and potentially a lightguide. These are arranged into modules side by side to form a ring, and several rings are placed together to form the scanner. The diameter of the scanner and the width of the FOV are therefore determined by the number and size of detectors in a single ring, while the axial FOV is determined by the number and size of the rings in the scanner.

The earliest version of current standard detector designs was the block detector [100], a small block of scintillator divided into regions using reflectors that vary in length, becoming longer toward the edge of the block (Figure 1.10 left). The design of the reflectors controls the light spread within the scintillator, depending on which pixel detects an event. There are several designs for the block detector, though one representative example of this detector is from the HR+ scanner from the 1990's, which uses an 8x8 block of pixels and four 19mm PMTs [62].

All current commercial scanners use blocks of fully discrete pixels, coupled to a lightguide that distributes light to an array of PMTs (Figure 1.10 middle). A single module for the discrete detector design would consist of many crystals (e.g., 23x44 array for the Philips Gemini TF and 13x13 for the Siemens mCT) coupled to an array of PMTs. The current standard design of scintillator detectors consists of a group of discrete crystals, each $\sim 4 \times 4 \times 20 \text{ mm}^3$ in dimension with a $\sim 70 \mu\text{m}$ gap between the pixels filled with reflective material, coupled to an array of PMTs $\sim 30 \text{ mm}$ in diameter (e.g., 39mm for the Philips Gemini TF and 25mm for the Siemens mCT). The design of the PMT array is varied in the size and arrangement of the PMTs (e.g., rectangular for the Siemens mCT

vs. hexagonal for the Philips systems), and is carefully chosen since the electronics scheme that reads out the data is tied to this design and is an important determinant in the performance of the system, particularly the count rate capability. As an example, the PMT layout of the LaPET scanner design is shown in Figure 1.11.

Dozens of detector blocks form one ring of the detector, with 2-8 rings forming the entirety of the scanner. Both pixelated and block detector designs operate by using the photodetector signals to determine the pixel in which a 511-keV photon interacts and scintillates; for pixelated designs, the scintillation spread is restricted within the pixel, so that a lightguide is used to spread light to a small region of PMTs to allow for positioning. Event positioning in clinical pixelated systems uses Anger logic (discussed in Chapter 3) [4, 82, 86, 98, 101-102].

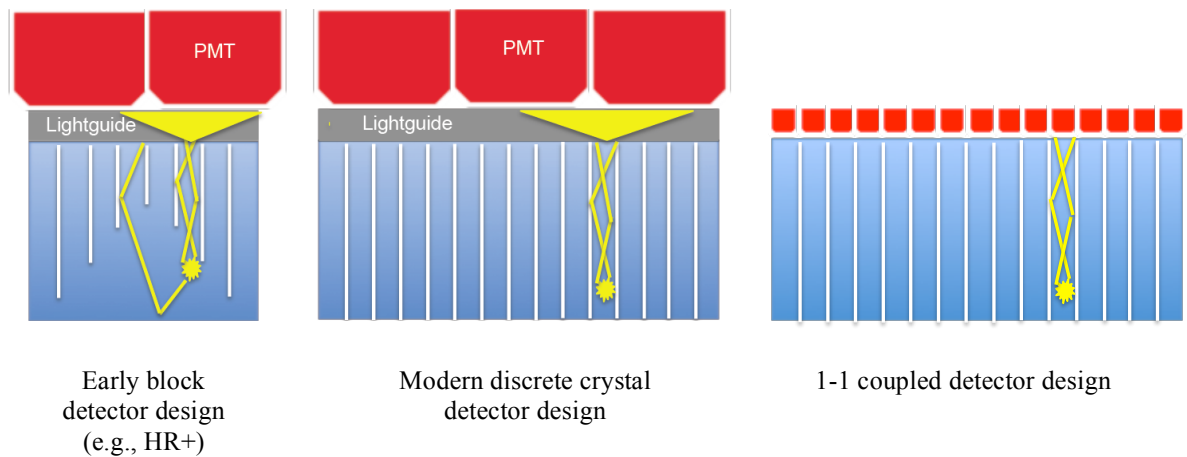


Figure 1.10: Diagram of various block detector designs; all current scanners use fully pixelated arrays read out by large PMTs or arrays of silicon photomultipliers.

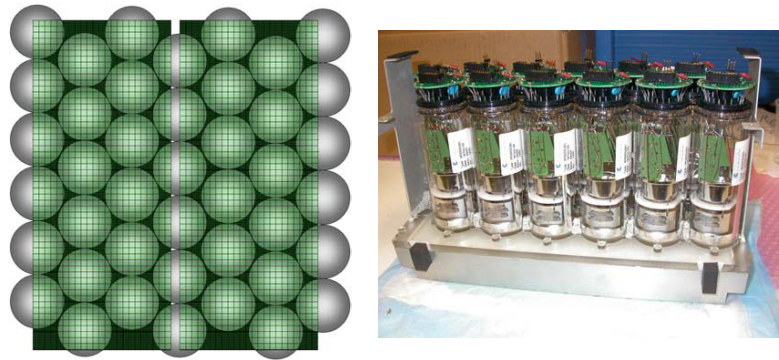


Figure 1.11: PMT layout in detector module in LaPET scanner. Left: Diagram of hexagonal PMT layout with crystals overlaid on top of PMTs. Right: Photograph of a detector module showing PMTs coupled to a lightguide and crystal array (Source: [35]).

The photodetector design has developed rapidly since the introduction of solid-state devices (avalanche photodiodes (APDs) and, later, SiPMs). Using these devices, the Philips Vereos has removed light multiplexing and brought the detector to a one-to-one coupling scheme (Figure 1.10 right), using LSO and a fully digital, compact detector that allows each pixel to be coupled to a single photodetector pixel [34].

1.6.4 Continuous Detectors

Advantages of pixelated systems include the relatively simple positioning scheme employed, a spatial resolution that decreases with pixel size, and good spatial linearity to the edges of the detector. Improvements to the performance of pixelated systems require the use of smaller pixels to improve resolution and position sampling or sophisticated solutions to provide DOI information (e.g., dual sided readout), resulting in necessary trade-offs in complexity and cost. Moreover, the advantages and disadvantages of modifying the pixel size have been studied and are well understood. In recent years, however, there has been a reemergence in interest in continuous detectors, in which

scintillation light from an event spreads within the scintillator and is measured by the photodetector (Figure 1.12); with the use of calibration scans, the photodetector signals may be decoded to determine the position of interaction [38]. The potential advantages offered by this design include: improved spatial resolution relative to that of the standard 4-mm pixels in pixelated systems, without loss in sensitivity; intrinsic DOI information determined by the light spread within the scintillator; continuous position sampling; and improved TOF resolution over typical clinical scanners because of the geometry of the block of scintillator. These come at the cost of more complex positioning algorithms, and a spatial resolution that is directly affected by the thickness of the detector, as explained below.

Earlier PET detectors in the 1980's and 1990's included large area plates of NaI(Tl) ($\sim 50 \times 30 \times 25 \text{ cm}^3$) coupled to arrays of large PMTs; these were limited largely by the poor sensitivity and count rate capability of NaI(Tl) [103]. Current detectors (Figure 1.12) instead consist of small blocks of LSO/LYSO (e.g., $\sim 50 \times 50 \text{ mm}^2$ in cross section and 8-25mm in thickness). The three advances that set current continuous crystal designs apart from the early NaI designs are:

1. The use of the modern scintillators LSO/LYSO, which improves the sensitivity and timing performance.
2. The use of more advanced position-sensitive photodetectors (MAPMTs and SiPMs).
3. More rapid electronics and computing, enabling the use of statistical positioning algorithms (described in Chapter 3).

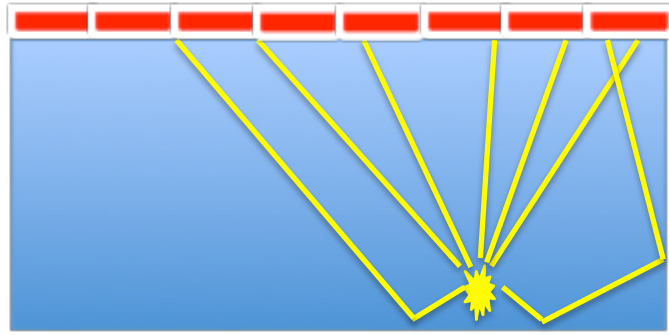


Figure 1.12: Diagram depicting current designs of the continuous detector, using small ($\sim 50 \times 50 \times 25 \text{ mm}^3$) blocks of scintillator coupled to a position sensitive photodetector.

While LSO-based systems allow for TOF information to be exploited, they force the detectors to be smaller than the NaI detectors, since LSO crystals cannot be grown in large slabs; these detectors are typically no larger than $\sim 50 \text{ mm}$ in each transverse direction and $\sim 25 \text{ mm}$ in thickness, leading to poor performance because of the edge reflections resulting from the high thickness-to-width ratio (aspect ratio). On the other hand, the high light output of LSO, along with the advanced photodetectors and electronics, allow for more advanced statistics-based positioning algorithms, which not only perform better than simple Anger logic, but are required to compensate for the small dimensions of the detector. Good performance in these systems relies on both good collection of light in the detector for high statistics and restricted light spread within the detector for proper positioning. In this design, each module would consist of a single block detector read out by a position sensitive photodetector, or potentially several block detectors coupled to one another and read out by several photodetectors. For these small area continuous detectors, the characteristics that affect the detector performance include:

1. The thickness of the detector, which determines the degree of light spread within the scintillator.

2. The aspect ratio of the detector.
3. Surface treatments to the detector, which affect the optical transport within the detector.
4. Scintillator light output.
5. The geometry of the photodetector, since this determines the sampling capability of the photodetector.

While the implementation of this detector design differs vastly from that of pixelated systems, in essence the difference between pixelated systems and small continuous detectors is the extent to which light spreads within the detector: while pixelated systems channel light from an event onto a lightguide that spreads the light locally onto the photodetector array, continuous systems allow light to spread within the detector before reaching the lightguide/photodetector. Continuous detectors, however, offer a very different spectrum of trade-offs in spatial resolution, sensitivity, and position sampling related to the light spread within the detector. In particular, in order to maintain the sensitivity of modern whole-body scanners, thick crystals must be used, degrading the resolution because of increased light spreading. Moreover, because this light spread is depth-dependent, the performance varies with DOI, particularly for thick crystals. Efforts to improve these limitations, however, may come at the cost of a loss of DOI information or degraded position sampling. This thesis is focused on these various trade-offs in the performance of continuous detectors associated with changes in the light spread within the bulk of the scintillator.

CHAPTER 2

Thesis

While all modern commercial PET/CT systems use pixelated detector arrays, current research designs of continuous detectors have demonstrated improved capability with regards to spatial resolution, position sampling, and DOI information. A number of challenges remain, however, most prominently the degradation of spatial resolution with increasing crystal thickness (needed for sensitivity), the depth-dependence of the response of the detector, and poor edge performance. Increased performance for purely continuous crystals comes at the cost of increased complexity, in the form of more photodetectors, increasingly long calibrations and positioning calculations because of more sophisticated positioning algorithms, and an increasing number of electronic channels to read out the data. The fundamental performance of thick detectors, however, may be improved by altering the light spread within the detector, and subsurface laser engraving has recently emerged as a potential technology to allow for this by creating semi-transparent barriers within the bulk of the scintillator, termed laser-induced optical barriers (LIOBs). This thesis centers on the use of this novel technology to improve the limitations of continuous detectors, particularly the poor performance within the entrance region and the depth-dependent light spread, and has two primary aims:

1. To investigate the impact of the various aspects of the detector (e.g., properties of the LIOBs, crystal thickness, positioning algorithms), and ultimately explore the trade-offs in performance inherent in altering the light spread within this detector.

For this purpose, the performance of thick detectors etched with LIOBs is characterized and the capability of this technology to improve continuous detectors is studied in the laboratory.

2. To understand the clinical implications, focusing on quantitative capability, of a detector with improved performance, using Monte Carlo simulations as well as patient data collected on clinical scanners.

This work therefore investigates modifications to scintillation light spread at three levels. The first is the bench-top level of laboratory experiments that involve characterizing the performance of these detectors individually, by collecting data from an apparatus consisting of a small radiation source collimated and directed at these detectors. The intermediate level involves system simulations of scanners composed of detectors with improved performance to determine the relative impact they have on scanner performance; in these simulations, phantoms (distributions of known activity and geometry) are imaged so that the simulations may be compared to similar phantom measurements on clinical scanners. Last, the clinical implications of this work will be studied by translating the performance of scanners measured using phantoms to quantitation in actual patients by using a modified version of a lesion embedding technique previously developed by our group.

Outline of Thesis

Chapter 3 expands on the discussion of continuous detectors given in the introduction by describing their operation and defining the major metrics that are used to characterize their performance. In order to place the effect of improvements in

scintillator design into proper context, the significance of the major components and limitations that affect the performance of these detectors is investigated. These factors also determine the extent to which the positioning information inherent in the detector may be decoded, and are therefore important to properly compare the performance between different detector designs. In particular, the impact of the photodetector and the various positioning algorithms, as well as of Compton scatter and the depth-dependent light spread, is studied. Measurements to accomplish this involved both Monte Carlo simulations and experiments with thick continuous crystals. The performance of the detectors is shown to be fundamentally determined by the light spread within the detector, and limited by the depth-dependence of the light spread and poor performance in the entrance region, motivating efforts to modify this aspect of the detector.

Chapter 4 is devoted to a relatively recent technology used to alter the performance of continuous detectors: laser induced optical barriers (LIOBs). The concept of the laser etching is introduced, and a novel detector design intended to improve light spread within the scintillator is described. The results of experiments that characterize the performance of this detector design are presented, along with those of experiments that explore the optical properties of the LIOBs; the results show an improved overall performance after etching the crystals with LIOBs. The performance characteristics of most interest for this investigation are spatial, energy, and DOI resolution, along with position sampling. Additionally, the results of simulation studies, using the results of the optical experiments to model the behavior of the LIOBs, are presented. These showed the effect of varying some of the parameters of the LIOBs (e.g., laser properties and the pattern of the LIOBs in the crystal) on the trade-offs inherent in these metrics, and

investigated the potential of this detector design and of sub-surface laser engraving as applied to detector development.

Chapter 5 explores the performance of improved detectors in a clinical scanner, using Monte Carlo system simulations. The system simulations used to model the scanners is first described. The performance of the scanners composed of various detectors is then determined using the simulations along with calculations that incorporate the other effects that affect spatial resolution (e.g., acollinearity, finite positron range); these are then compared to one another and against the benchmark of current (pixelated) clinical scanners. Specifically, the simulations aimed to study the impact of improved spatial resolution and position sampling, and show the improvement in CRC that results from transitioning from a pixelated detector design to a continuous design, and by improving the resolution of the continuous designs.

Chapter 6 translates the quantitative performance of scanners measured using phantoms to clinical quantitative performance, by comparing the performance of a clinical scanner and a research scanner using both phantom and patient data. This study involves the analysis of images derived using a modified version of a method to virtually embed lesions into patient images. The work elucidates the connection between phantom data and patient data, by comparing quantitative metrics on images of phantom data with embedded lesions to those of patient data with embedded lesions. This connection is further made by comparing the effect of post-reconstruction filters on these phantom and patient images. These studies conclude that quantitative metrics studied using phantoms indeed translate to patient studies, and therefore show that the improvements in CRC resulting from improved spatial resolution, measured using phantom studies in the

simulations, are representative of improvements in quantitative accuracy in patient studies.

CHAPTER 3

Performance of Continuous Detectors

3.1 Introduction

The positioning of events using continuous detectors relies on the decoding of the light spread within the detector, which is unique to each position within the detector (Figure 3.1). The photodetectors below the crystal sample the light distribution, so that for every event that is detected, there are as many data points that may be used for positioning as there are photodetector elements. The performance of continuous detectors is based on a number of factors that combine to limit the precision and accuracy with which an event may be localized. In this section, the importance of some of the major components of the detector design will be explored. These include the continuous scintillator, the photodetector, and the positioning algorithms, as well as the depth-dependence of the light spread and an important inherent limitation of all detectors, Compton scatter interactions in the detector. Because the overall performance of a detector is determined by the interplay of these factors, an understanding of the impact of each will ultimately allow for different scintillator designs to be accurately compared, and for the relative importance of improvements in the design to be determined in later sections.

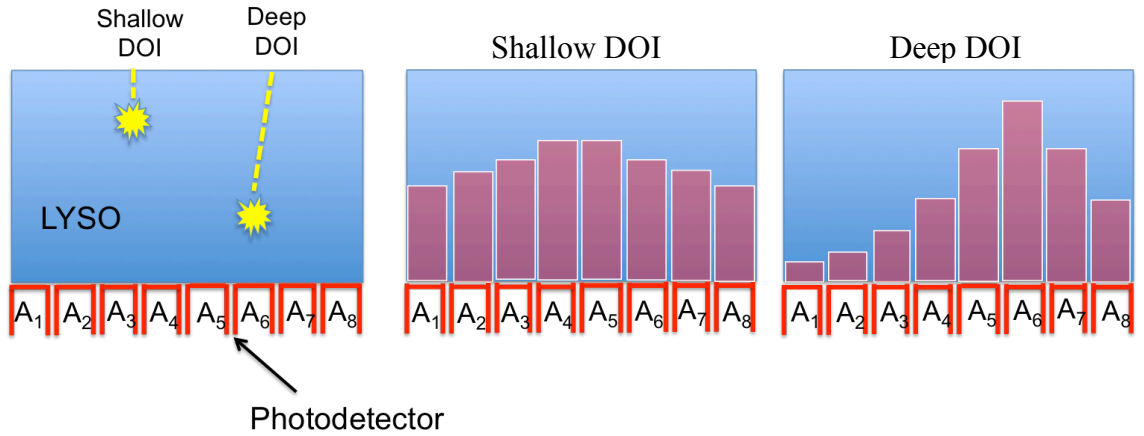


Figure 3.1: Light spread within continuous scintillators. Left: Diagram depicting events that occur at different DOIs and transverse positions within the crystal. Right: Histograms showing the position-dependent anode outputs; light spreads more at shallower depths and the anodes that detect the most light are located closest to the position of the event.

3.1.1 Fundamental Limitations

The resolution of continuous detectors is fundamentally limited by:

1. The light spread within the detector, measured using the light response function.
2. Compton scatter interactions in the detector.

Light Response Function

The light response function (LRF) is a useful metric to organize the data collected from the crystal measurements because it encapsulates the intrinsic performance of a given detector. The LRF of an anode is defined to be the average output of the anode as a function of source position. As an example, Figure 3.2 shows the results of an experimental measurement of a continuous detector irradiated along the side of the

crystal by scanning from edge to edge in discrete increments. The LRF is shown for one of the central row-column summed (discussed later) anode outputs, plotted as a function of the transverse position of the gamma beam. Each data point is computed by fitting the histogram of the output of the anode over all of the events to a Gaussian, and taking the peak and FWHM to be the mean and error bar of the LRF, respectively. Each LRF therefore conveys two pieces of information: shape and precision, which ultimately determine the intrinsic performance of the detector, as shown later.

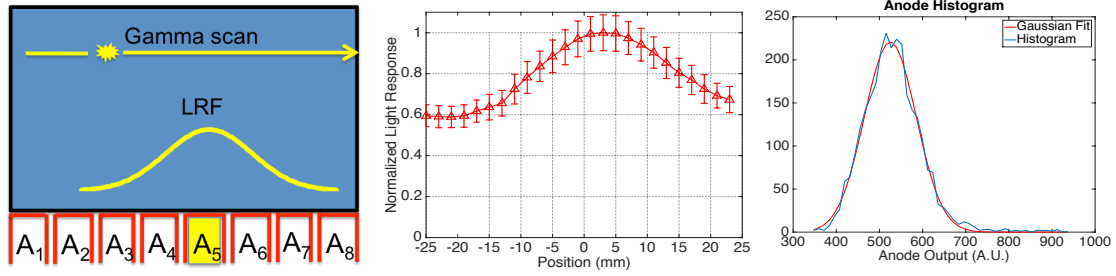


Figure 3.2: Diagram depicting the LRF, defined as the light collected at a particular anode as a function of source position. Left: Diagram of the definition of the LRF. Middle: Experimentally measured LRF at a fixed depth for a 50x50x25mm³ crystal. Right: Histogram of anode outputs for events in a row-column summed anode, with a Gaussian fit; the value and uncertainty of the LRFs are equal to the peak and standard deviation of the Gaussian fits, respectively.

Cramer-Rao Bound

As discussed in the introduction, positioning may be viewed as a form of parameter estimation, in which an unknown vector of parameters, θ , is estimated after measuring a vector of values that functionally depends on the unknown variables, $\mathbf{x}(\theta)$, with likelihood $f(\mathbf{x}|\theta)$. The maximum precision of this estimation may be determined

statistically with knowledge of only this functional dependence and the uncertainty of the measured values \mathbf{x} . Defining the Fisher information, $I(\theta)$, as

$$I(\theta) = \int \left[\frac{d}{d\theta} \log f(\mathbf{x}|\theta) \right]^2 f(\mathbf{x}|\theta) d\mathbf{x},$$

the lower bound on the variance of an unbiased estimator, σ , may be expressed:

$$\sigma = \frac{1}{nI(\theta)},$$

where n is the number of data points.

The LRFs here represent the data, from which the unknown position \mathbf{x} of the incident photon is to be estimated, so that a lower bound on the variance of this estimator may be determined by them. The distribution of photons at the anodes of the photodetector is most accurately described by a multivariate normal distribution. The probability of the anodes measuring the set of outputs $\mathbf{n}(\mathbf{x})$ may then be written:

$$L(\mu(\mathbf{x}), \mathbf{n}(\mathbf{x})) = \frac{1}{(2\pi)^{n/2} \sqrt{\det(\mathbf{V})}} \exp \left[-\frac{1}{2} (\mathbf{n}(\mathbf{x}) - \mu(\mathbf{x})) \mathbf{V}^{-1} (\mathbf{n}(\mathbf{x}) - \mu(\mathbf{x})) \right], \quad (3.1)$$

where \mathbf{V} is the covariance matrix and $\mu(\mathbf{x})$ is the vector of mean anode values.

The Cramer-Rao bound for this scenario may therefore be approximated:

$$\sigma_{lb}^2(x) \approx \left[\left(\frac{\partial \mu(x)}{\partial x} \right)^T \mathbf{V}^{-1} \left(\frac{\partial \mu(x)}{\partial x} \right) \right]^{-1} \quad (3.2)$$

Because of the large number of anodes, the correlations between the anode signals are usually not large [104] and the anode signals may be approximated as independent, with the Cramer-Rao bound approximated as:

$$\sigma_{lb}^2(x) \approx \left[\sum_{i=1}^N \frac{\left(\frac{\partial \mu_i(x)}{\partial x} \right)^2}{\sigma_i^2(x)} \right]^{-1}, \quad (3.3)$$

where N is the number of anodes and $\sigma_i(x)$ is the variance of the i^{th} anode signal. This form is particularly useful in demonstrating that the intrinsic performance of the detector is determined by:

1. The shape of the LRFs, or the rate with which they change ($d\mu/dx$), roughly encapsulated as the narrowness of the LRFs. In particular, narrower LRFs lead to better positioning, because these change most rapidly; the ideal LRF would be triangular, with a base that spans 1.5 PMT anodes [101].
2. The light output of the detector, which determines the uncertainty of the LRFs (σ_i).
3. The sampling of the photodetector, which determines the number of data points (N).

Compton scatter

As with pixelated systems, Compton scatter acts to increase the scintillator light spread at the photodetector, degrading the ability to decode the positional information (Figure 3.3). Nevertheless, the effect of Compton scatter on positioning differs in the two systems because pixelated detectors sample the light output discretely within each pixel, while the light from scattered interactions spreads throughout the scintillator.

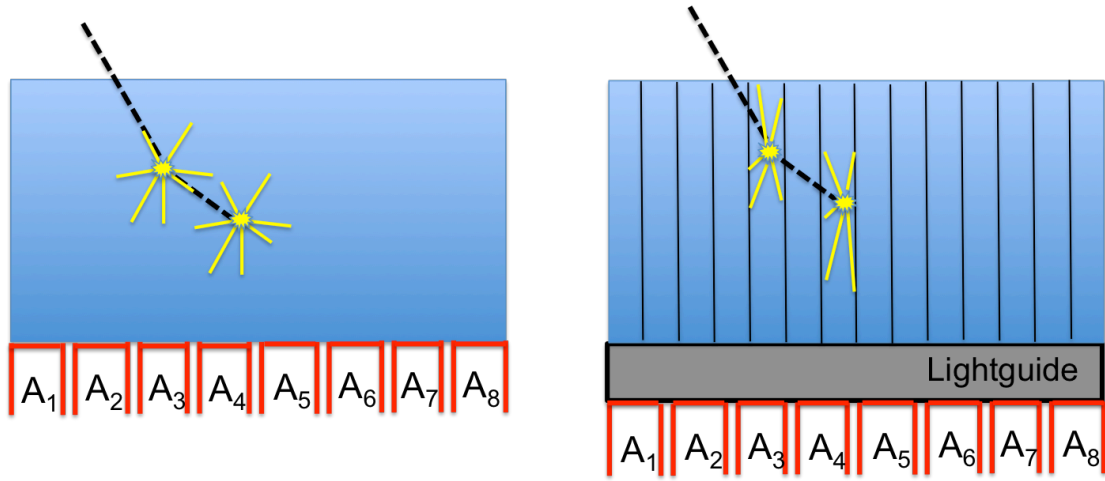


Figure 3.3: Diagram depicting Compton scatter within continuous (left) and pixelated (right) detectors. By scattering, the photon deposits its energy at multiple scintillation positions, thereby spreading the light more.

3.1.2 Depth-of-interaction

The interaction of 511-keV photons at various depths within a detector (DOI effect) affects all detector designs negatively by causing parallax, which degrades the overall spatial resolution of the scanner, and by increasing the time spread of photons within detectors, degrading the timing resolution of the systems. For continuous detectors, it additionally harms the detector transverse resolution because the light spread within the detector is dependent on the DOI (i.e., deeper events spread less before reaching the photodetector plane, leading to narrower LRFs). Because the light spread within the detector depends on the DOI, however, one of the advantages of continuous crystal systems over conventional pixelated systems is that intrinsic continuous DOI

information may be provided by the detector. This information may be used to determine and correct for the DOI effect.

DOI information derives from the same source as the transverse positional information – position-dependent patterns in light spread – and so this information may be extracted using similar algorithms as the transverse position. In the case of DOI, however, calibration data must be ascertained using more complex means since there is no simple method to obtain data at known fixed depths. A number of groups have devised clever and sometimes time-consuming methods to determine this, though these generally fall into two categories (Figure 3.4):

1. Angled gamma beams: if the angle and entrance position of the gammas on the detector face are known, then the calculated position of the gamma may be used to determine the depth at which an interaction takes place. Calibration data may then be obtained for each DOI [105].
2. Head-on data: the calibration data set consists of gamma beams oriented normal to the surface of the crystal. By choosing some DOI-dependent metric (e.g., the standard deviation of the anode signals) and calculating this metric for each event in the calibration data set, events from a single gamma position may be histogrammed based on this metric. The histogram of photoelectric interactions may then be derived by using the exponential probability of interaction (Beer's law) and the functional dependence of the metric on DOI. The histogram may ultimately be divided into groups based on DOI, and calibration data determined for each DOI. Because of its relative simplicity, this method is more prevalent in the literature [106-111].

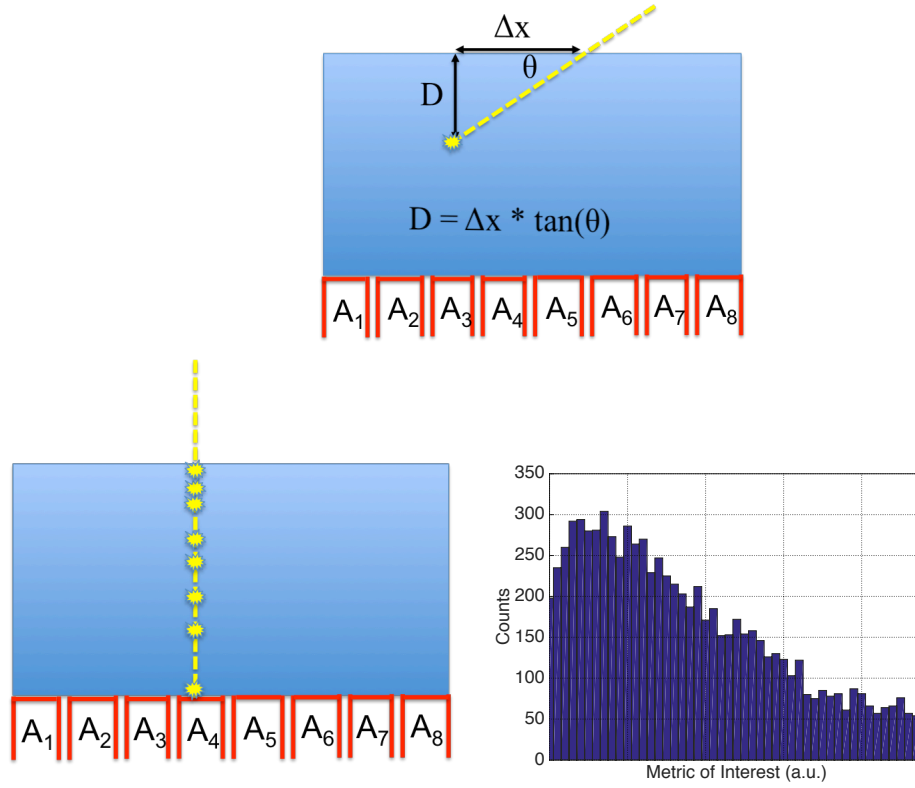


Figure 3.4: Methods to measure DOI information during calibration of continuous detectors. Top: Diagram depicting the calculation of DOI using angled gamma beams, in which the DOI is determined using the known transverse position and angle of incidence. Bottom: Diagram depicting the calculation of DOI using head-on scans, in which the probability of interaction decreases with depth (left), and a sample histogram of a DOI-dependent metric (right), from which DOI information is derived by gating events by the value of this metric.

3.1.3 Data Read-out

For each event, the position sensitive MAPMT produces a vector of numbers corresponding to the outputs of the anodes. For an 8x8 MAPMT, the read-out electronics can output data by one of two methods:

1. 64-anode scheme: all anodes of the photodetector are read-out and used in positioning the events. This method has the advantage of using all of the information provided by the MAPMT.
2. Row-column summing: the 8x8 array of anodes is summed along each direction, as shown in Figure 3.5, resulting in $8 \times 2 = 16$ channels for each event. This method has a number of advantages:
 - A. The channels output for each data point are reduced, thereby reducing the complexity of the read-out and the number of the positioning calculations
 - B. The calibration procedure is greatly simplified. 2D positioning for the 64-anode scheme requires calibration data at regularly spaced points on the crystal surface (Figure 3.6), which may potentially be simplified by fan beam scanning, by which a thin line of radiation is irradiated at known locations [112]. In contrast, because of the symmetry provided by the row-column summing scheme, this method would in theory allow calibration data to be collected at points along two orthogonal lines (either point beams or fan beams). Because of nonuniformities within the scintillator and the MAPMT, calibration could not likely be reduced further (e.g., calibrating a single quadrant) without suffering from artifacts or poorer performance, despite the symmetry of the crystal.
 - C. The summed output is less noisy than the individual channel output.

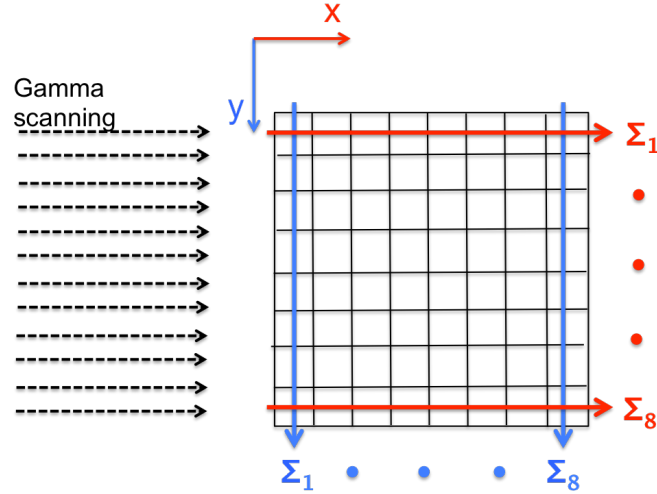


Figure 3.5: Diagram of row-column summing technique, by which the 64 anode signals are converted into 16 signals by summing along each orthogonal direction.

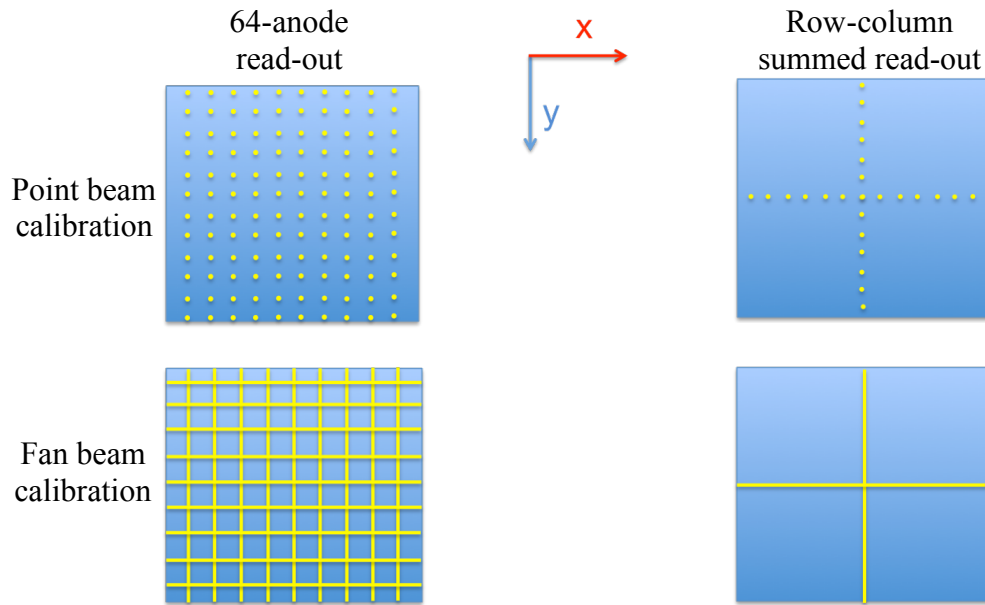


Figure 3.6: Diagram of various calibration schemes, in which data are collected using either point beams (depicted as points) or fan beams (depicted as lines) of gamma rays directed at the surface of the crystal at known, discrete positions. The row-column summed read-out technique requires less calibration data because the anode outputs are summed in each orthogonal direction, requiring one line of calibration points for each direction.

3.1.4 Positioning Algorithms

Once scintillation light from a coincident event is read out by the photodetector, the system must use this information to position each incident photon. Positioning algorithms may be divided broadly into Anger positioning algorithms and statistical positioning algorithms, which represent a large and varied class. The categories of statistical algorithms generally differ in their performance and complexity.

3.1.4.1 Anger Logic

Most commercial scanners use an Anger logic-based positioning algorithm. The simplest such positioning scheme involves computing an average of the PMT x- and y-positions, weighting each value by a factor related to the fraction of total energy collected in each PMT. This calculation often includes only the PMTs within a local cluster, so that the centroid calculation is given by:

$$x = \frac{\sum_{i=1}^N n_i p_{x,i}}{\sum_{i=1}^N n_i} \quad \text{and} \quad y = \frac{\sum_{i=1}^N n_i p_{y,i}}{\sum_{i=1}^N n_i}, \quad (3.4)$$

where (x, y) are the calculated x and y-positions of the incident photon, n_i is the output of PMT_i within the local cluster of N PMTs, and $p_{x,i}$ and $p_{y,i}$ are the x and y-positions of PMT_i .

The cluster of PMTs chosen for this calculation may be determined by only including PMTs whose output exceeds a certain threshold or by limiting the PMTs to include that with the maximum light output as well as the immediate PMT neighbors, in order to prevent noisy PMTs from distorting the calculations and to minimize dead time and pile-up. Most modern systems compute the positions after digitizing the PMT outputs.

Anger logic suffers from the nonlinear response of the PMT signal to the spatial position at which light interacts on the PMT, as well as from crystal nonuniformities and nonuniformities in PMT response, resulting in distortions such as the pincushion and barreling effects (Figure 3.7). The distortions that result from Anger logic may be corrected in pixelated systems, because the pixel in which the incident photon interacts is all that need be discriminated (Figure 3.7 Right); for continuous systems, however, nonlinearities in positioning may degrade resolution because events are positioned continuously.

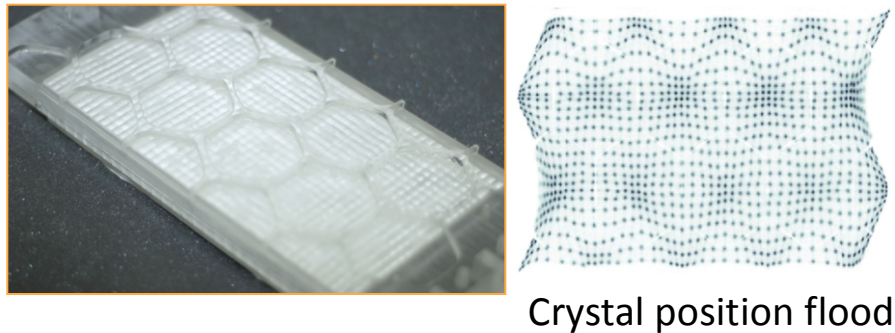


Figure 3.7: Flood map of an array of uniformly spaced crystals showing pincushion artifacts near the center and barreling artifacts near the edges of the PMTs. The flood map was taken from a current commercial Philips scanner using a pixelated array coupled to an array of PMTs in order to illustrate the artifacts that arise from using Anger positioning to solve a nonlinear positioning problem, here arising from nonlinearities in the PMT output with respect to source position.

3.1.4.2 Statistical Positioning Algorithms

The process of determining the position of an incident photon from the resulting photodetector output may also be viewed in light of statistical estimation theory, which broadly aims to determine the value of some unknown $N \times 1$ vector, θ , given a vector of values that functionally depend on the unknown variables, $\mathbf{x}(\theta)$. These methods generally use the information provided by the photodetector as well as prior information involving the dependence of the data on the incident photon interaction position, obtained using a calibration, resulting in improved accuracy and precision in the positioning estimation. While statistical algorithms are not used clinically, a number of these algorithms have been investigated, particularly as applied to continuous systems; these may be divided into three categories, which generally differ in their performance and complexity: maximum likelihood methods, nearest neighbor methods, and neural network methods [113]. Because the first two are used more extensively than the others in the field, and were the only ones used in this thesis because of their relative simplicity, they are discussed in more detail below.

Maximum Likelihood Methods

Maximum likelihood (ML) methods generally determine the unknown vector θ , by determining the value of θ that maximizes the likelihood function of the unknown parameter $L(\theta|\mathbf{x})$. The likelihood function is defined as: $L(\theta|\mathbf{x}) = \text{pr}(\mathbf{x}, \theta)$, with $\text{pr}(\mathbf{x}, \theta)$ the probability function of measuring values \mathbf{x} , given the unknown values θ , so that the maximum likelihood equation may be written as:

$$\theta = \underset{\theta}{\text{argmax}}(\text{pr}(\mathbf{x}, \theta)).$$

Because the logarithm of a function increases monotonically with the function, and because it is often easier to solve this equation using logarithms, the maximization equation may also be expressed as:

$$\theta = \operatorname{argmax}_{\theta}(\log(\operatorname{pr}(\mathbf{x}, \theta))).$$

To perform this estimation, therefore, the probability distribution function must be known prior to estimation. Note that the measured values \mathbf{x} may be noisy, which acts to limit the ability with which estimation may be performed, as described later.

ML methods as applied to gamma positioning were introduced by Gray and Macovski in 1976 [114]. In this context, the unknown values may include the x-, y-, and z-position of the incident photon, as well as the energy of the event. The likelihood of a photon being detected by a photodetector tile is given by a multinomial distribution, and because the number of photons emitted per scintillation event is so large, this is well approximated by a multivariate normal distribution:

$$L(\mathbf{M}, \mathbf{n}(\mathbf{x})) = \frac{1}{(2\pi)^{n/2} \sqrt{\det(\mathbf{V})}} \exp \left[-\frac{1}{2} (\mathbf{n}(\mathbf{x}) - \boldsymbol{\mu}(\mathbf{x}))^T \mathbf{V}^{-1} (\mathbf{n}(\mathbf{x}) - \boldsymbol{\mu}(\mathbf{x})) \right] \quad (3.5).$$

where \mathbf{x} is the incident photon position, $\mathbf{n}(\mathbf{x})$ is the vector of anode outputs, $\boldsymbol{\mu}(\mathbf{x})$ is the mean output of each anode, and \mathbf{V} is the covariance matrix of the anode signals.

Simpler algorithms assume the outputs of the PMT anodes are independent, so that the probability function of the overall interaction may be obtained by multiplying each of the individual probability distributions for the anode outputs. The likelihood of i^{th} anode measuring n_i photons given incident photon position \mathbf{x} can be then be modeled as a Poisson likelihood:

$$L(\boldsymbol{\mu}, \mathbf{x}) = \prod_{i=1}^N \frac{\mu_i(\mathbf{x})^{n_i} e^{-\mu_i(\mathbf{x})}}{n_i!}.$$

By taking the derivative of the logarithm of this likelihood function with respect to position \mathbf{x} and setting to zero, one obtains the equations for position estimation in this model:

$$\sum_{i=1}^N n_i w_i(\mathbf{x}) \approx 0, \quad (3.6)$$

$$w_i(\mathbf{x}) = \frac{\frac{\partial \mu_i(\mathbf{x})}{\partial \mathbf{x}}}{\mu_i(\mathbf{x})} - \frac{\sum_{i=1}^N \frac{\partial \mu_i(\mathbf{x})}{\partial \mathbf{x}}}{\sum_{i=1}^N \mu_i(\mathbf{x})} . \quad (3.7)$$

Here, $\mathbf{n}(\mathbf{x})$ is the vector of anode outputs, $\boldsymbol{\mu}(\mathbf{x})$ is the vector of mean anode outputs, and $\mathbf{w}(\mathbf{x})$ are weighting functions that are obtained in a separate calibration step involving the collection of data at known locations. Note that during implementation, the resulting value in eq. 3.6 may never reach 0 because of noisy data, so that the minimum is taken instead.

Similarly, a Gaussian model [115] can also be applied, for which the likelihood of the i^{th} anode measuring n_i photons given incident photon position \mathbf{x} is modeled by a Gaussian distribution. Similar steps to the derivation for the Poisson model may be followed to lead to the minimization equation. The major difference between this model and the previous model is that for the Gaussian model, the standard deviation of the output of each anode for a given incident photon position is measured and used in addition in the mean light output, while for the Poisson, the standard deviation is assumed to be equal to the square root of the mean output. Both models assume that the PMT anode outputs are linear with respect to the energy deposited and that the PMT outputs are independent of one another.

Nearest Neighbor (NN) Methods

NN methods, in contrast to ML methods, do not assume a parameter that must be estimated (i.e., they are non-parametric) and generally attempt to classify unknown data by comparing them to prior training data divided into known classes and determining the class that matches most closely to the unknown data. A common version of these algorithms is the k-NN method, in which the class with the k closest neighbors is determined to be that in which the unknown data belong.

As applied to gamma positioning, one method [111] to perform this calculation is to collect reference events at regularly spaced positioning points in a given detector; for reference event j at reference position p, the resulting N photodetector outputs are given by vector $\mu^{j,p} = (\mu^{j,p}_1, \mu^{j,p}_2, \dots, \mu^{j,p}_N)$. The photodetector outputs for a given event to be positioned \mathbf{n} , are compared to those of each reference event, commonly using the Euclidian distance D:

$$D^{j,p} = \sqrt{\sum_{i=1}^N (n_i - \mu^{j,p}_i)^2} . \quad (3.8)$$

The k events with the smallest value of D are selected, and the most frequent position j among these events is selected as the incident photon position.

Another version of this algorithm [116] determines the average photodetector output for each position p, n^p_{ref} . The average outputs are compared to the outputs for a given test event using the Euclidian distance as well:

$$D^p = \sqrt{\sum_{i=1}^N (n_i - \mu^p_i)^2} , \quad (3.9)$$

and the position p at which D is a minimum is chosen as the incident photon position.

3.2 Experimental Set-up

3.2.1 Hardware

To study the crystals tested in this thesis, the following apparatus was designed inside a light-tight box, as depicted in Figure 3.8. Each continuous crystal was coupled using optical grease (BC-630) to a Hamamatsu H8500 MAPMT. The performance of the crystal was measured by aiming gamma rays normal to the surface of the crystal and collecting data from the photodetector. Data were acquired in two configurations (Figure 3.8):

1. Head-on configuration, in which the crystal was irradiated normal to its front face, and the beam scanned from edge-to-edge (y-axis) down the center of the crystal ($x=0\text{mm}$).
2. Side-on configuration, in which the crystal was irradiated along one of its sides to fix the DOI (z-axis), and the beam scanned from edge-to-edge (y-axis) at several depths.

To precisely direct gamma rays at the scintillator, a narrow beam of 511-keV photons must be aimed at the crystal. For this purpose, a small ($<0.5\text{mm}$ in diameter) and weak ($\sim 20\text{ }\mu\text{Ci}$) ^{22}Na source was placed between the continuous crystal and a reference detector, consisting of a $4\times 4\times 20\text{mm}^3$ LYSO crystal wrapped in Teflon and grease coupled to a Photonics XP20D0 PMT. The radiation from the source was electronically collimated by triggering on true coincidence events detected at both detectors, and energy gating on the 511-keV photons at each detector. The coincidence triggering and energy gating served both to isolate the 511-keV photons from the ^{22}Na spectrum (especially

important because of the presence of 1272-keV photons in this spectrum), and to collimate the photons into a beam $\sim 1\text{mm}$ in diameter. To ensure a small beam, the distance of the source to the reference crystal was >6 times the distance from the source to the continuous crystal (Figure 3.9). The distance from the source to the continuous crystal was $\sim 5\text{mm}$, to allow for an acceptably high count rate ($\sim 250\text{ cts/min}$) while avoiding issues with pile-up.

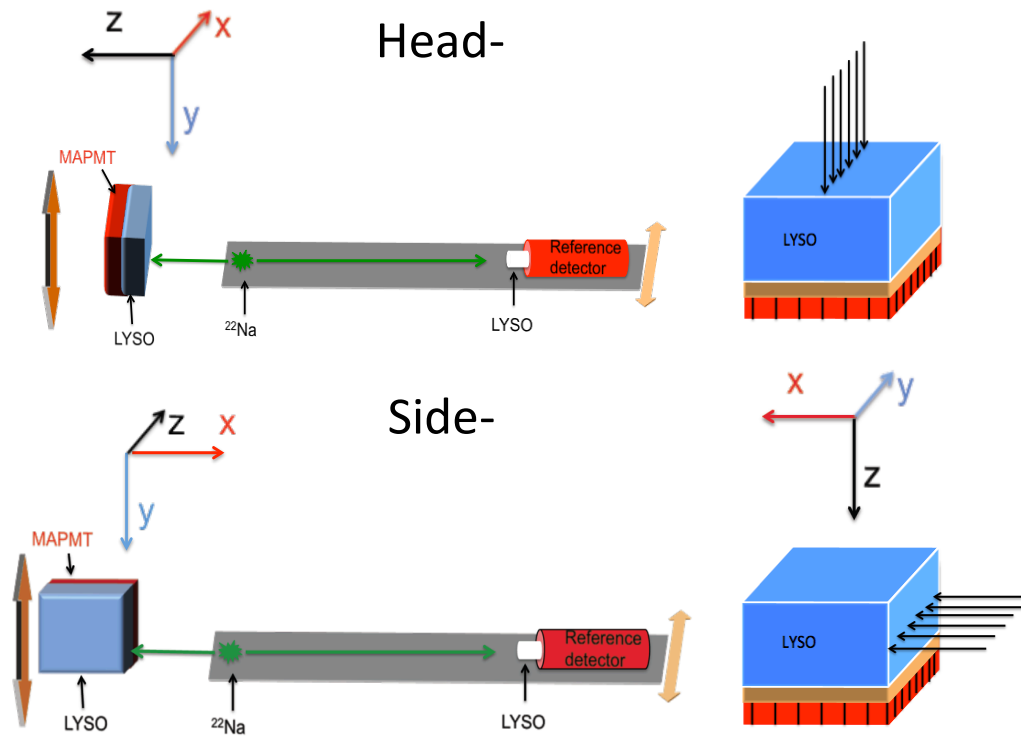


Figure 3.8: Schematic of apparatus designed to study continuous detectors. The continuous crystal was coupled to a MAPMT, and a ^{22}Na source placed between the continuous detector and a reference detector was used to direct a collimated gamma beam at the crystal. Left: Apparatus designed to study continuous detectors in head-on and side-on configurations. The reference detector was translated horizontally to vary the DOI in the side-on configuration, while the continuous detector was translated vertically in discrete increments to scan along the transverse direction of the crystal. Right: Diagram depicting scanning the crystal in the head-on and side-on configurations.

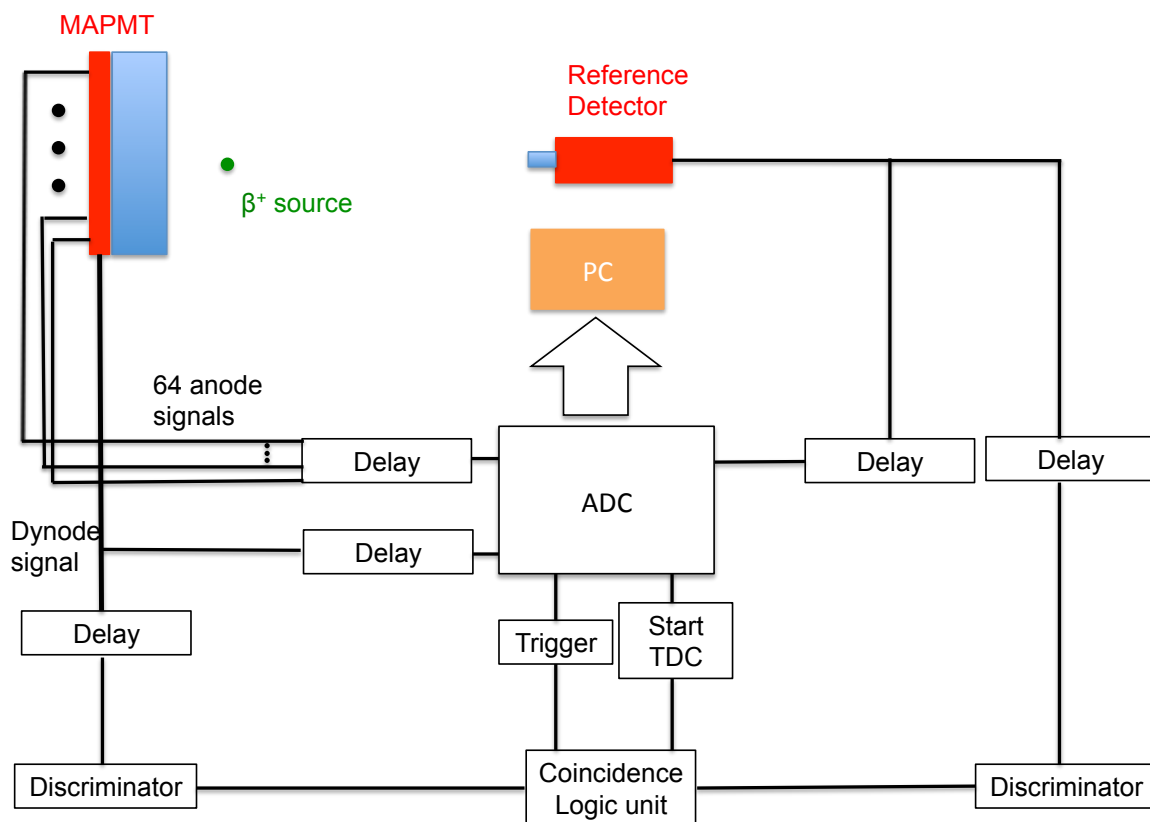


Figure 3.10: Schematic of the electronics set-up used for the measurements, in which the dynode signal of the MAPMT is operated in coincidence with the reference signal, and these signals are read out along with the individual 64 anodes.

3.2.3 Crystal Treatment

The continuous crystals were each cleaned and wrapped in several (>5) layers of Teflon on all sides except that being coupled to the photodetector, in order to maximize light collection. A layer of black tape was added after wrapping with Teflon, in order to hold the Teflon in place and as a precaution to minimize the light that reached the crystal if exposed to outside light. The exit surface of the crystal was coupled to the photodetector with a smooth layer of optical grease. Because LYSO has an afterglow,

measurements were taken after configuring the apparatus and leaving it in the dark for at least 24 hours [88].

3.2.4 Data Collection

The gamma beam was scanned across the crystal using a computer-controlled set-up. The continuous detector was fixed to a motor and translated vertically in discrete steps, while the source and reference detector were fixed relative to one another and to a horizontal motor; for each horizontal and vertical position, a fixed number of events were collected. Collected data from the crystals were used to both calibrate and position the events and were processed in MATLAB (The MathWorks Inc.) after data collection. The data were collected at 25 points in 2mm intervals; calibration data were then interpolated to 0.25mm points.

To measure the energy resolution of the detector, the FWHM of the dynode signal was calibrated and divided by the incident radiation energy. To perform the calibration, a ^{137}Cs source was used to determine the channel number of the peak at 662keV. The resolution was then calculated as:

$$\Delta E = \frac{\text{FWHM}_{\text{channels}} * C}{511 \text{ keV}}, \quad (3.10)$$

where the calibration factor C was calculated as

$$C = \frac{662 \text{ keV} - 511 \text{ keV}}{\text{channel number}(662 \text{ keV}) - \text{channel number}(511 \text{ keV})}. \quad (3.11)$$

3.2.5 Testing Data Acquisition Count Rate

Because the source was not physically collimated, all photons that are emitted within a solid angle subtended by the detector will reach the detector and have the potential to be absorbed and scintillate within the detector. This increases the random coincidence rate as well as the likelihood of pulse pile-up, which occurs when two events are absorbed close enough in time and space (e.g., in the same continuous detector) that the resulting scintillation light emissions are combined. Pile-up is a fundamental limitation of all detectors that increases with count rate and leads to a loss in spatial resolution, as events will be mispositioned because of the combined light spread, as well as a loss in detected counts, as events are removed from the energy gate if the summed energy exceeds the upper gate.

3.2.5.1 Methods and Materials

To test for the effect of random coincidences and pile-up in this work, their likelihood of occurring was calculated with two measurements:

1. The random coincidence rate was compared to the total coincident rate, to verify that the collected data did not consist of a significant fraction of random events. Here, the random coincidence rate was estimated using the delayed gate approach, in which one of the coincidence signals is delayed enough that the true coincidence events do not overlap in time; this value is theoretically given by: $R_{\text{randoms}} = 2\tau r_1 r_2$, where r_1 and r_2 are the singles rates of the continuous and reference detector using the high threshold, 2τ is the coincidence window.

2. To verify the absence of pile-up in the apparatus, an estimate of the average time between two uncorrelated events in the continuous detector, T_{singles} , was measured from the singles rate at a low voltage threshold (~ 50 mV), $R_{\text{singles, LT}}$, using $T_{\text{singles}} \sim 1/R_{\text{singles, LT}}$, to verify that it was significantly larger than the coincident gate.

3.2.5.2 Results

The results of the validation of the apparatus are shown in Table 3.1. The top row compares the event rate for coincidence events to the singles rates for a high voltage threshold (to remove events below the photopeak) and for the lowest voltage threshold (~ 50 mV); note that the singles rate includes the counts from the natural background of Lu^{3+} . The last column lists the measured random coincidence rate, and shows that it is very low compared to the total coincidence event rate.

Further, the average time between two uncorrelated events (T_{singles}) in the continuous detector is shown to be much larger than the timing window within which two events must be triggered to be registered as a coincidence event, so that pulse pile-up is shown to not impact this set-up.

Table 3.1: Comparison of singles and coincidence rates for detector set-up. The low coincidence rate using the delayed coincidence method, compared to the normal coincidence rate, indicates that random coincidences are not affecting the apparatus significantly. The large time between the singles events in the MAPMT (T_{singles}) compared to the coincidence gate indicates that pile-up is not affecting the apparatus significantly.

Rates (cts/s)	High Threshold	Low Threshold	Delayed Coincidence
Coincidence	4.0 (Coinc. gate $\sim 10^{-7}$ s)		$2.2 \cdot 10^{-2}$
MAPMT Singles	$1.0 \cdot 10^4$	$3.3 \cdot 10^4$ ($T_{\text{singles}} \sim 3 \cdot 10^{-5}$ s)	
PMT Singles	$5.2 \cdot 10^1$		

3.3 Simulations

3.3.1 Monte Carlo Simulations in PET

Monte Carlo (MC) simulations have become an invaluable tool in the field of nuclear medicine, as they provide a means to study properties of scanners that are impossible to study otherwise, serve as a quick and inexpensive method to study new designs and optimize detector design, and provide objective data to measure the performance of scanners (e.g., quantitation and detectability) and reconstruction correction techniques. Because nuclear imaging is based on stochastic processes, MC methods are well suited for modeling the behavior of imaging. While a number of different MC packages exist for modeling PET scanners, they all are fundamentally based on the same principles: random number generation, sampling of probability distribution

functions (PDFs), physical modeling of interactions of radiation with matter, and a method to tally the output of the simulation.

Detector simulations specifically model the process of scintillation photon generation and absorption, in order to characterize the performance of the detector. The most popular codes used for this purpose include GATE/GEANT4, DETECT2000, and SCOUT [120-122]; the code used in this thesis was that developed at the University of Pennsylvania, Montecrystal, because of the ability to easily alter the parameters of the system, as well as its speed [101, 123-124]. Montecrystal consists of two separate codes, implemented after the user has specified the geometry and composition of the detector: the first to model the interactions of incident 511-keV photons with the detector and the second to track the movement of scintillation photons through the detector to the photodetector.

The photons may be introduced into the detector as a beam of chosen thickness oriented at a chosen angle relative to the surface of the detector, with the position of interaction chosen by the user; alternatively, the depth-of-interaction of the photons may be fixed by the user. The distance the photons travel before interacting in the detector is determined using Beer's law, with the appropriate total mass absorption coefficient dependent on both energy and scintillator composition. The energy of any scattered photons as well as the angle at which they scatter are sampled using the Klein-Nishina differential cross-section. After each interaction, scintillation photons are emitted, based on the energy of the detected event and the scintillator light yield (e.g., 51000 photons/keV for LYSO). Each incident photon is tracked until the original 511-keV

photon and each scattered photon have undergone photoelectric absorption or passed through the crystal.

The second code tracks each scintillation photon from the position at which it is emitted until it is absorbed by the photodetector, absorbed by the crystal, or passes through the crystal. Montecrystal, like other detector MC methods used for nuclear medicine, ignores electron transport because of the short ranges of the electrons involved (because of their low energies). The photon may interact with a number of surfaces along its path, including: the walls of the crystal, any reflector within the crystal or wrapped around the crystal, a lightguide between the scintillator and the photodetector, the glass wall of the photodetector, and the photocathode. The model for photon interactions with these surfaces is common to similar simulation codes, and includes three types of interactions (Figure 3.11):

1. Mirror-like (specular spike) reflections off of smooth surfaces.
2. Specular reflections off of a rough surface (specular lobe), described as a surface whose local surface (modeled as microfacets) is angled relative to the normal of the surface as a whole, with the PDF of the angle given by a Gaussian with user-defined width.
3. Diffuse (Lambertian) reflections off of rough surfaces, with the PDF for reflections at angle θ given by $\cos(\theta)$, relative to normal.

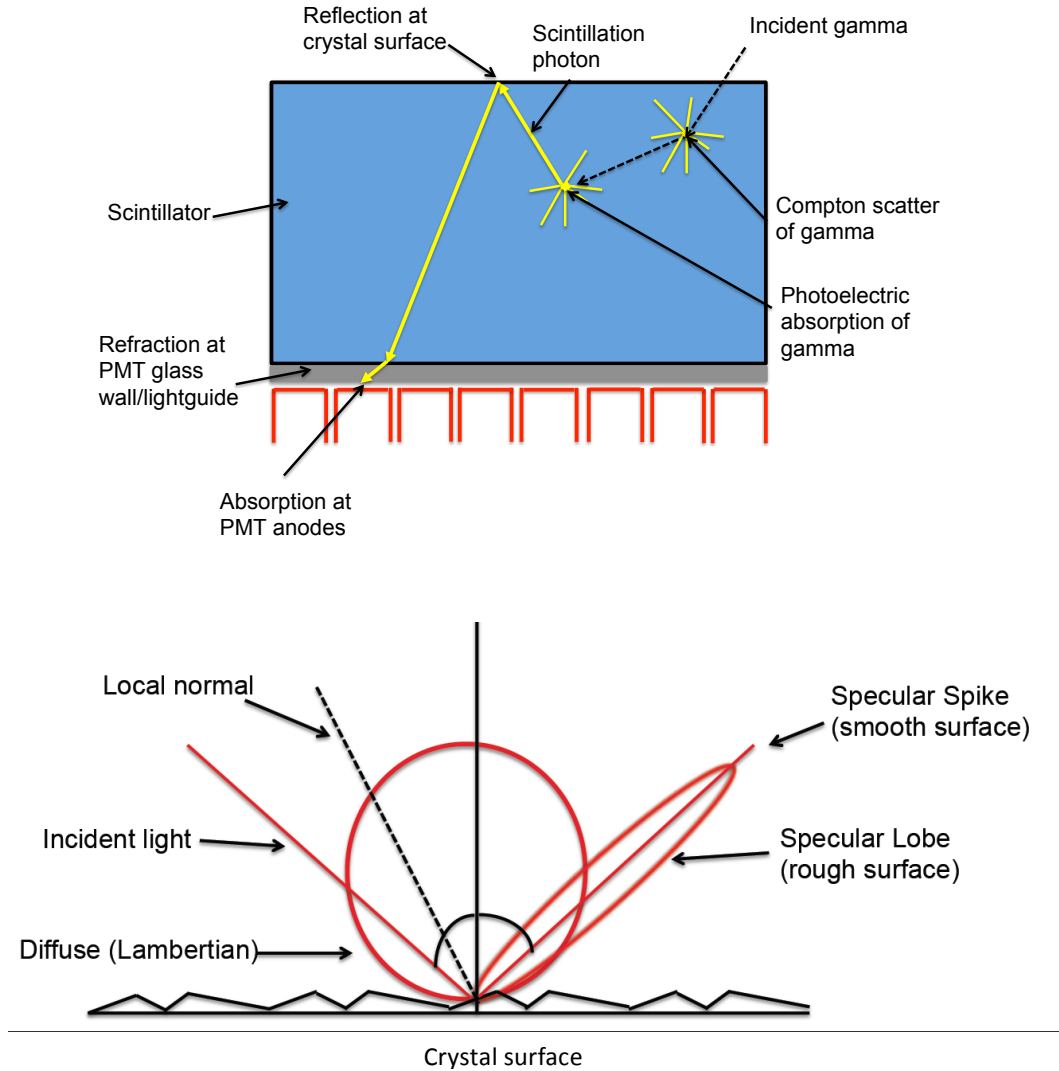


Figure 3.11: Model of interactions of photons within detector. Top: Diagram of the various interactions of incident photons and scintillation photons within the detector. Bottom: Diagram of the model of reflections used in the simulations, in which surface reflections are modeled using specular spike distributions, specular lobe distributions, or diffuse distributions.

In order to better match experimental conditions, the Montecrystal MC code previously developed by this group was modified in two ways:

1. The photodetector was modeled as reflective. Previous versions of the code described the detector as absorptive and transmissive; however, studies [125-128] have measured the index of refraction and reflectivity of bialkali photocathodes. Based on these measurements, the index of refraction of the H8500 was chosen to be 3.3; because a well-defined model for the PDF of reflection has not been measured, the photocathode was modeled as a diffuse reflector, based on visual observation of light reflected from the cathode.
2. Reflections at the polished walls of the crystals were modeled as ~99% specular and ~1% diffuse, based on measurements described in chapter 4; previous versions of the simulation modeled these walls as 100% specular.

As before, an air gap was modeled between the crystal surface and the Teflon wrapping, and reflections from the Teflon wrapping were modeled as Lambertian, based on measurements of the reflectivity profile from this surface [129-132]. Each interaction was modeled as one of these three, while interactions with a given surface as a whole could be described as a combination of these, with the probability of each type of interaction specific to each surface [117-119].

The number and position of photons absorbed by the photocathode are tallied for each detected event. After all events have been simulated, the output of the simulation includes the output of each photodetector anode for each detected event, as in actual radiation experiments, and can also include information unavailable to actual experiments, such as the exact position of interaction of the incident photon.

3.3.2 Validation of Detector Simulations

3.3.2.1 Methods and Materials

The simulations were tested by comparing them to experimental measurements for two crystals that were studied experimentally: a $50 \times 50 \times 25 \text{ mm}^3$ crystal, polished on all sides, and a $48 \times 48 \times 14 \text{ mm}^3$ crystal, roughened on the entrance surface.

3.3.2.2 Results

Comparisons of the LRFs for the simulations and experiments are shown in

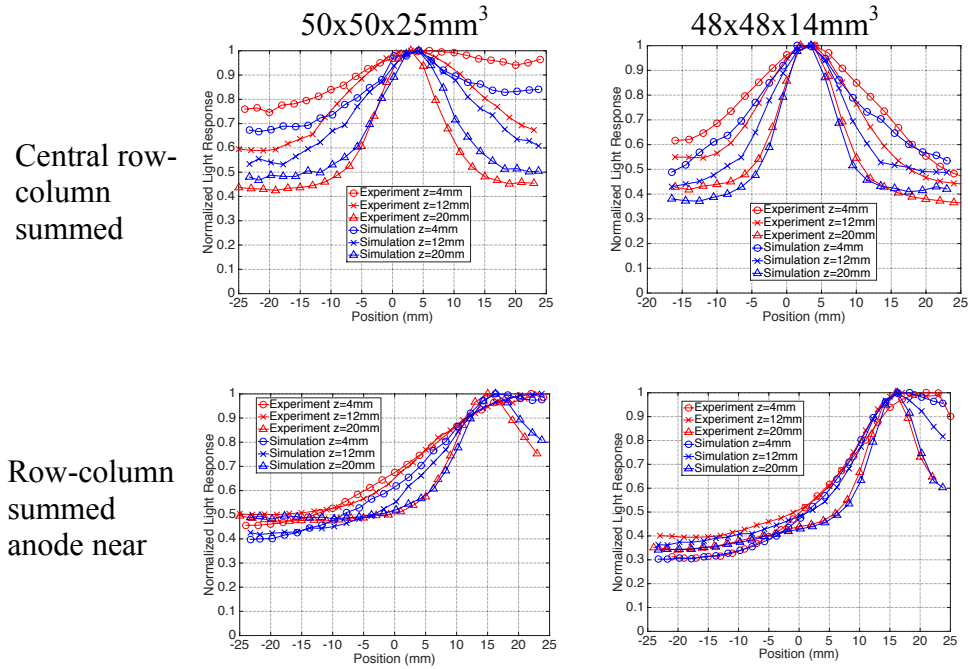


Figure 3.12: Comparison of the LRFs resulting from the simulations and experimental measurements for the 25mm (left) and 14mm thick (right) crystals, and for both a central (top) and near-edge (bottom) row-column summed anode. LRFs are shown for three depths (z-direction). The LRFs from the simulations and experimental measurements do not match exactly, but the simulations reflect the general effects of the DOI and reflections from the walls in the light spread.

The simulations do not exactly match the experimental measurements, indicating that the model of photon interactions in the continuous detector is incomplete. This is largely a consequence of the approximations that are made for the interactions of the photons with the walls of the crystal, Teflon, and the photodetector (Figure 3.11), because of the difficulty in precisely measuring these for this system. Research has shown that these interactions may be complex and difficult to model [129, 131], leading to inevitable discrepancies when using a simple model; more realistic models therefore will likely require measurements of the optical interactions at the surfaces of the specific crystals, photodetector, and reflective wrapping used and incorporation of the empirically derived surface interactions. Nevertheless, the simulations accurately reflect the general effects of DOI and reflections from the walls in the light spread, so that keeping the limitations of the model in mind, the simulations are useful for understanding the relative effects of the various parameters in the continuous detector, and invaluable for isolating certain effects within the detection process (e.g., depth, Compton scatter).

3.4 Continuous Crystal Light Spread

3.4.1 Impact of Light Spread

The LRFs for all of the row-column summed anodes, and for a central row-column summed anode at several depths, are shown in Figure 3.13 for a 25mm and a 14mm thick crystal. Several fundamental properties of continuous crystals are displayed here. The LRFs on one side of the crystal are seen to be fairly symmetric with those on the other side, so that the performance of the crystal may be characterized with half of the crystal. Additionally, the light spread is more restricted as the depth of interaction

increases because the incident photons are closer to the photodetector, both allowing the photodetector to receive more direct (i.e., unreflected) light as well as resulting in less light spread before reaching the photodetector (as indicated in Figure 3.1). The corresponding spatial resolution is shown here as well, illustrating that narrower light spread indeed leads to improved spatial resolution, as predicted by the Cramer-Rao bound (eq. 3.3). Similarly, the 14mm thick crystal is seen to have improved spatial resolution compared to the 25mm thick crystal at each depth, because of the more restricted light spread within the crystal; note that the spatial resolution also improves with depth for the thinner crystal.

These data also illustrate one of the fundamental limitations of thick continuous detectors: light reflections from the sides of the detector broaden the LRFs, particularly near the edges and at shallow depths, thereby degrading the resolution and linearity close to the walls of the detector. This effect ultimately leads to a loss in the sensitive area for the detector (i.e., the area with acceptable spatial resolution) and a loss in sensitivity for the scanner overall.

The positioning measurement is shown to be quite linear until the edges of the crystal (Figure 3.14). This linearity is a result of the smooth, monotonic change of the LRFs with respect to position, as well as the use of a statistical positioning algorithm (here, the nearest neighbor algorithm). While non-linearities in the positioning (i.e., measured beam position vs. actual beam position) may be corrected prior to reconstruction, non-monotonic changes cannot, because the one-to-one correspondence of measured position to actual position is lost.

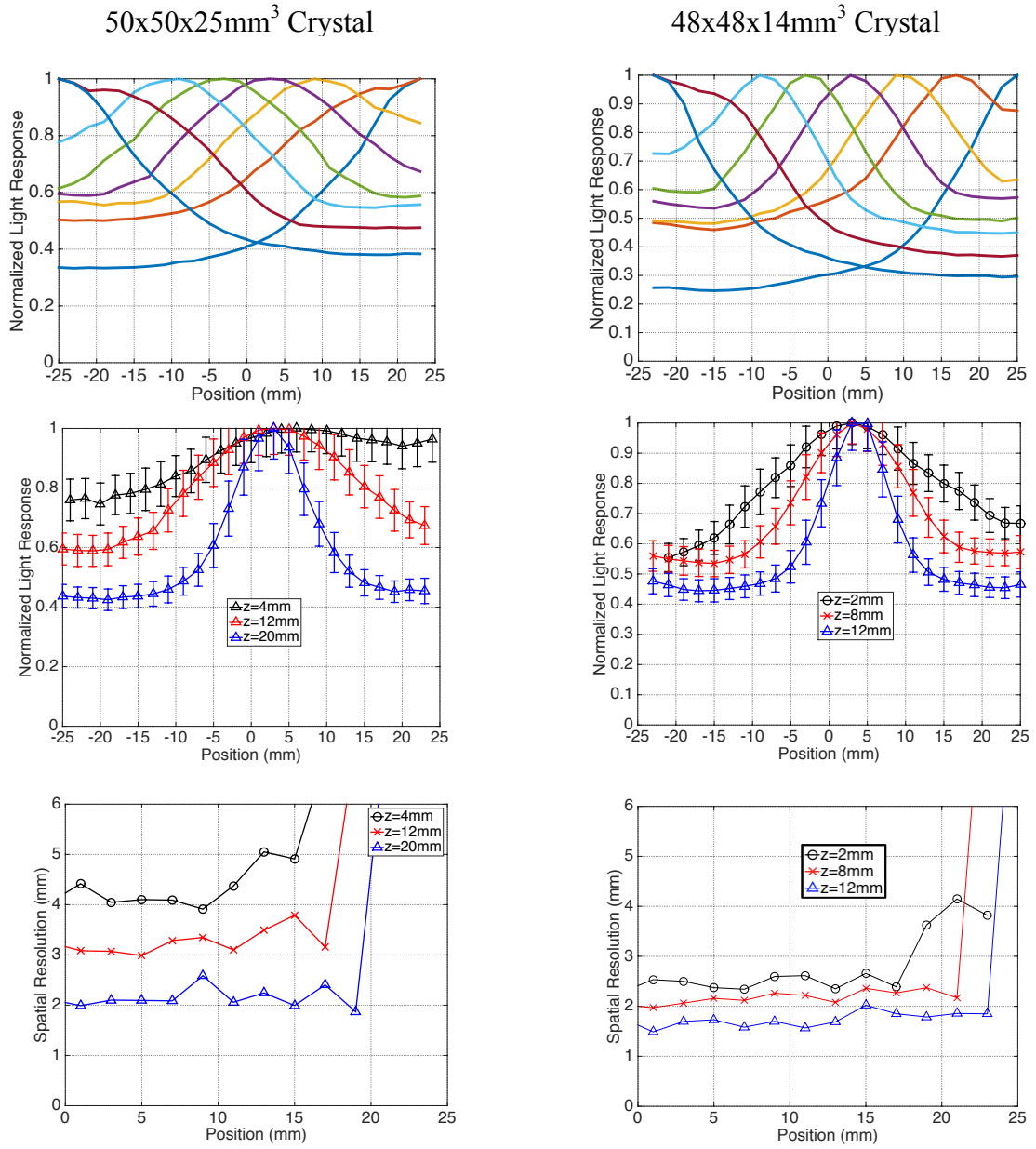


Figure 3.13: LRFs for a single row-column summed anode and spatial resolution at various fixed depths for a $50 \times 50 \times 25 \text{ mm}^3$ crystal and a $48 \times 48 \times 14 \text{ mm}^3$ crystal. Top: LRFs for the 8 row-column summed anodes for a middle DOI; Middle: Central row-column summed LRFs at various DOIs. Bottom: Spatial resolution at various DOIs using the NN algorithm. These data show the depth-dependence of the light spread and the improvement in resolution that results from more restricted light spread.

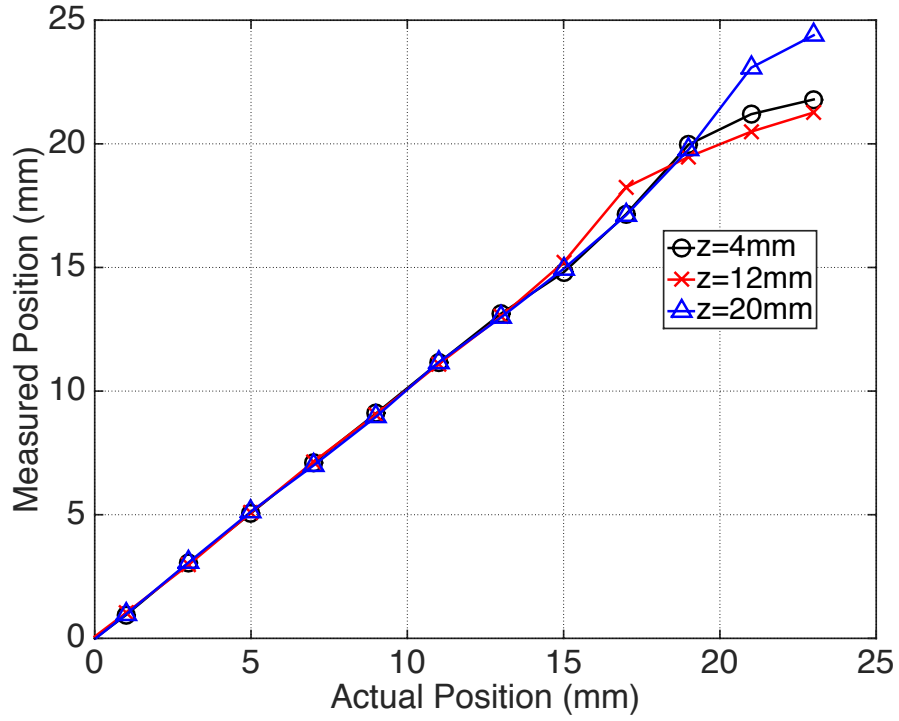


Figure 3.14: Positioning linearity for a $50 \times 50 \times 25 \text{ mm}^3$ crystal for three fixed DOIs, showing the linearity in the central region of the crystal and monotonic change of the measured beam position with actual beam position.

3.4.2 Head-on LRFs

The LRFs for the head-on scan fall between the shallow and middle depths, as expected from the attenuation of LYSO (0.87 cm^{-1}), which results in $\sim 57\%$, 28% , and 15% of detected events interacting within $[0-8\text{mm}]$, $[8-16\text{mm}]$, and $[16-25\text{mm}]$, respectively (Figure 3.15). The magnitude of the uncertainty, however, is larger because:

1. Events from a head-on scan interact at various depths within the crystal, acting to combine the LRFs at the various depths within the crystal.
2. Compton scatter within the crystal that leads to events that interact at multiple depths within the crystal.

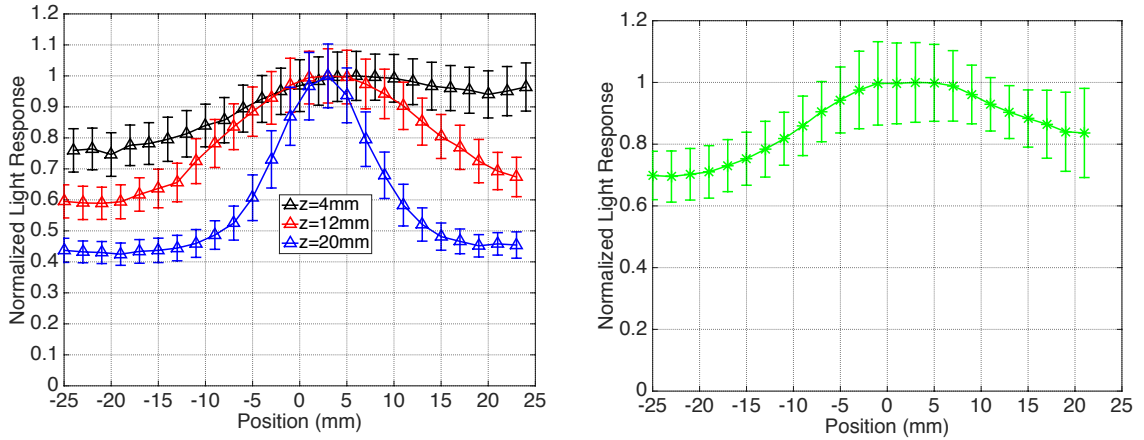


Figure 3.15: LRFs for a side-on and head-on scan for a $50 \times 50 \times 25 \text{ mm}^3$ crystal. Left: LRFs from side-on scans taken at various fixed depths, for a central row-column summed anode. Right: Head-on LRF for a central row-column summed anode, showing that in shape, head-on LRFs fall between the shallow and middle depths, and have larger uncertainty.

3.5 Interactions at the Crystal Walls

Continuous detector designs operate by decoding the position of the detected annihilation photon from the scintillation light spread. An understanding of the manner in which the positional information of the incident photon is conveyed by the scintillation photons is therefore useful for analyzing detector designs, to determine how best to modify the continuous crystal to improve performance. Each scintillation event results in the isotropic emission of photons at the point of interaction, and the information carried by a photon in a continuous crystal is affected by:

1. The distance traveled by the photon before being absorbed by the photocathode, because greater distances result in PSFs at the photodetector plane that are more spread out.

2. Reflections at the walls and Teflon wrapping of the crystal, because these extend the distance of the photons to the photocathode and (in the case of diffuse reflections) randomize their direction, both acting to spread out the PSFs at the photodetector plane.
3. Absorption of photons within the crystal or Teflon layer and loss of photons through the Teflon layer.

In order to clarify the effect of interactions at the side surfaces and entrance surface, the photons that are emitted from a scintillation event may be grouped into three categories, based on their original direction of travel (Figure 3.16). The photons traveling in each direction carry different amounts information regarding the position of interaction; the information carried by photons from each category, as well as the fraction of total photons that fall into each category, depends on the DOI, resulting in an overall dependence of positional information with DOI.

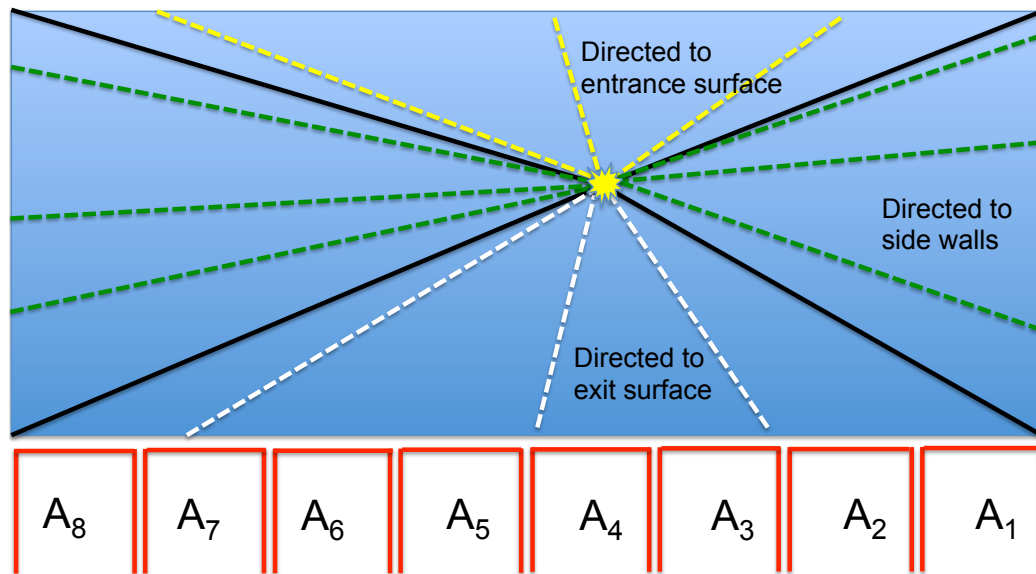


Figure 3.16: Diagram depicting the division of scintillation photons by direction. Photons were divided into those directed at the entrance surface, exit surface (toward the photodetector), and side surfaces of the crystal.

A. Photons directed toward the exit surface (toward the photodetector)

The photons that carry the most information are those that are directed toward the photodetector, since these will travel the shortest distance before being absorbed by the photodetector and will on average reflect less than the other photons, resulting in a PSF that is most narrow.

B. Photons directed toward the entrance surface

The photons emitted toward the entrance surface must reflect from the top surface or Teflon wrapping at least once before reaching the photodetector, increasing light spread relative to those directed toward the exit surface.

C. Photons directed toward the side surfaces

The photons emitted toward the side surfaces will likely reflect many times before reaching the photodetector, if at all. Because of the air gap between the crystal (index of refraction ~ 1.85) and Teflon wrapping, the probability of transmitting through the crystal to the Teflon layer is large. Moreover, because of the diffuse reflections from the Teflon layer, as well as refraction occurring at the air-crystal interface when reentering the crystal, photons reentering the crystal will most likely be directed to another side surface, leading to a greater light spread at the photodetector and increasing the probability that the photons will be absorbed by the crystal or transmitted through the Teflon wrapping before being detected.

3.5.1 Methods and Materials

To determine the relative information carried by these photons, simulations were run in which a gamma beam was scanned down the center ($x=0\text{mm}$) of a $50\times 50\times 25\text{mm}^3$ crystal at two fixed depths (with only photoelectric interactions), $z=4\text{mm}$ and $z=20\text{mm}$ (Figure 3.17). For each simulation, photons from each category were isolated and their resulting LRFs measured. Additionally, histograms of the position at which the scintillation photons are detected were plotted for the categories of scintillation photons; here, the scintillation position was fixed in the center of the crystal in the transverse directions and at a shallow and deep depth.

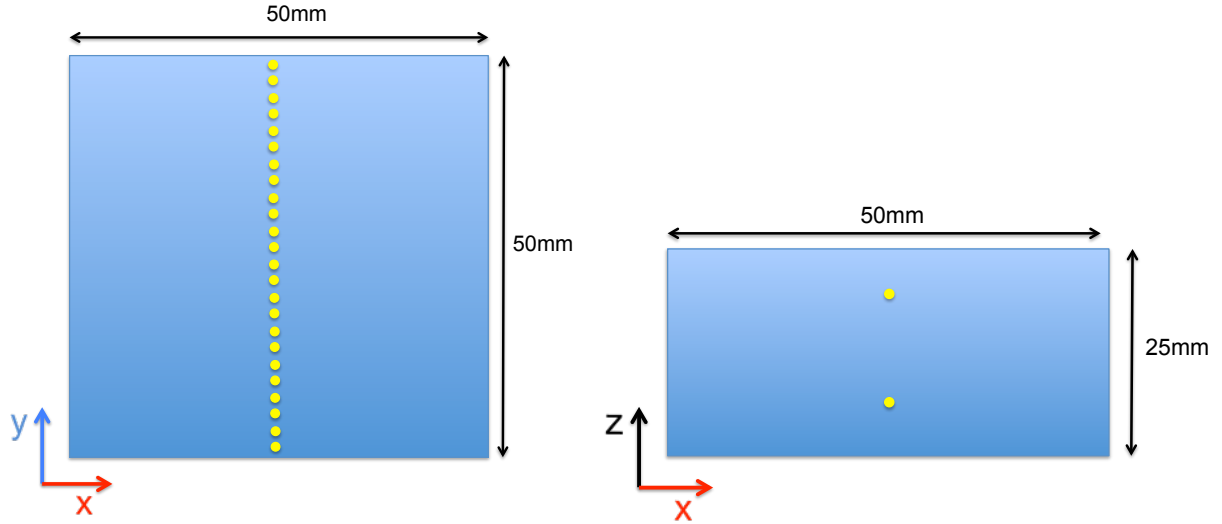


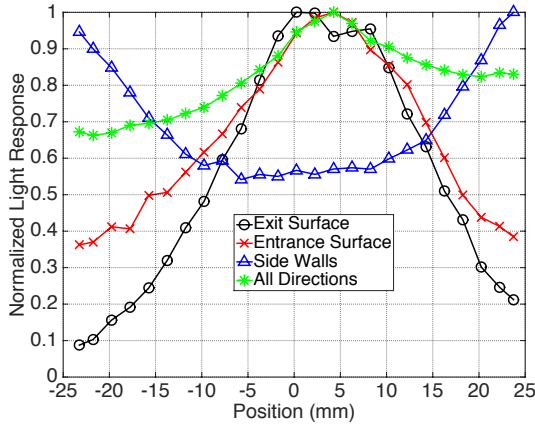
Figure 3.17: Diagram of scan positions for simulation studies of the information carried by photons directed toward the exit surface, entrance surface, and side surfaces of the crystal. Data were collected using gamma beams scanned along the transverse direction at two depths.

3.5.2 Results

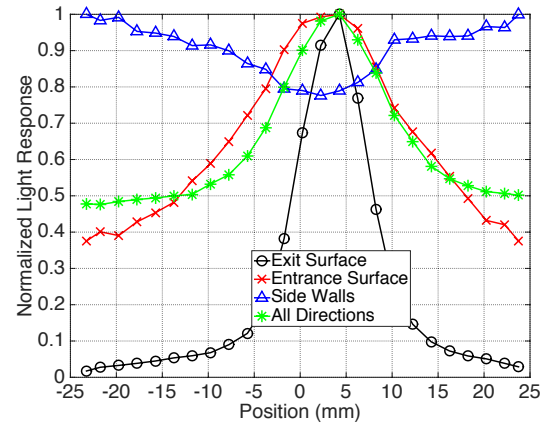
The LRFs for the photons directed toward the various surfaces are plotted in Figure 3.18 for two fixed depths, for a 25mm thick continuous crystal; the fraction of photons detected at the photodetector for each group of photons is shown in Table 3.2 for a central and edge transverse position and for the two depths. The LRFs for the photons emitted toward the exit surface are the most narrow, while those directed toward the entrance surface are slightly wider. Those directed toward the side surfaces are the most wide and do not carry positioning information. The positioning histograms reflect these results, with the photons directed toward the photodetector spread out the least, followed by those directed toward the entrance surface and the side surfaces. In the center, as the incident photon position nears the exit surface, the fraction of photons directed to the exit

surface increases, while at positions near the edge walls, most of the detected photons are directed to the side surfaces.

The deleterious effect of the photons that are emitted towards the side surfaces has prompted research into the value of painting the walls of continuous crystals black in order to improve performance, particularly at the edges [133-139]. This treatment indeed results in improved spatial resolution, despite the loss of photons, and a larger usable field-of-view. The disadvantage of this treatment, however, is a degradation in energy resolution: if all photons directed at the side surfaces were absorbed, this would result in a minimum loss of 25%-70% of photons (Table 3.2), depending on the location of the detected event, which (based on Poisson statistics) would degrade energy resolution by 15-40%; this is a lower estimate because photons that interact with the entrance and exit surfaces first may reflect and interact with the sides later. Similarly, the entrance surface of continuous crystals is rarely painted black, because photons directed to this surface carry enough positional information that the improvement in resolution, if any, would not warrant the loss in energy resolution.



$z=4\text{mm}$ (only photoelectric)



$z=20\text{mm}$ (only photoelectric)

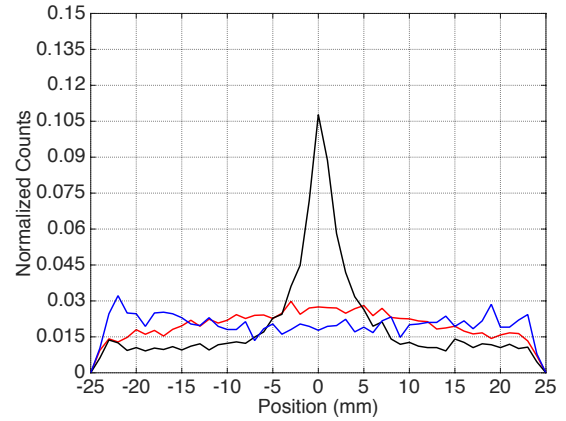
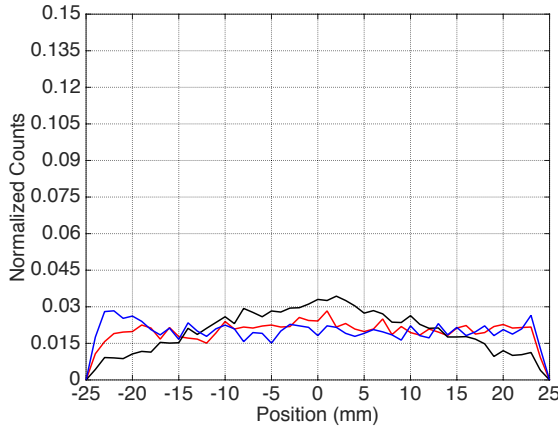


Figure 3.18: Simulated LRFs and positioning histograms for photons emitted in various directions for a 50x50x25mm³ crystal. Top: LRFs for photons emitted in various directions. Bottom: Histograms, normalized by the sum of the counts, of the position along a transverse axis of the detection point at the photodetector, for photons emitted in various directions (colors match those in top plot); the gamma interaction was fixed at the center of the crystal in the transverse direction. These data show that photons directed toward the exit surface carry the most information, while those toward the entrance surface carry less, and those directed at the side surfaces carry no information.

Table 3.2: Fraction of photons detected by photodetector for photons directed toward each crystal surface at two depths and two transverse positions.

Fraction of Photons	z=4mm	z=20mm
x=0mm	Entrance Surface: 40% Exit Surface: 25% Side Surface: 34%	Entrance Surface: 27% Exit Surface: 29% Side Surface: 44%
x=20mm	Entrance Surface: 29% Exit Surface: 18% Side Surface: 53%	Entrance Surface: 20% Exit Surface: 26% Side Surface: 53%

3.6 Impact of Photodetector

3.6.1 Methods and Materials

Research in photodetectors is an active field because of their impact on the overall performance of a PET detector; the primary features of a photodetector that affect the performance of the continuous detector are its quantum efficiency, noise, and sampling (size of pixels). To study the effect of the photodetector on continuous detector performance, and in particular the effect of varying the quantum efficiency and noise, the performances of the continuous crystals using two photodetectors were compared:

1. The Hamamatsu H8500, discussed in section 1.4.1.

2. An early model of a SiPM fabricated by Radiation Monitoring Devices (RMD) and termed a solid-state photomultiplier (SSPM), consisting of an 8x8 array of readout chips, divided into 16 quadrants (~ 12800 pixels/quadrant), with $\sim 19\%$ photon detection efficiency for blue light.

The detector was operated using a power supply that set a bias voltage of 35V, in excess of the breakdown voltage of 27.2V, and using preamplifiers mounted close to the SSPM to increase the signal. In order to measure the temperature dependence of this detector and to maximize its performance, the detection apparatus was set up in a freezer, and measurements were taken at several temperatures between -35°C and 24°C for the 14-mm crystal.

3.6.2 Results

The results of experiments with the SSPM are shown in Figure 3.19 for the 14-mm crystal and at various temperatures, showing improved performance as temperature decreases. For reference, the resolution measured with the H8500 is also shown, showing improved performance with the H8500 at room temperature over the SSPM at the lowest temperature used. As an indication of the noisiness of the detectors, the energy resolution of the detectors as a function of temperature is shown in Table 3.3, and the RMS noise of the SSPM is plotted as a function of temperature in Figure 3.20. The noise and energy resolution decrease sharply as the temperature is lowered from room temperature, with a modest improvement in lowering from -17° to -35° . The excellent energy resolution at room temperature further indicates that the H8500 is indeed relatively noise-free.

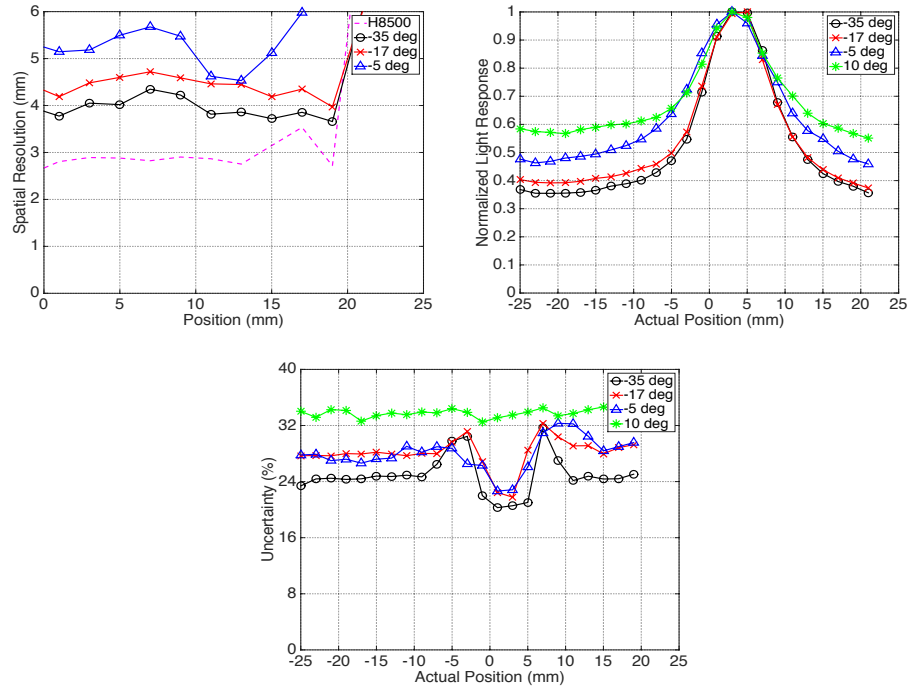


Figure 3.19: LRFs for a central row-column summed anode, spatial resolution, and uncertainty for measurements using the 14mm thick crystal coupled to the SSPM. Top: Spatial resolution and LRFs as a function of temperature. Bottom: Uncertainty of the central row-column summed LRF; the dip near $x=3\text{mm}$ is the point at which this row-column summed anode receives the most light. The performance of the SSPM is seen to improve as the temperature is lowered.

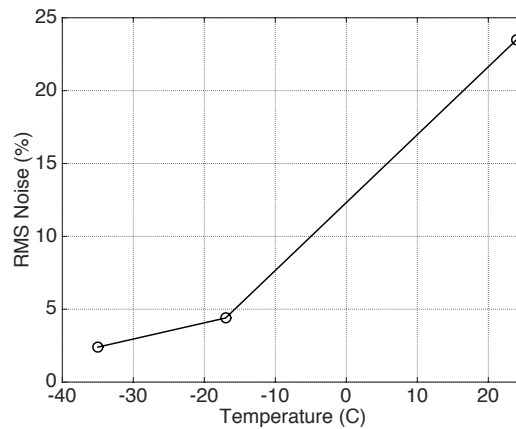


Figure 3.20: RMS noise of the SSPM as a function of temperature, showing that the RMS decreases with temperature.

Table 3.3: Energy resolution of three crystals coupled to the SSPM as a function of temperature. Energy resolution improves as temperature is lowered, because the SSPM noise decreases.

Temperature (°C)	14mm SSPM	14mm H8500
24		9.8%
10	37%	
-5	14%	
-17	14%	
-35	11%	

3.7 Impact of Photodetector Read-out

The size and arrangement of the photodetector elements determine how finely the light spread at the photodetector face is sampled, and represents an example of the inherent compromise between resolution and noise, as smaller pixels also lead to less light collection. This compromise in turn results in a functional dependence of spatial resolution on the read-out of the data (eq. 3.3): while the increase in the number of data points allowed by using all of the anodes that sample the light distribution (i.e., 64-anode read-out) is expected to improve spatial resolution, the increase in the noise inherent in the data points may degrade resolution compared to schemes that sum the anodes (i.e., row-column summing read-out). While the number of anodes used by a photodetector is limited by the number of available position-sensitive photosensors, the method of

analyzing the data output by the photosensors may thus be varied to adjust the sampling of the data.

3.7.1 Methods and Materials

To determine the effect that limited sampling has on the row-column summing scheme, the 64-anode and row-column summing read-out schemes were compared using the H8500 and the experimental SSPM device, as well as crystals of two different thicknesses (25mm and 14mm), to measure the effect that noise and light spread has on the positioning schemes.

3.7.2 Results

Comparisons of the row-column summed and 64-anode read-out schemes (Figure 3.21) show a consistent improvement in resolution by $<0.5\text{mm}$ when using the 64-anode read-out scheme for both the 14mm and 25-mm crystal when using the H8500. The 64-anode scheme results in degraded performance when using the SSPM, however, because of the increased noise of this photodetector.

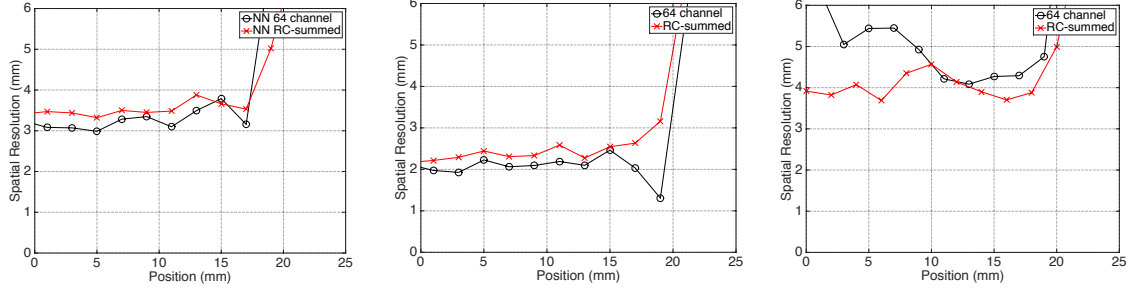


Figure 3.21: Comparison of spatial resolution using the NN algorithm with the 64-anode and row-column summed read-out schemes for: the 25mm thick crystal and H8500 (left), 14mm thick crystal and H8500 (middle), and 14mm thick crystal and SSPM at -35°C (right). Using all 64 anodes improves the performance with the H8500, but shows degraded performance with the SSPM due to noise in the photodetector.

3.8 Impact of Positioning Algorithms

3.8.1 Methods and Materials

A number of statistical algorithms were tested in this work. These algorithms differ from one another in the way in which they use the known information encapsulated by the light response functions in order to position unknown events. The precision of the algorithms must be weighed against computational efficiency: more precise algorithms are computationally more intensive, and may thus be impractical. An exhaustive study of positioning algorithms is outside the scope of this work; for the purposes of this study, a number of relatively practical algorithms were compared against one another and to the simple Anger logic algorithm in their positioning performance. These tests are additionally important to determine the suitability of these algorithms for accurate comparisons of different detector designs.

A. ML Algorithms

Three ML algorithms were investigated, differing only in the PDFs that were maximized:

1. Multivariate-based: while this algorithm is the most accurate, it is more computationally demanding, and requires many more variables (the covariance matrix) to be measured, potentially allowing for more noise to enter into the position estimate.
2. Gaussian-based: this algorithm eliminates the covariances from the computation (assuming they are zero), but still takes into account the variances of the light response
3. Poisson-based: this is the simplest algorithm, which assumes that the light output at each anode follows a Poisson distribution.

B. NN Algorithms

Two NN algorithms were investigated:

1. The average NN method, in which each test event is compared to an average reference set, and the distance calculated according to equation 3.9.
2. A weighted NN method, in which each event (with anode outputs \mathbf{n}) is compared to an average reference set μ^p at position \mathbf{p} , and the distance D^p to each anode is weighted by the uncertainty of the LRF, σ_i , according to:

$$D^p(x) = \sqrt{\sum_{i=1}^N \left(\frac{(n_i(x) - \mu_i^p(x))}{\sigma_i(x)} \right)^2} . \quad (3.12)$$

These algorithms were compared to one another and to the theoretical Cramer-Rao lower bound, using both experimental measurements and simulations; in order to determine the effect of scintillation photon statistics on the performance of the algorithms, these simulations were run using both the normal scintillation light output, as well as with a large ($>5x$) the number of scintillation photons; note that these algorithms are expected to be asymptotically efficient in the limit of very large statistics.

Because of the electronic collimation scheme, the radiation beam used to collect the data spreads with depth. To minimize the effect of beam spreading, events were gated (Figure 3.22) to include only those whose maximum row-column summed output in the x-direction (perpendicular to scanning) is the anode located immediately beneath the incident gamma beam for the head-on configuration (anode 4) and closest to the point of entry for the side-on configuration (anode 1). This gating scheme was validated by comparing to the performance of the positioning algorithms without gating and by gating on the anode one removed from that closest to the incident position for the side-on scan (anode 2).

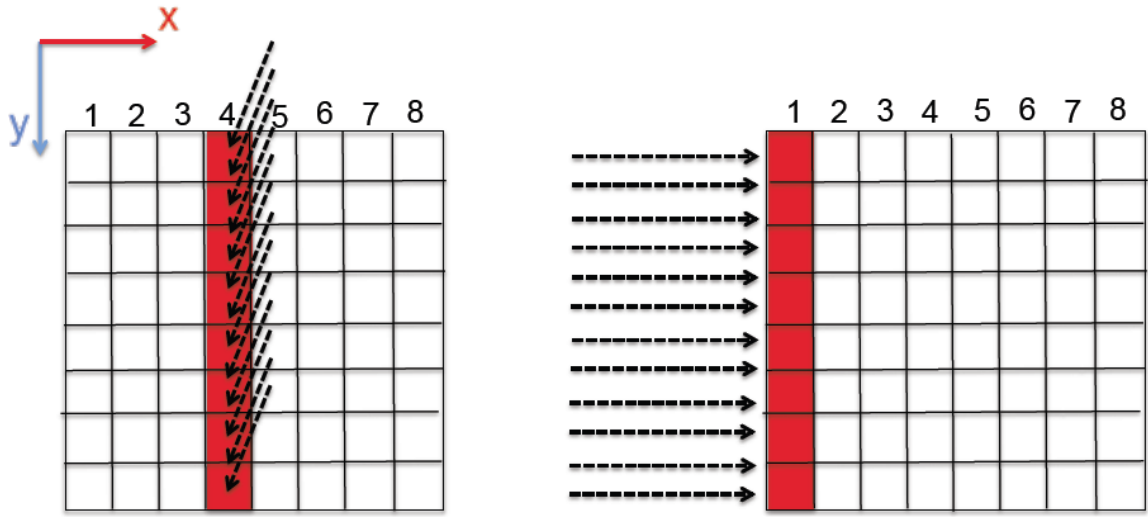


Figure 3.22: Gating on row-column summed anodes (red) for head-on (left) and side-on (right) scans. Gating was performed in order to minimize the effect of the beam spread within the crystal.

3.8.2 Results

3.8.2.1 Gating Events on Maximum Anode

The effect of gating the events by the maximum anode is shown in Figure 3.23, which also shows the resolution for events gated on anode 2. Though the beam width is not Gaussian, the overall resolution of the crystal will be a convolution of the PSF resulting from the detector resolution and the beam width:

$$\Delta x_{meas} = \text{PSF}_{\text{det res}} \otimes \text{PSF}_{\text{beam}} \approx \sqrt{\sigma_{\text{det res}}^2 + \sigma_{\text{beam}}^2}$$

For the side-on scan, events whose maximum anode is one removed from that closest to the surface are $\sim 6\text{mm}$ deeper in the crystal, leading to a larger beam width. Therefore, to minimize the effect of the beam width, only results for gated events will be included in further comparisons.

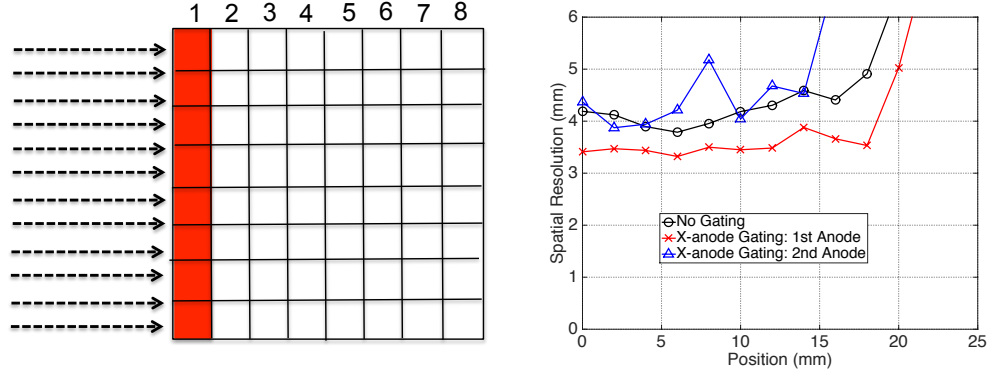
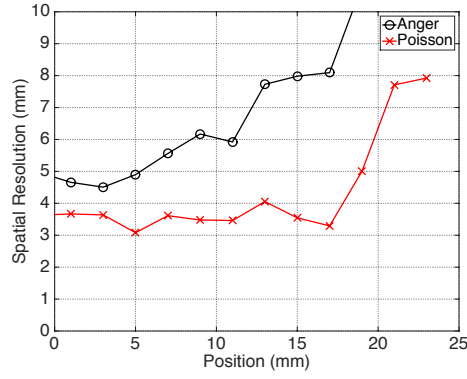


Figure 3.23: Diagram of gating schemes (left) and spatial resolution (right) for $50 \times 50 \times 25 \text{ mm}^3$ crystal at $z=12\text{mm}$ for different gating strategies. Gating on anode 1 was therefore performed for all experiments to minimize the effect of the beam spread within the crystal.

3.8.2.2 Positioning Algorithms

The effect of the variations in the ML positioning algorithm are shown in Figure 3.24 for both the row-column summed and the 64-anode read-out schemes. All ML models show similar performance, and are superior to Anger logic, particularly at the edges of the crystal.



Row-column summed

64-anode output

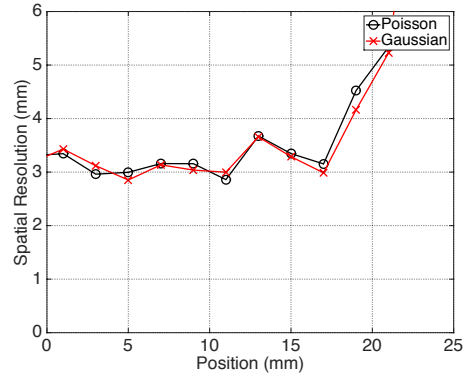
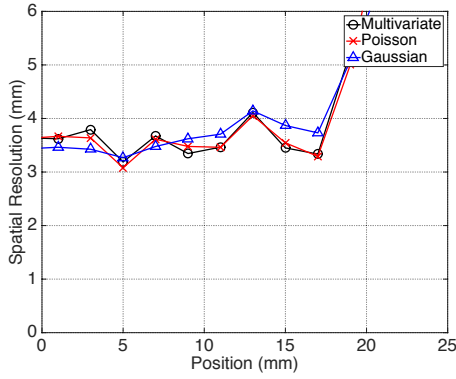


Figure 3.24: Comparison of performance of the ML positioning algorithms. Top: Comparison of Anger logic and Poisson ML algorithms. Bottom: Comparison of ML algorithms for row-column summed (left) and 64-anode read-out schemes (right). Data are shown for a 25mm thick crystal at $z=12\text{mm}$, but are representative of other depths and crystal thicknesses. The ML algorithms show similar performance to one another and improved performance relative to that of Anger logic.

The results of comparisons of the NN algorithms are shown in Figure 3.25; the average model and the weighted model are seen to perform equivalently to one another.

Comparisons of the mean NN algorithm and Poisson-based ML algorithm, for both the row-column summed and 64-anode read-out schemes, are shown in Figure 3.26, showing comparable performance between the two and indicating that either algorithm may be used to decode the information from continuous crystals. These algorithms are also

compared to the Cramer-Rao lower bound, showing that both algorithms are statistically inefficient, with a resolution that is $\sim 1\text{-}1.5\text{mm}$ larger than the lowest possible bound. The simulations indicate that with a larger scintillation light output, the Cramer-Rao lower bound is much closer to being reached using these algorithms, showing that low statistics is the main cause for the underperformance of the positioning algorithms.

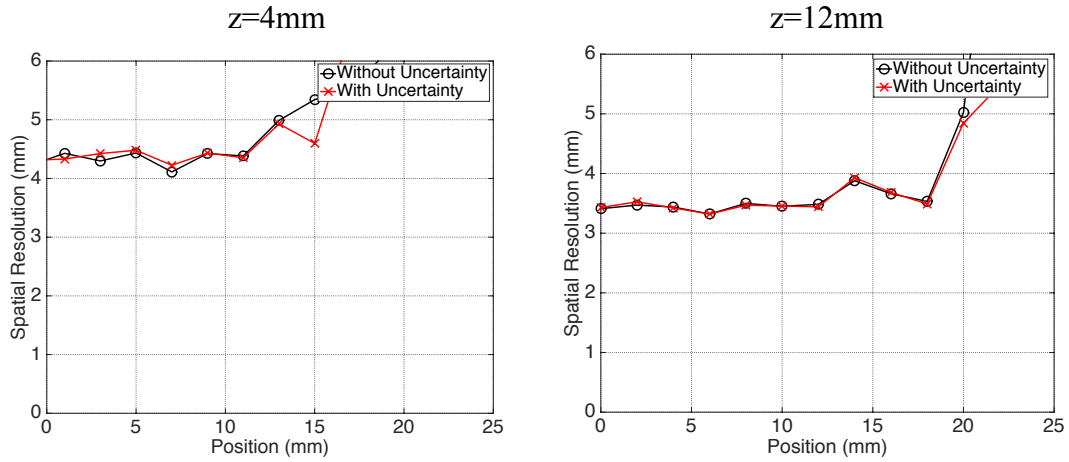
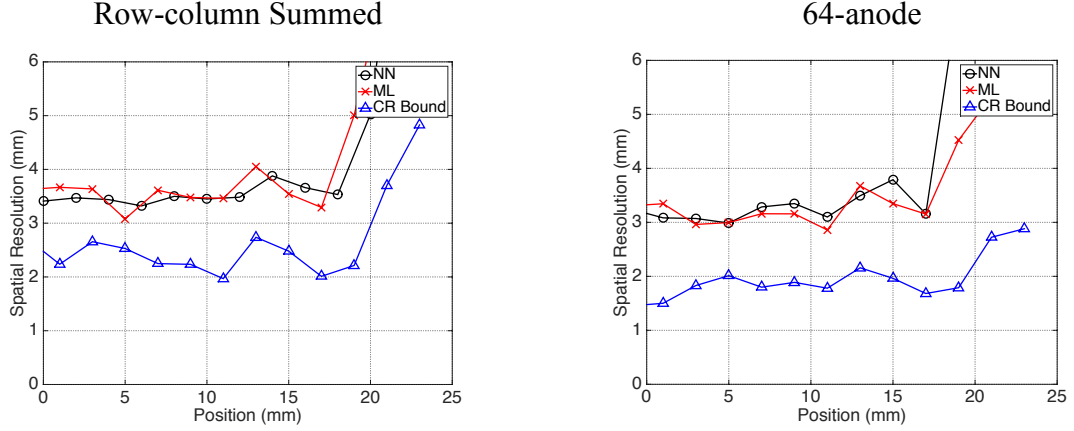
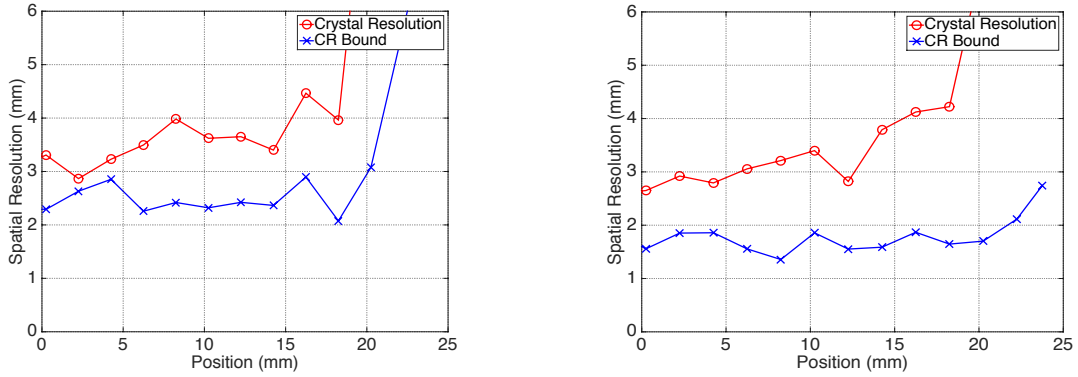


Figure 3.25: Comparison of NN positioning algorithms that do and do not incorporate the uncertainty of the LRFs, for $z=4\text{mm}$ (left) and $z=12\text{mm}$ (right) for the row-column summed read-out scheme. Data are shown for a 25mm thick crystal, but are representative of other depths and crystal thicknesses. The NN algorithms show similar performance.

Experiments



Simulations: Normal Statistics



Simulations: High (>5x) Statistics

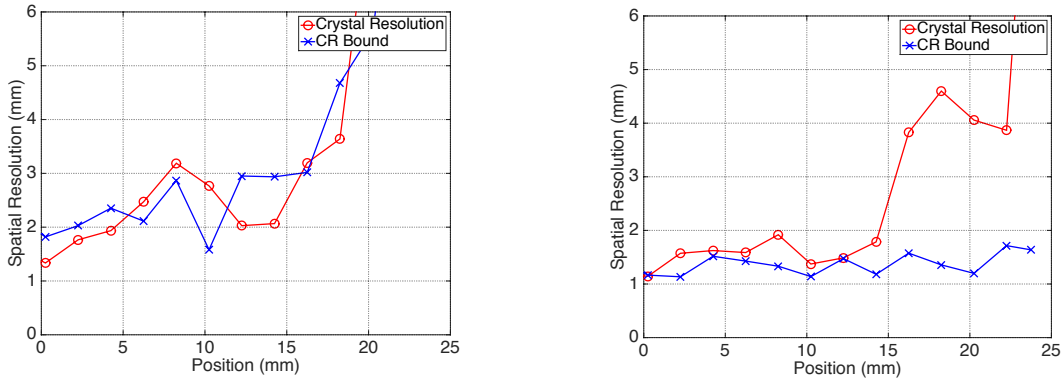


Figure 3.26: Comparison of NN algorithm, ML algorithm, and Cramer Rao bound for row-column summed (left) and 64-anode read-out schemes (right). Top: Experimental measurements. Middle: Simulations with normal scintillation statistics. Bottom: Simulations with high scintillation statistics. The NN and ML algorithms show similar performance to one another, but are shown to underperform relative the Cramer-Rao lower bound, because of insufficient photon statistics.

3.9 Impact of Compton scatter

3.9.1 Methods and Materials

Compton scatter limits the performance of all detector designs, by blurring the scintillation light spread of the 511-keV events (Figure 3.2). To compare the effect of Compton scatter on both systems, simulations were run for each detector, both with and without Compton scatter, and analyzed using the same positioning algorithm, to determine the effect of Compton scatter on positioning in continuous detectors.

3.9.2 Results

Figure 3.27 compares the results of head-on and side-on simulation scans with and without Compton scatter, using the row-column summed NN algorithm, for a 25mm thick crystal. It is seen that for both side-on and head-on scans, Compton scatter degrades the spatial resolution by blurring the transverse light spread. For head-on scans, Compton scatter additionally acts to spread the light distribution among several depths.

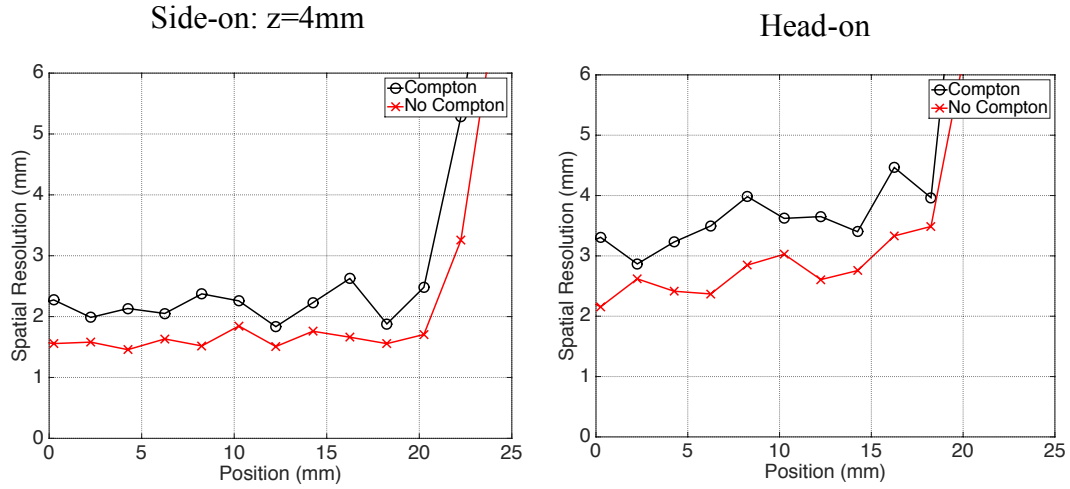


Figure 3.27: Simulated spatial resolution for side-on (left) and head-on (right) configurations for the $50 \times 50 \times 25 \text{ mm}^3$ crystal, with and without Compton scatter. Compton scatter is shown to degrade the resolution of the continuous detectors.

3.10 Impact of DOI

3.10.1 Methods and Materials

While this thesis was not focused on a rigorous investigation of algorithms to measure DOI, an estimate of the performance of continuous systems in measuring DOI is important to compare to modified detector designs. Because DOI algorithms feature an added level of complexity beyond transverse positioning algorithms, practicality was weighed against precision when choosing the positioning algorithm to perform DOI. Therefore, row-column summed data were used and the head-on calibration was preferred over the use of angled gamma beams as a method for calibration, because of its relative simplicity (Figure 3.6). The standard deviation of the 64 anode signals was

chosen as the depth-dependent metric used to divide the head-on data into depth-specific data, by dividing this histogram into regions spaced according to Beer's law. The depth-gated events may then be used to implement a 3D version of the NN algorithm described previously, by correlating the 3D positioning to each set of anode signals.

The use of head-on data to obtain depth-gated data was first verified by comparing LRFs from depth-gated head-on data and side-on scans at known depths, using the row-column summed outputs. While the LRFs for the two data sets are hypothesized to be similar near the center of the crystal, the behavior of the side-on and head-on data were expected to differ near the edge of the detector because the side-on data will be directed near the corners of the detector, where light loss is more likely, unlike the head-on data (Figure 3.8). To estimate the DOI resolution, therefore, this algorithm was implemented using side-on data for both the calibration and positioning, to avoid artifacts resulting from these differences; in a real detector, head-on data would be used to calibrate the head-on (or near head-on) events that would be positioned.

The impact of the DOI on head-on performance was measured by comparing the spatial resolution and positioning linearity of a head-on scan before and after implementation of the DOI algorithm. It was further investigated by comparing the performance of the side-on scans using both side-on and head-on calibration weights to determine the impact of using a single head-on calibration for positioning.

3.10.2 Results

A histogram of the standard deviation of the 64 anode signals for a beam positioned near the center and near the edge of the 50x50x25-mm³ crystal is shown in

Figure 3.28. LRFs for events gated at particular depths are plotted for a central and near-edge row-column summed anode and compared to the side-on LRFs, showing good similarity for the central anodes and more discrepancy near the edges for the edge anodes (Figure 3.29); this is likely a result of light loss near the corners of the crystal. Figure 3.30 shows the impact of using a single set of head-on calibration weights to position events at three representative depths: the resolution and positioning linearity is shown to degrade at the edges at deeper depths, where the LRFs differ significantly from the head-on weights (Figure 3.15). Use of the head-on weights is shown to have less of an impact at $z=4\text{mm}$ and $z=12\text{mm}$ because the LRFs at these DOIs are more similar to the head-on LRFs than at deeper DOIs. The effect of using a 3D positioning algorithm that uses the DOI information from the head-on calibration scan is an improvement in the edge performance of the crystal, resulting in an extension of the useable field of view in one dimension by $\sim 8\text{mm}$ (4mm in each direction), increasing the overall field of view in both directions by $\sim 30\%$ (Figure 3.31 Top). The DOI resolution as a function of transverse position for the three depths shows that the DOI resolution degrades at the edges and improves with depth, as with the transverse resolution.

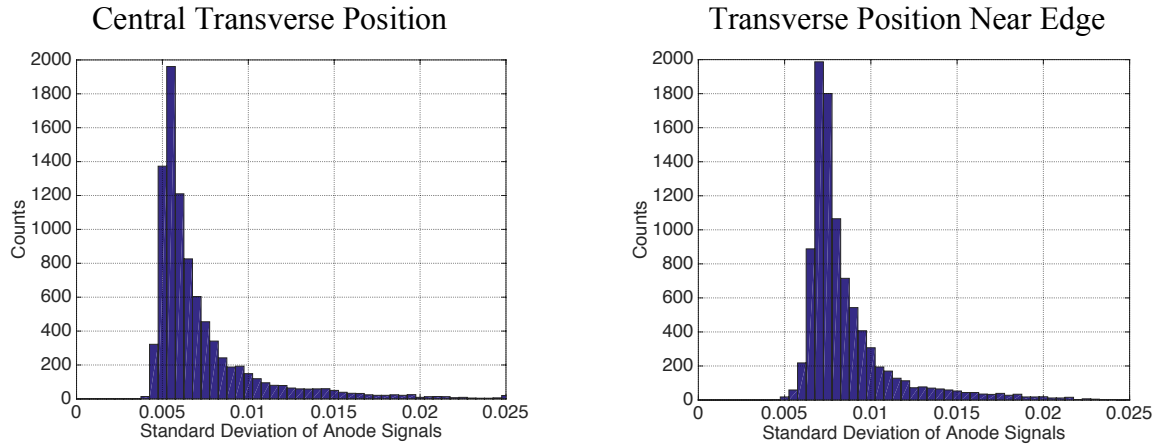


Figure 3.28: Histogram of the standard deviation of the 64 anode outputs for a head-on scan for a central beam position and a beam position near the edge of the detector. These are used to determine DOI information by gating events appropriately on the standard deviation.

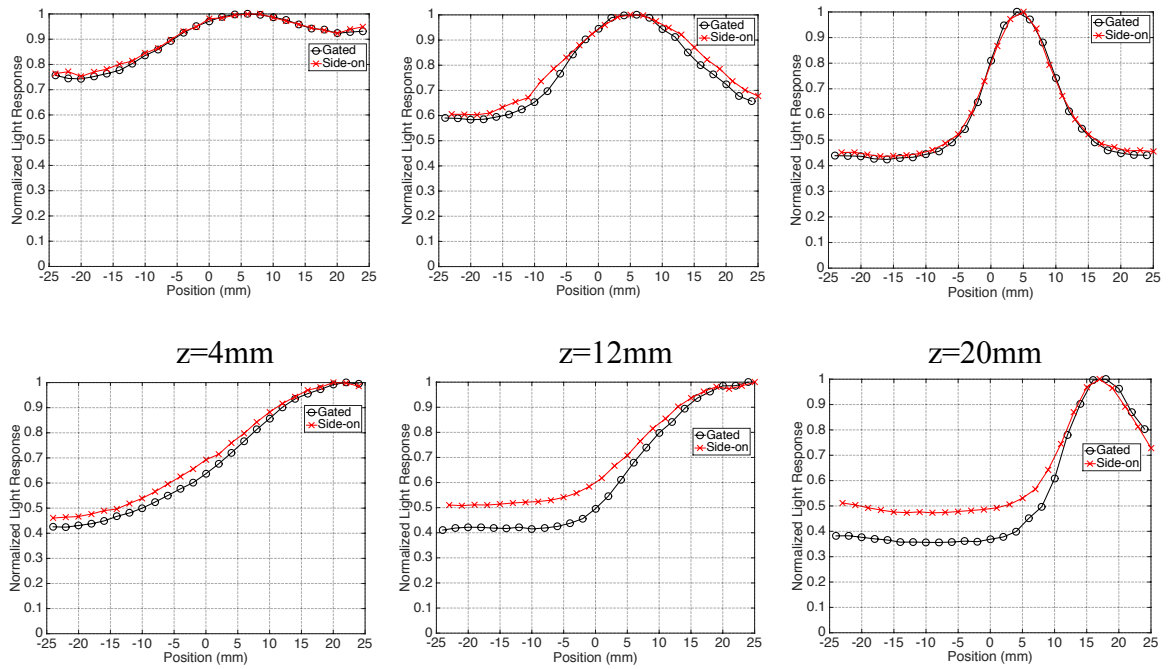


Figure 3.29: Comparison of LRFs from side-on scans and head-on scans gated by the standard deviation of the anode signals. Top: Central row-column summed anode. Bottom: Row-column summed anode near edge. The central row-column LRFs match closely, while those near the edge show more of a discrepancy, likely because of light loss at crystal corners for side-on scans.

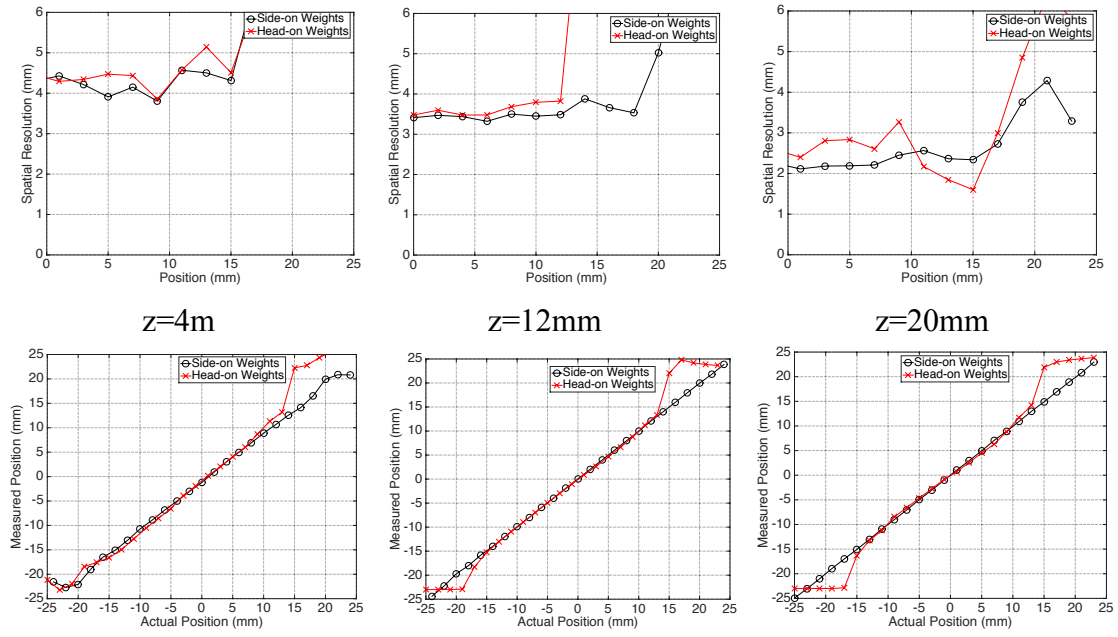


Figure 3.30: Spatial resolution (top) and positioning linearity (bottom) of side-on scans using side-on and head-on calibration data for three different DOI. Better agreement is seen at $z=4\text{mm}$ and $z=12\text{mm}$, where the side-on and head-on LRFs are more similar.

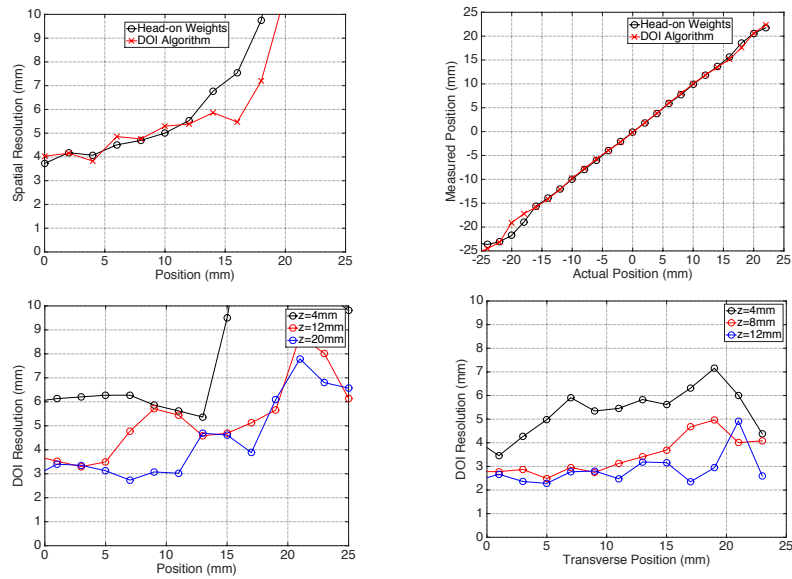


Figure 3.31: DOI information in continuous systems. Top: Spatial resolution (left) and positioning linearity (right) of head-on scan with and without DOI information for the 25mm thick crystal. DOI is shown to improve to extend the usable field of view by 4mm in each direction. Bottom: DOI resolution for three depths for the 25mm (left) and 14mm (right) thick crystals.

3.11 Discussion

This section introduced the important factors in the performance of continuous detectors and illustrated the performance of continuous detectors, along with the many factors that affect this performance. The depth dependence of the spatial resolution was shown, and the improvement in resolution with decreasing crystal thickness shown as well by comparing the 14mm and 25mm thick crystal results. The major disadvantage in the use of the 14mm thick crystal is decreased coincidence sensitivity; this decrease is $\sim 34\%$ for LYSO (attenuation coefficient $\sim 0.087\text{mm}^{-1}$). Note that modern whole body scanners use crystals of thickness $\sim 22\text{mm}$ for this reason. This trade-off in spatial resolution and sensitivity/noise is one of the fundamental limitations of continuous detectors; the challenge of achieving good performance with thick detectors is investigated in this work because of the need for adequate sensitivity. Additionally, the degradation of the resolution and positioning linearity at the edges of the crystal are seen. These studies did not seek to optimize the field-of-view of the detector; however, improved performance at the edges is possible [111, 139] and would be a target of future studies.

Effect of Scintillation Photon Direction

Simulations show that the LRFs for the photons directed toward the photodetector and the entrance surface are narrower than those for photons emitted in all directions, and that these photons therefore carry the most information. The photons directed towards the sides of the crystal carry no information because of reflections with the crystal wall and Teflon wrapping, however, and act to degrade the overall resolution,

particularly near the edges of the crystal. The trade-off in spatial and energy resolution that results from painting the surfaces black is outside the scope of this work, but is an interesting problem involving the optimization of resolution and noise characteristics of the detector, brought about by the selective painting of parts (or all) of the side surfaces. The overall resolution degrades at the edges because reflections from the side surfaces become more predominant as the detected event location nears the edges. The overall LRFs narrow with depth because the LRFs of the photons directed toward the photocathode become narrower and more predominant as the DOI increases. Any modifications made to the bulk of continuous detectors should therefore be evaluated in the context of the effect on the spread of photons emitted in each direction, since the direction of emission strongly affects the contribution to the LRF.

Effect of Photodetector

Results showed that the preliminary SSPM tested in this work became less noisy as temperature decreased, as expected. Nevertheless, comparisons of the energy resolution, used to compare the noise inherent in the photodetectors (section 1.3.2), showed that the SSPM is noisier than the H8500 even at the lowest temperature studied. While the noise of the photodetector cannot be improved much beyond the H8500, the quantum efficiency can, with both the H8500 and the SSPM studied here having a QE ~19%. Indeed, SiPMs are attracting a great deal of interest, with recent scanners built using these, because state-of-the-art SiPMs are much less noisy and feature a QE ~40%. Much of the current research with continuous detectors uses SiPMs, for this reason [139-

143]. A comparison with this preliminary model of SSPM nevertheless illustrates the effect of photodetector noise on detector performance.

Effect of Photodetector Read-out

The improvement in performance with the 64-anode read-out schemes may be understood as a consequence of using more data: using the 64-anode read-out schemes, unknown data are compared against calibration data in two dimensions, instead of one. While positioning with the H8500 improved with the 64-anode scheme for both crystals, data from the SSPM are noisy enough that using data sampled this finely to position the events degrades the performance. The major disadvantages of this algorithm were detailed in section 3.1.2; the results show that for the crystals used in this work, an improvement of $<0.5\text{mm}$ may be obtained at the expense of 8 times more data read out, and an order of magnitude increase in the number of computations and calibration time. While this improvement is smaller than that offered by the more sophisticated algorithms (e.g., k-NN) discussed previously, the increase in complexity is less as well. Because of the improved performance, comparisons made in the remainder of this work use the 64-anode NN algorithm (unless otherwise noted), in order to best estimate any differences in performance between scintillators by maximizing the information read-out by the photodetector.

Effect of Positioning Algorithms

The statistical algorithms were shown to have superior performance to Anger logic, particularly at the edges; this is expected because statistical algorithms are able to

include non-linearities in their model, while Anger logic uses a simple weighted mean, which relies on a linear change in the anode outputs with respect to position. The statistical algorithms require many more computations, however: while Anger logic requires a weighted mean in each direction for all local anodes, statistical algorithms require calibration scans over the face of the detector (25 points for each direction in this study), as well as a calculation for every interpolated point on the calibration grid ($\sim .25\text{mm}$ in this study) for each direction. While the multivariate distribution most accurately represents the likelihood of photon detection by the PMT anodes, the correlation among the anodes is small enough that this model does not lead to a better positioning than those that assume independent distributions. Between the simpler ML algorithms studied, the Gaussian model most closely reflects the statistics of photon detection, both because of the finite energy resolution of the crystal, and because the large number of photons emitted per scintillation event and the 8×8 photodetector used results in a binomial distribution for each anode that is better approximated by the normal distribution.

To understand the effect of the deviance of the uncertainty from the Gaussian model, the derivative of the likelihood with respect to x may be taken:

$$P(x) = \prod_{i=1}^N \frac{1}{\sqrt{2\pi}\sigma} e^{-\frac{(n_i - l_i(x))^2}{\sigma(x)^2}}$$

$$\frac{dP}{dx} = \left[\sum_{i=1}^N \left(\frac{1}{2\sigma} + 2 \frac{(n_i - l_i(x))^2}{\sigma(x)^3} \right) \sigma'(x) + 2 \frac{(n_i - l_i(x))}{\sigma(x)^2} l_i'(x) \right] P(x)$$

The maximum of the likelihood corresponds to the point at which dP/dx is minimized. Because the factor $(n_i - l(x))$ will approach zero at the point of minimization, these terms will dominate the minimization of dP/dx . As long as the shape of $\sigma(x)$ does

not change drastically at the point at which it is a maximum, deviations of $\sigma(x)$ from the Gaussian model will be relatively insignificant. Because the Gaussian model does not improve the resolution, the FWHM of the PDFs of each anode represents a parameter that may add noise to the estimation of the position. The Poisson model is therefore favored for the ML algorithms.

The similar performance of the NN algorithms may be understood using similar logic to that applied to the ML algorithms. Describing the function to be minimized, $D_e(x)$:

$$D_e(x) = \sqrt{\sum_{i=1}^N \left[\frac{(n_{i,e}(x) - l_i(x))}{\sigma_i(x)} \right]^2},$$

and taking the derivative with respect to x , shows that the dD_e/dx , which must be minimized, obeys the relation:

$$\frac{D_e(x)}{dx} \approx \left[\sum_{i=1}^N \left(\frac{n_{i,e}(x) - l_i(x)}{\sigma_i(x)} \right) \left(n'_{i,e}(x) - l'_i(x) + \frac{\sigma'_i(x)}{\sigma_i(x)} \right) \right] D_e^{-1}(x),$$

Because of the factor $(n_i - l(x))$, the inclusion of the uncertainty does not alter the solution greatly, as long as it is relatively smooth.

Comparisons of the results to the Cramer-Rao bound indicate that the ML and NN algorithms implemented here have not reached full efficiency. A thorough investigation and optimization of positioning algorithms is outside the scope of this thesis, though in general, the positioning algorithms discussed in this work could be expanded by exploiting more of the calibration data by, for example, dividing the calibration data into subsets based on their similarity in light distribution. The major disadvantage to

algorithms that use more of the calibration data is increased complexity and computing time for both calibration and positioning. These algorithms may be compared to one of the most computationally intensive algorithms used in the field, the k-NN algorithm, for which every calibration is used to position the events. The number k is determined by empirically optimizing the performance of the algorithm. The k-NN algorithm therefore uses as much of the information from the calibration data sets as possible, and research has shown improved performance with these algorithms, with reported transverse resolution measurements of $\sim 1.7\text{mm}$ for a $32\times 32\times 20\text{mm}^3$ crystal, polished on all sides and wrapped in Teflon [139]. The computational demands of this algorithm, however, are intensive and involve several orders of magnitude of more calculations, challenging the feasibility of these algorithms, since the ability of these algorithms to process events in real-time at clinical count rates has yet to be demonstrated.

Compton Scatter

The effect of Compton scatter on continuous crystals is dependent on a number of factors, including the thickness of the crystal, since the likelihood of detecting Compton scattered photons (and therefore the likelihood of scattered events passing the energy gate) increases with crystal thickness. For the 25mm thick crystal studied in this work, Compton scatter was seen to degrade the FWHM resolution for head-on scans by $\sim 0.5\text{-}1.0\text{mm}$.

DOI

The estimated DOI resolution was measured to be $\sim 4\text{-}6\text{mm}$ in the central transverse 30mm of the crystal for the 25mm thick crystal. Use of a 3D algorithm using this information led to an increase in the field of view for a head-on scan of $\sim 8\text{mm}$ in one

transverse dimension. This result highlights the effect of the depth-dependent light spread, which requires that the positioning be made more complex in order to compensate for it and maximize the sensitivity of the detector.

As with the transverse resolution, more intensive algorithms may be devised to improve the DOI resolution, leading to reported values of ~ 3.7 mm with crystals of similar dimension, at the cost of greater complexity with calculations occurring for all 3 dimensions [139]; in general, crystals of various thicknesses have shown good DOI performance with the use of sophisticated algorithms [140-142]. Use of DOI information has been shown through simulation studies to lead to improved quantitative performance for scanners near the edges of the field-of-view [45-46]; however, because of the use of pixelated detectors, no commercial whole-body scanner implements a DOI correction. Nevertheless, the algorithm described here illustrates the DOI information inherent in continuous detectors and allows for a comparison to modified detectors.

3.12 Conclusions

This section investigated some of the factors that affect the properties of continuous crystals, allowing for a baseline against which to compare any changes made to the crystals. A transverse resolution of ~ 3 mm and ~ 5 mm near the center of the 25mm thick crystal for shallow DOI and deep DOI, respectively, and 1.5-2.5mm for the 14mm thick crystal, is attained. The 64-anode positioning schemes were shown improve resolution by < 0.5 mm compared to the row-column summed algorithms, though the former algorithms require more data to be read-out; this algorithm is used later to compare detectors because of its improved performance. While more intensive

algorithms exist that improve the performance of positioning, the NN and ML algorithms investigated here show similar performance with the use of the H8500 MAPMT, which was shown to be relatively noise-free and suitable for these detector studies. A DOI resolution of 4-6mm and 2-6mm is attained for the 25mm and 14mm thick crystals, respectively, within the central region of the crystal, using a row-column summed NN algorithm.

The major limitations to the thick continuous detector design were also shown, most notably the depth-dependence of the light response, the poor spatial resolution in the entrance region of the crystal, and the poor edge performance. While the performance may be improved with intensive computational solutions and improved photosensors, the detector is fundamentally limited by the nature of the light spread within the scintillator. This light spread is responsible for the improvement in spatial resolution as crystal thickness decreases and DOI increases; here, a difference of ~ 2.5 mm between the 25mm thick crystal at shallow DOI and the 14mm thick crystal at deep DOI was shown. This motivates efforts to modify this light spread in order to explore the trade-offs in performance in continuous crystals associated with this aspect of the detector and to ultimately improve the performance.

CHAPTER 4

Modifying Scintillation Light Spread with Laser Induced Optical Barriers

4.1 Introduction

The performance of a continuous crystal may be improved by several means. Alterations to the bulk of the crystal may be made in addition to other methods to improve performance (e.g., different configurations of the crystal and photodetector), or they may be made in their place as a potentially more practical alternative. In this section, the effect of modifications to the scintillation light spread on the performance of continuous crystals is explored, by investigating the impact of laser induced optical barriers (LIOBs) etched within the crystals. The optical properties of the LIOBs were studied to generally characterize the LIOBs and the effect of varying the parameters of the etching process on their properties, and to improve the Monte Carlo simulation model of their behavior. The overall performance of a detector etched with LIOBs in a grid pattern was characterized as well, by etching several thick continuous detectors. Monte Carlo simulations, informed by the optical measurements, were then used to explore the impact of altering the light spread on crystal performance, by varying the properties of the LIOBs; these results may additionally be used to guide next steps regarding the etching parameters for this detector design.

4.1.1 Improving the Performance of Continuous Systems

Chapter 3 showed that thick continuous crystals are limited by poor spatial resolution in the entrance region of the crystal, as well as a depth-dependent light spread. While improvements in the intrinsic capability of the scintillator (e.g., light output, crystal dimensions) or the photodetector would certainly improve the performance of continuous detectors, these are dependent on current technology. Many attempts have thus been made in the field to improve the performance of continuous detectors by modifying the design of the detector. These can generally be classified into one of three categories, described below. Small blocks of LYSO coupled to either a position-sensitive MAPMT or SiPM are used in these works.

4.1.1.1 Variations in Scintillator/Photodetector Configuration

All current clinical scanners are arranged so that for each detector module, the scintillator faces the patient and the coupled photodetector is behind the scintillator, coupled to the exit side (Figure 4.1). This is known as back-sided readout, and is chosen primarily because of its practicality: this configuration allows incident photons to interact with the scintillator without passing through the photodetector, and more easily allows the readout wires from the photodetector to exit the scanner. Because the performance of continuous detectors strongly depends on the light spread measured by the photodetector, the readout configuration affects the performance of these detectors. There are two alternative configurations that have been studied:

1. Front-sided readout: The photodetector is placed on the entrance side of the scintillator. This configuration is advantageous because of the attenuation

coefficient of LYSO, which results in more detected events interacting within the entrance half of the crystal than the exit half for thick crystals. The light spread of events in the entrance region of the crystal is narrower at the entrance surface, and photodetection at this surface thus leads to better spatial resolution. Studies have shown improvements in transverse resolution of ~20-25% and in DOI resolution of ~20% with front-sided read-out compared to back-sided readout [115].

2. Dual-sided readout: Two photodetectors are used for each scintillator, one on the entrance side, and the other on the exit side of the crystal. This configuration uses information from both sides of the scintillator to result in better light collection, better and more uniform transverse performance, and improved DOI capability. Studies have reported an improvement in transverse resolution of ~10% compared to front-sided readout [143].

The major disadvantages to these designs are:

- A. Designs with the photodetector coupled to the entrance surface of the scintillator are more complex because the cables that read out the photodetector signals must be designed to exit the scanner in some way.
- B. Dual-sided readout suffers from the additional burden of twice as many readout cables and twice as much data to read out and process.
- C. Detectors on the entrance region must not significantly attenuate the incident photons to be detected, and the photodetectors must be radiation resistant. For these reasons, SiPMs must be used for these designs.

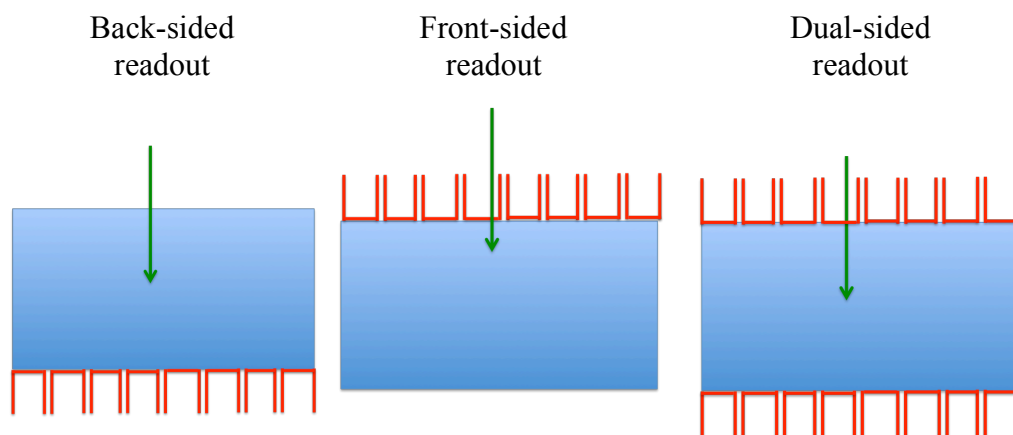


Figure 4.1: Various configurations of the scintillator and photodetector used to decode the light spread within the continuous scintillator.

4.1.1.2 Surface Treatments

The continuous crystal itself may be modified to improve performance by restricting the light spread within the scintillator. The simplest method to achieve this is to treat the surface to alter the reflections of photons. The surface polish is one example of these surface treatments. Studies most often use polished side surfaces because roughening the side surfaces has been shown to lead to a worse spatial resolution. There are advantages to both surface finishes for the entrance surface, however: a polished entrance surface results in a narrower light spread and better spatial resolution, while a roughened entrance surface leads to improved light collection and a slightly better energy resolution; most detectors in current continuous detector studies use a polished entrance surface because of the better spatial resolution. As discussed in Chapter 3, studies have investigated painting the sides of the crystal surface black, to limit the reflections at the side surfaces that degrade the resolution [133-138], at the expense of degraded energy resolution. Last, almost all studies wrap the crystals with a reflector to greatly improve

light collection; usually, this consists of either Enhanced Specular Reflector (ESL) or Teflon (used in these studies).

4.1.1.3 Alterations in the Bulk of the Crystal

The scintillator may be more substantially altered as well, by introducing interfaces that control the amount of light spread within the scintillator. Studies that have attempted this are limited. For example, the University of Washington has investigated a novel type of detector, dMiCE, in which pixels are separated by tapered reflectors that allow light to transmit through to other pixels in a depth-dependent manner. The studies showed that individual pixels could be resolved, while DOI information could be inferred by measuring the degree of light spread within the detector [144, 145]. At the University of Pennsylvania, Kaul et al. [138] investigated the performance of a thick block of LYSO, in which mechanical cuts were introduced partly into the entrance surface of the crystal, and demonstrated improved spatial resolution at shallow depths within the scintillator, in which interactions are most likely to occur, leading to an overall improvement in spatial resolution in the detector. More recently, groups have investigated a novel method to alter the crystal that involves using a laser to etch barriers, known as laser induced optical barriers (LIOBs), into the detector; these are discussed later.

4.1.2 Fundamentals of Laser Etching

In general, methods that use lasers to create barriers may be divided into two categories: ablation and sub-surface laser engraving. Ablation involves the use of a focused laser beam to melt the crystal material from the surface of the crystal inward; the resulting barrier within the crystal consists of a crystal-air interface. This process is

analogous to physical cutting of the crystal, in that crystal material is destroyed and barriers may only be introduced by disturbing the surface of the crystal. Sub-surface laser engraving (SSLE) involves the use of a laser beam that is focused inside the crystal; if the crystal is transparent to the frequency of laser light used, the laser may disturb the crystal locally at the focal spot. Here, the barrier that is created consists of small disruptions in the crystal structure known as microcracks. The crystal is therefore etched from the inside outward, allowing for the introduction of barriers within the crystal. Because of the flexibility afforded by internal etching, SSLE was chosen to etch the crystals in this work.

SSLE represents a very broad class of etching, because of the large number of parameters that may be varied in the etching process. Some of the important parameters are discussed below.

1. Laser type: a number of options exist (e.g., CO₂ lasers, excimer lasers) for this process, but solid-state lasers are common for the purposes of etching into solid materials, because they represent a good balance between edge quality, which is dependent on the duration of the laser pulse, and cost. Among solid-state lasers, a number of choices exist for both the active medium and the host material, which both act to determine many of the properties of the laser. Nd:YAG lasers are the most commonly used solid-state lasers, and were chosen for this work because they provided good etching quality. The energy diagram of the lasing process with Nd³⁺ lasers is shown in Figure 4.2.
2. Laser frequency: the laser frequency is generally determined by the active medium and host, though one of the advantages of solid-state lasers is harmonic

generation, in which integer multiples of the primary frequency laser light may be created and isolated.

3. Mode of Operation: Nd lasers are capable of being run in either pulsed mode, in which the active medium is lased in short pulses, or continuous mode. The advantage of running the laser in pulsed mode is that a large amount of energy may be delivered in a short time period to deliver a cleaner (i.e., no crystal melting) etching.
4. Repetition rate: The rate at which the laser is pulsed is limited by the lifetime of the upper state during the lasing process.
5. Pulse length: the duration of each laser pulse, often characterized by the FWHM, is also important to the quality of the LIOB and is dependent on a number of factors, including the active medium, the cavity length, and the repetition rate.

Shorter pulses are preferred for etching and micromachining for two reasons:

- A. The pulse length must be compared to the characteristic time of heat dissipation in the material, determined by the characteristic time for the transfer of heat between the crystal lattice and the free electrons in the crystal. If the length of the pulse is longer than this time, heat will spread within the crystal, leading to a heat-affected zone and imprecise etching. In particular, ultrashort pulses ($<1\text{ ns}$) allow for photon absorption by valence electrons -- which allows for the breakage of bonds -- before heat is absorbed by the material.
- B. Shorter pulses allow for larger peak powers, which allow for high enough photon intensities that multiphoton absorption occurs, leading to

disruption of transparent media, such as crystal, without substantial heating.

The major disadvantages of shortening the pulse length is that in general, pulse energy decreases and the cost of the laser increases [146-151].

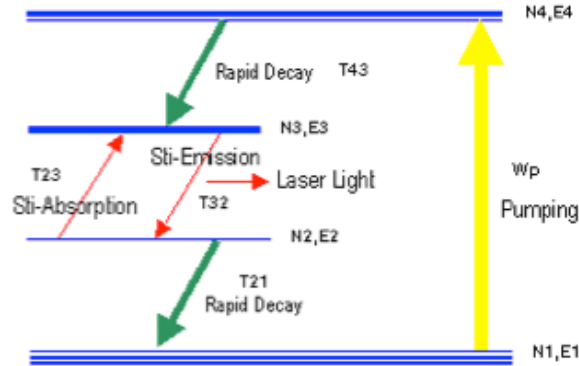


Figure 4.2: Energy level diagram for Nd^{3+} laser.

4.1.3 Laser-induced Optical Barriers

In recent years, the etching of LIOBs within continuous scintillators using highly focused lasers has been studied for its applicability to alter the bulk of the crystal [152-160]. One of the advantages of this technique is the number of possibilities afforded by the range of depths within the crystal and the range of optical properties with which the etchings may be made. Some of these research efforts are described below:

1. Pixelation

Some groups have investigated using this technology to replace the mechanical pixelation currently performed for pixelated detector designs. Advantages to using LIOBs instead of physical reflectors include less material loss with each barrier, and therefore the possibility of a more finely spaced grid of etchings, as well as potential cost

savings, since the cost per pixel increases dramatically as the pixel size becomes smaller. Research in the field has shown that pixels may be discriminated with thin detectors etched very finely (e.g., 6.5:1 cross-talk ratio for a 20x20x5-mm³ crystal with pixels with a 0.8-mm pitch) [152-154].

2. Light-sharing

Research has also been conducted to exploit the ability to etch these barriers in patterns difficult or impossible to achieve with the physical cuts. The University of Washington has investigated using LIOBs to replace the physical reflectors in their dMiCE detector design [155], because one of the major drawbacks of this detector was the complicated reflector design. The goal of this work was a continuous crystal etched with barriers that transmit light in a depth-dependent manner. The University of Chiba similarly used this light-sharing concept to design a crystal segmented with LIOBs into a 3D grid with a pitch of 2mm in each direction [156-157], to be coupled on all six sides by a photodetector; the LIOBs in this case replaced the air gaps from a previous design of this detector in which individual crystal segments were coupled together without a reflector [158].

The work in this thesis intends to use the semi-transparency of the barriers to modify the light spread within the detector, using the unique effect they have on the light spread within the scintillator. The flexibility afforded by the etching process is also exploited, so that both the physical pattern (including depth) of the etching design and the optical properties of the barriers are important variables to the functioning of this detector. This technology is ultimately used to explore the trade-offs associated with

altering the light spread in thick continuous detectors in ways that are impossible otherwise.

4.2 Optical Properties of LIOBs

4.2.1 Details on Laser Etching

This work was performed in collaboration with Radiation Monitoring Devices, Inc. using two ND:YAG lasers operated by Photomachining, Inc. The lasers were run at double the frequency to produce green light (532 nm), with a repetition rate of 100-200 kHz, a pulse length of 12ps, and a scan speed $\sim 70\mu\text{m/s}$. Each of the LIOBs used in this work consisted of two passes. To etch a single pass LIOB (Figure 4.3 A), the laser is focused at a particular depth to create a microcrack, and the crystal translated horizontally (perpendicularly to the direction of the beam) with the laser etching to create a thin line at that depth. The crystal is then translated vertically (along the direction of the beam) by a small amount ($\sim 10\mu\text{m}$) and the crystal translated horizontally again with the laser etching to etch above the first line. This raster scan is repeated until an etching of the desired height is reached. In contrast, to etch a double pass LIOB, the raster scan is altered such that after the first line of the etching is made, the crystal is translated vertically at half of the previous height, as well as horizontally (perpendicularly to the length of the etching) by a small amount ($\sim 10\mu\text{m}$), so that lines are etched in the crystal in a ladder pattern until the desired depth is reached (Figure 4.3 B). The double pass LIOB is therefore thicker and more opaque because the crystal is etched at two horizontal positions.

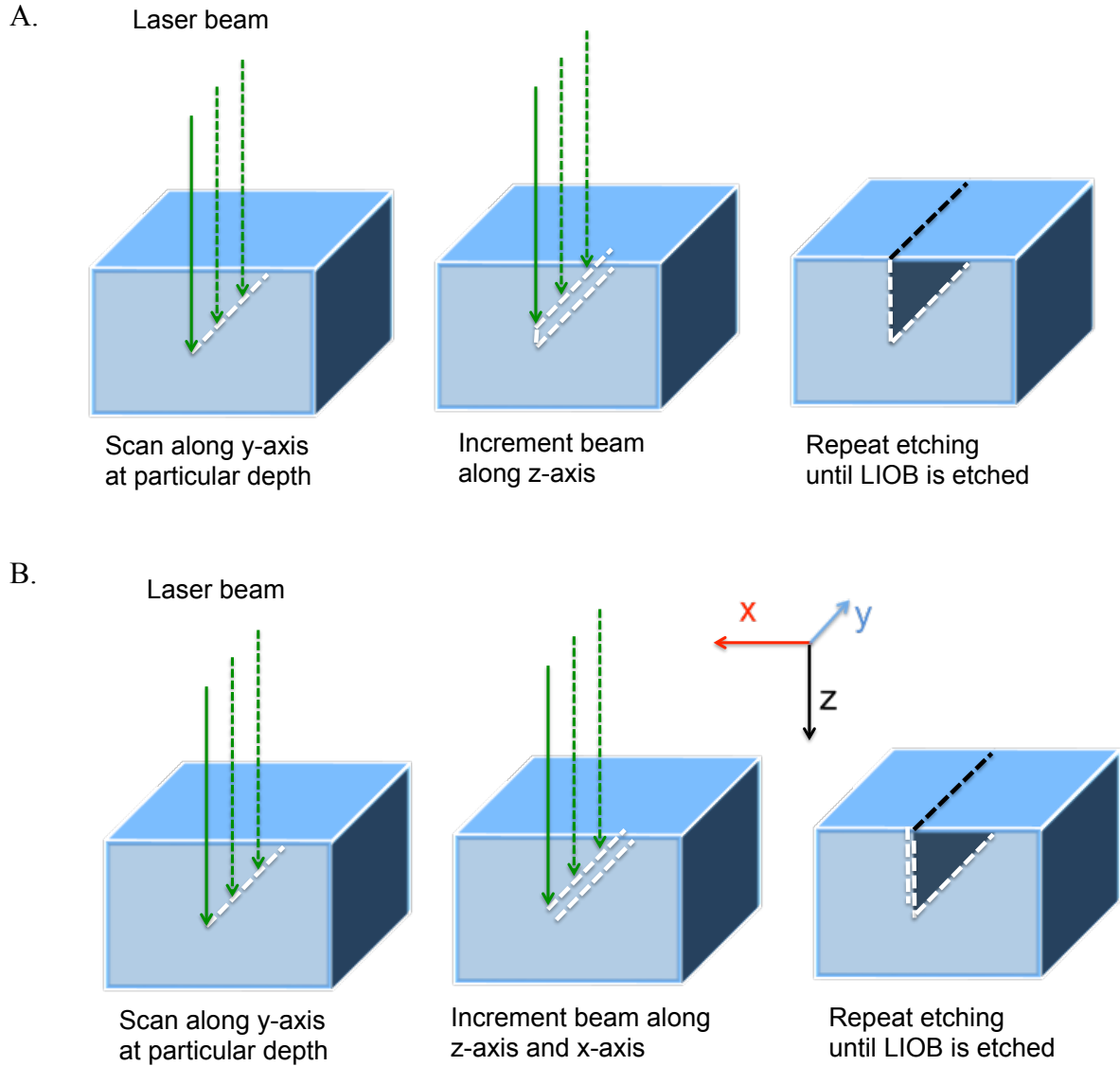


Figure 4.3: Diagram of etching procedure. A: Diagram of single pass LIOB etching. Here, a laser is directed at a particular depth and scanned horizontally along the desired length of the LIOB. The laser is then incremented vertically and scanned across again; this process is repeated until the desired height of the LIOB is reached. B: Diagram of double pass LIOB. This process differs from that of the single pass LIOB because the laser is incremented both vertically and horizontally (perpendicularly to the scanning) before scanning horizontally.

4.2.2 Optical Measurements: Model

The optical behavior of the LIOBs was modeled according to reflection [117-119, 161] and transmission models described in the literature; this model is diagrammed in Figure 4.4. Here, incident light is hypothesized to interact with the LIOBs by one of three mechanisms: transmission, reflection, and absorption, each with a separate probability of occurrence.

1. The transmitted light is modeled as consisting of light directly transmitted, in which the direction of light is unchanged, and diffuse transmission, in which the direction of transmitted light is given by a Lambertian probability distribution.
2. The reflected light is modeled as consisting of light specularly and diffusely reflected (Figure 4.4).
3. Absorption is neglected in this model, because the etched crystals do not show a decrease in light output, as discussed later in the results.

The interactions of light with the etchings are therefore described by the following equations:

$$L_T = T * L_I = L_S + L_D \quad (4.1)$$

$$L_S = f_s * L_T \quad (4.2)$$

$$L_D = (1-f_s) * L_T \quad (4.3)$$

$$L_R = R * L_I = L_{RS} + L_{RD} \quad (4.4)$$

$$R + T = 1, \quad (4.5)$$

where: L_I , L_T , L_S , L_D are the intensity of the incident beam of light, transmitted light, directly transmitted light, and diffusely transmitted light, respectively.

L_R , L_{RS} , L_{RD} is the intensity of the reflected light, specularly reflected light, and diffusely reflected light, respectively.

T , R are the transmission and reflection coefficients of the LIOB, respectively.

f_s is the fraction of transmitted light that directly transmits through the LIOB.

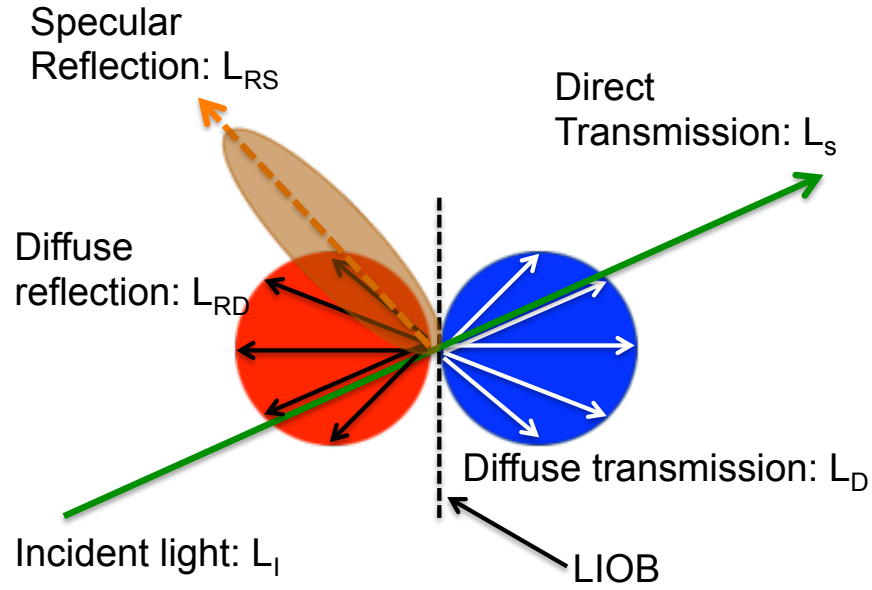


Figure 4.4: Model of the interaction of light with the LIOBs. Reflected light is modeled as consisting of specularly reflected light (specular spike and specular lobe) and diffusely reflected light. Transmitted light is modeled as consisting of directly and diffusely transmitted light.

4.2.3 Optical Measurements: Samples

The optical characteristics of the LIOBs were explored using small samples of LYSO that were prepared by cutting one block of LYSO into several small cubes, each $\sim 10 \times 10 \times 7 \text{ mm}^3$ in dimension, so that the composition of each of the LYSO cubes was the

same; the size of the cubes was chosen so that a large number of samples could be obtained. The cubes were then polished, so that light could be transmitted through the crystals. The cubes were etched with double pass LIOBs in the center of one of the $10 \times 10 \text{ mm}^2$ faces of the crystal, extending $\sim 3 \text{ mm}$ from the surface into the crystal (Figure 4.5). The crystals were etched on two different dates by 2 different lasers, a Lumera and a Lumentum laser: the Lumera was run at 100 kHz up to 4W in power to avoid cracking the crystal, while the Lumentum was run at 200 kHz up to 6W in power to avoid cracking the crystal. The laser parameters were based on recommendations from technical experts to balance our goals of etching semi-opaque barriers partially into thick crystals, while mitigating the risk of cracking the crystal. The parameters of the etchings were varied for each of the crystals etched by a particular laser. On the Lumera, two laser powers were used for 3 cubes each, 3W and 4W, while three different settings were chosen for the distance between the two passes, ranging from $5 \mu\text{m}$ to $20 \mu\text{m}$. On the Lumentum, several laser powers ranging from 3W – 6W were used, while the settings for the distance between the passes ranged from $5 \mu\text{m}$ to $20 \mu\text{m}$. In order to explore the effect of larger gaps between the microcracks, the spacing between the microcracks in the vertical direction was increased as the spacing in the horizontal direction increased. These settings resulted in LIOBs that were $\sim 20\text{-}40 \mu\text{m}$ in thickness. A summary of the various settings used is given in Table 4.1.

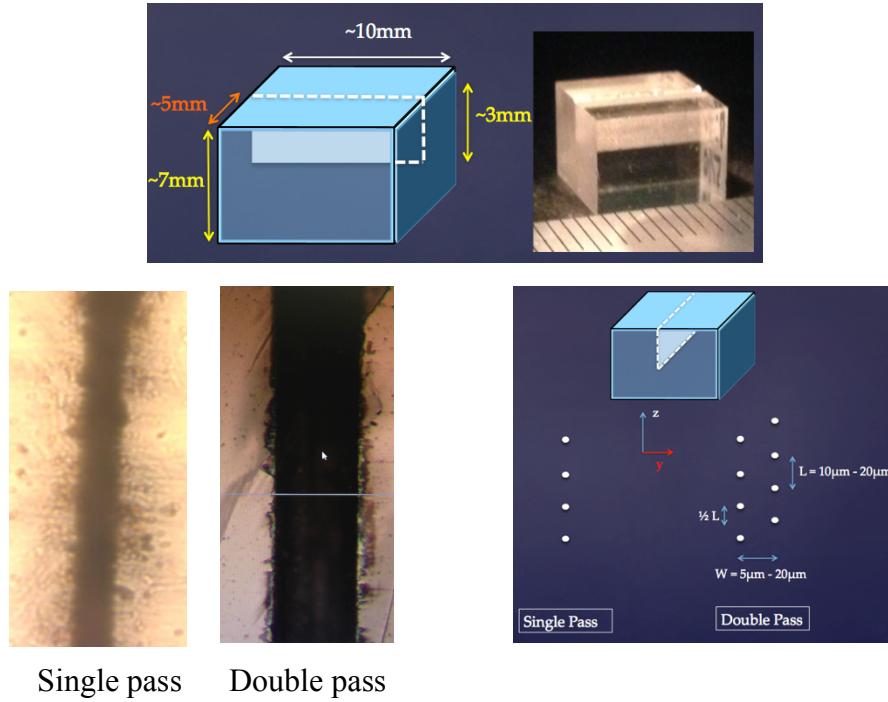


Figure 4.5: Etched LYSO cubes. Top: Diagram and photograph of an etched LYSO cube. Bottom Left: Microscopic images of a single pass LIOB and a double pass LIOB, showing two darkened regions (laser etching) separated by a lighter region, with total thickness $\sim 30\mu\text{m}$. Bottom Right: Diagram of the etching parameters for the LIOBs.

Table 4.1: Summary of LIOB parameters used for the cubes.

Lumera Power: y, z spacing:	3W 5 μm , 10 μm	3W 8 μm , 12 μm	3W 20 μm , 20 μm	4W 5 μm , 10 μm	4W 8 μm , 12 μm	4W 20 μm , 20 μm
Lumentum Power: y, z spacing:			5W 20 μm , 20 μm	6W 5 μm , 10 μm	6W 8 μm , 12 μm	6W 20 μm , 20 μm

4.2.4 Optical Measurements: Apparatus

The apparatus designed to study the response of the LIOBs to optical light is diagrammed in Figure 4.6. A beam collimator was fixed to be parallel with the optical table, very close ($<1\text{mm}$) to the small cube (to minimize the diameter of the beam), which was held fixed to a vertical translation stage, with a PMT located behind the crystal and fixed to a horizontal translation stage. Each motor could translate in increments $< 0.1\text{mm}$. A 5mm blue LED was fixed in place at one end of the two-piece collimator. The first piece consisted of two 1.0mm pinholes fixed to either end of a 320-mm tube that was $\sim 5\text{mm}$ in diameter; the inner walls of the tube were painted black to minimize reflections of light within the tube. A 75-mm tube that was 0.84-mm in diameter was inserted into one of the pinholes, with 10 mm protruding from the tube, to further collimate the beam and allow for close positioning of the collimator to the crystals. The collimation resulted in a $\sim 1\text{-mm}$ beam at 5mm from the tube. Light was pulsed using a square wave generator, so that the peak-to-valley of the signal was used as a measure of the amount of light detected, in order to eliminate the effect of any background light. The light was measured with a Hamamatsu R1635 PMT (diameter=10mm), which was either uncollimated or collimated so that light could only pass through a narrow vertical slit of width $\sim 0.5\text{mm}$.

4.2.5 Optical Measurements: Experiments

4.2.5.1 Transmitted Light

To determine the overall transmission coefficient (T) and the fraction of light that is directly transmitted (f_s), two experiments were conducted, depicted in Fig 4.6.

1. The PMT was positioned far from the crystal, so that only the directly transmitted light would be measured; to isolate the effect of the LIOBs, the measurement of light passing through the etched portion of the crystal was divided by the measurement when passing through the unetched portion:

$$V_{\text{etched}}/V_{\text{unetched}} = f_s * T, \quad (4.6)$$

with V_{etched} and V_{unetched} equal to the voltage when light passed through etched and unetched regions of crystal, respectively. The collimator was attached to the PMT to verify the profile of the beam.

2. Another experiment positioned the PMT very close to the crystal, so that both the directly transmitted light and a large fraction of the diffusely transmitted light would be measured by the PMT:

$$V_{\text{etched}}/V_{\text{unetched}} = f_s * T + (1-f_s) * T * F, \quad (4.7)$$

where F is the fraction of diffusely scattered light collected by the PMT, calculated with simulations (described below).

The results of these experiments were used to solve the two equations simultaneously to determine T and f_s . Each of these experiments is described in more detail below.

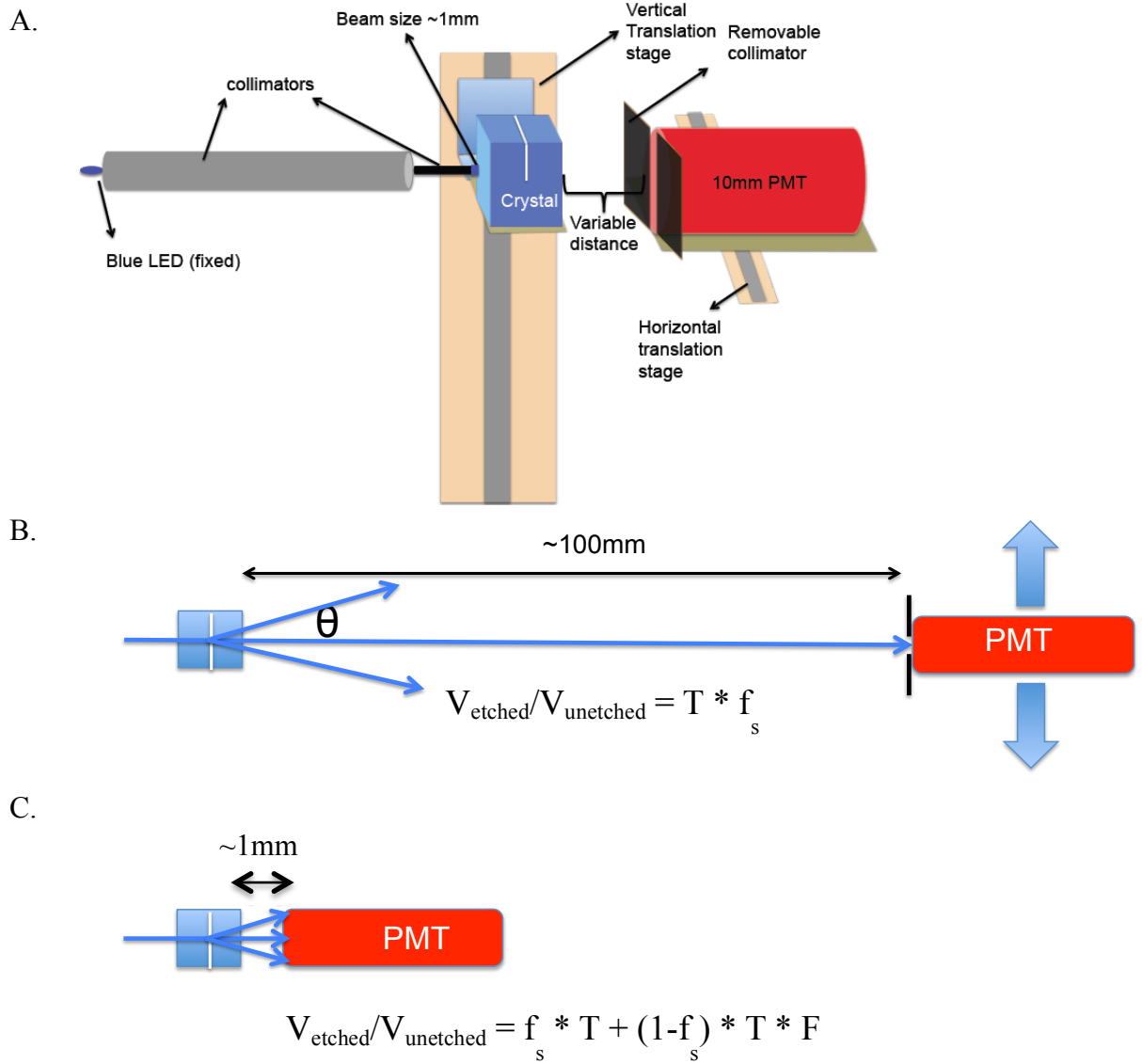


Figure 4.6: Experimental design to measure the optical properties of the LIOBs. A: Diagram of the apparatus used to measure the optical properties of the LIOBs. A blue LED is collimated into a beam that is directed into the crystal, which may be translated vertically, and detected by a PMT, which may be translated horizontally. B: Experiment designed to measure directly transmitted light. C: Experiment designed to measure directly and diffusely transmitted light.

1. Isolate Direct Transmission

The crystal was fixed normal to the beam and oriented so that the beam of light passed perpendicularly to the etching (Figure 4.7). The PMT was collimated and moved far (~100mm) from the crystal, to isolate the directly transmitted light. The crystal was translated vertically in discrete increments, and the PMT translated horizontally in increments <0.1mm to measure the profile of light when passing through air and both the unetched and etched regions of the crystal.

The profile of the directly transmitted light was validated by scanning the collimated PMT across the transmitted beam, and comparing the profile of the beam through the etched region to that through the unetched region and through air. When passing through the unetched crystal, the beam in air will pass through the both walls of the crystal. Because such small angles are subtended by the collimated PMT, the effect of refraction is neglected, and the angular profile of the light transmitted through the etched region of the crystal, $PSF_{LIOB,trans}(\theta)$, is described by:

$$PSF_{etched}(\theta) = PSF_{LIOB,trans}(\theta) \otimes PSF_{unetched}(\theta) \quad (4.8),$$

where PSF_{etched} , $PSF_{unetched}$, and $PSF_{LIOB,trans}$ are the point spread functions resulting from light passing through the etched region of the crystal, unetched region of the crystal, and the LIOB.

If the PMT is located far from the source of the beam, the profile of the beam may be approximately derived from the measured voltage as a function of scanning position, $V(y)$, by $y=L*\tan(\theta)$. The measured profile $V(y)$ is a convolution of the actual profile and a box filter of width equal to the collimator width (<0.5mm); because the beam width

is larger than the collimator width, this effect was not deconvolved to avoid noisier results. The PSFs of the LIOBs were deconvolved from the PSFs of the crystal wall and the profile of the beam in air using Weiner deconvolution.

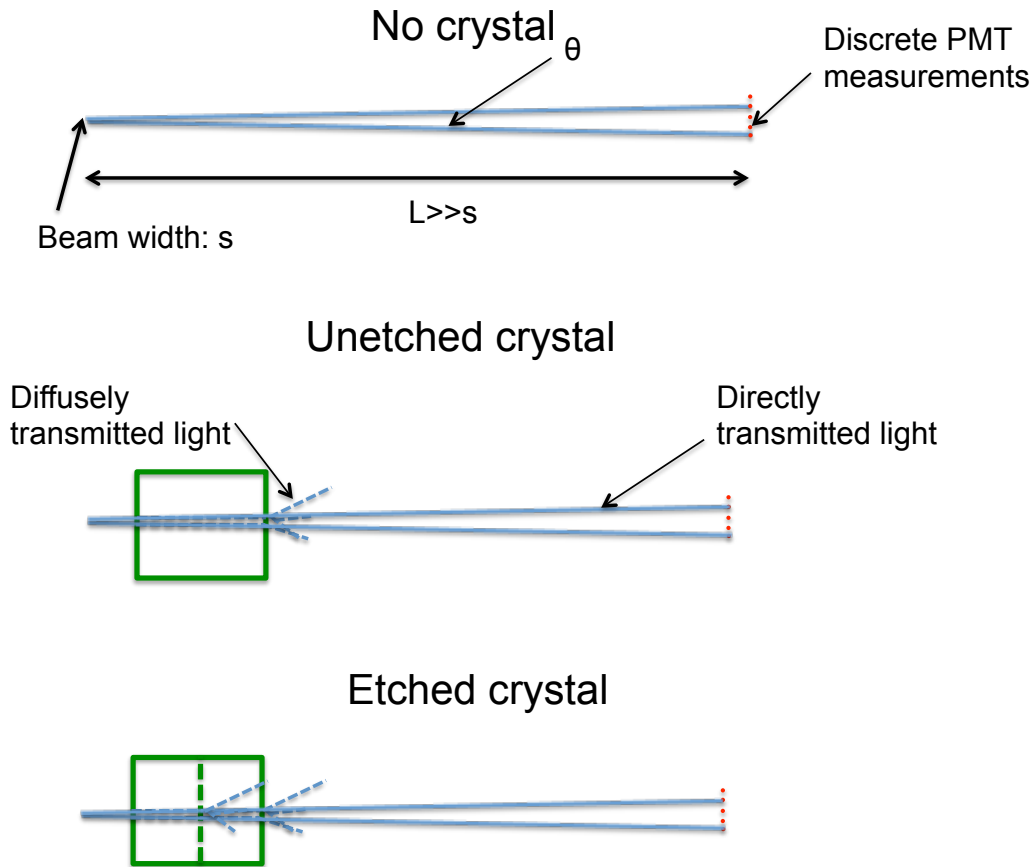


Figure 4.7: Diagram of the measurements of the profile of the directly transmitted light using the set-up diagrammed in Figure 4.6 B, in which the beam is transmitted through air, the unetched region of the crystals, and the etched region of the crystals. A PMT collimated on its front face measures light at discrete points to determine the profile of the beam.

2. Direct and Diffuse Transmission

The PMT was fixed normal to the direction of the light and positioned close (~1mm) to the exit surface of the crystal to measure the total flux of light passing through the cube (Figure 4.6 C). The beam collimator was again ~1mm from the crystal to minimize the size of the beam. The position of the beam was fixed in the middle of the crystal in the horizontal direction, and the crystal was translated vertically in increments of 0.5mm to vary the position on the crystal through which the beam passed. The fraction of light passing through the etchings was taken to be the average over the central 2mm of each LIOB (described later). For several of crystals, this measurement was repeated four times, after removing the crystal and setting it back in place, in order to estimate the uncertainty of the optical measurements.

Because of the solid angle subtended by the PMT as well as internal reflection within the cube, a large fraction of the diffusely transmitted light will not reach the PMT. The fraction of diffusely transmitted light collected by the PMT in this configuration was estimated using Monte Carlo simulations of the partly etched crystal, in which the scintillation light was directed normal to and at the center of the LIOBs (Figure 4.8). With the transmitted light modeled as purely diffuse, the fraction of transmitted light that passed through the crystal and reached the PMT was calculated. These simulations include the effects of reflections from the crystal walls, and therefore implicitly correct for this effect as well.

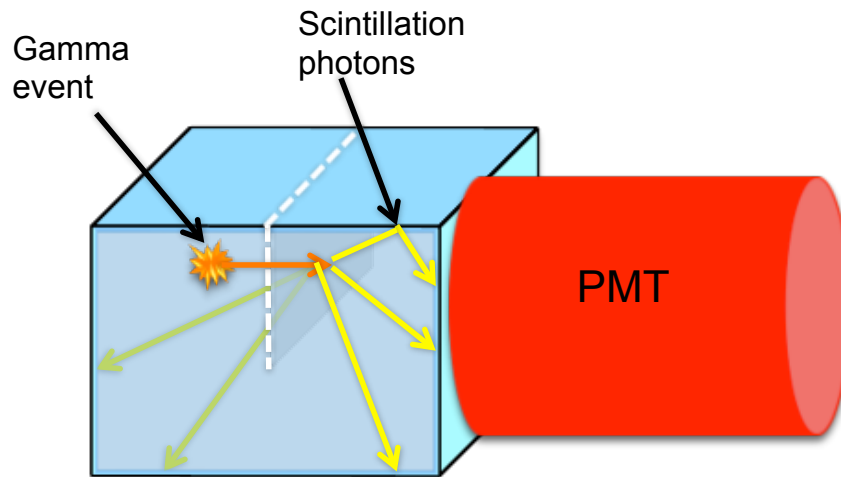


Figure 4.8: Diagram of the simulation used to determine the fraction of diffusely transmitted light measured by the PMT. A beam of scintillation light is directed through the LIOB at a fixed point; the LIOB is modeled as purely diffusely transmissive in order to isolate the diffusely transmitted light.

4.2.5.2 Reflected Light

Reflections from the wall of the crystal are expected to consist primarily of mirror-like specular reflections, while the reflective properties of the LIOBs are modeled as both specular and diffuse. To measure the profile of the reflected light, the crystal was fixed at an angle $\theta \sim 55^\circ$ relative to the beam and close to the beam collimator, while the PMT was angled normal to the light reflected from the crystal wall, and $\sim 5\text{mm}$ from the surface of the crystal at its closest point (Figure 4.9). The crystal was translated vertically and the PMT translated horizontally to measure the profile of light when reflecting from the crystal surfaces and the etchings.

The profile of light reflected from the unetched region of the crystal is hypothesized to consist of two specular peaks, one for each surface of the crystal, with the peak corresponding to reflection from the back surface lower in amplitude than the

first peak by the square of the transmission probability of the light. The profile of light reflected from the LIOBs may be derived from the measured profile of the light reflected from the etched region of the crystal by subtracting the profiles of the light reflected from the crystal surfaces. This profile is examined to determine the presence of a specular peak or lobe between the two peaks measured in the unetched region, while diffuse reflections are not expected to result in a significant change between the peaks.

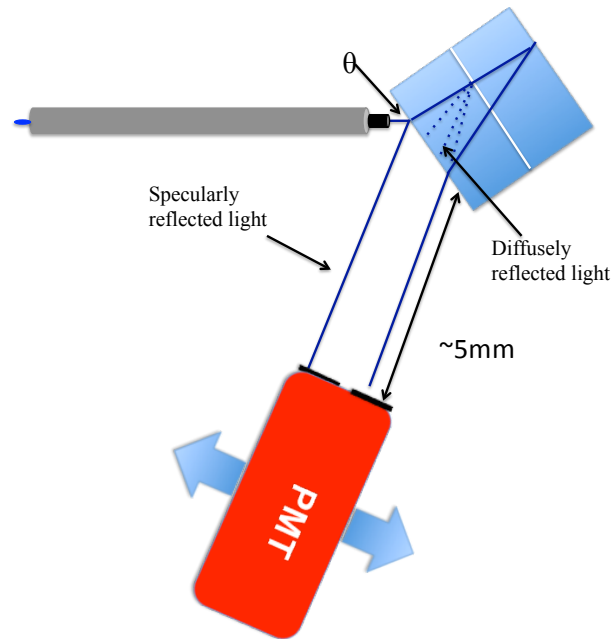


Figure 4.9: Design to measure the reflectivity profile of the LIOBs. The collimated beam of light was placed close to the crystal at an angle ($\theta \sim 55^\circ$), and the profile of the reflected beam was measured by scanning the PMT perpendicularly to the direction of the beam reflected from the crystal wall. The crystal was translated vertically to vary the position on the crystal at which the beam was directed.

4.2.5.3 Transmission as a Function of Vertical and Horizontal Position

To measure the transmission of light as a function of horizontal position along the LIOBs, the cube was oriented so that the etching extended vertically down the crystal.

The PMT was positioned close to the crystal and left uncollimated, and the voltage measured at discrete points as the crystal was translated vertically. Similarly, to measure the transmission of light as a function of vertical position along the LIOBs, the cube was oriented so that the etching extended horizontally across the crystal, and measurements were taken as the crystal was translated vertically (Figure 4.10).

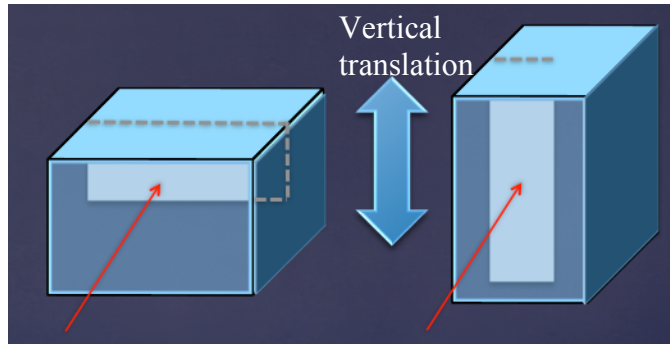


Figure 4.10: Diagram of experiment to measure the behavior of the LIOBs as a function of vertical (left) and horizontal (right) position on the LIOB. The crystal was translated vertically so that the beam passed through different points on the LIOB.

4.2.6 Results

4.2.6.1 Transmitted Light

Figure 4.11 shows sample profiles of the beam measured with the PMT positioned far from the crystals, when the beam passed through air, the unetched region of the crystals, and the etched regions of the crystals (Figure 4.7); these profiles are normalized by the sum of the light in order to compare the profiles. The PSFs of the light spread from two of the LIOBs are shown as well. The profiles of the beam through the unetched and etched regions of the crystal are very similar to that of the profile in air,

with the PSF in each case subtending an angle of $<1^\circ$, indicating the crystal wall and LIOBs do not act to spread the beam greatly.

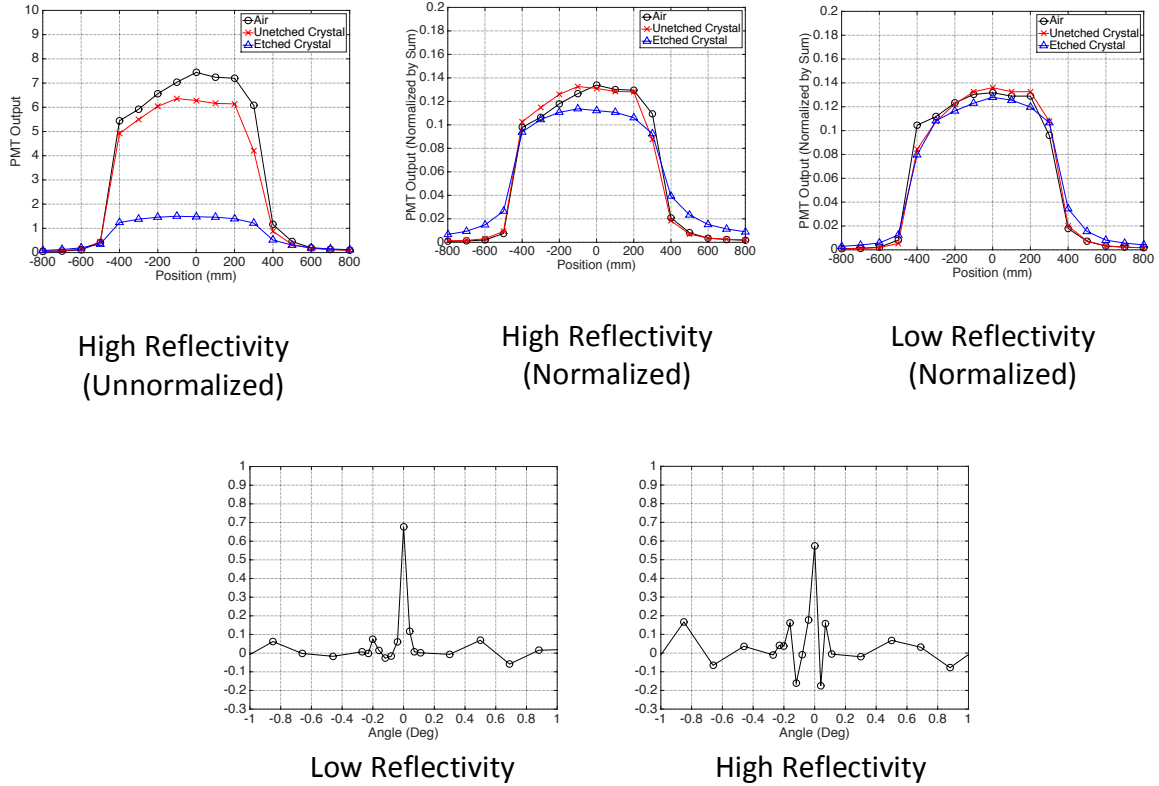


Figure 4.11: Measurements of directly transmitted light for sample cubes with high and low reflectivity. Top: Profiles of light transmitted through air and the unetched and etched regions of the crystals, both unnormalized and normalized by the sum of the collected light. Bottom: PSFs of the light spread through the crystal wall and LIOBs.

Figure 4.12 shows a plot of the fraction of light directly transmitted through the LIOBs as a function of average reflectivity coefficient, for the various etched cubes.

Note that for the unetched crystal studied, f_s is measured to be $\sim 1\%$, expectedly low

because of the smooth polish of the crystals. In general, the fraction of directly transmitted light increases as reflectivity decreases.

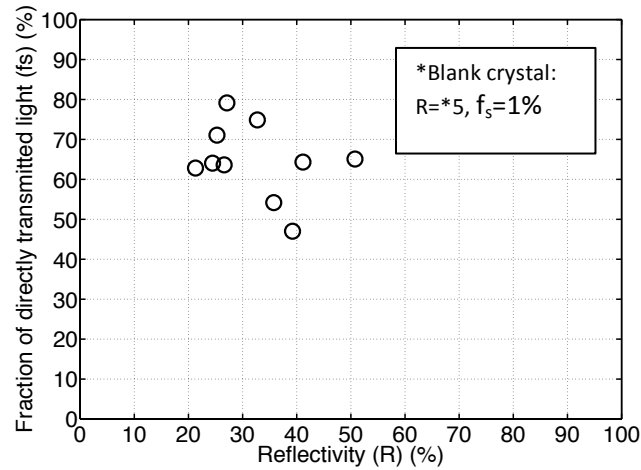


Figure 4.12: Scatter plot of the fraction of transmitted light that is directly transmitted (f_s) vs. average reflectivity (R) for the various crystals.

Comparisons of the reflectivity of the crystals etched using both lasers shows that the opacity of the etchings generally increases with laser power, particularly for the wide spacing, and that among these, the etchings made with a medium and wide spacing between the passes are the most opaque (Table 4.2). The trends observed among the etched crystals are consistent between the two lasers used, and the total reflectivity of all of the etched crystals ranged from ~20% to ~50%. The standard deviation of these measurements was <5%, although the reproducibility of the etching process was not tested (e.g. by etching several crystals with the same parameters).

Table 4.2: Reflectivity (R) for crystals etched using the lasers. The crystals used to characterize the profile of transmitted light are highlighted in red.

Lumera	3W Narrow spacing	3W Medium spacing	3W Wide spacing	4W Narrow spacing	4W Medium spacing	4W Wide spacing
Reflectivity	21	24	21	27	41	39
Lumentum			5W Wide spacing	6W Narrow spacing	6W Medium spacing	6W Wide spacing
Reflectivity			36	27	33	51

4.2.6.2 Reflected Light

The measured distribution of light reflected from the unetched regions of the crystal (Figure 4.13) indeed consists of two peaks; the distance between the peaks is $5.6 \pm 0.1\text{mm}$, which agrees with the expected difference of $6.6\text{mm} \pm 0.9\text{mm}$, based on the angle of the beam and size of the crystal. The reflection profiles from the etched region of the crystals are clearly seen to lack a peak corresponding to the specular reflection at the LIOB, and to have behavior consistent with that of a diffuse reflector.

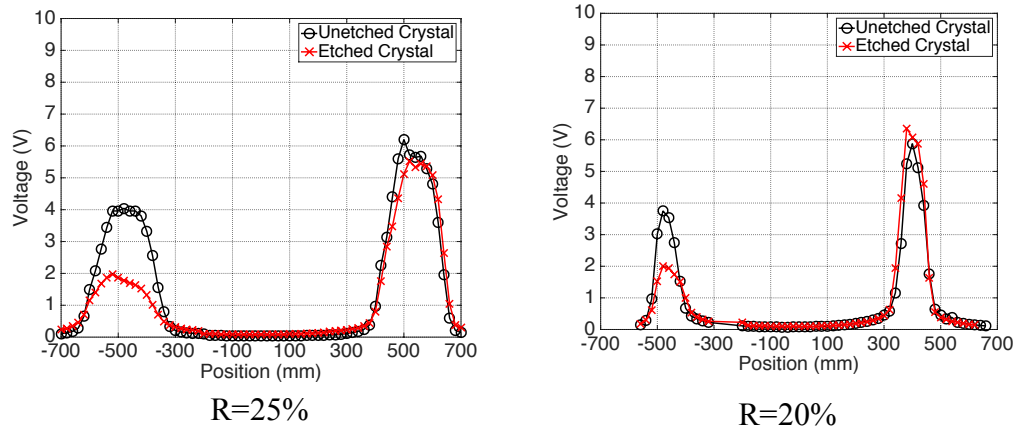


Figure 4.13: Profiles of light reflected from the unetched and etched regions of the crystals for two crystals. The two peaks shown are the result of reflections from the crystal front and back surfaces.

4.2.6.3 Transmission as Function of Vertical and Horizontal Position

Figure 4.14 plots the PMT voltage as a function of horizontal beam position, normalized to the voltage at a middle position, for four of the LYSO cubes. The PMT voltage is relatively constant along its horizontal position, indicating that transmission is constant along this axis. Along the vertical axis of the etching, the PMT voltage undergoes a steep change as the beam of light passes from the unetched region of the crystal to the etched region, as expected (Figure 4.14 bottom). The more opaque LIOBs are more variable in opacity along the depth of the etching, with the measured voltage varying as much as 30% within the etched region, indicating the etching is less opaque toward the edges. An average over a range of depths was taken to characterize the reflectivity of each LIOB. Because the beam was $\sim 1\text{mm}$ in diameter and the etchings were $\sim 3\text{mm}$ deep, averages were taken at beam positions spanning 2mm, to avoid positions in which the beam was partially beyond the etched region.

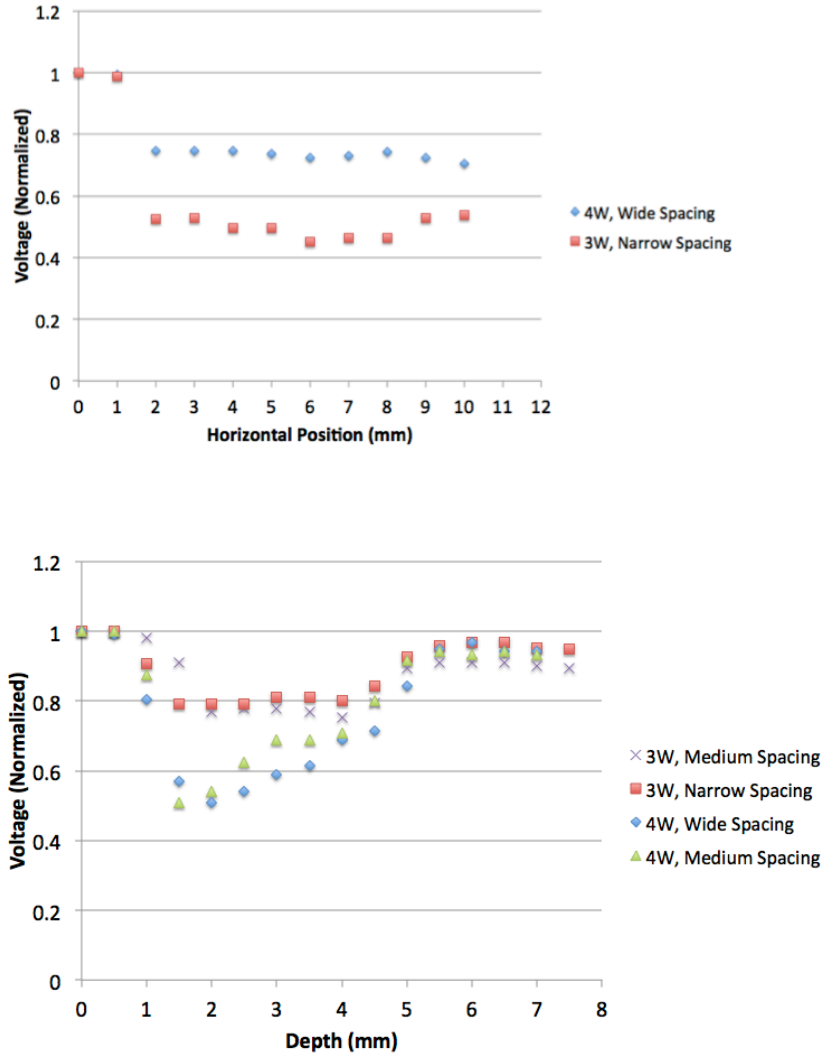


Figure 4.14: Normalized voltage of PMT as a function of horizontal position along etching length (top) and etching depth (bottom). The plots show the relative constancy of the transmission coefficient along the length of the etchings, and the variation along the depth.

4.3 Position Measurements with Etched Continuous Crystals

4.3.1 Etched Crystal Designs

The goals in designing a detector involving continuous crystals etched with LIOBs were:

1. To improve the spatial resolution of the detector, particularly in the entrance region, where it is worst.
2. To reduce the depth-dependent light response of the detector, while retaining as much DOI information as possible.
3. To allow for the continuous sampling inherent in continuous detectors.

The last requirement precludes etching the continuous crystal into discrete pixels. In order to achieve these goals, a design similar to that in [138], in which the thick continuous crystals were etched partly into the entrance region in a grid pattern, was explored. While experiments with this design using mechanical cuts were successful, the major disadvantages were the crystal loss associated with cutting the crystal with a physical blade and the limitations in the placement and characteristics of the barriers. Informed by preliminary simulations with this design using LIOBs, the semi-transparency of the barriers was expected to affect the light spread differently than the mechanical cuts did, and in particular to allow for LRFs that changed monotonically with depth, if transmissive enough; moreover, these barriers were thinner than achievable with a blade, and could be etched within the crystal. To determine the feasibility and performance of this detector design, several thick LYSO detectors were etched in this

pattern and their performance characterized. These crystals are listed below and diagrammed in Figure 4.15:

1. 50x50x25-mm³ crystal, polished on all sides and etched twice, each with a set of 8mm deep etchings in a grid pattern, with a pitch of 2mm: the first set extended from the entrance surface inward (single layer of LIOBs), and the second set began ~1mm below the end of the first set and extended ~17mm inward (double layer of LIOBs); the second set of etchings was offset from the first layer in each direction by ~1mm in order to improve the sampling capability of the detector. To etch the second set of LIOBs, the laser was focused through the exit surface (beginning ~16mm within the crystal) because the laser cannot focus through previously etched LIOBs. Each set of etchings used a 4W laser power on the Lumera (only laser available at this time), with a wide spacing between the two LIOB passes, because these parameters led to the most reflective LIOBs, based on the samples studied (Table 4.2). After the single layer of LIOBs was etched, the crystal was studied in two configurations: with the etched region serving as the entrance region and reversed, so that the etched region served as the exit region (coupled to the MAPMT), to further study the effect of the LIOBs.
2. 48x48x14-mm³ block, polished on the 4 side surfaces and the exit surface, and etched with 5-mm deep LIOBs that extended from the entrance surface inward, in a grid pattern with a pitch of 2mm. Because the entrance surface was roughened, the crystal was etched by focusing the laser through the exit surface. These LIOBs were made with the Lumentum using a 5W laser power, with a wide spacing between the two LIOB passes.

To estimate the opacity for the sets of LIOBs introduced into the thick crystals, optical measurements were performed in which the small beam of blue light was transmitted through the crystals perpendicular to the side surfaces, and the voltages compared to that measured in the unetched regions (Figure 4.16). The PMT was close to the crystal to measure both directly and diffusely transmitted light.

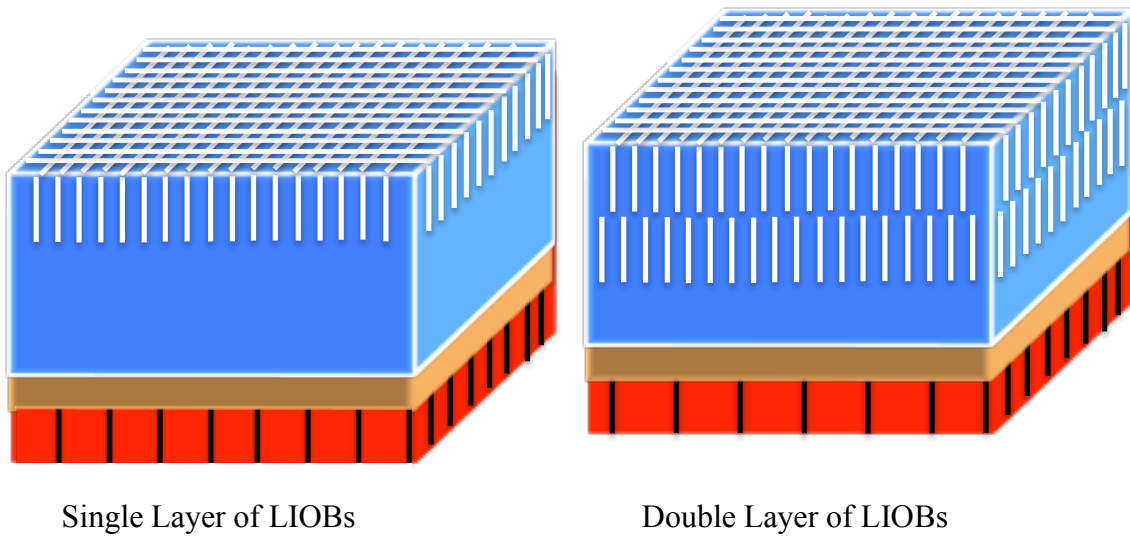


Figure 4.15: Diagram of the etched thick continuous crystals studied in this work. Left: Single layer of LIOBs. Etching in the entrance region of the crystals was intended to improve the resolution in this region, while retaining the continuous sampling of the crystal and reducing the depth-dependence of the LRFs. Right: Double layer of LIOBs. Etching the second layer of LIOBs was intended to improve the resolution at middle DOIs, while allowing for fine position sampling of the crystal.

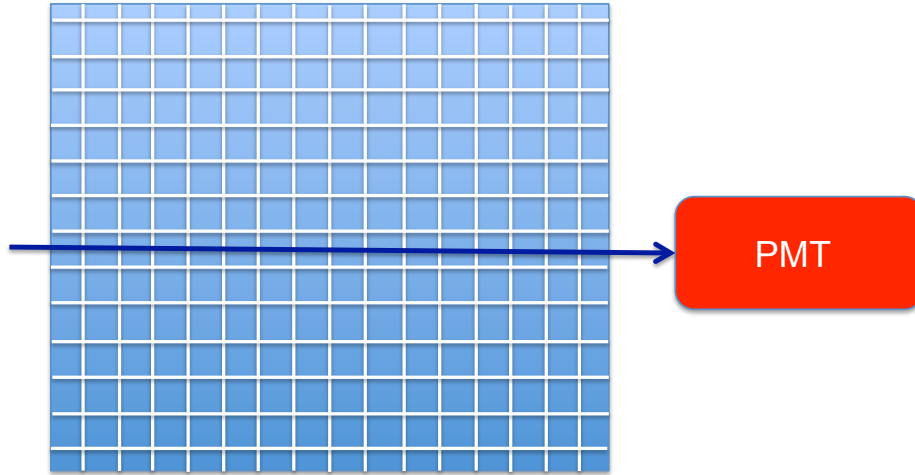


Figure 4.16: Diagram of the measurement to estimate the relative opacity of the LIOBs etched in the thick crystals: a beam of blue light is directed through the etched layer of the crystals and the output compared among the various crystals to determine the relative transmission through the crystals.

4.3.2 Comparison of Etched Crystals to Unetched Crystals: Single Layer of LIOBs

Figure 4.17 displays photos of the etched crystals, showing that the crystals were successfully etched without cracking (the chipping shown in the 14-mm crystal was sustained during transport). The precision with which these barriers are made is also clear; each LIOB is $\sim 30\mu\text{m}$ in thickness, so that they are quite thin and do not occupy a large fraction of the crystal volume. The spatial resolution, calculated using the 64-anode NN algorithm, is shown for the 14mm and 25mm thick crystals at three representative depths before and after etching in the entrance region in Figure 4.18. The three depths are located in different regions of the crystal: a shallow depth near the entrance surface (within the etched region), a deep depth near the photodetector (outside the etched

region), and a middle depth between the two (outside the etched region). In each case, the single set of LIOBs improved the spatial resolution in the etched depths of the crystal: for the 14-mm crystal, the resolution improved by ~ 0.3 mm, while for the 25-mm crystal, it improved by ~ 0.8 mm. The resolution outside of the etched region, however, is unchanged for the 14-mm crystal and slightly degraded for the 25-mm crystal, where the resolution degraded by ~ 0.4 mm for each depth. Similarly, the etching procedure results in more restricted LRFs at the shallow depths, as desired, but they also lead to wider LRFs at deeper depths, resulting in a degraded spatial resolution at these depths. This may be compared to the mechanical cuts introduced earlier [138], which resulted in a narrower light spread (and improved resolution) at all but the deepest depths, particularly in the entrance region (Figure 4.19).

The values of spatial resolution averaged over a central region of the crystal extending 12 mm from the center of the crystal in each direction are also summarized in Table 4.3. The averaged resolution, calculated by weighting by the probability of interaction for a head-on incident beam, represents an upper limit on the performance achievable with the detectors. Here, the resolution within the central transverse region of the etched detectors improved by ~ 0.2 mm and ~ 0.3 mm for the 14 mm and 25 mm thick crystals, respectively, showing a slight improvement with the etched crystals.

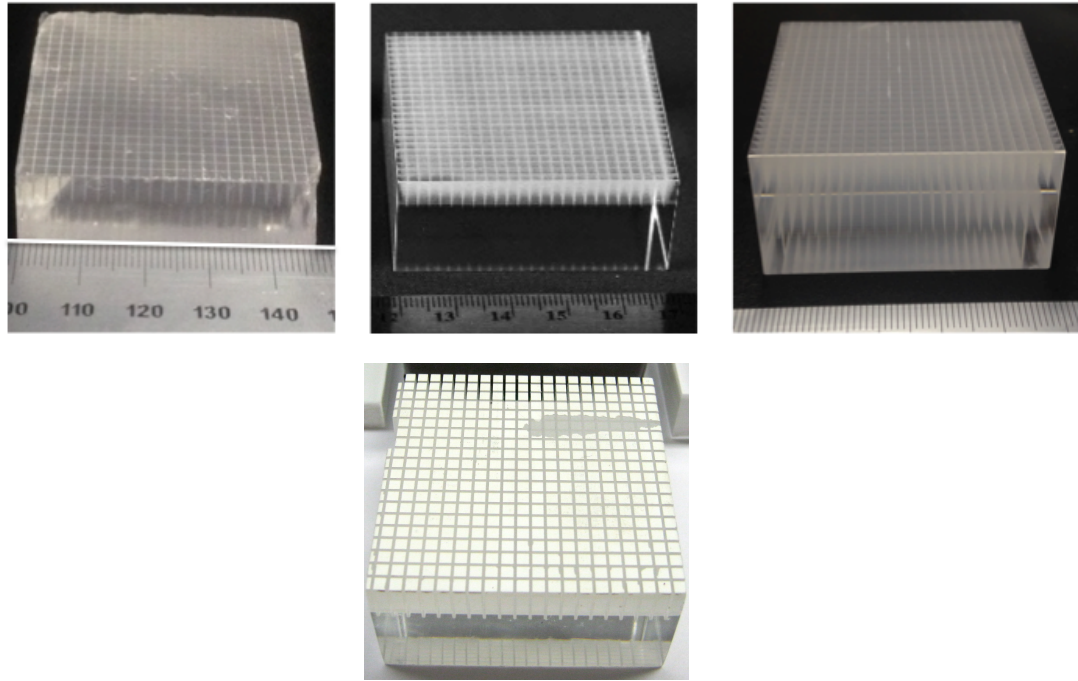


Figure 4.17: Photographs of etched and mechanically cut crystals. Top: Photographs of the 14mm thick etched crystal (left) and 25mm thick crystal etched with a single layer (middle) and double layer (right) of LIOBs. Bottom: Photograph of the 25mm thick crystal mechanically cut in the entrance region with 8mm deep cuts in a grid with a 2mm pitch (Source: [162]).

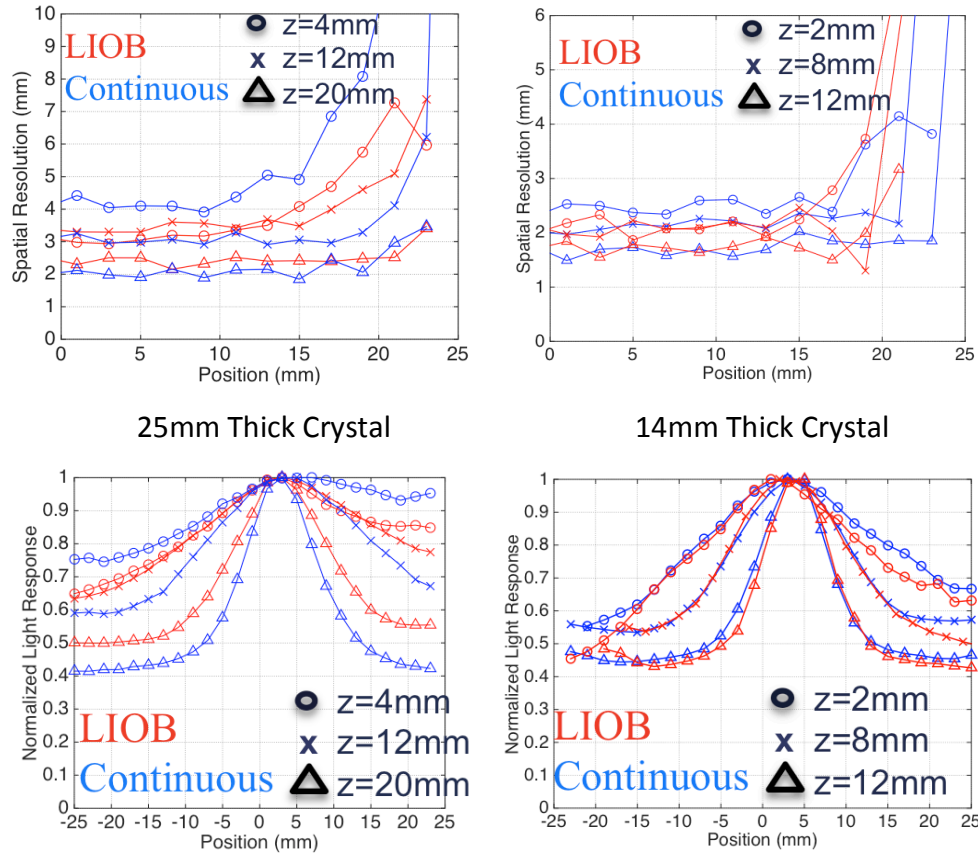
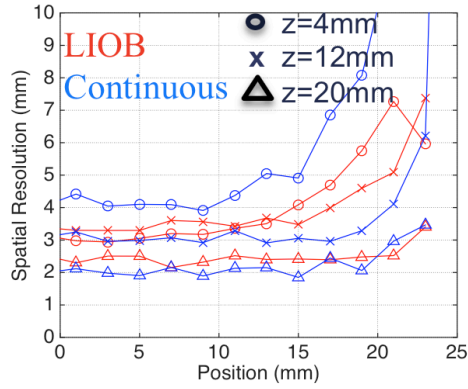
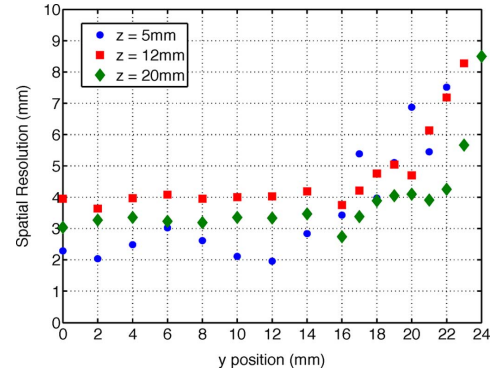


Figure 4.18: Comparison of etched crystal to continuous crystal for the 25mm thick crystal (etched with 8mm deep LIOBs) (left) and the 14mm thick crystal (etched with 5mm deep LIOBs) (right). Curves of spatial resolution (top) and LRFs for a central row-column summed anode (bottom), are shown for three depths: within the etched region ($z=4\text{mm}/2\text{mm}$ for the 25mm/14mm thick crystals), within a middle region ($z=12\text{mm}/8\text{mm}$ for the 25mm/14mm thick crystals), and within a deep region ($z=20\text{mm}/12\text{mm}$ for the 25mm/14mm thick crystals).



25-mm crystal
etched with LIOBs



25-mm crystal
mechanically slotted [142]

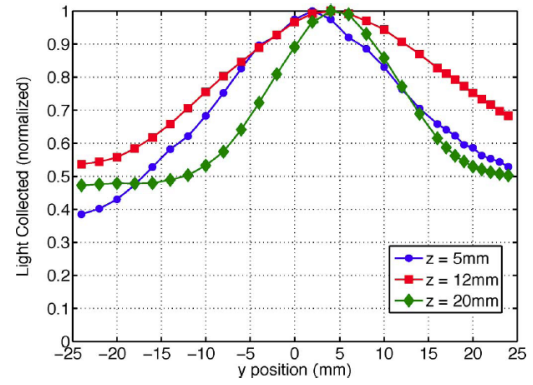
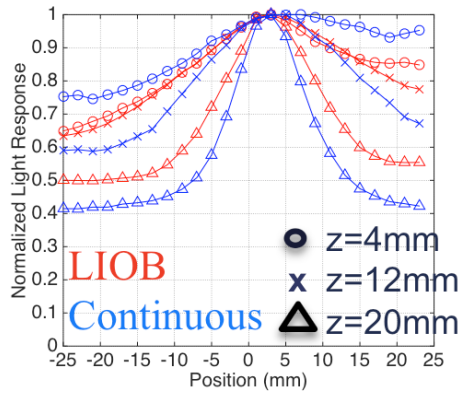


Figure 4.19: Comparison of the 25mm thick etched crystal (etched with 8mm deep LIOBs) to continuous crystal (left) and mechanically cut crystal (right), using curves of spatial resolution (top) and LRFs for a central row-column summed anode (bottom), for three depths: within the etched region ($z=4\text{mm}/2\text{mm}$ for the 25mm/14mm thick crystals), within a middle region ($z=12\text{mm}/8\text{mm}$ for the 25mm/14mm thick crystals), and within a deep region ($z=20\text{mm}/12\text{mm}$ for the 25mm/14mm thick crystals).

Table 4.3: Spatial resolution (mm) of the etched crystals averaged over a large central region of the crystal (12mm in each direction from the center). The first three rows of values are computed at a fixed depth, while the last row is the average of the three fixed depth values, weighted by the probability of interaction for a normally incident beam.

	14mm Continuous	14mm LIOB	25mm Continuous	25mm Single LIOB	25mm Double LIOB	25mm Mech. Cut
Shallow	2.45 ± 0.03	2.11 ± 0.04	4.07 ± 0.06	3.28 ± 0.09	3.15 ± 0.10	2.36 ± 0.15
Middle	2.17 ± 0.04	2.06 ± 0.03	3.11 ± 0.04	3.52 ± 0.07	3.49 ± 0.09	3.97 ± 0.05
Deep	1.65 ± 0.03	1.69 ± 0.04	2.09 ± 0.05	2.46 ± 0.05	2.49 ± 0.06	3.14 ± 0.03
Weighted Average	2.25 ± 0.02	2.01 ± 0.02	3.51 ± 0.04	3.23 ± 0.04	3.15 ± 0.05	2.93 ± 0.06

4.3.3 Light Spread in Etched Region

The LRFs for more depths are shown in Figure 4.20 for the 14mm thick crystal etched with 5mm deep LIOBs and the 25mm thick crystal etched with a single layer of 8mm deep LIOBs. The LRFs are equivalent within one standard deviation within the first 5mm for the 14mm thick crystal, and the first 8mm for the 25mm thick crystal; at deeper DOIs, the LRFs are narrower still, resulting in an essentially monotonic change in LRF.

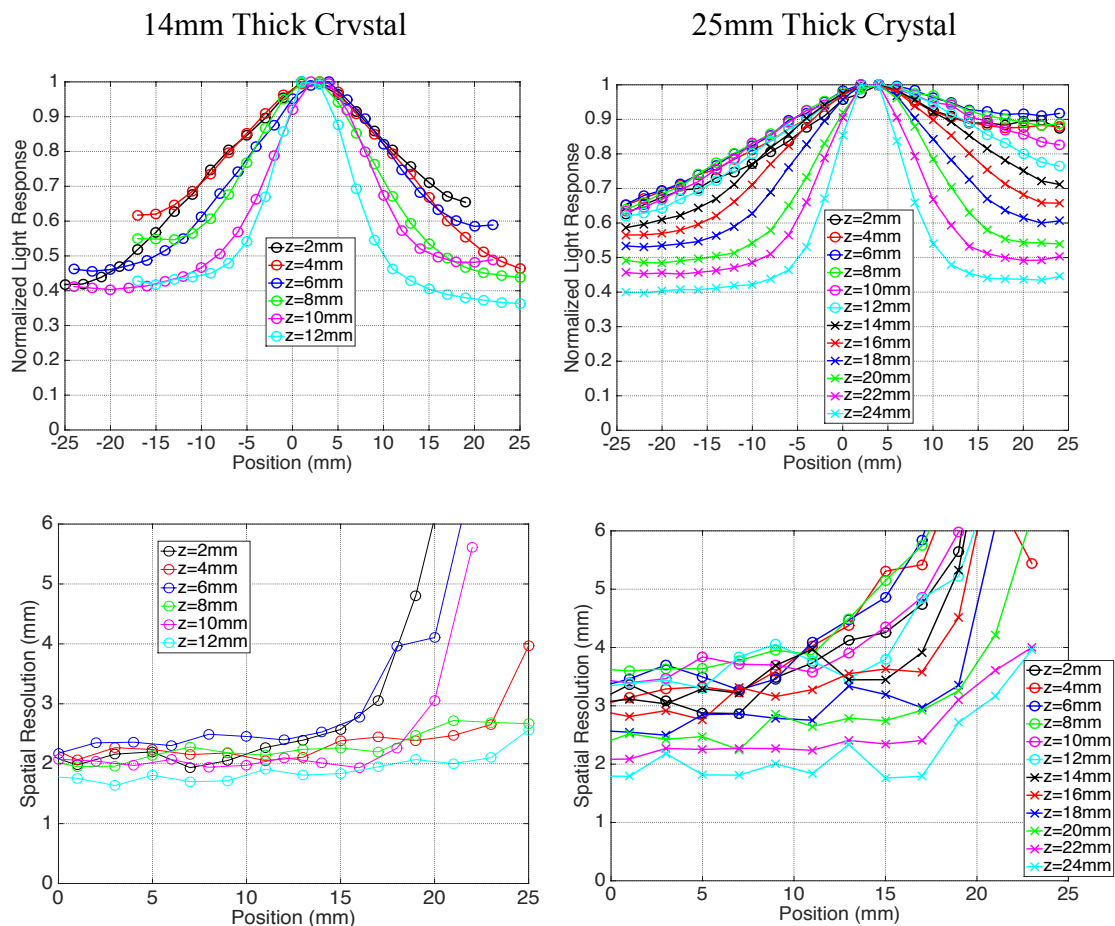


Figure 4.20: LRFs and spatial resolution as a function of depth for the 14mm thick crystal etched with 5mm deep LIOBs (left) and the 25mm thick crystal etched with 8mm deep LIOBs (right). The LRFs generally change monotonically with depth, and do not change greatly within the etched region.

4.3.4 DOI Performance

The DOI resolution of the 25mm thick etched crystal is shown in Figure 4.21. The resolution is seen to be degraded in the entrance region of the crystal, where the LRFs are very similar: at the depths $z < 16\text{mm}$, the DOI histograms do not change adequately with beam depth for DOI information to be ascertained. The DOI resolution is still good outside of this etched region, however. This reduction in the depth-dependence of the LRFs has therefore degraded the resolution, though it is still good enough to separate events in the first part of the crystal ($\sim 16\text{mm}$). This may be compared to the DOI resolution of the crystal before etching of 4-6mm throughout the depths.

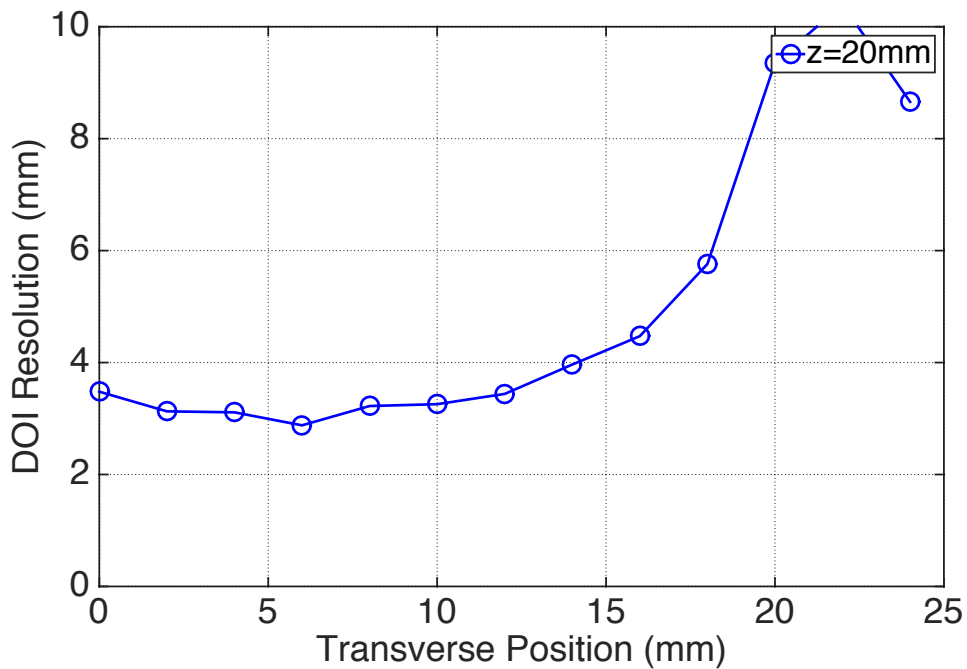


Figure 4.21: DOI resolution of the 25mm thick crystal etched with a single layer of LIOBs. For the depths $z < 16\text{mm}$, the DOI histograms do not change adequately with beam depth for DOI information to be ascertained; for the other depths, DOI information is retained.

4.3.5 Etched Region Coupled to MAPMT

With the etched region of the crystal coupled to the MAPMT (and serving as the exit surface), the LRFs at each depth are degraded (Figure 4.22), serving as further evidence that the LIOBs act to spread light that impinges upon them from outside the etched region. This includes within the etched region, where the light spread is degraded because the photons that are emitted toward the entrance surface lose information. Because of the degraded performance, this configuration was not investigated further.

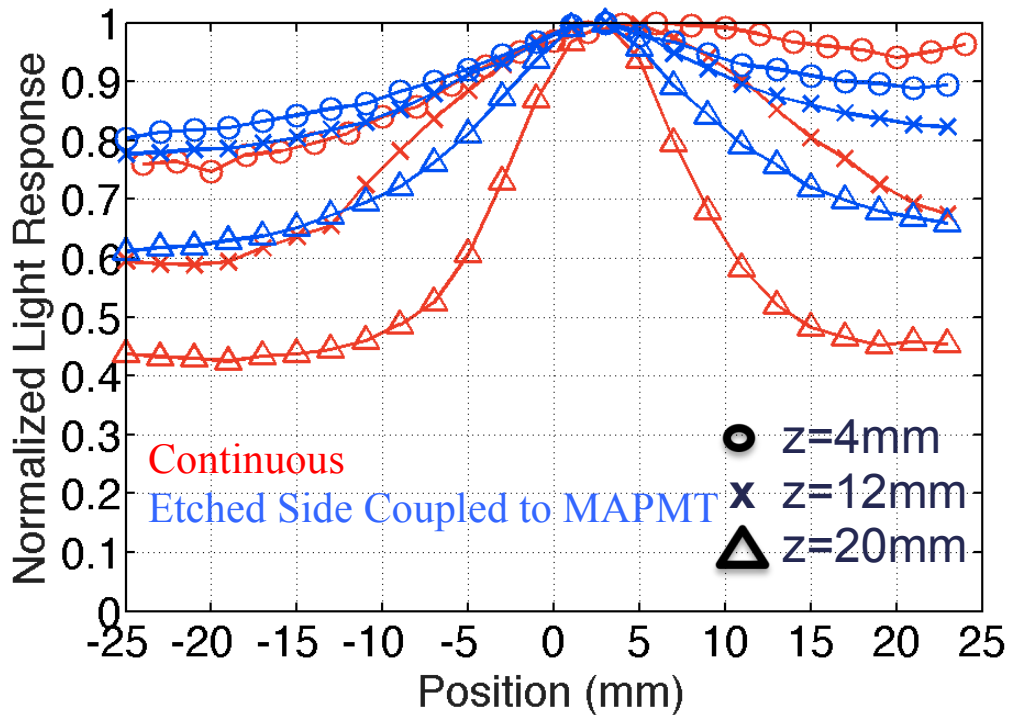


Figure 4.22: Comparison of central row-column summed LRFs for the 25mm thick continuous crystal and the etched crystal (8mm deep LIOBs), with the etched region coupled to the MAPMT. Coupling in this configuration leads to a broader light spread and degraded performance, and so was not investigated further.

4.3.6 Double Layer of LIOBs

While the second layer of LIOBs was expected to improve performance, particularly in the middle DOI, the two sets of LIOBs did not significantly affect spatial resolution or the LRFs. The negligible effect is likely because of the low opacity of the LIOBs (discussed below) (Figure 4.23).

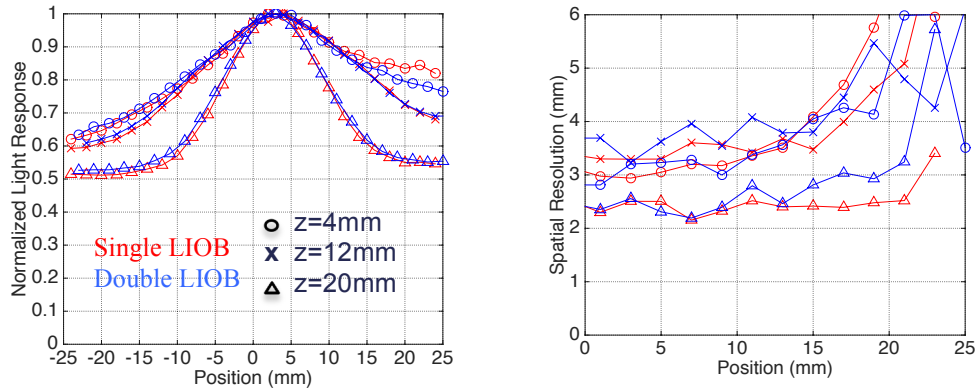


Figure 4.23: LRFs and spatial resolution for the 25mm thick crystal etched with a single layer and double layer of LIOBs. The second layer of LIOBs did not significantly affect the performance of the crystals.

4.3.7 Opacity of LIOBs Etched Within Thick Crystals

The results of the spatial resolution measurements on the thick crystals are supported by the results of the optical measurements (Figure 4.16) on the LIOBs etched within the crystals (Table 4.4), which show that the first layer of LIOBs in the 25mm thick crystal is opaque enough that the PMT measured a value consistent with background when passing through the LIOBs, while the second set of LIOBs, as well as the set within the 14mm thick crystal, registered a value significantly larger. While these

results cannot be used to measure an absolute value of reflectivity for the LIOBs, because of reflections within the various etchings, they may be used to compare the opacity of the various sets of LIOBs

Table 4.4: Ratio of PMT voltage through the etched region to the PMT voltage through the unetched region, for various thick etched crystals. The reflectivity of the LIOBs in the various thick crystals are thus compared.

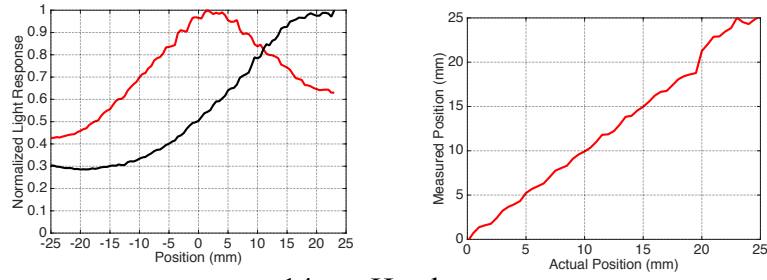
Crystal	Voltage Through Etched Region / Voltage Through Unetched Region (%)
25mm Entrance LIOB	4%
25mm Middle LIOB	10%
14mm Entrance LIOB	18%
Background	3%

4.3.8 Position Sampling

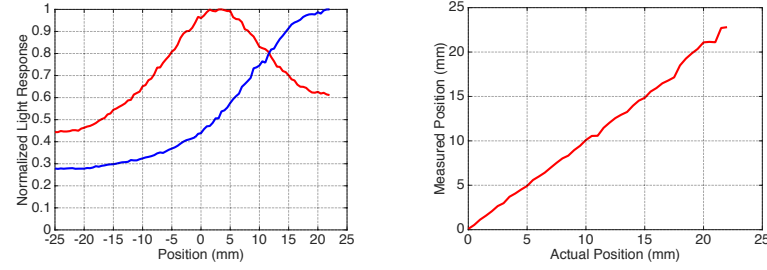
The effect of the etchings on the position sampling is shown in Figure 4.24, which shows plots of the measured position as a function of actual beam position at various depths for the 14mm and 25mm (single layer) thick etched crystals for scans in which data was gathered in increments of 0.5mm, instead of the usual 2mm, in order to sample the response of the crystal between the LIOBs. For both crystals, at shallow depths, positioning information between the LIOBs is lost as the plot of measured position flattens within the 2mm gaps (i.e., deviations from linear response). This is

reflected in the LRFs, which also flatten in these gaps. In the unetched regions of the crystals, however, the positioning information remains continuous, resulting in smooth plots of position. The plots of positioning for head-on scans show the overall sampling provided by the detector, and show that positioning information is not completely lost between the LIOBs, as the position plots change in slope in these regions, but do not flatten completely. The sampling is therefore found to be intermediate between that of a pixelated detector and a continuous detector. In an actual detector, this change in slope would have to be corrected using a bias correction.

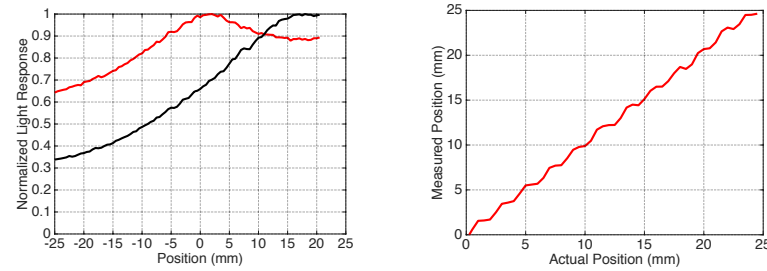
14mm Shallow DOI



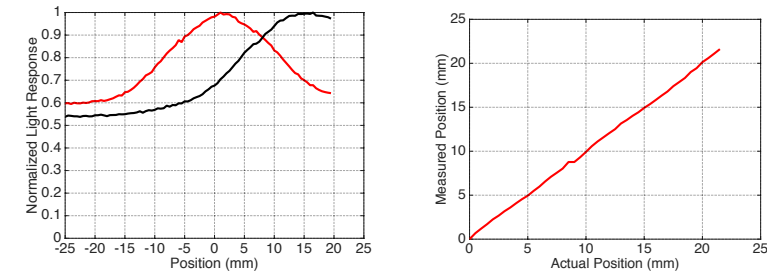
14mm Head-on



25mm Shallow DOI



25mm Middle DOI



25mm Head-on

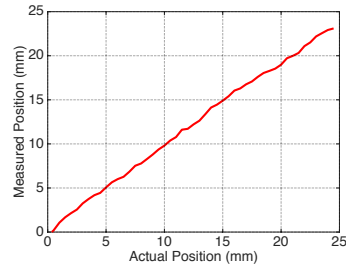


Figure 4.24: LRFs and positioning plots for etched crystals for side-on scans (fixed depths) and for a head-on scan. Positioning information is discretized within the etched region of the etched crystals, but is retained within the etched crystals for the head-on scan.

4.3.9 Light Output

A summary of the light output and energy resolution for the 25mm and 14mm thick crystals used in this work is shown in Table 4.5. Each etched crystal showed a slightly greater light output after etching; the 25-mm crystal had an energy resolution of $\sim 12\%$, while the 14-mm crystal had a resolution of $\sim 10\%$. The improvement in light output indicates that the etchings act to prevent light from escaping from the entrance surface of the crystal, and do not absorb a significant fraction of the impinging light.

Table 4.5: Light output and energy resolution of various crystals. Note that the energy is measured in arbitrary units of channels that may be used to compare the relative light output of the various crystals.

Crystal	25mm Polished Continuous Surface	25mm Single Set LIOB	25mm Two Sets LIOB	14mm Single Set LIOB
Energy (channels)	310	360	360	430
511 keV Energy res. (%)	12.5%	11.9%	12%	10.2%

4.4 Simulations

The measurements of the optical properties of the LIOBs were used to model them in the Montecrystal simulations in order to explore the performance of the general detector design involving thick crystals etched partly in a grid pattern.

4.4.1 Model

The optical experiments were used to model the optical behavior of the LIOBs. Because the response of the LIOBs to light directed at steep angles with respect to the etchings was difficult to measure with the small crystals used in the optical measurements, and because of the diffuse reflectivity and partially diffuse transmission, the response of the LIOBs was modeled as independent of angle. The overall model used in the simulations is as follows (Figure 4.4):

1. The reflection distribution was modeled as completely Lambertian and independent of angle.
2. The diffuse transmission distribution of the LIOBs was modeled as Lambertian and independent of angle, while the angle of directly transmitted light was modeled as unchanged, regardless of angle of incidence.
3. The fraction of directly transmitted light was linearly related to the reflection coefficient, using a linear fit based on the data in Figure 4.12.

4.4.2 Methods and Materials

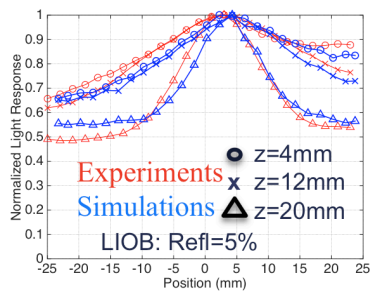
The experimental measurements of these detectors were first compared to simulations of the same detector designs, in order to measure the properties of the LIOBs used in the thick crystals. In particular, the measurements of the 25mm thick crystal etched with a single layer and double layer of LIOBs and of the etched 14mm thick crystal were used for these comparisons. The simulations were then used to test the

impact of two of the parameters of this detector design, focusing on the effect on resolution and position sampling:

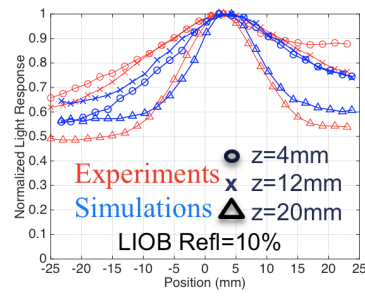
1. Opacity: the reflectivity was varied from 0% (continuous) to 100% (fully opaque).
2. Grid depth: the depth of the etchings was varied from 4mm to 12mm for the 25mm thick crystal.

4.4.3 Simulations of Etched Crystals

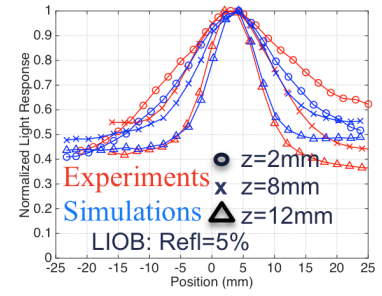
The LRFs resulting from the simulations again match those of the experiments in trend, and differ from the experimental measurements in a similar fashion as with the unetched crystals (Figure 3.12). Although a reflectivity of ~40% was expected based on the crystal measurements, simulations using a reflectivity of 5-10% better match the experimental results for the 25mm and 14mm thick crystals. The second layer of LIOBs is shown to have very little impact if the reflectivity of the LIOBs is low (Figure 4.26). If the etchings are more opaque, the second layer is seen to improve the LRFs at all depths.



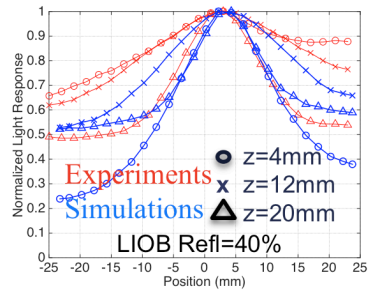
25-mm crystal:
Reflectivity=5%



25-mm crystal:
Reflectivity=10%

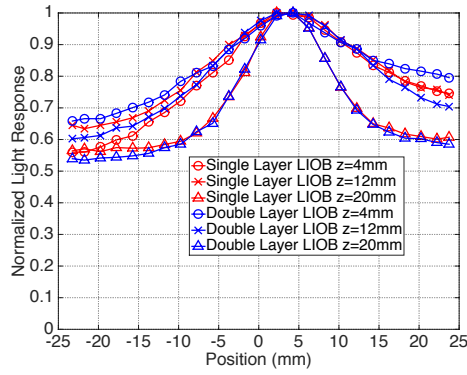


14-mm crystal:
Reflectivity=5%

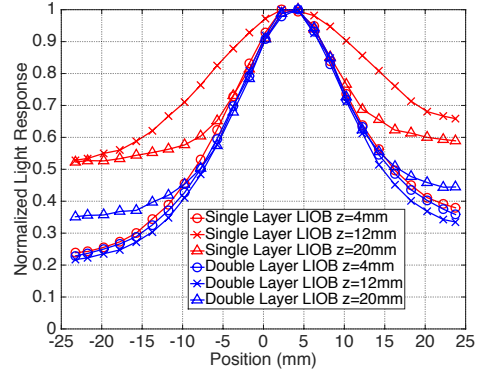


25-mm crystal:
Reflectivity=40%

Figure 4.25: Comparison of simulations to experimental measurements, showing LRFs for a central row-column summed anode for the 25mm and 14mm thick crystals etched with a single layer of LIOBs. While a value of $\sim 40\%$ reflectivity was expected based on optical measurements, the values of 5-10% lead to better matching.



Reflectivity=5%



Reflectivity=40%

Figure 4.26: Comparisons of simulated LRFs for a central row-column summed anode for a single and double layer of LIOBs etched into the 25mm thick continuous crystal. Use of more reflective (e.g., reflectivity=40%) LIOBs in the second layer is seen to show more of a difference when compared to the crystal etched with a single layer.

4.4.4 Light Spread Caused by LIOBs

Within the etched region, the photons directed toward the exit and side surfaces are slightly narrower, resulting in narrower overall LRFs. Outside of the etched region, however, the photons directed toward the entrance and exit surfaces are more spread out in the etched crystal, because of the diffuse nature of the transmission and reflection from the LIOBs, leading to scattering within the LIOBs (Figure 4.27). The overall LRFs in this region are therefore wider after etching.

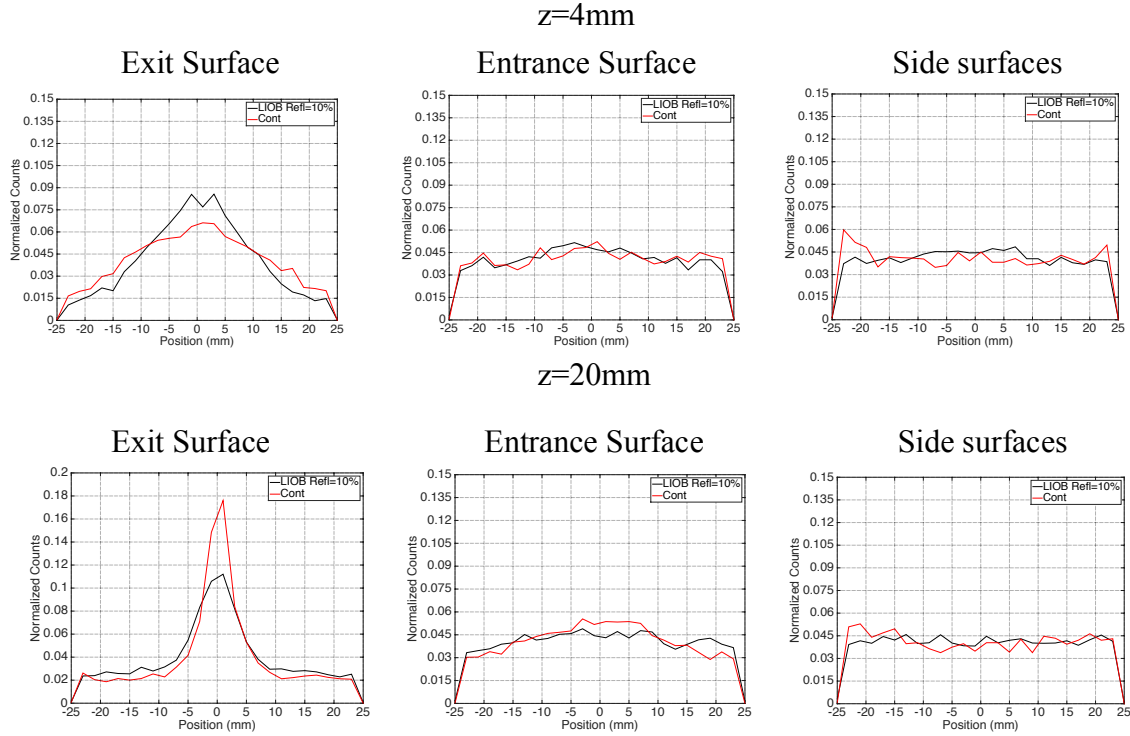


Figure 4.27: Positioning histograms for photons directed toward the entrance surface, exit surface, and side surfaces of the etched and continuous crystals for two DOIs for the 25mm thick crystal. Within the etched region ($z=4\text{mm}$), photons directed toward the exit and side surfaces show a narrower distribution in the etched crystal, leading to narrower overall LRFs for all photons in this region. Outside the etched region ($z=20\text{mm}$), photons directed toward the entrance and exit surfaces are wider after etching, leading to wider overall LRFs.

4.4.5 Varying Etching Parameters

Figures 4.28-4.29 shows the LRFs at two DOIs, as well as the LRFs and positioning linearity for head-on scans, for a 25mm thick crystal with varied etching properties. As expected, the LRFs become narrower as the reflectivity and depth of the LIOBs increase, while the positioning transitions from a continuous system to a discretized system for a large enough opacity or depth. If either of these parameters is large enough, the light spread within the etched region will become more restricted than

outside the etched region, similar to the mechanically cut crystal (Figure 4.19), resulting in a non-monotonic change of LRF with depth. Moreover, these LRFs will be comparable to those of the 14mm thick crystal (Figure 3.12), indicating the spatial resolution attainable will similarly improve. This non-monotonic change would have implications on the DOI capability of the detector, as continuous DOI information would no longer be present, although two-layer DOI information would still be possible, as in [162].

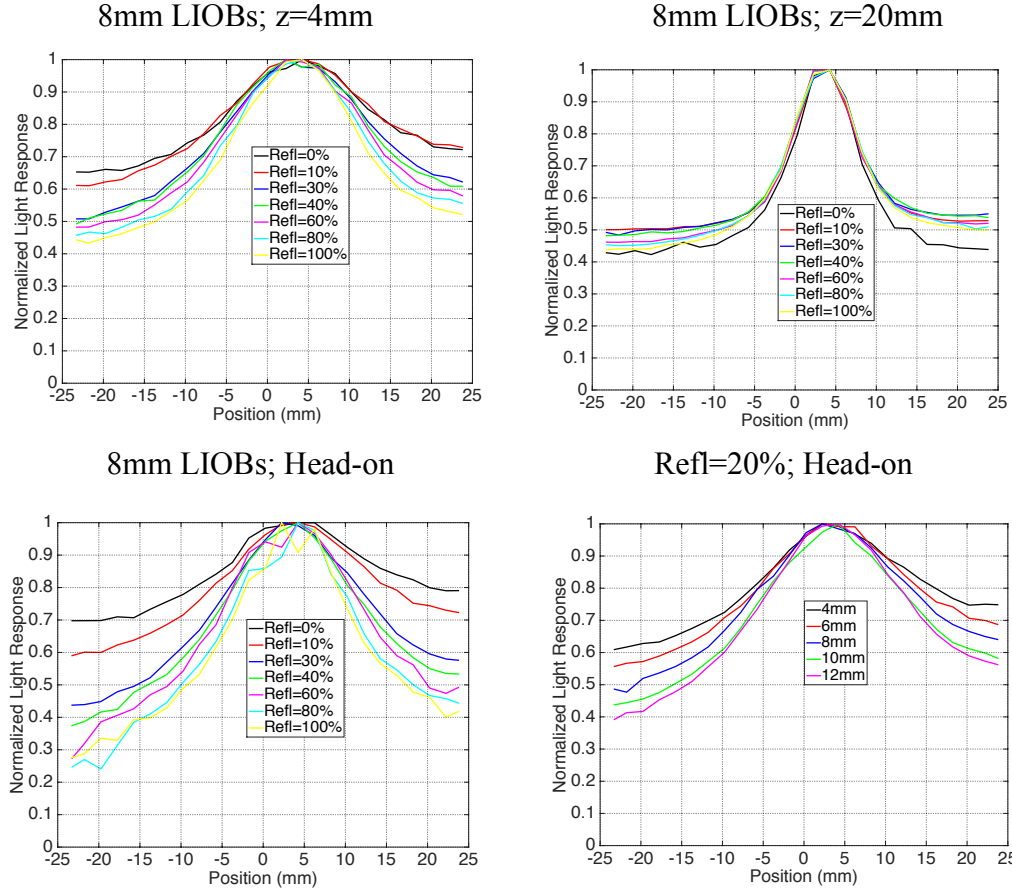


Figure 4.28: LRFs for the $50 \times 50 \times 25\text{-mm}^3$ crystal etched with LIOBs of varying opacity and depth. Top: The reflectivity was varied, while the LIOB depth was fixed at 8mm for two DOIs: $z=4\text{mm}$ (within etched region) and $z=12\text{mm}$ (outside etched region). Bottom Left: The reflectivity was varied, while the LIOB depth was fixed at 8mm for a head-on irradiation. Bottom Right: The LIOB depth was varied, while the reflectivity was fixed at 20% for a head-on irradiation.

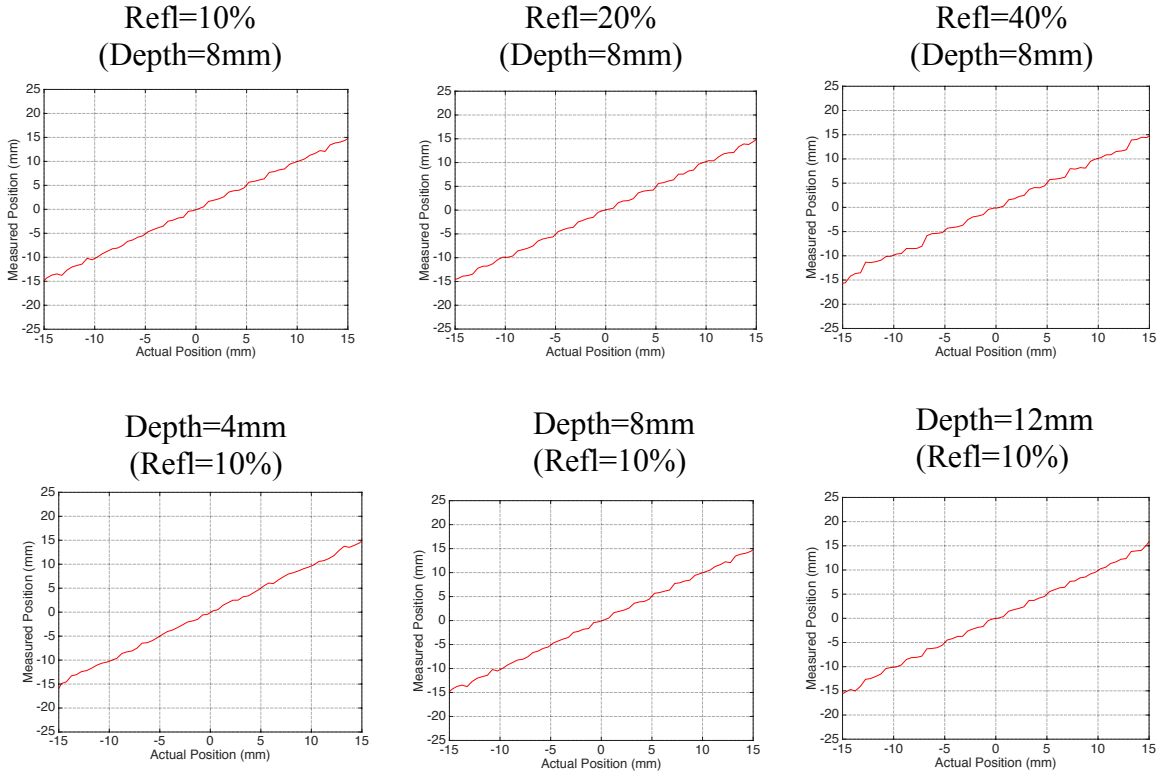


Figure 4.29: Positioning linearity for the 50x50x25-mm³ crystal etched with LIOBs of varying opacity and depth.

4.5 Discussion

1. The optical measurements indicated that the LIOBs generally behave as semi-transparent barriers that widely disperse reflected light and transmit light both directly and diffusely. The fraction of transmitted light that is directly transmitted increases as the reflection coefficient decreases; this result is reasonable since in the limit of 0% reflectivity, the LIOBs are expected to have a negligible impact on the scintillation light. While the exact profile of the reflected light was not measured because very little reflected light was collected through the PMT collimator at each position, the LIOBs

were shown to reflect the light widely, consistent with the hypothesized Lambertian distribution. Among the etched cubes, those with a wider spacing between the passes were the most opaque and varied most with laser power. This result is possibly because etching over the same region of the crystal does not disrupt the crystal structure more than a single pass, so that a wider spacing between the passes leads to greater thickness (and therefore greater opacity) in each LIOB; these thicker LIOBs may therefore also be more sensitive to laser power. Although the range of reflectivity measured among the LYSO cubes was ~20% to ~50%, there is no reason to expect that more opaque etchings could not be obtained, possibly with more passes or greater laser power.

2. The etchings act to spread light that impinges upon them from outside the etched regions of the crystal, while acting to restrict light spread within the etched region. Additionally, the LIOBs etched within the thick crystals were transmissive enough that the resulting LRFs changed monotonically with depth, in contrast to the mechanical cuts described earlier, in which the shallow depths had narrower LRFs than the deepest depths. More opaque etchings generally act to restrict the light spread more, but these gains must be weighed against any loss of positional or DOI information within the etchings.

3. The thick crystals investigated in this work all sustained etching without cracking, resulting in a grid-like pattern of very thin LIOBs. The crystals etched with a single layer of LIOBs showed improved performance in their etched regions, and the weighted average of the spatial resolution for the continuous crystals improved after etching,

although the impact of the LIOBs differed from that seen with the mechanical cuts; this is a consequence of the greater opacity of the mechanical cuts, as well as their likely different optical properties. This average resolution is difficult to achieve because of Compton scatter, though it can be used to compare the overall performance of the two detector designs. The LRFs were seen to be less depth-dependent after etching; while this result is beneficial because the depth-dependency of the LRFs was shown to limit the field of view of the continuous detector in the previous section, the resulting DOI information inherent in the detector was also shown to be degraded. The results of this investigation demonstrate the feasibility of etching both a single layer and two layers of LIOBs, and encourage further experiments with this design, using etchings with different parameters.

4. The simulations of the etched crystals matched the experiments in trend, similar to the results with the continuous crystal. A reflectivity of ~5-10% in the simulations resulted in a better match of the LRFs with the experimental measurements for the 25mm and 14mm thick crystals than the value expected from the laser parameters used in the etching (40%). There are a number of possible sources of the discrepancy seen here:

- A. It is possible that the performance of the laser varied over the long periods of time (~10 hr.) required to etch the thick crystals. Indeed, the reflectivity of the more opaque LIOBs demonstrated a variation with depth, which was not modeled in the simulations for the sake of simplicity.
- B. While the crystals studied in the optical experiments were etched through shallow distances because the only available samples were ~7mm thick, several of the

LIOB sets were etched deep within the crystals (~17mm deep for the second set of LIOBs on the 25mm thick crystal, and ~9mm deep for the 14mm thick crystal).

The properties of the etchings may differ when etching very deeply into the crystal.

- C. Several months had elapsed between the etching of the first set of LIOBs on the 25mm thick crystal and the measurement of the crystals. It is possible that the performance of the laser varied between these times.

Nevertheless, the optical measurements were useful to generally characterize the behavior of the LIOBs and to determine a range of LIOB properties that could be etched. Although limitations in the model used by the simulations precluded their being used to predict the exact performance of an etched crystal, the model of the optical behavior of the LIOBs was shown to be predictive of the general behavior of the etched crystals.

5. While the etched crystals show only modest improvement in performance, more opaque or deeper LIOBs were seen in simulations to be one option to increase the impact of the etchings. Varying these parameters, however, involves a trade-off between improved spatial resolution, continuous position sampling, and LRFs that vary monotonically with depth. For example, using the methods described here, the spatial resolution may be improved to be comparable to that of the 14mm thick crystal, although this may only be possible by sacrificing continuous position sampling. Additionally, an improvement in spatial resolution and a decrease in the depth-dependence of the light spread come at the cost of continuous DOI information, though this may be retained

discretely. One option to retain fine sampling was seen to be etching two layers of LIOBs, offset from one another by half of the grid pitch; using LIOBs that are opaque enough, this is a potentially more feasible alternative to discretizing the crystal into 1-mm pixels, since etching a 1-mm grid of LIOBs may not be possible without cracking the crystal.

6. Future experiments must be conducted to determine if a crystal could withstand etching with more opaque LIOBs or a denser grid of LIOBs without cracking, though the success of the experiments that were conducted are encouraging. In addition to testing the spatial performance of these designs, the full TOF performance of these crystals must be characterized, although preliminary experiments with small pixels etched with LIOBs only showed a slight decrease in timing performance, and so the etching treatment is not expected to significantly impact timing resolution. With added data against which to validate and fine-tune the model of the simulations (e.g. measurements of the behavior of the LIOBs as function of incident angle), the simulations may be used to optimize the etching parameters for a given task (e.g., minimizing spatial resolution while allowing for adequate DOI information).

4.6 Conclusions

This chapter investigated the optical behavior of the laser induced optical barriers, as well as the feasibility and potential of a detector design consisting of a continuous crystal etched partly into the entrance region. Optical measurements showed that the etchings behave as diffuse reflectors and display both direct and diffuse transmission,

with the fraction that directly transmits increasing as reflectivity decreases. The LIOBs investigated showed a range of reflectance ranging from 20% to 50%, with the fraction that directly transmits ranging from 50% to 80%. Etching thick crystals in a grid pattern with LIOBs improved the performance of the crystals within the etched region, but degraded the performance outside of this region, ultimately resulting in an average improved spatial resolution of $\sim 0.2\text{mm}$ for the 14mm thick crystal and the $\sim 0.3\text{mm}$ for the 25mm thick crystal; the second set of LIOBs did not improve the performance greatly.

Compared to the mechanical cuts introduced earlier, the LIOBs investigated were much thinner, but resulted in less of an impact on the light spread; however, the feasibility of etching the crystals successfully in this manner has been shown with an improvement in performance using etching parameters that were not optimized to minimize spatial resolution. Furthermore, simulations demonstrated the trade-offs in performance that may be obtained by altering the light spread with these etchings. With fairly transmissive etchings, continuous position sampling is retained while DOI information is decreased, though this may also be viewed as desirable because the depth-dependence of the light spread has been largely decreased. By either increasing the opacity or the depth of the LIOBs, the light spread in the entrance region may be decreased, improving the resolution and allowing for a two-level DOI scheme, though this may come at the cost of decreased position sampling. The experiments showed the feasibility of etching a second set of LIOBs as well; while these did not significantly improve the performance, more opaque etchings are seen as another alternative to achieve good resolution with good position sampling. Nevertheless, the relative gain in

overall scanner performance associated with each of these variables is crucial to understanding their importance; these may be explored by simulating scanners composed of detectors that vary some of these characteristics.

CHAPTER 5

System Simulation Study of the Impact of Improved Detectors

5.1 Introduction

While an improvement in spatial resolution for the detectors that comprise a scanner is clearly advantageous, the overall performance of a scanner is determined by many interrelated variables. In order to explore the impact of improved detector performance on the overall quantitative performance of scanners, simulations of complete scanners composed of a number of different detectors were performed using system simulations. These simulations were designed to isolate the detector performance from the other factors that degrade resolution (section 1.3), before calculating the effects of these factors on overall performance.

5.1.1 System Simulations: EGS4

System simulations of imaging systems are designed to model the overall performance of scanners. These codes use information regarding the geometry and composition of the object being imaged, the geometry of the scanner, and the performance of the detector and the positioning algorithm, in order to track annihilation photons from the object and ultimately output positioning, timing, and energy information for each event. There are a number of popular codes, including GATE/GEANT, SIMSET, EGS4, and SIMIND; these have been used in the field to study

a number of different aspects of PET scanners (e.g., spatial resolution, dead time, scatter, correction algorithms) [163-165]. The work in this thesis used EGS4 for system simulations; this code and its implementation are described below (Figure 5.1).

The electron gamma shower (EGS) code is a general code that models the transport of electrons and photons. Advantages to this code include its widespread use and flexibility. Furthermore, previous work at the University of Pennsylvania has adapted this code to simulate imaging with PET scanners, and has tested the validity of the code by comparison to data from actual scanners [101-102, 166]. The code consists of two parts: simulation of the gamma events/gamma tracing, and conversion of the gamma event locations in the detectors to relevant information for reconstruction. Simulation of a gamma photon begins by sampling from the radiation distribution of the object being imaged to determine the location of the gamma event. Here, two 511-keV photons are emitted 180° from one another at this location (acollinearity and the positron range effect are not modeled). Each photon is tracked through the object being imaged, modeling Compton scatter within the object with the Klein-Nishina cross section. The gamma-tracing component of Montecrystal is then used to track the incident photons within the detector, and determine the positions of interaction in all three dimensions.

For the second component of the simulation, the individual scintillation photons are not tracked, and instead the positioning, energy, and timing information of the detected photon is sampled using the PSF as well as the energy and timing response of the detector. Energy and timing gating are included in the simulation to determine the events that are accepted. The output of the simulation includes information regarding positioning, timing, and energy for all events, as well as specifically for true coincidence

events, scattered events, and random coincidence events; this information is output in the form of list-mode data that may be reconstructed. Corrections (e.g., scatter, attenuation) may be applied as in clinical scanners using an analytical transmission image for simple objects, such as cylindrical phantoms [166].

5.1.2 Image Reconstruction

As discussed in the introduction, iterative algorithms are used most prevalently in the field, and are used exclusively in this work because of their advantages. Iterative algorithms comprise a large collection of algorithms, which represent different methods of using the information gathered from the detected events to form a useful image. Of those used in the field, the most common group of algorithms is the maximum likelihood expectation maximization algorithm (MLEM), which operates by modeling the probability of measuring the image data with a Poisson likelihood function, and maximizing this function. Of these, the most popular is the ordered subsets expectation maximization (OSEM) [167-168] algorithm, which is a faster version of the MLEM algorithm. Additionally, images that are reconstructed using iterative methods are defined using a superposition of basis functions, which may also be varied; two of the more popular basis functions are non-overlapping cubic voxels and Kaiser-Bessel functions, known as blobs, which are chosen because of their favorable properties for reconstruction (e.g., the smoothness and symmetry of the functions) [167-168]. The image is then represented by effectively interpolating the blob images into discrete pixels (voxelizing the image), typically using pixels $4 \times 4 \times 4 \text{ mm}^3$ in dimension.

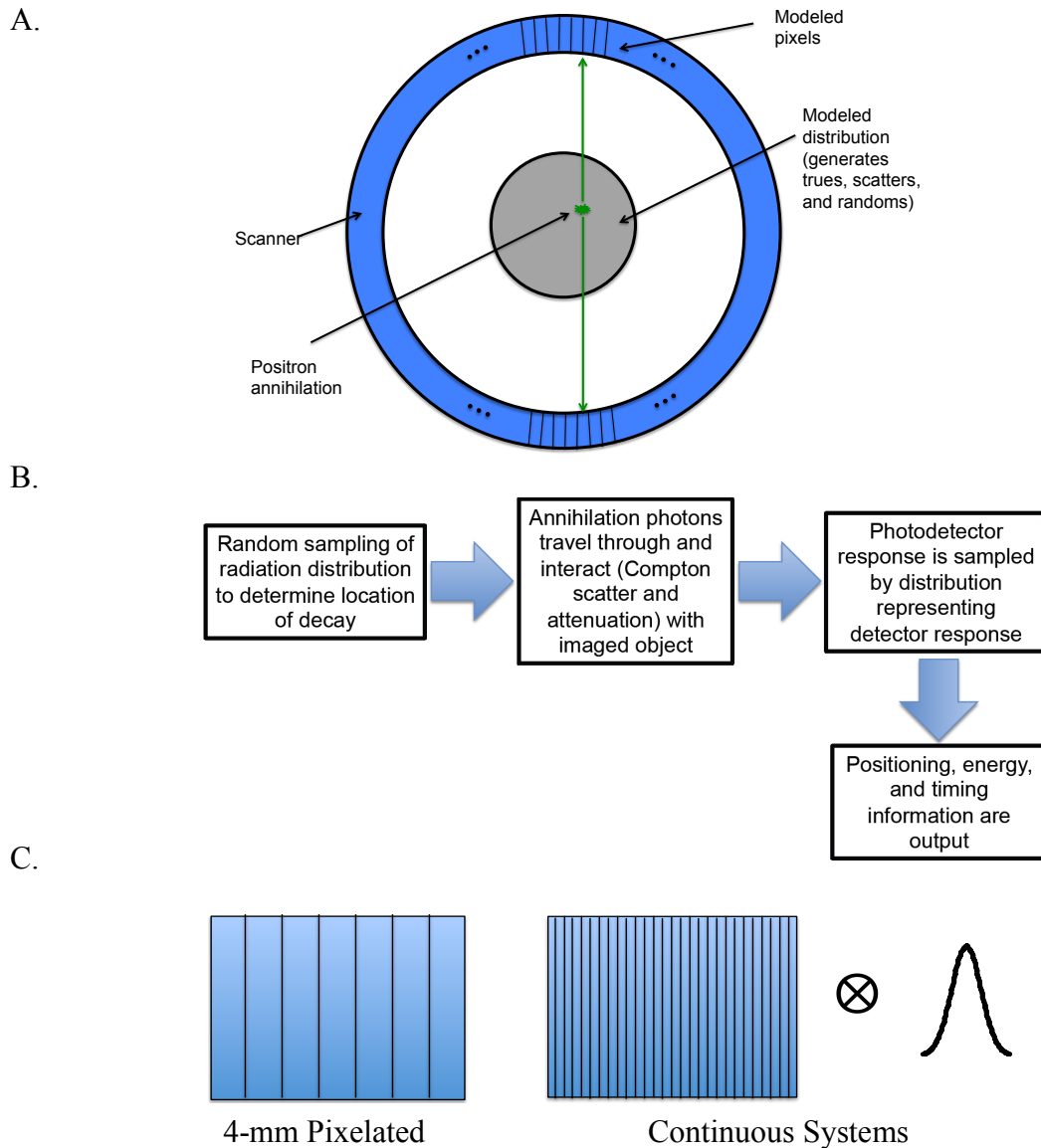


Figure 5.1: Diagram of model used in EGS4 system simulations. A. Diagram depicting gamma generation and detection in EGS4 simulations. B. Block diagram of model used in simulations. C. Models of detectors used in the EGS4 simulations, for which the continuous detectors are modeled using arrays of 1-mm pixels and the positions blurred using Gaussian filters of varying widths.

5.2 Methods and Materials

5.2.1 Systems and Phantoms

Several systems were compared, each composed of a different LYSO detector, including a standard clinical pixelated detector and very finely pixelated detectors with varying spatial resolution. The clinical pixelated detector was modeled using $4 \times 4 \times 20 \text{ mm}^3$ crystals with a pitch of 4.07 mm, to match that of current scanners, while continuous detectors were approximated using a finely pixelated detector with $1 \times 1 \times 20 \text{ mm}^3$ pixels with a 1-mm pitch; to vary the resolution of the continuous detectors, the measured position of interaction for each event was convolved with a Gaussian kernel of various widths prior to image reconstruction. The 1-mm sampling resulting from the finite pixel size was considered fine enough to have a negligible impact on the overall resolution and was chosen to avoid excessively long reconstructions, since the reconstruction time increases as the number of LORs increases. The FWHM of the kernels were chosen to be $\sim \{1 \text{ mm}, 2 \text{ mm}, 3 \text{ mm}, \text{ and } 4 \text{ mm}\}$; the value of 2 mm approximates the best-reported performance of an unetched continuous detector as well as the performance of the etched 14 mm thick crystal, while the value of 3 mm approximates the measured performance of the 25 mm thick crystal etched with 8 mm LIOBs, chosen for the simulation as an initial reference. Moreover, the detector simulation studies (Figure 4.26) indicate that with an appropriately chosen opacity and etching depth, the resolution may be improved (albeit with the potential loss of continuous sampling), warranting an investigation into improved resolution. All scanners

had an axial length of 180mm and a diameter of ~84cm, as well as a TOF resolution of 600ps.

Two studies were designed to characterize these scanners:

1. An image quality phantom of diameter 20cm, consisting of a warm background and hot spheres (contrast ratio ~10:1) ranging from 2.5-37mm in diameter. For each scanner, two simulations were run, simulating a phantom with six hot spheres in each: spheres ranged from 2.5-10mm in one simulation and ranged from 10-37mm in the other. This models the NEMA/Electrotechnical Commission (IEC) image quality (IQ) phantom. The images were quantified using the mean CRC, defined by National Electrical Manufacturers Association (NEMA) [93] in equation 1.4, as would be done clinically. CRC_{mean} was chosen here as one image quality metric to study because it is affected strongly by the system spatial resolution (Figure 5.2).
2. A phantom consisting of point sources, approximated as spheres of radius=0.5mm, embedded within a warm background. The ratio of the point source activity to background activity was chosen to be ~100:1, though because of the partial volume effect, the measured peak-to-valley is much lower. The points were located slightly off-center from the axis of the scanner and extended radially from the center of the scanner to 230mm. This study was designed to measure the spatial resolution as a function of radial distance for each scanner. These images were reconstructed using the same OSEM reconstruction algorithms as used to reconstruct the image quality phantoms, in order to directly relate the results of the two experiments (Figure 5.2).

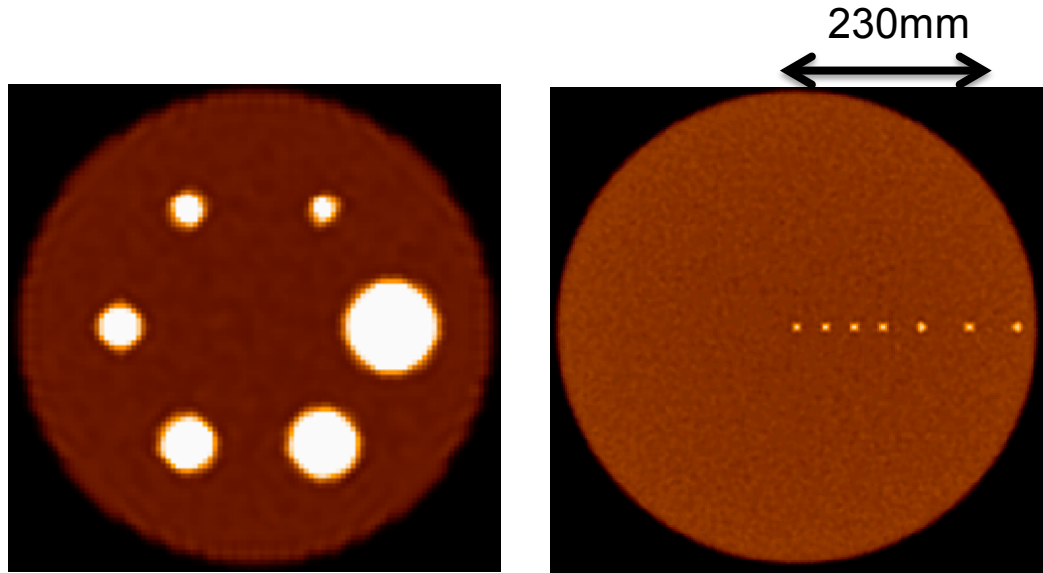


Figure 5.2: Images of the simulated IEC phantom and point source simulation used to characterize the various scanners. Left: Central slice of the cylindrical IEC phantom consisting of a warm background region with hot spheres ($\sim 10:1$ activity ratio). For each scanner, two simulations were run, simulating a phantom with six hot spheres on each: spheres ranged from 2.5-10mm on one simulation and ranged from 10-37mm on the other. Right: Image of a point source simulation, in which point sources were simulated in a warm background, with the source located near the center of the scanner axially, and beginning at the center of the scanner and extending radially to near the edge of the field-of-view.

5.2.2 Experiments

Initially for these studies, only true events were simulated (i.e., events scattered within the object were not included), acollinearity and the positron range effect were not included, while Compton scatter within the detector was modeled. These simulations were therefore designed to isolate the effect of the detector performance, including the effect of the crystal pitch/resolution of the detector as well as the effect of DOI.

Attenuation correction of the IEC phantom was performed by mathematically creating an image of the phantom composed of water and calculating an attenuation correction

sinogram, using the attenuation coefficient of water. Attenuation correction was not performed for the other study, since it was not concerned with contrast, so that the results were unaffected by attenuation correction. Normalization correction was not performed, because this is expected to have a minor effect on the results because of the high stopping power of LYSO, as well as the symmetry of the geometry and crystal properties in the simulated scanners (which in actual scanners is not fully realized because of nonuniformities among the many crystals); the minor impact of the normalization correction is supported by previous simulation studies. All images were reconstructed using an ordered subset expectation maximization algorithm, using either voxel or blob basis functions [168]. The type and size of the basis functions varied with the scanner being simulated and were chosen to optimize the values of CRC_{mean} based on the size of the detector pixels used in the scanner: for the continuous systems, 1-mm basis voxels were used to reconstruct the images, which were displayed using 1-mm voxels; for the 4-mm pixelated system, blobs on a 6-mm grid were used to reconstruct the images, which were displayed using 2-mm voxels.

The experiments that were conducted using the simulations are listed below:

Improved Detector Spatial Resolution and Position Sampling

The improvement in scanner performance achieved using a scanner with continuous detectors was studied by comparing the scanner with 4-mm pixelated detectors to that with the various continuous (1-mm pixelated) detectors. The effect of continuous sampling was measured by comparing the 4-mm pixelated scanner to a continuous detector with a 4-mm Gaussian blurring.

PSF Estimation

In order to determine the relationship of point source resolution to contrast recovery, a calculation was performed using MATLAB, in which a sphere of variable radius and with uniform activity, located in a background of uniform activity at a contrast ratio of $\sim 10:1$, was convolved with Gaussian filters of varying width (Figure 5.3). The CRC_{mean} of the resulting image was then measured by calculating the average voxel value in a VOI of diameter equal to the sphere, as in clinical studies. The CRC_{mean} values calculated by using the measured PSFs of the point source simulations were then compared to those of the IEC phantom simulations; the calculation was also used to determine the PSFs that lead to good agreement with the simulated CRC_{mean} values, denoted as PSF_{CRC} .

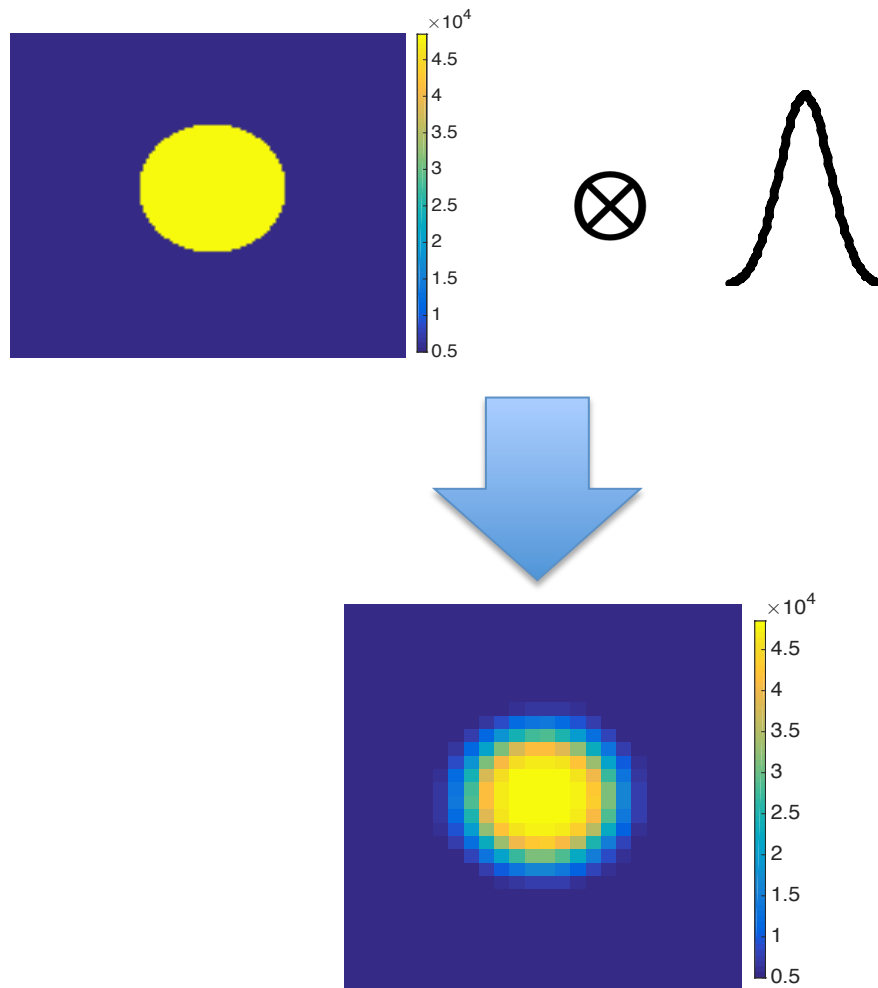


Figure 5.3: Diagram illustrating calculation in which a uniform sphere in a uniform background is blurred with a Gaussian PSF, and the CRC of the resulting blurred image is calculated using a VOI of diameter equal to the sphere diameter. Here, one slice through the sphere is shown for simplicity.

Overall Scanner Resolution

To determine the overall quantitative performance of the scanners composed of these detectors, the impact of the various effects that act to degrade the performance of the scanners was estimated. Many of these effects may be estimated to combine in quadrature to determine the overall spatial resolution of the scanners [37].

1. Scatter: To estimate the impact on CRC of only simulating true coincidences, the effect of Compton scatter in the object being imaged was measured by comparing simulations with scatter to those without scatter. When scatter was included, scatter correction was performed using Single Scatter Simulation [169-170], as would be done clinically.
2. The effect of the basis function size and image voxel size were measured by comparing the results of images reconstructed with varying basis function sizes and voxelized using both 2-mm and 1-mm voxels.
3. The effect of photon acollinearity and the positron range effect were measured by estimating the point source resolution of the various scanners using the known distribution of these effects. While photon acollinearity leads to a Gaussian blurring (eq. 1.1), the positron range effect is non-Gaussian; its distribution was modeled as a sum of two exponential functions:

$$P(x) = Ce^{-k_1x} + (1 - C)e^{-k_2x}, \quad (5.1)$$

where C , k_1 , and k_2 are constants related to the isotope. For ^{18}F , the values used were $C=0.516$, $k_1=0.379 \text{ mm}^{-1}$, and $k_2=0.31 \text{ mm}^{-1}$ [43, 171].

To estimate the overall blurring, a random number generator was used to sample from the various distributions and convolve the measured PSF_{CRC} of the simulations with these two effects. Note that in order to separate the resolution of the scanner from the effect of voxelizing the image, a Gaussian function with the measured FWHM of the point source simulations was voxelized in MATLAB, and the effect on the measured FWHM was calculated prior to the convolution. The resulting PSFs were then applied to

the CRC calculations, with specific attention paid to the 5.5mm sphere, since this size is near the limit of detectability for current scanners.

5.3 Results

Figure 5.4 shows sample images of the IEC phantom with spheres ranging from 2.5mm to 10mm, obtained from the 4-mm pixelated and continuous (1-mm pixelated) systems. The images show that each of the spheres may be discerned and that the images are free from artifacts. Note also that the smaller spheres are better visualized with the continuous scanner, because of the improved spatial resolution. Figure 5.5 shows a plot of CRC_{mean} vs. sphere size for the 4-mm pixelated system for three trial simulations. The results show good agreement between the trials, while the random uncertainty of the CRC_{mean} measurements increases as sphere size decreases, and is $\sim 7\%$ for the smallest sphere included in the study. The CRC_{mean} values of the images converge quickly (Figure 5.6); for these studies, iteration 10 was used throughout to ensure convergence.

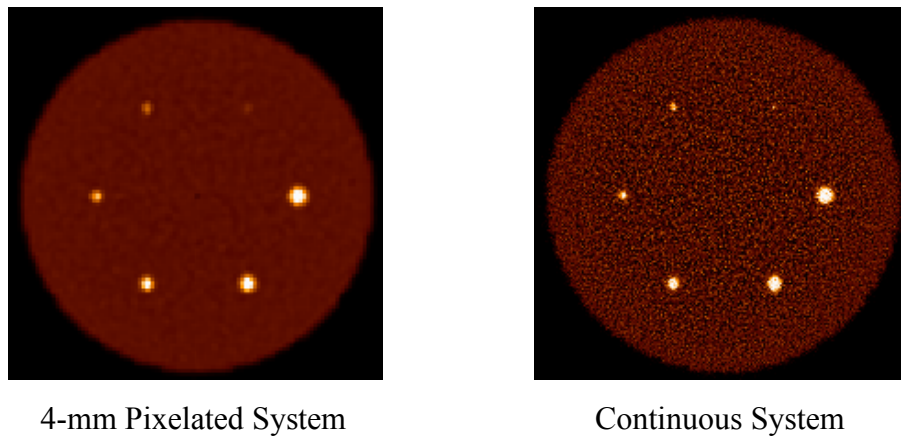


Figure 5.4: Central slice of the simulated IEC phantom for the 4-mm pixelated and continuous (1-mm pixelated) systems. Each of the spheres may be distinguished from the background and the images are free from artifacts.

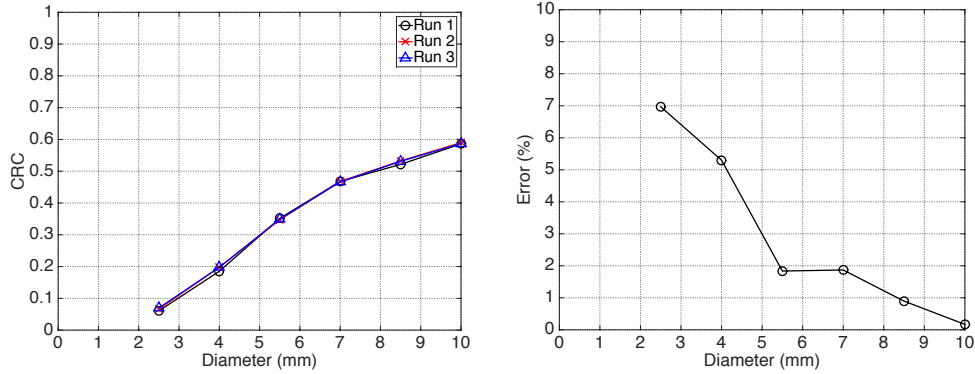


Figure 5.5: CRC_{mean} of the 4-mm pixelated system for three independent trials (left) and standard deviation of the measurements (right), showing the low uncertainty of the measurements made with the simulations.

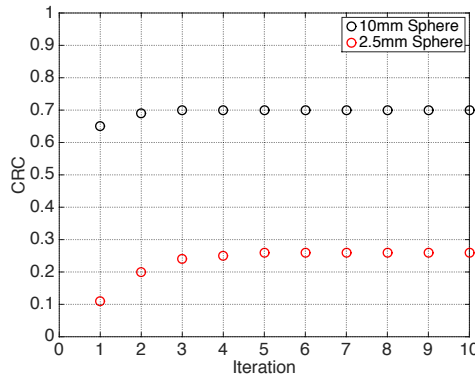


Figure 5.6: CRC_{mean} for two spheres as a function of reconstruction iteration for the continuous system. Iteration 10 was used for these measurements to ensure convergence.

Figure 5.7 shows that CRC_{mean} for the continuous system increases as the reconstruction basis function (blob/voxel) size decreases, and the size of the image voxel decreases. In order to maximize the resolution of these systems, the smallest basis function and image voxel size that avoided undersampling (aliasing) artifacts were used for each system. A comparison of the point source resolution and curves of CRC_{mean} for the various detectors are shown in Figure 5.8. The plots show an improvement in point

source resolution, and a corresponding improvement in CRC_{mean} , in moving from a 4-mm pixelated system to a 4-mm continuous system, because of the smaller reconstruction basis functions that the improved position sampling allows. Further improvements are seen as the resolution of the continuous systems improves. Although not shown, the values of point source resolution were converged by iteration 10, so that this iteration was used for all values shown.

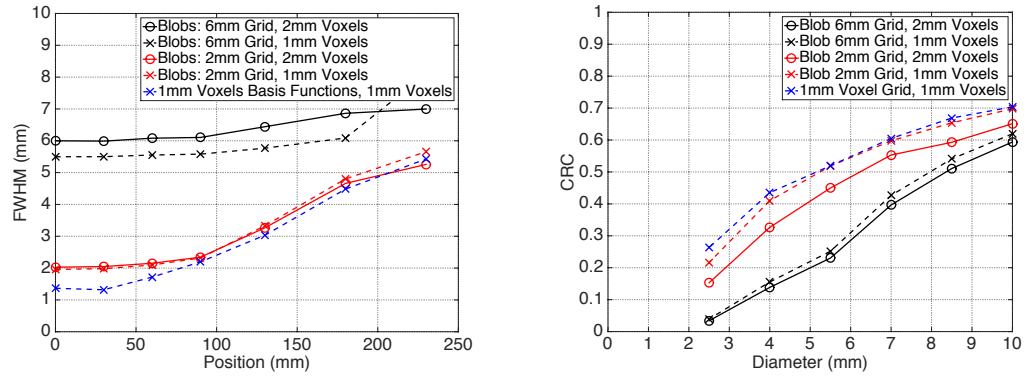


Figure 5.7: Point source resolution (left) and curves of CRC_{mean} (right) for the continuous system, reconstructed using various basis function grids and voxelized using 1-mm and 2-mm voxels. Both the point source resolution and the CRC_{mean} improve as the basis function decreases in size and the image is displayed using smaller voxels.

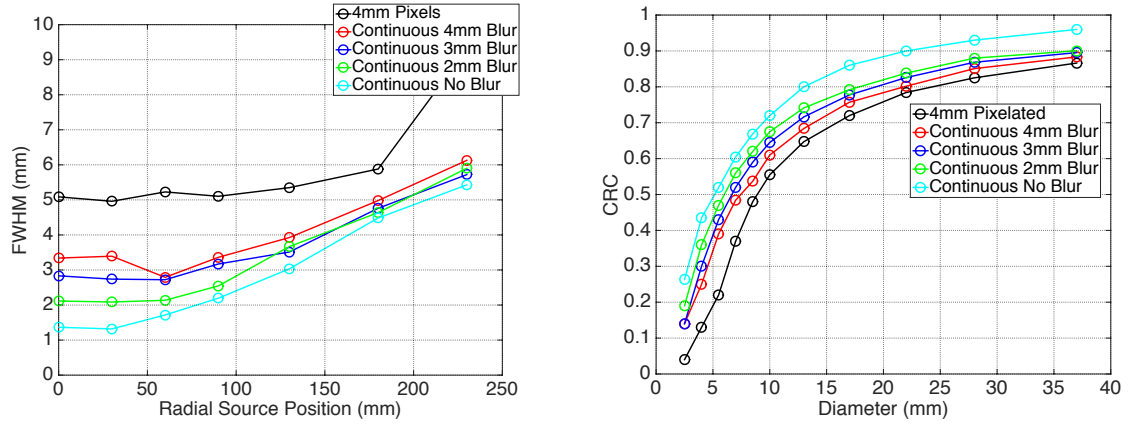


Figure 5.8: Point source resolution as a function of radial source position (left) and CRC_{mean} as a function of sphere diameter (right) for the 4-mm pixelated system and the various continuous systems. For the continuous systems, 1-mm basis voxels were used to reconstruct the images that were displayed using 1-mm voxels; for the 4-mm pixelated systems, blobs on a 6-mm grid were used to reconstruct the images that were displayed using 2-mm voxels.

Object scatter does not affect point source resolution or CRC_{mean} for these phantom studies if corrected for properly, as shown by the low percent difference in Figure 5.9, and so was neglected in order to expedite the simulations and reconstructions.

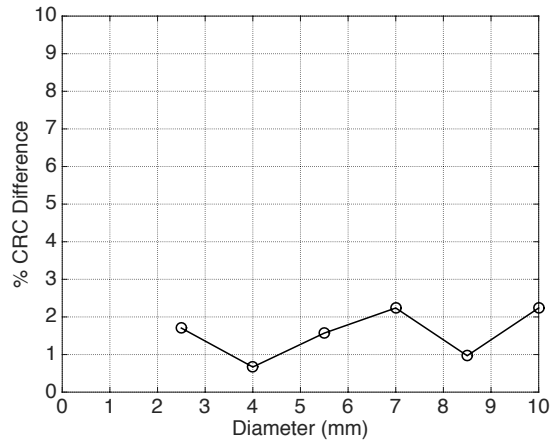


Figure 5.9: Percent difference between the CRC_{mean} measured in simulation for the 4-mm pixelated system when excluding and including object scatter (with scatter correction). The small difference between the CRC_{mean} measurements after correcting for scatter justifies the use of simulations in which only true coincidences were simulated.

The accuracy of the calculation in MATLAB translating the measured point source resolution to CRC_{mean} is shown in Figure 5.10. The predicted CRC_{mean} for the 4-mm pixelated system agrees with the simulation results within 12% for all spheres; the PSF of the point source simulations for the 4-mm pixelated system was therefore taken to be the PSF_{CRC} . Greater discrepancy is seen for the continuous systems, indicating that the effect of scanner resolution on image quality cannot be fully modeled using a convolution with a Gaussian PSF. The 3-mm resolution continuous system is shown as an example: the best agreement for this system at sphere sizes between 5.5mm and 10mm resulted from a PSF of 3.3mm, rather than the measured resolution of 2.7mm; this factor of ~ 1.2 discrepancy was found for each of the continuous systems with resolution > 2 mm, and is possibly a function of the LOR sampling space (1-mm pixels) and reconstruction algorithm used.

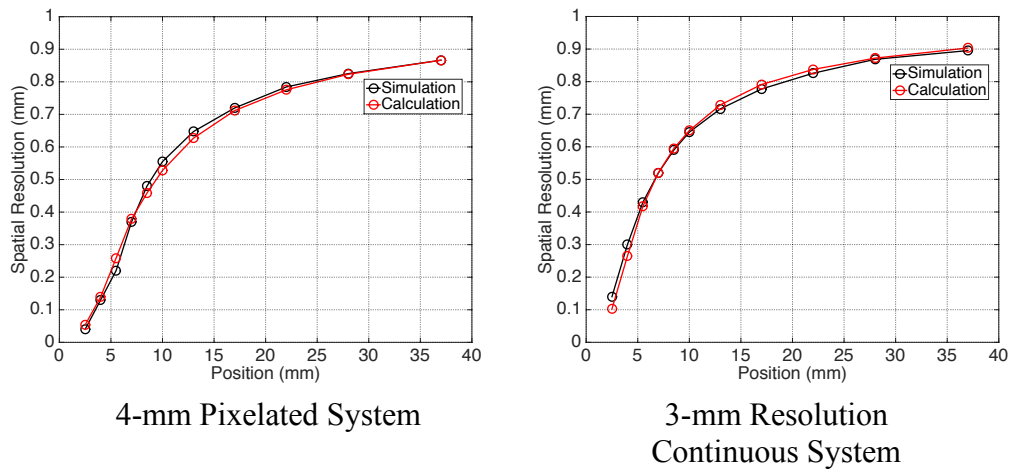
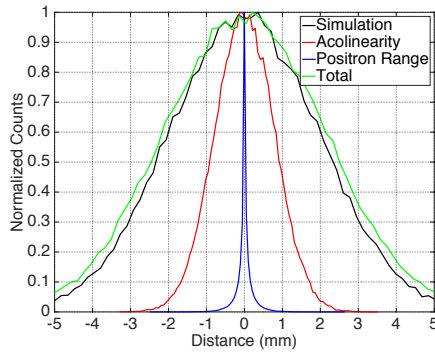
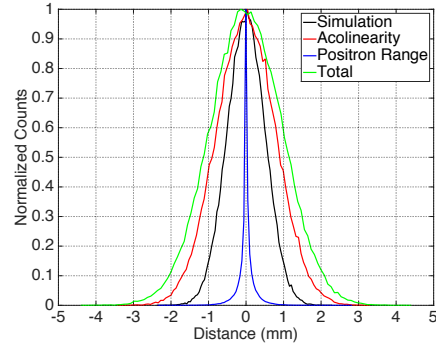


Figure 5.10: Comparison of CRC_{mean} curves measured using IEC phantom simulations and when calculating using the PSFs measured in the point source simulations. Note that for the continuous system, the best agreement was made using a PSF of 3.3mm.

The result of convolving the measured values of resolution in these simulations with the effects of acollinearity and finite positron range are shown in Figure 5.11. The measured distributions were fit well by a Gaussian, so that the measured point spread functions were estimated using a Gaussian fit. Note that the effect of acollinearity on the overall scanner resolution is larger for the 1-mm pixelated scanners, because the intrinsic resolution is lower for these systems. The range in resolution for the continuous systems near the center of the scanner was ~ 3 -4.5mm after including these effects. The corresponding CRC_{mean} curves calculated analytically also decreased after inclusion of these effects (Figure 5.12). CRC is increased by $\sim 19\%$ and $\sim 14\%$ for the 5.5-mm and 10-mm spheres, respectively, in moving from a 4-mm pixelated system to a 3-mm continuous system. In moving to a 2-mm continuous system from the 4-mm pixelated system, CRC is increased by $\sim 22\%$ and $\sim 19\%$ for the 5.5-mm and 10-mm spheres, respectively.



4-mm Pixelated System



Continuous System

Figure 5.11: PSFs for the various factors that affect system spatial resolution for the 4-mm pixelated system and the continuous system. Acollinearity was shown to have a greater effect with the continuous system than with the 4-mm pixelated system because of the lower intrinsic spatial resolution of the continuous system.

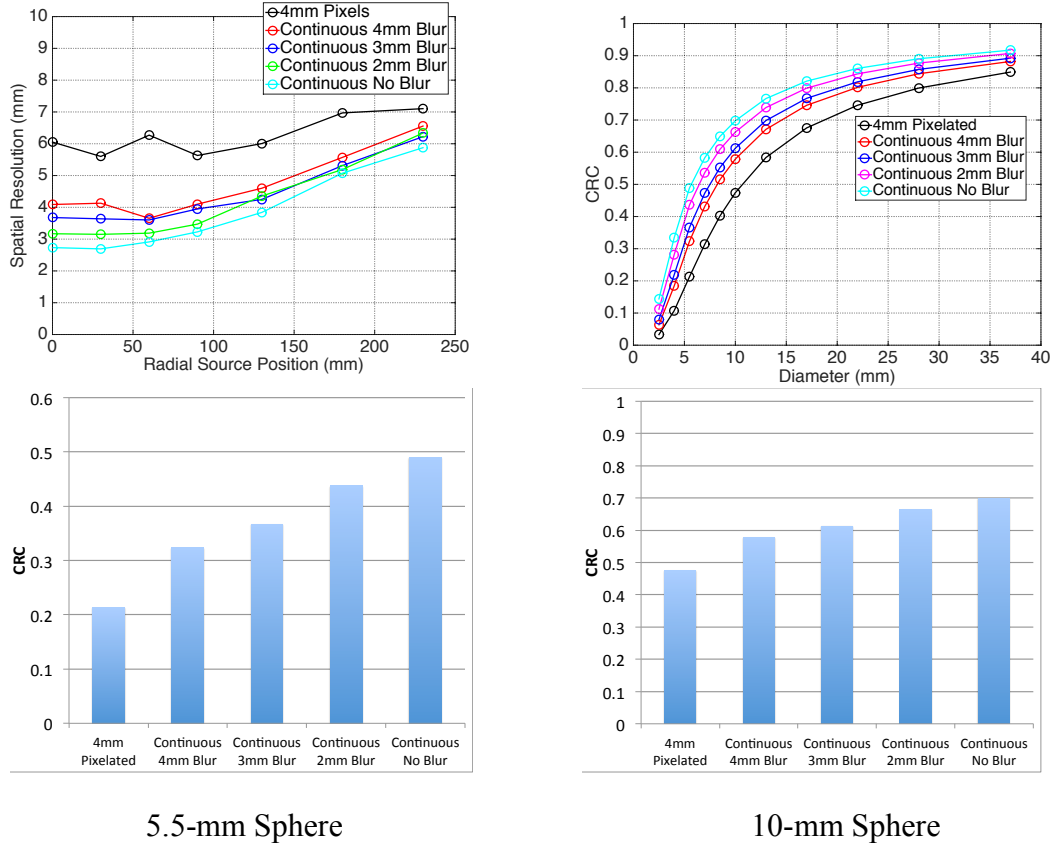


Figure 5.12: Point source resolution as a function of radial source position and CRC_{mean} as a function of sphere diameter for the 4-mm pixelated system and the various continuous systems after convolving all resolution effects. Top: Point source resolution (FWHM) (left) and curves of CRC_{mean} (right) for the various systems after convolving all resolution effects. Bottom: CRC_{mean} values for 5.5-mm and 10-mm spheres for the various systems.

5.4 Discussion

Some of the improvement in transitioning from a pixelated to a continuous system is the result of the improved reconstruction algorithms that are possible because of the improved sampling offered by the continuous system; the simulations showed an improvement of $\sim 5\%$ for 5.5-mm spheres in transitioning from a 4-mm pixelated system

to a 4-mm continuous system. The pixel size of the detector in general limits the number of LORs that sample an image; the finite number of LORs ultimately limits the basis grid spacing used for reconstruction, since use of too fine a grid will result in the LOR space undersampling the image, which leads to aliasing artifacts.

These results may be compared to the simulation study in Tabacchini et al. [172], which demonstrated an average CRC_{mean} for 5-mm lesions of ~ 0.3 for a similar continuous detector (back-sided readout); note that in their work, the effects of acollinearity were modeled into the simulation, which acts to degrade the resolution, while images were reconstructed with 2-mm voxels. Their work showed that a pixelated detector with ~ 3 mm pixels would be required to match the CRC_{mean} and lesion detectability performance of such a detector. Surti et al. [45] similarly showed a CRC_{mean} of $\sim 23\%$ for 5-mm spheres near the center of a scanner with 4-mm pixels and a TOF resolution of 600ps, without including the effects related to the physics of positron annihilation. This value increased to $\sim 34\%$ using a detector with 2.6-mm pixels, similar to the value for the 2.9-mm pixelated system in [172] and the value for the 3-mm resolution continuous system studied in this work.

The positioning histograms were well fit by a Gaussian when including all effects because many of the effects were Gaussian; of the two that were not – the detector width and the positron range effect – the width of the detector contributed much more significantly to the blurring. Even after including all of the factors that degrade spatial resolution, a statistically significant improvement in resolution and CRC_{mean} is made when transitioning to a continuous system with 4-mm resolution and then again when the

resolution is improved to 3mm. The impact of this improved resolution on quantification is greater for smaller lesions, as expected.

The simulations also showed that the CRC_{mean} values for small sphere sizes for the scanner with continuous detectors lie between those of the clinical pixelated system and the finely pixelated system, matching the trend in spatial resolution among the detectors. The improvement in CRC_{mean} provides motivation for efforts to improve the spatial resolution of continuous detectors, and highlights the potential difference in performance between 25mm and 14mm thick continuous crystals, as well as the potential difference between continuous and etched crystals. The resolution of the etched 25mm thick detector was $\sim 3.5\text{mm}$ in this work, while that of the etched 14mm thick crystal was $\sim 2.2\text{mm}$, resulting in an increase in CRC of $\sim 10\%$ for small sphere sizes.

CRC_{mean} was studied to estimate the improvement in image quality because this metric is directly affected by spatial resolution, though other metrics may be used as well, particularly metrics to quantify noise. Both spatial resolution and noise are important in describing the detectability of the imaging system, quantified by metrics such as the contrast-to-noise ratio. Similarly, while the bias of the measurement of CRC_{mean} was studied, the precision was not vigorously investigated in this study. While this study serves as an exploratory study of the benefit of improved detector performance, further studies should therefore evaluate both aspects of image quality, and describe the compromise between the two inherent in using the various detectors.

5.5 Conclusions

Monte Carlo system simulations were used to estimate the effect of improved detector performance on the overall performance of the scanner. Initial simulations modeled the effect of the detector performance and showed a steady improvement in system performance with improved detector resolution. An analytical calculation was used to convolve other resolution effects as well, and showed an overall improvement in scanner resolution and CRC_{mean} when transitioning from a pixelated system to a continuous system (e.g., 11% for 5.5-mm spheres) and further improvement when the detector resolution improves from 4mm to 2mm (e.g., 11% for 5.5-mm spheres).

These results place into context the detector measurements and simulations discussed in the previous chapter. While the presence of other effects decreases the improvement in resolution seen with modified continuous crystals, the quantitative performance is still measurably improved with a detector resolution of $\sim 3\text{mm}$ and $\sim 2\text{mm}$, similar to that attained with the 25mm and 14mm thick etched crystals, respectively. Moreover, the results demonstrated the increase in CRC that may potentially be achieved using appropriately designed LIOBs. Use of CRC_{mean} in this study was used to show an improvement in contrast recovery achievable with the improvements in detector performance that have been investigated using laser induced optical barriers. For these studies, phantom measurements were used to quantify the performance of the simulated scanners, as is done on clinical scanners. The relevance of this work to clinical performance with patient studies, however, was not shown; this is discussed in the following chapter.

CHAPTER 6

Translation of Phantom-based Quantitation to Patient Quantitation

6.1 Introduction

The previous sections described the impact of detector performance on overall scanner performance and quantitation using bench-top experiments and simulation studies of phantoms. The quantitative performance of scanners in patient studies, however, is the important end result for both clinical and research studies, and must be related to performance measured using standardized objects. Moreover, the impact of the reconstruction strategy (e.g., reconstruction algorithm and post-filter) must be considered as well as the scanner detector design, because the wide range of choices available lead to differences in quantitative performance. The following study is accepted for publication [173] and was conducted as part of the larger NCI-funded Harmonization Initiative, which uses phantom scans to measure scanner performance and allow for scanner-specific reconstruction parameters to be determined. The primary goal of this study was to test the correspondence between quantification in phantom and patient images and validate the use of phantoms for the characterization of patient images. This study ultimately allows conclusions to be drawn regarding clinical scanner performance based on the phantom studies discussed earlier, drawing a connection between the detector performance studied in the laboratory setting and clinical scanner performance.

Additionally, this work highlights the impact of the reconstruction strategy in determining image quality, placing improvements in scanner performance into better context.

6.1.1 Connection between System Simulations and Clinical Scanners

The system simulations were validated by comparing the IEC phantom measurements made on the 4-mm pixelated system simulations, after including all of the resolution degrading effects, with the values from IEC phantom measurements on a Philips Healthcare Vereos system, chosen because this system has similar specifications regarding crystal size and pitch to that used in the simulations [34]. The measured phantom data from the Ingenuity TF system were collected in 3 separate runs and averaged, in order to minimize uncertainty; each run was reconstructed using a similar algorithm as the simulated data. Figure 6.1 shows good agreement for all sphere sizes between the simulated and clinical data. This study therefore connects the simulation phantom studies and the phantom studies on clinical scanners, motivating a study to further connect the clinical phantom studies to patient studies.

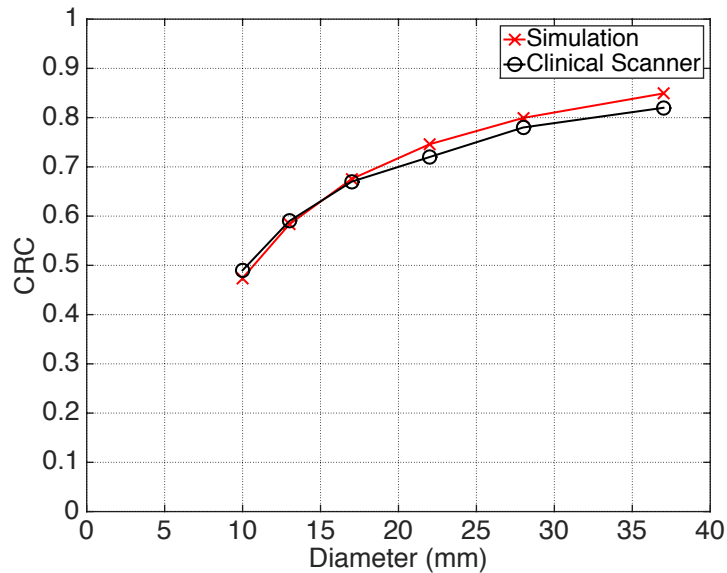


Figure 6.1: Comparison of CRC resulting from phantom scans on the Philips Healthcare Vereos and from simulations of a 4-mm pixelated system; similar image reconstruction and data corrections are applied for each scanner.

6.1.2 Harmonization

The various factors that hinder the ability to absolutely quantify images during clinical evaluation, by introducing biases and degrading precision, were discussed in section 1.5.3. The value of a multicenter study, in which data may be collected from a number of different scanners operated at several institutions, is especially dependent upon reducing the variability of quantification across the various scanners and sites involved, as better precision allows for a reduction in the number of subjects needed to obtain statistically significant findings. For this reason, efforts have been made to reduce the sources of variation for these studies. Much of this effort has been focused toward standardizing the protocol of a PET/CT scan in order to mitigate the issues unrelated to

scanner and reconstruction performance: calibration, patient preparation, FDG administration, and scanning procedure [81-82, 174].

Differences in reconstruction protocol as well as scanner hardware, however, lead to variations in performance, not only among the many models of scanners available, but also within the same scanner operated at different institutions [175]. Moreover, improvements in performance brought about by improved detector performance, as seen in the previous chapter, are expected to exacerbate these differences. These findings have prompted a number of organizations (e.g., the North American Quantitative Imaging Biomarker Alliance, European Association Research Ltd accreditation program, and Clinical Trials Network of the Society of Nuclear Medicine and Molecular Imaging) to undertake efforts to harmonize scanners through standardization of image reconstruction and image analysis methods. Previous work in the field [176] developed a protocol that determined Gaussian post-reconstruction filters that harmonized the performance of various scanner makes and models to that with the worst performance. Because the resulting measurements of uptake are degraded, however, other harmonization strategies are needed.

The University of Pennsylvania and the University of Washington are currently part of a multi-institutional National Cancer Institute (NCI)-funded harmonization study led by the University of Iowa. The NCI harmonization project aims to determine the reconstruction parameters and post-filtering necessary for harmonization of oncologic studies and to assess the impact of harmonization on multicenter studies [177]. These various organizational efforts all use standardized measurements with the NEMA IQ phantom [93] (Figure 6.2), which consists of 6 fillable plastic spheres, chosen from a

range of 8.5-44mm in diameter, and a central non-radioactive cylinder filled with foam beads to approximate lung matter, immersed in a plastic container with a background volume of 9.7L. The background and sphere compartments of the phantom are filled with liquid radioactive material (e.g., ^{18}F) and then used to measure the contrast recovery coefficient as a function of sphere size, sampling at the finite number of sphere sizes, and at two sphere:background contrast ratios: 9.7:1 and 4.85:1. The measurements are acquired on the various systems to determine scanner-specific acquisition and reconstruction protocols to achieve harmonization, defined here as minimizing in some sense (e.g., root mean square difference) the distance between the curves of CRC as a function of sphere diameter. It has been found that an overall harmonization between different scanners is possible through a choice of reconstruction parameters that may include a post-filtering procedure, but that it may not provide the same agreement for all sphere sizes [177].

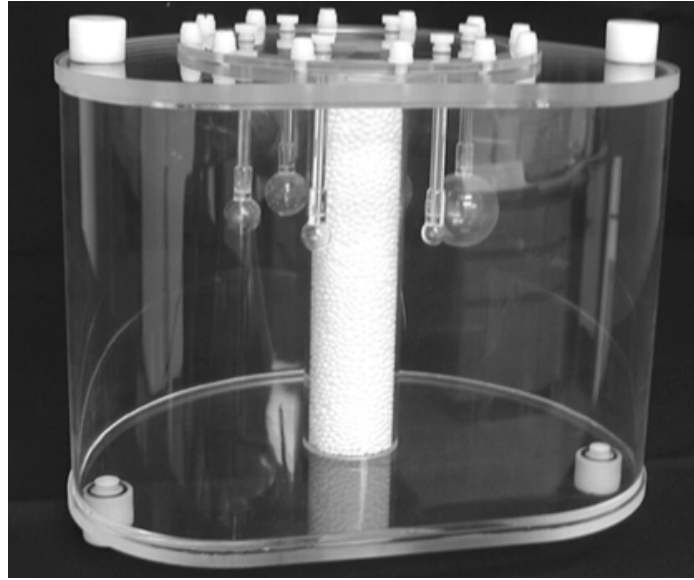


Figure 6.2: NEMA image quality phantom used to quantify the performance of scanners. The phantom consists of 6 fillable spheres, chosen from a range of 8.5-44mm, and a central cylinder non-radioactive “lung” filled with foam beads, immersed in a background region.

The NCI harmonization project uses a broader range of sphere sizes than other efforts, in order to impose stricter requirements on the harmonization. The project is designed to further study the trade-off between harmonization and optimization (CRC values closest to their ideal value of 1), as well as to characterize the penalty incurred in increased noise resulting from efforts to improve the CRC. To this end, the project involves the collection of phantom data among many different scanners and institutions and the measurement of CRC for many versions of reconstruction algorithms and parameters. Additionally, it aims to test the use of post-filters that increase the measured value of uptake as a method of harmonization.

While harmonization using phantom scans has been shown, its consistency when

applied to patient studies for the various harmonization strategies has yet to be demonstrated. Several studies have undertaken this task and made important progress [178-180]. Lasnon et al. [178] studied the use of Gaussian filters during reconstruction, optimized using phantom images, to harmonize the SUV values of patient lesions in various organ locations; data from patient images reconstructed using list-mode OSEM without PSF modeling were harmonized to the same data reconstructed with PSF modeling. Quak et al. [179] followed this study with an investigation into the use of a proprietary post-filter, EQ.PET, to harmonize patient lesions from three different scanners and concluded that harmonization of patient SUV values using phantom scans was possible with suitable post-filters. Armstrong et al. [180] studied the impact of using time-of-flight (TOF) information on the ability to harmonize scanners and assessed two harmonization strategies: matching the maximum SUV (SUV_{max}) in a lesion and matching the voxel variance (i.e., image noise) of images from a single scanner reconstructed with different methodologies.

The primary goal of the work described here was to test the correspondence between quantification in phantom and patient images and validate the use of phantoms for harmonization of patient images. The study is distinguished from previous work in its aim to directly measure the impact of phantom harmonization on patient harmonization by comparing quantification metrics for phantom and human subject studies where lesions of known uptake have been embedded synthetically into the subjects. This work also explores the use of a post-reconstruction deconvolution filter as a tool to harmonize by increasing the CRC of one scanner, in addition to the use of post-reconstruction smoothing filters that decrease the CRC of scanners, as these are proposed methods of

harmonization being adopted by some clinical trials. While the work is part of the larger Harmonization Initiative, it also serves to illustrate the effect of improved scanner performance on quantitation, by the comparing the performance of different scanners, as well as the strong effect of the reconstruction algorithm, which is separate from that of the detector performance discussed previously.

6.1.3 Post-filters

Two filters were used in this work, because they are proposed methods of harmonization being adopted by some clinical trials. The first is the common Gaussian post-filter, used generally in order to smooth images and specifically for the harmonization effort to reduce the values of CRC and SUV in the images to a common value for a given sphere size. This filter involves the 3D convolution of a Gaussian function, characterized by its FWHM, resulting in an effective decrease in spatial resolution.

The second filter studied was a deconvolution post-filter, because such filters allow the user to improve the image resolution without additional reconstruction and are computationally efficient. In general, deconvolution methods are used to correct for the blurring brought about by the finite spatial resolution of imaging devices, and are based upon mathematically calculating the original input image given the final image and information regarding the PSF of the imaging device. Any attempt at image restoration is limited by the available data in an image: while blurring acts to attenuate low or mid-frequency components of data, higher frequencies in the data are lost, so that image restoration can never fully recover the original. Moreover, the nature of the restoration

problem that deconvolution attempts to solve is ill-conditioned, so that deconvolution that acts to restore these higher frequency components of the image tends to amplify noise and may lead to artifacts (e.g., edge enhancement and ringing artifacts); for this reason, these operators are often applied using some type of regularization that smoothes images [54, 68].

The deconvolution filter studied in this work is the Lucy-Richardson (LR) deconvolution post-filter [181-183]; this filter is analogous to the methodology implemented by Philips for point spread function (PSF) modeling. The LR iterative algorithm is based on the MLEM algorithm and assumes Poisson statistics; as applied for this work, it used a spatially variant PSF model, based upon point source measurements at various points in the field of the view of the relevant scanner. It has been previously investigated for PET applications, using the method of sieves to control noise. This regularized algorithm is given by:

$$f_{k+1} = \frac{f_k}{h * s} \left(h * s * \frac{g}{f_k \otimes s \otimes h} \right),$$

where f_k is the original image, g the distorted image, h is the scanner PSF, s is the sieve-kernel, \otimes is the convolution operation and $*$ the correlation operator [184-186].

6.1.4 Phantom Studies

Figure 6.3 shows CRC_{mean} and CRC_{max} as a function of sphere diameter from the Philips Ingenuity TF PET/CT scanner for a phantom scan; here, a single 30 minute scan was divided into ten 3-minute scans, and the average value plotted with the error bar given by the standard deviation of the ten measurements to estimate the statistical uncertainty. Although CRC_{mean} varies smoothly with diameter, CRC_{max} is less predictable

and illustrates the benefit of using the additional spheres of intermediate size. CRC_{max} also shows greater variability over the 10 replicate scans (larger error bars); for CRC_{mean} the error bars are smaller than the symbol sizes. Last, CRC_{max} is seen to exceed 1 (perfect recovery) at times, because it is calculated as the value of the voxel with maximum intensity, and therefore subject to a measurement bias that increases with image noise.

An example of using the NEMA IQ phantom to harmonize two whole-body PET scanners from different vendors is shown in Figure 6.4. Note that for this study, and for all subsequent phantom measurements, all spheres are hot, in contrast to the prescribed NEMA measurement in which the two largest spheres are cold. Here we see a comparison of the Siemens mCT [187] and Philips Ingenuity TF PET/CT scanners, both used clinically in the PET Center at the University of Pennsylvania. Both scanners use TOF reconstruction, but the default reconstruction used for the mCT is with PSF modeling, whereas the default reconstruction used for the Ingenuity is without PSF modeling. It is seen that in order to achieve a high degree of harmonization of the CRC_{mean} , the Siemens images need to be filtered with a Gaussian post-filter (with kernel of 4-mm FWHM), whereas CRC_{max} values match best without any PSF or post-filtering applied to either scanner.

This comparison is shown to demonstrate the effect that the reconstruction algorithm has on the performance of the scanner, as well as some of the pitfalls in the use of algorithms to compensate for spatial resolution, including the bias introduced into the CRC_{max} ; reconstruction algorithms therefore cannot be used to compensate completely for inherent differences in scanner performance. Moreover, an overall harmonization

between different scanners is seen to be possible through a choice of reconstruction parameters that may include a post-filtering procedure, although it may not provide the same agreement for all sized spheres or for all clinical metrics. To illustrate the complexity of the harmonization effort, Figure 6.5 shows curves of CRC_{max} for many scanner makes and models using standard scanner reconstruction parameters, along with the average CRC curve; the distance of the individual CRC curves to the average CRC curve is minimized in the effort to achieve harmonization.

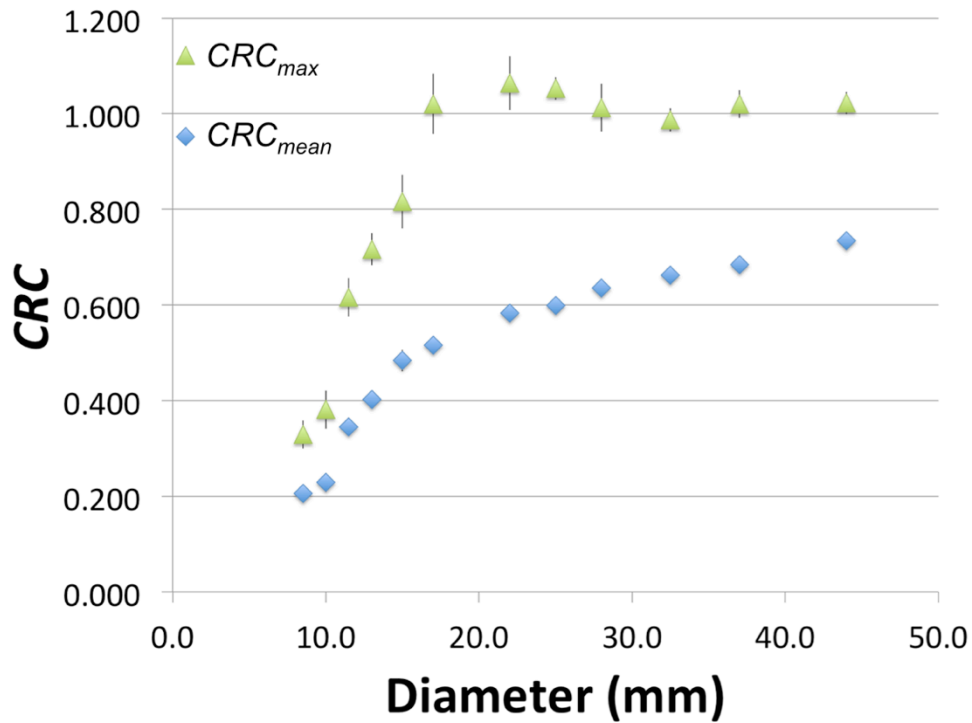
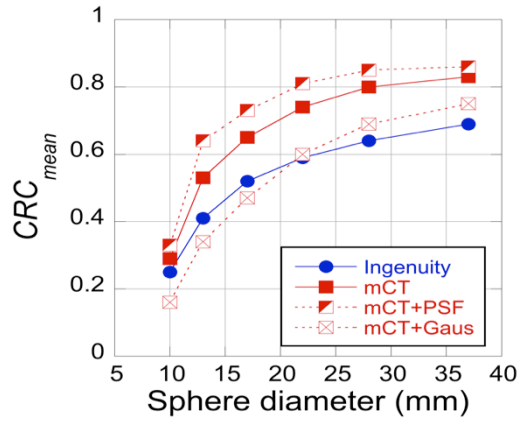


Figure 6.3: Curves of CRC_{mean} and CRC_{max} versus sphere diameter for the NEMA IQ phantom scanned on the Ingenuity TF. One acquisition included the standard NEMA sphere sizes (10, 13, 17, 22, 28, and 37 mm); a second acquisition used the intermediate-sized spheres (8.5, 11.5, 15, 25, 32, and 44 mm). There were 10 replicate studies of 3min for each acquisition, and the sphere/background activity ratio was 9.7:1. The error bars are the standard deviations over the 10 replicate studies.

A.



B.

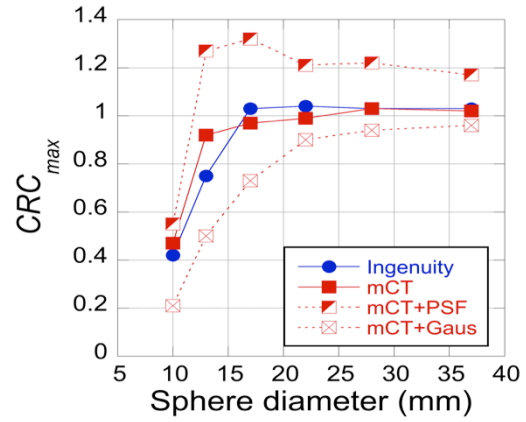


Figure 6.4: Comparison of (A) CRC_{mean} and (B) CRC_{max} values as a function of sphere size for NEMA IQ phantom data on the Siemens mCT and Philips Ingenuity TF scanners. The Siemens mCT data were reconstructed without and with PSF modeling; the data without PSF modeling were also post-filtered with a 4-mm Gaussian to better harmonize the CRC_{mean} results with those from the Ingenuity.

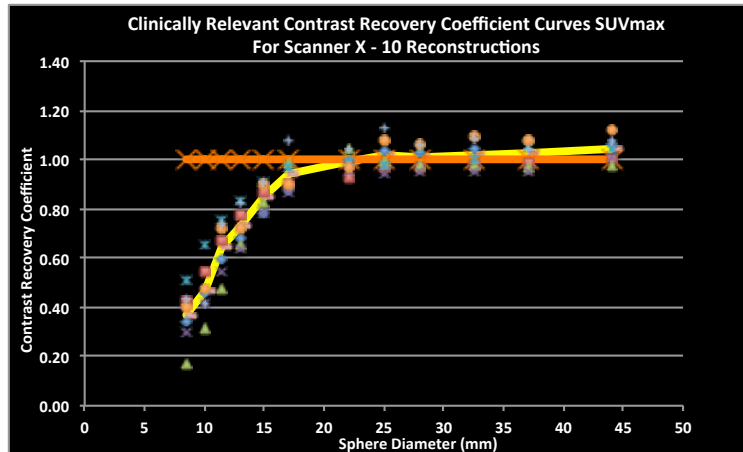


Figure 6.5: Curves of CRC_{max} collected for the Harmonization Initiative for several makes and models of PET scanners, before harmonization. The average value of the CRC curves (solid yellow curve) and the ideal CRC curve (i.e., $y=1$) (solid orange line) are given as well. (Adapted from: [177]).

6.2 Materials and Methods

6.2.1 Phantom Studies

The phantom used was the NEMA IQ phantom, and the filling and acquisition protocol prescribed by the NCI Harmonization Initiative were used. The phantom was filled with $\sim 20\text{MBq}$ of ^{18}F in the background. The standard set of glass-walled spheres from the NEMA IQ study (diameters: 10, 13, 17, 22, 28, and 37 mm) were all filled with activity at a sphere:background ratio of 9.7:1, as prescribed by the NCI harmonization protocol. While the NCI Harmonization Initiative calls for plastic-walled spheres, we have measured no appreciable difference in contrast recovery results with the different wall materials. For this project, we focus only on the 10-, 17-, and 28-mm diameter spheres for later comparison with patient data. The phantom data were acquired in list-mode for ten 3-min acquisitions. For this study, one of the 3-min scans was used in the lesion embedding studies for comparison with subject data, while the ten 3-min scans on the Ingenuity TF were merged to form a 30-min dataset for validation of the lesion embedding technique.

6.2.2 Scanners and Reconstruction Algorithm

Two scanners were used for the comparison of the phantom and human subject studies in this investigation: the Philips Ingenuity TF and a prototype time-of-flight (TOF) scanner developed at the University of Pennsylvania, LaPET [16, 188]. These scanners were chosen because they use a common framework for generating list-mode data, thereby enabling the same methodology of lesion embedding to be applied. Their intrinsic performance characteristics also differ sufficiently to result in different CRC

performance. The Ingenuity TF uses $4 \times 4 \times 22\text{-mm}^3$ lutetium oxyorthosilicate (LYSO) pixels and has a spatial resolution of 4.9mm at a radial offset of 1cm, an energy resolution of 11.6%, and an intrinsic timing resolution of 495ps. LaPET uses $4 \times 4 \times 30\text{-mm}^3$ LaBr_3 crystals with a modified electronics design and has a measured spatial resolution of 5.8mm, an energy resolution of 7%, and an intrinsic timing resolution of 375ps. To control the reconstruction of the data sets, data from both scanners were reconstructed using an off-line list-mode TOF OSEM algorithm without resolution modeling, using 5 iterations with 25 chronological subsets, which approximates the clinical reconstruction protocol on the Ingenuity TF. The same reconstruction parameters (“default reconstruction”) were deliberately chosen rather than separately optimizing the reconstruction for the two scanners, so differences in performance between the systems and the need for harmonization would be evident. All corrections for physical effects (e.g., scatter, attenuation, randoms) were applied during reconstruction. All images were reconstructed using blob basis functions and interpolated to 2-mm voxels in the final image.

6.2.3 Lesion Embedding Technique

Embedding lesions of known uptake into subject data allows for quantification of lesion uptake under clinical conditions, since the ground truth is known. The lesion embedding technique [77-78, 189] involves scanning spheres filled with ^{18}F in air at known locations in the field-of-view of the scanner. List-mode events from a particular sphere are randomly interspersed with the subject’s list-mode data to create a fused data set, with the number of added events chosen to achieve a desired activity ratio, where this

calculation takes into account events already present in the subject's background in the region of the sphere, as well as geometric factors related to the specific location of the sphere. The number of added events to insert a lesion of known uptake ratio relative to the local background may be described by:

$$N^+ = (a_o * B_{LB} * V_{sph} - B_{LB}) * V_{sph} * \left(\frac{N_{list}}{A_{tot}}\right),$$

where N^+ is the number of sphere events to be added, a_o is the desired uptake ratio (e.g., ~10:1), B_{LB} is the local background of the patient in the volume where the spheres are to be inserted, V_{sph} is the volume of the sphere to be inserted, and N_{list} and A_{tot} are the number of list events and total activity, respectively, in the entire sphere data set; the factor of $\left(\frac{N_{list}}{A_{tot}}\right)$ corrects for the geometric factors as a function of sphere position.

In order to include the effects of attenuation by the subject that were not present during the sphere-in-air acquisition, events from the sphere's list-mode data are randomly removed according to the probability of attenuation along the line of response of each event prior to merging the datasets, using the subject's attenuation sinogram. The resulting number of sphere events approximates that which would have been detected from a lesion inside the subject. The lesion-embedding technique implicitly includes partial volume blurring of the sphere as well as spill-in of activity from the neighboring background of the subject into the region of the sphere.

Because sphere data are collected in air, events from the spheres could not scatter outside the sphere (e.g., in the phantom/patient background). Since the embedded sphere events accounted for <1% of the total events in the merged datasets, no attempt is made to model the very small additional scatter that would have been introduced if the lesion

had been present in the subject. Data with embedded lesions are therefore corrected using the same scatter and randoms corrections as the original data without lesions.

The lesion embedding algorithm was updated from previous versions to compensate for self-attenuation of the sphere filled with water, which impacts the calculation of the number of sphere events to embed. While this effect is small for the 10-mm lesions used in previous studies, self-attenuation within larger spheres is non-negligible. Reconstructing spheres with attenuation correction leads to an average change in the reconstructed sphere image counts and a corresponding reduction in the number of sphere events to be embedded of 3.7%, 9.1%, and 17%, compared to reconstructing without attenuation, for the 10-, 17-, and 28-mm spheres, respectively.

For this study, data were collected with three spheres that were identical to those used in the NEMA IQ measurement, with diameters of 10, 17, and 28mm, spanning a range of sphere sizes where the curves of CRC vs. sphere diameter change most rapidly (Fig. 6.3). The spheres were filled with ^{18}F and scanned on each scanner, with 10 million events per position collected (acquisitions were ~30s) to ensure that a sufficient number of events were collected to allow for lesions to be embedded at the desired activity ratio with respect to background. Approximately 50 positions per sphere were collected on each scanner, with each position separated from the others by at least 3cm center-to-center to avoid overlap.

The lesion insertion methodology was tested on the Ingenuity TF using the summed 30-min scan of the NEMA IQ phantom. The longer scan duration was chosen to minimize variability in the results caused by statistical noise, so any discrepancies between embedded spheres and those measured in the phantom could be discerned. This

measurement was repeated on three separate days to determine the uncertainty of the measurement including all sources of measurement error, including those due to human error. Eight spheres of each of the three sizes were embedded into the background region of one of the 30-min phantom scans, in locations that did not overlap with the NEMA spheres. To avoid overlap between the embedded lesions, separate fused phantom data sets were created for each sphere size. Because the spheres measured in the phantom (“measured spheres”) have a cold wall (thickness = 1mm) that reduces the spill-in of activity from the background into the volumes of interest [190], while embedded lesions do not displace background activity and are thus wall-less, a numerical correction was performed on the measured sphere results to account for the cold wall. The correction factors for volumes of interest (VOIs) with diameters equal to the inner diameter of the spheres ranged from 1.01 for the 28-mm sphere to 1.06 for the 10-mm sphere, which has a larger ratio of surface area to volume inside the sphere and thus shows a greater effect of the cold wall on VOI results. The cold wall correction was applied to all measured sphere CRC_{mean} results; a cold wall correction was not applied to CRC_{max} results, since the location of the voxel with maximum uptake relative to the center of the sphere is not known (i.e., the maximum voxel is not necessarily at the exact center of the sphere). The CRC values for the embedded lesions were then compared to the average corrected CRC values of the measured spheres in the phantom. A similar comparison was performed for the LaPET scanner, although only a single 3-min phantom study was available.

6.2.4 Clinical Metrics

The CRC was used in this study as a proxy for the SUV used clinically, as other groups have done [77, 189]. CRC is the metric used in the NCI harmonization project, defined by NEMA [67] as in eq. 1.6. In this study, S was chosen to be equal to the average voxel value within the lesion, calculated using a VOI of the same diameter as the lesion (the measured inner diameter of the sphere) and centered over each lesion (for CRC_{mean}), or to the maximum value within the VOI (for CRC_{max}). B_{local} was calculated for each sphere by averaging the voxel value of the same (single) VOI as that used to calculate S for CRC_{mean} but drawn on the phantom or subject image without lesions embedded. Unlike clinical studies, in this work we know the true size and uptake of the lesions. Mean, maximum, and peak values of CRC were determined; because the 1-cm^3 VOI is larger than a 10-mm sphere, CRC_{peak} was not calculated for the 10-mm spheres.

6.2.5 Subject Studies

Whole-body data were acquired for four subjects on each scanner using ~ 550 MBq of [^{18}F]-FDG (3 min / bed position); scanning was performed 60 min post-injection for the Ingenuity TF subjects and ~ 100 min post-injection for the LaPET subjects, which were acquired sequentially following a clinical scan on a different system. Since this study used lesion-free patient data and looked only at lesions embedded at a known uptake with respect to the local background, the variation in post-injection time has little impact on the results. The Ingenuity TF subject data were obtained retrospectively and were anonymized before being included in this study. The LaPET subject studies were performed as part of a research study [77]; the institutional review board of the University

of Pennsylvania approved this study, and all subjects signed a written informed consent before the study. The four subjects had values of body mass index(BMI) ranging from 25-38 (Ingenuity TF) and 25-36 (LaPET) and were free of any lung or liver lesions; different subjects were scanned on the two systems. For the Ingenuity TF scanner, the transmission image was derived from a low-dose CT scan. For the LaPET scanner, a transmission image acquired using a rotating ^{137}Cs point source was used for attenuation correction [191].

For each subject, 3-8 lesions of each size were embedded into both the right lung and liver background regions. Lesions were added such that no two lesions overlapped on the same image. The range in number of lesions used reflects the fact that the larger lesions could not always fit in the same, non-overlapping places as the smaller lesions, and organ sizes varied among the subjects. Lesions were embedded at a constant ratio of lesion uptake to local background (a_0) of 9.7:1 to achieve constant CRC. To reduce the statistical variability of the LaPET results, which had fewer spheres measured at locations that overlapped with the subjects' lung and liver regions, five different sets of events for each sphere location were embedded in the lung and liver, and the results averaged. The CRC values were then averaged over all lesion locations in all four subjects for each organ studied (lung and liver).

6.2.6 Effect of Post-filtering on Phantom and Subject Measurements

Harmonization of scanners may be performed using post-filters on one or both of the scanners to achieve agreement between the curves of CRC vs. sphere size for the scanners. The post-filters were first applied to phantom and subject data from the

Ingenuity TF to assess how well subject and phantom results track. Two post-filtering methods were investigated for this study. (1) To decrease the CRC of the lesions, a Gaussian post-filter, as has been used in previous investigations [176-177], was applied; for this study, the post-filter was applied to the images using MATLAB. Two Gaussian filters with a full-width at half-maximum (FWHM) of 4mm and 6mm were used. These filter widths were found to provide the degree of change needed to harmonize CRC_{mean} results from the Ingenuity TF with those from the LaPET scanner, as described below. (2) The CRC of the lesions was also increased using a Lucy-Richardson (LR) deconvolution post-filter; for this study, one iteration was used with a 6-mm sieve blur; these were determined empirically based on the favorable compromise between the improvement in resolution and noise. While the LR filter was not applied to the Ingenuity TF data during harmonization to the LaPET (next section), LR post-filtering is the method of resolution modeling available on the Ingenuity TF and was used here to study how well the subject and patient data tracked for both image blurring and sharpening. The changes in measured CRC with these post-filters relative to no post-filtering were compared between phantom and subjects to determine how well the phantom and subject results tracked. A similar analysis was performed separately for the LaPET data for the LR filter.

6.2.7 Harmonization of Scanners

Harmonization of the CRC values of the Ingenuity TF and LaPET scanners was accomplished with phantom scans by applying various post-filters to the images from both scanners, using a Gaussian filter to systematically reduce CRC and the LR post-filter to increase CRC. No standard metric yet exists to characterize how different (or

harmonized) scanners are; the root mean squared percent difference (RMS_{pd}) over the 3 lesion sizes between the CRC values was used in this study as a metric to characterize the overall difference between the scanners. The RMS_{pd} conceptually acts in a similar way to a least squares harmonization performed on the entire CRC vs. diameter curves (e.g., as in [174]), but this metric measures the relative differences in CRC, unlike the least squares difference, which measures absolute differences in CRC. The percent difference of CRC values between the scanners for a given sphere size i ($\% \text{diff}(i)$) was defined as

$$\% \text{diff}(i) = \frac{\text{CRC}_1 - \text{CRC}_2}{(\text{CRC}_1 + \text{CRC}_2)/2} * 100 \quad (6.1)$$

where the CRC values were averages over all spheres of a given diameter for each scanner. For this study, subscript 1 refers to the Ingenuity TF, and subscript 2 refers to the LaPET system. The RMS_{pd} of the CRC values was calculated over the 3 sphere sizes as

$$\text{RMS}_{\text{pd}} = \sqrt{\frac{1}{3} \sum_{i=1}^3 \% \text{diff}(i)^2}. \quad (6.2)$$

Because the optimal harmonization strategy will depend on the imaging situation (e.g., several different scanners at one institution, the same scanner model at multiple sites, or multiple different scanners at different sites), three harmonization strategies were studied, two based on minimizing the differences between the CRC_{mean} values and one chosen to minimize the differences between CRC_{max} values of the three spheres. One of these strategies used only Gaussian post-filtering on one scanner, while the other two strategies used a hybrid approach of LR post-filtering on one system with Gaussian post-filtering on the other. Several strategies were chosen, since it may not be possible to harmonize both metrics simultaneously for certain combinations of scanners using a

single strategy given that the curves of CRC_{mean} and CRC_{max} as a function of diameter can have different shapes, as seen in Figure 6.4. The strategies were as follows: (1) The LaPET images had no post-filtering applied, while the CRC values for the Ingenuity TF were decreased using a 6-mm FWHM Gaussian post-filter applied to the reconstructed images; the 6-mm width was empirically determined to be optimal by filtering with a range of Gaussian filters to minimize the RMS_{pd} between the CRC_{mean} values measured in the phantom on the two scanners. (2) The CRC values for the LaPET scanner were increased using the LR post-filter with 1 iteration and a 6-mm sieve blur, while the CRC values of the Ingenuity TF were simultaneously decreased using a 4-mm FWHM Gaussian post-filter that was determined empirically to minimize the RMS_{pd} of the CRC_{mean} values between the Ingenuity TF scanner and LaPET system with LR filtering, since the LR post-filter alone provided suboptimal harmonization. (3) The CRC values for the LaPET scanner were increased using the LR post-filter, as in strategy 2, while the CRC values of the Ingenuity TF were simultaneously decreased using a 2.5-mm FWHM Gaussian post-filter that was determined empirically to minimize the RMS_{pd} of the CRC_{max} values between the Ingenuity TF scanner and LaPET system with LR filtering. The same filters were then applied to the subject scans.

6.3 Results

6.3.1 Measured vs. Embedded Spheres in Phantom

Table 6.1 shows a comparison of CRC_{mean} and CRC_{max} values for the measured spheres and embedded lesions in the NEMA IQ phantom for the 30-min scans on the Ingenuity TF scanner. Table 6.2 shows a similar comparison for a single 3-min scan on

the LaPET scanner. The uncertainties of the embedded lesion CRC values were calculated as the standard error of the mean (SEM) of the 8 embedded lesion values. The individual results for the three replicates of measured spheres on the Ingenuity TF are shown in parentheses in Table 6.1 rather than calculating the SEM because of the limited number of measurements. Based on the agreement between the measured and embedded CRC values, particularly for the 17- and 28-mm spheres, and the reduced variability seen for the embedded lesions compared with the variability of the measured spheres, lesions embedded in the phantom were used for the remainder of this work in the comparisons with the subject data.

Table 6.1: Comparison of CRC_{mean} (top) and CRC_{max} (bottom) on the Ingenuity TF scanner for measured spheres and lesions embedded into the NEMA IQ phantom.

	10 mm	17 mm	28 mm
CRC_{mean}			
Measured	0.35 (0.41, 0.33, 0.31) ^a	0.58 (0.58, 0.59, 0.58)	0.69 (0.68, 0.68, 0.70)
Embedded	0.390 ± 0.005^b	0.59 ± 0.01	0.684 ± 0.003
CRC_{max}			
Measured	0.64 (0.78, 0.58, 0.56)	0.95 (0.96, 0.94, 0.95)	1.00 (0.96, 1.00, 1.04)
Embedded	0.69 ± 0.01	1.00 ± 0.02	1.02 ± 0.01

^a Results are shown in parentheses for the 3 separate phantom measurements.

^b Uncertainties shown are the standard error of the measurement (SEM) of the 8 embedded lesion values.

Table 6.2: Comparison of CRC_{mean} (top) and CRC_{max} (bottom) on the LaPET scanner for measured spheres and lesions embedded into the NEMA IQ phantom.

	10 mm	17 mm	28 mm
CRC_{mean}			
Measured	0.25	0.45	0.58
Embedded	0.253 ± 0.003^a	0.446 ± 0.002	0.58 ± 0.01
CRC_{max}			
Measured	0.46	0.84	1.01
Embedded	0.43 ± 0.02	0.81 ± 0.02	0.99 ± 0.03

^a Uncertainties shown are the SEMs of the 8 embedded lesion values.

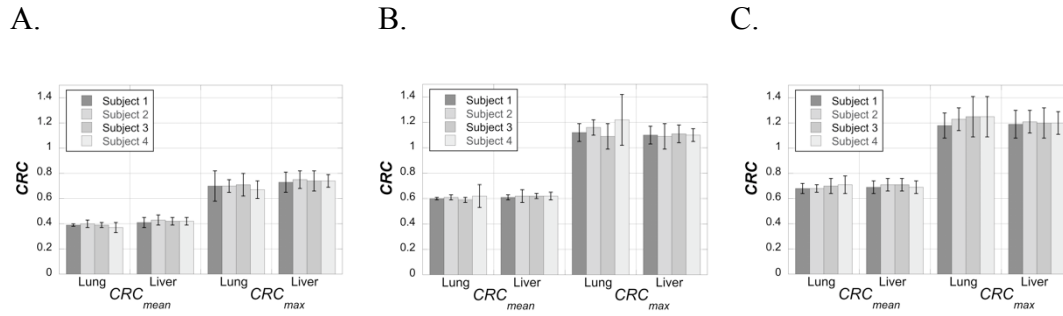


Figure 6.6: Average CRC_{mean} and CRC_{max} values for (A) 10-mm, (B) 17-mm, and (C) 28-mm lung and liver lesions for each of the patients on the Ingenuity TF. 8-16 lesions were embedded in each subject's lung and liver for a total of 34 and 55 lesions in the lung and liver, respectively, in all subjects. The error bars are the standard deviations over the lesions in each patient and organ. The BMI values for subjects 1-4 were 25, 28, 28, and 38 kg/m^2 , respectively.

6.3.2 Embedded Spheres in Phantom vs. Subjects

Figure 6.6 shows the average CRC_{mean} and CRC_{max} values for the 10-, 17-, and 28-mm lung and liver lesions in each of the patients on the Ingenuity TF. The results demonstrate that the CRC values do not vary significantly among the patients. The average CRC (both mean and maximum values) for each subject were within 10% of the overall average values over all 4 subjects for all sphere sizes. For that reason, the subject results were averaged over all subjects and all lesions in each organ in the rest of the study. Table 6.3 shows the CRC_{mean} and CRC_{max} values for the embedded lesions in the 3-min phantom scan and the subjects' lung and liver regions for the Ingenuity TF and LaPET scanners without any post-filtering. Results shown for the lung and liver regions are averages over all of the lesions of a given size in the four subjects. The uncertainties listed in Table 6.3 are the SEMs of the lesion values (8 lesions embedded in the phantom and a total of 24-34 lesions in the lung and 49-57 lesions in the liver for the Ingenuity TF and 12-14 lesions in the lung and 15-20 lesions in the liver for the LaPET). The average CRC_{mean} values of lesions embedded in the lung and liver were well correlated with those for the lesions of the same size in the phantom; all values for lesions in the lung and liver were within 5% for the Ingenuity TF (range: -2.5% to 5.0%) of the respective phantom values and 5% for the LaPET (range: -4.4% to 0.0%). The percent differences of the average CRC_{max} values for lesions embedded in the lung and liver were also within 5% of those in the phantom for the Ingenuity TF (range: -1.4% to 4.2%) and ~6% for the LaPET (range: 2.3% to 6.1%). There was no systematic correlation in the difference between phantom and subject results with sphere size.

Table 6.3: Comparison of CRC_{mean} and CRC_{max} on the Ingenuity TF (top) and LaPET (bottom) scanners without post-filtering for lesions embedded in the phantom and lung and liver regions in the subjects.

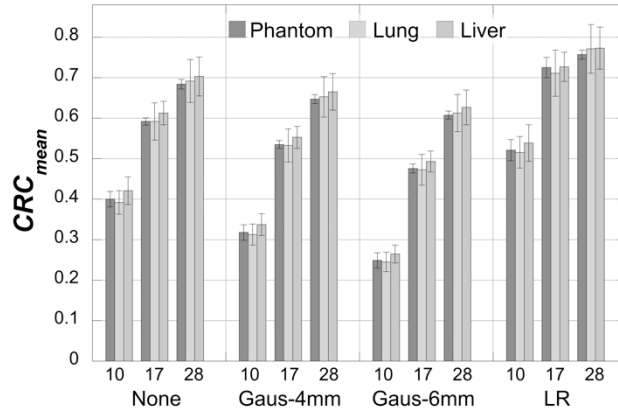
	CRC_{mean}			CRC_{max}		
	10 mm	17 mm	28 mm	10 mm	17 mm	28 mm
Ingenuity TF:						
Phantom	0.40 ± 0.007^a	0.59 ± 0.003	0.68 ± 0.004	0.71 ± 0.02	1.07 ± 0.01	1.18 ± 0.02
Lung	0.39 ± 0.005	0.59 ± 0.009	0.69 ± 0.009	0.70 ± 0.01	1.12 ± 0.02	1.23 ± 0.02
Liver	0.42 ± 0.005	0.61 ± 0.004	0.70 ± 0.006	0.74 ± 0.01	1.10 ± 0.01	1.20 ± 0.01
LaPET:						
Phantom	0.25 ± 0.003	0.45 ± 0.002	0.58 ± 0.01	0.43 ± 0.02	0.81 ± 0.02	0.99 ± 0.03
Lung	0.24 ± 0.003	0.43 ± 0.005	0.56 ± 0.01	0.44 ± 0.01	0.85 ± 0.02	1.05 ± 0.01
Liver	0.25 ± 0.007	0.45 ± 0.007	0.58 ± 0.01	0.45 ± 0.01	0.83 ± 0.02	1.05 ± 0.02

^a Uncertainties shown are the SEMs of the lesion values.

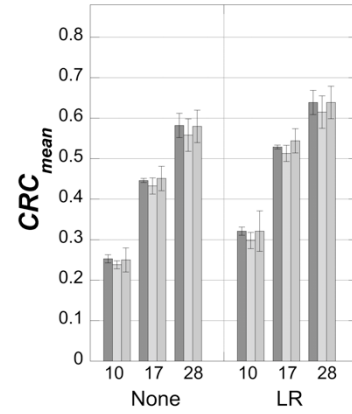
6.3.3 Effect of Post-filtering on Phantom and Subject Measurements

Figure 6.7 (left) shows the average CRC_{mean} and CRC_{max} values on the Ingenuity TF for the phantom and lung and liver regions without any post-filter and after application of 4-mm Gaussian, 6-mm Gaussian, and LR post-filters; the percent changes in these values with respect to the results without post-filtering (Table 6.3) are listed in Table 6.4. Results are also shown in Figure 6.7 (right) for the LaPET scanner without post-filtering and with the LR post-filter, with the corresponding percent changes listed in Table 6.4. The uncertainties shown in the table were determined by error propagation of the SEMs of the CRC values with and without post-filtering. Differences between the changes with post-filtering for lesions embedded in the phantom and those in the subjects are within measurement uncertainty. However, the relative impact of the filters on the CRC metrics is dependent on the size of the lesion, as expected.

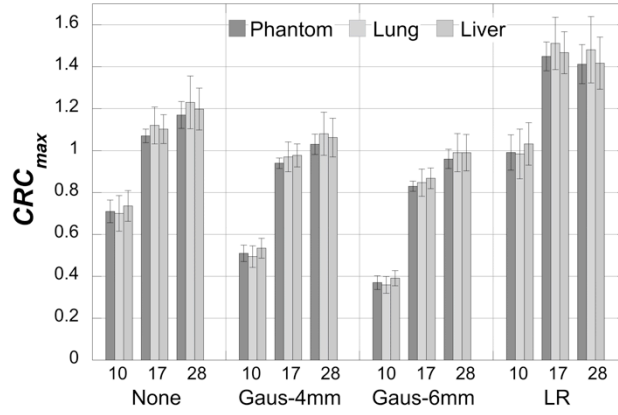
A.



B.



C.



D.

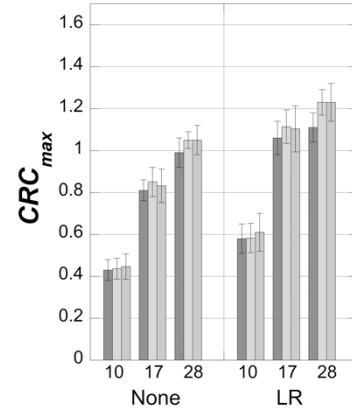


Figure 6.7: Comparison of average (top) CRC_{mean} and (bottom) CRC_{max} values for 10-, 17-, and 28-mm lesions before and after application of various post-filters on the (left) Ingenuity TF and (right) LaPET scanners for the lesions embedded in the phantom and lung and liver regions in the subjects. The post-filters on the Ingenuity TF included 4-mm FWHM Gaussian, 6-mm FWHM Gaussian, and Lucy-Richardson (LR) deconvolution post-filters; only the LR post-filter was applied to LaPET images. The results shown are averages over multiple lesions embedded in the phantom and lung and liver of each subject: 8 lesions in the phantom and 3-8 lesions in each subject's lung and liver; the results for the four subjects were averaged together for these comparisons. Error bars shown are the standard deviations of the measurements.

Table 6.4: Percent change^a in CRC_{mean} and CRC_{max} on the Ingenuity TF scanner after application of various post-filters for lesions embedded in the phantom and lung and liver regions in the subjects. Results are also shown for LR post-filtering on the LaPET scanner.

	CRC _{mean}			CRC _{max}		
	10 mm	17 mm	28 mm	10 mm	17 mm	28 mm
4-mm Gaussian						
Phantom	-21 ± 2 ^b	-10 ± 1	-5 ± 1	-28 ± 3	-12 ± 1	-13 ± 2
Lung	-20 ± 2	-10 ± 2	-6 ± 2	-29 ± 2	-13 ± 2	-12 ± 2
Liver	-20 ± 2	-10 ± 1	-5 ± 1	-27 ± 1	-11 ± 1	-11 ± 2
6-mm Gaussian						
Phantom	-38 ± 2	-20 ± 1	-11 ± 1	-48 ± 3	-22 ± 1	-19 ± 2
Lung	-38 ± 1	-20 ± 2	-11 ± 2	-49 ± 2	-24 ± 2	-19 ± 2
Liver	-37 ± 1	-20 ± 1	-11 ± 1	-47 ± 1	-21 ± 1	-17 ± 1
Lucy-Richardson						
Phantom	29 ± 3	19 ± 1	10 ± 1	39 ± 5	33 ± 2	18 ± 3
Lung	32 ± 3	20 ± 4	11 ± 2	41 ± 4	35 ± 3	20 ± 3
Liver	30 ± 3	19 ± 1	10 ± 1	40 ± 2	33 ± 2	18 ± 2
Lucy-Richardson (LaPET)						
Phantom	27 ± 3	19 ± 1	10 ± 3	35 ± 10	31 ± 6	12 ± 4
Lung	25 ± 3	18 ± 2	10 ± 3	33 ± 6	31 ± 4	17 ± 2
Liver	28 ± 6	21 ± 2	10 ± 3	37 ± 6	33 ± 4	18 ± 3

^a The percent changes were calculated for the values shown in Figure 6.7 with respect to the corresponding values without filtering (Table 6.3).

^b Uncertainties shown were determined by error propagation of the SEMs of the CRC values with and without post-filtering.

6.3.4 Harmonization of Scanners

Figure 6.8 shows CRC_{mean}, CRC_{peak}, and CRC_{max} values for the different sphere sizes in the phantom for the Ingenuity TF and LaPET scanners with the default reconstruction for each scanner and for the harmonization strategies described earlier. Tables 6.5 and 6.6 show the percent differences between CRC_{mean} and CRC_{max} values,

respectively, for lesions in the phantom and subjects for the two scanners before and after harmonization. The uncertainties reported in the tables were determined by error propagation of the SEMs of the CRC measurements for the multiple lesions in the phantom, lung, and liver of the 4 subjects on the two scanners. The RMS_{pd} of the CRC_{mean} values for lesions in the phantom and in the lung and liver exceeded 30% before harmonization. Using strategy 1, the RMS_{pd} values for CRC_{mean} were reduced to <8% for both the phantom and subjects; with strategy 2, the RMS_{pd} values for CRC_{mean} were reduced to <5%. The corresponding harmonization of the CRC_{max} values was not as good, with RMS_{pd} reduced from >30% to only <12% with strategy 1 and <15% with strategy 2, although the results are consistent between phantom and subject measurements. Using strategy 3, which was based on harmonization of CRC_{max} values from the phantom measurements, the RMS_{pd} of CRC_{max} was reduced to <6% in the subject data, with the corresponding RMS_{pd} of CRC_{mean} reduced to <14%, demonstrating slightly more variation between phantom and patient measurements, especially for the 10-mm sphere.

6.4 Discussion

The average CRC_{mean} values for the lesions embedded in the phantom on the Ingenuity TF (Table 6.1) were within 1.7% (range: -0.9% to 1.7%) of those for the measured spheres in the phantom for the 17- and 28-mm spheres; a larger difference (11.4%) was observed between the embedded and measured 10-mm spheres. Similar results were seen for the LaPET scanner (Table 6.2), although there was only one phantom measurement. The measured results for CRC_{max} on the Ingenuity TF also show

more variation for the smallest 10-mm sphere. We have measured little statistical variation in shorter replicate phantom scans (standard error of the mean over 10 3-min scans: $<3\%$ for CRC_{mean} and $<4\%$ for CRC_{max}); therefore, the larger variability observed in the 30-min scans for the measured 10-mm sphere in Table 6.1 is likely a result of non-statistical or human errors (e.g., small air bubbles during filling), despite our best efforts to carefully fill the spheres for each acquisition. The results illustrate the trade-offs associated with harmonization based on measured uptake in small spheres: small spheres are important to measure differences in CRC related to spatial resolution but are more susceptible to non-statistical errors. The good overall agreement in CRC values between the embedded lesions and the physical spheres and the small variability of CRC values for the embedded lesions in the phantom demonstrate the utility of the lesion-embedding technique as a proxy for actual lesions in patient studies.

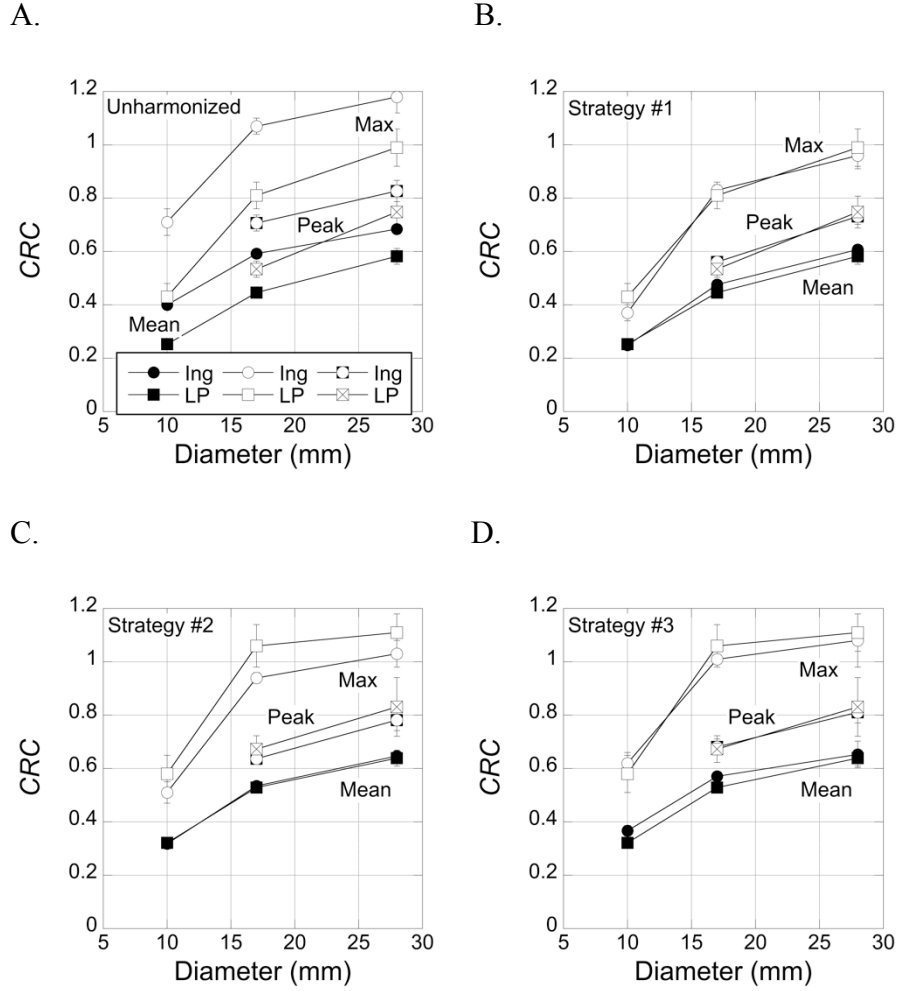


Figure 6.8: Comparison of CRC_{mean} , CRC_{peak} , and CRC_{max} values as a function of sphere diameter for phantoms on the Ingenuity TF and LaPET scanners (A) without harmonization and using (B) harmonization strategy 1 (6-mm Gaussian post-filter applied to the Ingenuity TF), (C) harmonization strategy 2 (4-mm Gaussian post-filter applied to the Ingenuity TF and LR deconvolution post-filter applied to LaPET), and (D) harmonization strategy 3 (2.5-mm Gaussian post-filter applied to the Ingenuity TF and LR deconvolution post-filter applied to LaPET). Error bars shown are the standard deviations of the measurements.

Table 6.5: Percent differences^a between CRC_{mean} on the Ingenuity TF and LaPET scanners for lesions embedded in the phantom and lung and liver regions in the subjects before and after harmonization.

Unharmonized	10 mm	17 mm	28 mm	RMS _{pd} (%)
Phantom	-45 ± 2	-28 ± 1	-16 ± 2	32
Lung	-49 ± 2	-31 ± 2	-21 ± 2	36
Liver	-51 ± 3	-30 ± 2	-19 ± 2	36
Strategy #1				
Phantom	1 ± 3 ^b	-6 ± 1	-4 ± 2	5
Lung	-3 ± 2	-9 ± 2	-9 ± 2	8
Liver	-6 ± 3	-9 ± 2	-8 ± 2	8
Strategy #2				
Phantom	1 ± 3	-1 ± 1	-1 ± 2	1
Lung	-5 ± 2	-4 ± 2	-6 ± 2	5
Liver	-5 ± 3	-2 ± 1	-4 ± 2	4
Strategy #3				
Phantom	-13 ± 2	-8 ± 1	-2 ± 3	9
Lung	-19 ± 2	-11 ± 2	-10 ± 2	14
Liver	-19 ± 3	-8 ± 1	-8 ± 2	13

^a % Difference was calculated using equation (6.1).

^b Uncertainties shown were determined by error propagation of the SEMs of the CRC values for the two scanners.

Table 6.6: Percent differences^a between CRC_{max} on the Ingenuity TF and LaPET scanners for lesions embedded in the phantom and lung and liver regions in the subjects before and after harmonization.

Unharmonized	10 mm	17 mm	28 mm	$RMS_{pd} (\%)$
Phantom	-48 ± 5^b	-27 ± 3	-18 ± 3	34
Lung	-46 ± 4	-28 ± 3	-16 ± 2	32
Liver	-49 ± 3	-28 ± 2	-14 ± 2	33
Strategy #1				
Phantom	16 ± 6	-2 ± 3	3 ± 3	9
Lung	20 ± 4	0 ± 3	6 ± 2	12
Liver	13 ± 3	-4 ± 2	5 ± 2	9
Strategy #2				
Phantom	14 ± 6	12 ± 3	7 ± 3	11
Lung	17 ± 4	14 ± 3	13 ± 2	15
Liver	13 ± 4	12 ± 2	15 ± 2	13
Strategy #3				
Phantom	-6 ± 6	5 ± 3	2 ± 4	5
Lung	-4 ± 4	5 ± 3	6 ± 2	5
Liver	-6 ± 3	5 ± 2	8 ± 2	6

^a % Difference was calculated using equation (6.1).

^b Uncertainties shown were determined by error propagation of the SEMs of the CRC values for the two scanners.

Figure 6.6 indicates that CRC is consistent across subjects and also shows that CRC is relatively insensitive to differences in background uptake (i.e., lung vs. liver). The lack of inter-subject variation supports our treatment of the lesions in all subjects as a single ensemble for each organ. As seen in Table 6.3, CRC_{mean} values for the lung and liver for all lesion sizes were within 5% of the values for lesions embedded in the phantom for both scanners, indicating that phantom CRC values with cold wall correction represent patient CRC values well. In addition, the variability of CRC values for lesions embedded in all subjects is of similar magnitude as that observed in the phantom for all sphere sizes. Figure 6.7 and Table 6.4 show that all post-filters studied led to changes in CRC_{mean} and CRC_{max} that were consistent across the phantom and subject organs and indicate that phantom measurements can predict the effect of post-filters (e.g., as may be

utilized for harmonization) on patient CRC measurements. In addition, application of the LR post-filter on the two scanners led to consistent changes in uptake measurement, especially for CRC_{mean} . This result is further supported by the results of harmonization between the Ingenuity TF and LaPET scanners in Figure 6.8, and Tables 6.5 and 6.6. Both the CRC metrics and quantitative techniques studied, therefore, are seen to generally translate well from phantom studies to patient studies for the two background regions studied.

The Ingenuity TF has systematically higher CRC values than the LaPET scanner using the unharmonized reconstruction. This is due primarily to the better spatial resolution of the Ingenuity (4.9mm vs. 5.8mm), illustrating the effect of improved detector resolution; the better TOF resolution of the LaPET scanner (375ps vs. 495ps) has little effect on the CRC and more impact on the precision of the measurement, not explicitly measured in this study. The approach demonstrated in this work for two systems with different spatial and TOF resolutions is general, however, and the results will apply to other scanners, including future generation systems with better spatial and/or TOF resolution. While the deconvolution filter studied here did not degrade the precision of the metrics studied, deconvolution operators in general are associated with an increase in noise, as noted earlier, resulting in trade-offs in accuracy and precision that limit the extent to which they can be applied.

Both strategies 1 and 3 resulted in good harmonization of both CRC_{mean} and CRC_{max} between the two scanners; strategy 2 resulted in the closest harmonization of CRC_{mean} but poorer harmonization of CRC_{max} . For CRC_{peak} , the results after harmonization using the three strategies were in between those for CRC_{mean} and CRC_{max} ,

with strategy 2 showing the poorest harmonization. Although the particular strategies chosen to harmonize CRC_{mean} for the scanners did not lead to perfect harmonization of all CRC values between the two systems, especially CRC_{max} , they nonetheless tracked well between phantom and subjects over the range of sphere sizes studied. The strategy selected to harmonize CRC_{max} (strategy 3) similarly resulted in suboptimal harmonization of CRC_{mean} values while the phantom and subjects tracked well. The results for CRC_{peak} also tracked well between the phantom and subjects (not shown).

The ability to harmonize two scanners depends on a number of factors, including the dependence of measured CRC on sphere diameter [177]. Application of the post-filters to images from the two scanners significantly reduced differences between the two CRC curves, as measured by the RMS_{pd} , although the differences for the 10-mm CRC_{mean} values were not as close for the phantom, lung, and liver lesions. These results indicate that optimal harmonization over a range of lesion sizes (10-28 mm) can be difficult to achieve. In addition, none of the strategies chosen completely harmonized CRC_{mean} , CRC_{peak} , and CRC_{max} metrics together. Although the RMS_{pd} values for CRC_{mean} and CRC_{max} were reduced with all strategies studied, different strategies led to better agreement (lower RMS_{pd}), depending on which metric was used for harmonization. This result suggests that harmonization should be done using the clinical metric of interest (i.e., maximum vs. peak vs. mean uptake value).

Figure 6.8 also shows the impact of harmonization on the accuracy of the uptake measured in the phantom. While harmonization strategy 1 led to better agreement of CRC_{mean} between the two scanners, the CRC_{mean} values of the Ingenuity TF dropped by 38, 20, and 11% for the 10-, 17-, and 28-mm spheres, respectively. Strategies 2 and 3

used Lucy-Richardson deconvolution post-filtering of the LaPET data, so those values increased (+35% for CRC_{mean} of the 10-mm sphere) with a decrease (28% for the 10-mm sphere) in the Ingenuity TF values, due to the use of a Gaussian post-filter. These results show that caution is needed in developing harmonization strategies, since scanner harmonization can be achieved in many ways but with different effects on bias. In addition, different harmonization strategies will also influence the precision of uptake measurements (not studied in this work), and both accuracy and precision will play a role in determining the optimal harmonization strategies.

While only a single activity ratio was used in this study, phantom studies with different activity ratios have shown only small differences in CRC values, and using a different activity ratio would not have affected the choices of strategies for harmonization or the resultant comparisons made in this study between phantom and subject data. Embedded lesions were placed in both the lung and liver organs in multiple patients, since multiple lesions could reliably be placed in these organs and these two organs represent different background environments. No systematic differences between lung and liver results were observed and the results are expected to be representative of lesions in other organs. The variability of the measured sphere results in the phantom, particularly for the 10-mm sphere, indicates that multiple measurements are critical for phantom-based harmonization efforts although many phantom measurements can become impractical.

In this work lesions embedded in subject data were used to demonstrate how well phantom quantitative metrics translate to patient studies. The embedded lesions used as surrogates for clinical lesions differ from actual tumors that may not be spherical and do

not necessarily have uniform uptake. However, this study represents an important first step towards validating the use of phantoms in the development of harmonization strategies, and illustrates the close connection between phantom results and patient results. Furthermore, based on the good agreement between phantom and subject data in this study, no need is seen to perform similar patient studies for future harmonization efforts.

6.5 Conclusions

This study used a lesion embedding technique to insert lesions into a phantom and lung and liver regions of subjects scanned on two TOF-PET scanners to determine the validity of basing scanner harmonization on phantom measurements. The validity of the lesion embedding technique for this study was demonstrated by comparing embedded lesions to measured spheres in a phantom and showed good correlation. The viability of using a phantom to track the expected changes with post-filtering in subjects was also shown. Our results demonstrate that the phantom CRC performance predicts patient CRC performance with and without post-filtering strategies; simultaneously achieving good harmonization (i.e., RMS_{pd} under 5% over a range of lesion sizes) of both the CRC_{mean} and CRC_{max} metrics using the same post-filters, however, was shown to be difficult.

These results support the further development of harmonization protocols using phantom studies as their basis, as they are predictive of clinical performance. The study therefore draws an important connection between the phantom measurements studied in the previous chapter, and allows the conclusions regarding improved detector performance to be extended to quantification in clinical studies. Moreover, this work

highlights the importance of both scanner resolution (and detector resolution) and image reconstruction in determining quantitative performance shown in the previous chapter. Because of the limitations of post-filtering as a means to improve image resolution, improvements in scanner performance are seen to hold important implications in the use of PET for clinical studies. Moreover, the improved performance brought about by the use of improved detectors will lead to interesting new challenges in the overall Harmonization Initiative.

Thesis Summary and Conclusions

This thesis investigated a novel detector model for improved spatial resolution as well as the effect of its potentially improved spatial resolution and position sampling on a clinical quantitative task. It studied the effect of modifying the light spread within continuous detectors in order to improve upon the limitations of poor performance in the entrance region and depth-dependent light spread within the scintillator that result from the use of thick detectors, used to retain good sensitivity. To achieve this, it used laser induced optical barriers to alter the performance of these detectors, and further studied the resulting impact on the quantitative performance of a whole scanner, and connected the improvements measured by objective phantom-based measurements to clinical metrics of interest. The major conclusions from this work are:

1. Continuous crystals offer the potential for improved spatial resolution compared to conventional 4-mm pixelated systems, and offer the benefit of continuous position sampling and DOI information. Nevertheless, they are limited by a depth-dependence in their performance, as well as relatively poor resolution in their entrance region. Statistical positioning algorithms offer vastly improved performance over conventional Anger logic for continuous detectors, although this comes at the cost of increased complexity and time (e.g., two orders of magnitude greater number of computations for the algorithms studied here). Further improvements in the positioning algorithm, by increasing the number of channels, using more complex statistical models, and exploiting more of the calibration information, require even more complexity. This warrants efforts to

alter the fundamental light spread within the detector in order to improve performance.

2. The LIOBs reflect light diffusely, and transmit light both directly and diffusely. Measurements on small cubes that were etched with a variety of laser settings ranged from ~20% to 50% in reflectivity, though the full range of possibilities was not explored. Continuous detectors were successfully etched with a grid of LIOBs that extended partly into the entrance region of the crystals and with a pitch of 2mm; the 25mm thick crystal was also etched with a second set of LIOBs in the central depths of the crystal. Measurements with these crystals were encouraging: etching led to a slight improvement in performance in the etched regions, as desired, and unchanged or slightly degraded performance outside these regions. The depth-dependence of the LRFs was decreased, at the expense of less DOI information. Nevertheless, simulation studies indicated that these LIOBs were not optimized to minimize spatial resolution, and furthermore that varying the laser parameters or etching design results in a compromise between resolution, DOI performance, and position sampling. Specifically, increasing the opacity or depth of the LIOBs results in a further narrowing of the overall light spread, and allows for a fine-tuning of the resolution at the potential cost of discretized position sampling and a loss of DOI information. The laser induced optical barriers are therefore a feasible method to modify the light spread within the detector, and the grid pattern investigated is one option to improving the overall resolution, although further optimization is needed.

3. Simulation studies showed that after including the resolution degrading effects present in a whole-body scanner, the use of 2mm resolution continuous detectors instead of 4mm pixelated detectors results in an improvement in CRC by $\sim 22\%$ and $\sim 19\%$ for sphere sizes of 5.5mm and 10mm, respectively. Improvements in detector resolution therefore result in a measurable improvement in image quality.
4. Studies using the lesion embedding technique with actual patient and phantom data show that the CRC of embedded lesions is equivalent in patient and phantom background regions, and that the effect of post-filters track well between the two. The quantitative results obtained using the simulation studies of the phantom data may therefore be extrapolated to patient studies, showing that improved detector performance indeed leads to improved clinical performance.

There remains work to be done before continuous detectors of any type would be implemented in a clinical scanner. While recent scanners are built with arrays of SiPMs, the electronics in a continuous system would be made more complex by reading out all the channels (or at least a fraction of them using row-column summed readout) prior to applying the positioning algorithm, unless the position is read out in real time (e.g., using an FPGA); the ability to implement the more complex positioning algorithms in real time must then be demonstrated. Additionally, a robust and feasible calibration scheme must be demonstrated on a clinical system, although the demonstration of the use of fan beams will likely prove useful for this (Chapter 3).

The laser induced optical barriers studied in this work are a potential method to improving the performance of continuous detectors and allowing for improved resolution.

LIOBs show great promise because of the precision with which they can be made, the unique characteristics that they offer as a reflector in the bulk of the crystal, and because of the great flexibility they offer in fine-tuning the performance of continuous detectors. While the impact of the scintillation light spread using this technology was demonstrated in this work using this technology both theoretically and on the level of the bench-top, the robustness and cost of this detector on a large scale have yet to be demonstrated. In particular, the reproducibility of continuous crystals grown in mass quantity and of the laser etching process must be investigated.

The specific performance measured for the detectors studied in this work are also a function of the materials used. LYSO was chosen because LSO/LYSO are currently the most popular scintillators used today; however, there are alternative scintillators. LaBr_3 has been a scintillator of interest for some time and is used in the experimental LaPET scanner because of its improved timing resolution and greater ($>2x$) light output. The major disadvantage to this detector is its lower sensitivity, which is particularly important in PET scanners. This requires thicker crystals to compensate, which comes at the cost of increased parallax error and an increased depth-dependence to the light spread. While a continuous crystal could allow for DOI information to be measured, the degradation in spatial resolution with crystal thickness is problematic. Moreover, the advantage of the greater light output when using the statistical positioning algorithms must be weighed against the increased Compton scatter fraction ($>2X$) entailed in this scintillator: while the increased light output would decrease the uncertainty of the anode measurements (by $\sim 40\%$), Compton scatter was shown to be an important factor of the resolution of the detector, resulting in a degradation in spatial resolution of $\sim 1\text{mm}$ in

25mm thick LYSO crystals. Preliminary simulation studies have been conducted studying the performance of this scintillator in a continuous detector. The design with LIOBs could potentially be useful in this instance, if the design were fine-tuned to offer improved spatial resolution with the potential for enough DOI information to offset the added parallax error brought about by the thicker crystals. At the other end of the spectrum, thinner crystals could potentially be used in a longer scanner to offer comparable sensitivity with much improved spatial resolution and DOI information. Again, the etchings offer another option to improve upon the resolution even more, at the cost of degraded DOI resolution.

Similarly, while the H8500 MAPMT was useful for this work, SiPMs offer potentially improved quantum efficiency, the ability to be used in the PET/MR scanner, as well as significantly reduced cost. A finer anode grid than the 6-mm 8x8 grids seen most often is also a possibility, though the increase in hardware and computational complexity must be warranted. Additionally, high quantum efficiency MAPMTs are now available, with quantum efficiencies as high as 43% [192], that would lead to less noisy measurements and improved spatial resolution.

Continuous detectors therefore represent a broad class of detectors with inherent trade-offs in performance (e.g., spatial resolution, sensitivity, position sampling, DOI) that may be explored by varying the properties of the detector (e.g., scintillator, photodetector, thickness, surface properties). This work focused on some of these trade-offs by modifying the scintillation light spread within the detector through the use of laser induced optical barriers, and investigated the effect on overall scanner performance. Ultimately, the choice of parameters is dependent on the application: thin unetched

crystals may suffice for a scanner that requires excellent resolution along with DOI information without a large sensitivity, while scanners for which improved resolution is desired without the need for DOI information would benefit from LIOBs etched into the entrance region. Whole-body systems without the need (or computational capability) for DOI information would gain from the improved resolution of the designs studied for the 25mm thick crystal, using more opaque LIOBs; in contrast, using the barriers to optimize the trade-off in spatial resolution and DOI resolution for a given crystal thickness in a whole-body scanner is an interesting and worthwhile study as well. The results in this work demonstrated the use of this technology to affect light spread and explored the potential of the barriers to improve and fine-tune the performance of these detectors.

BIBLIOGRAPHY

1. Barrett HH and Myers KJ. *Foundations of Image Science*. Hoboken, NJ: Wiley-Interscience, 2004.
2. Bushberg JT. *The Essential Physics of Medical Imaging*. Philadelphia, PA: Wolters Kluwer Health/Lippincott Williams & Wilkins, 2012.
3. Epstein CL. *Introduction to the Mathematics of Medical Imaging*. Philadelphia, PA: Society for Industrial and Applied Mathematics, 2008.
4. Wernick MN and Aarsvold JN. *Emission Tomography: The Fundamentals of PET and SPECT*. Amsterdam: Elsevier Academic, 2004.
5. Bryan RN. *Introduction to the Science of Medical Imaging*. Cambridge: Cambridge UP, 2010.
6. Bolus NE. "NCRP Report 160 And What It Means For Medical Imaging And Nuclear Medicine". *J Nucl Med Techn*. 2013;41:255-260.
7. Delbeke D and Segall GN. "Status Of And Trends In Nuclear Medicine In The United States". *J Nucl Med*. 2011;52:24S-28S.
8. Buck AK, Herrmann K, Stargardt T, et al. "Economic Evaluation of PET and PET/CT in Oncology: Evidence and Methodologic Approaches". *J Nucl Med*. 2010;51:401-412.
9. Mettler FA, Bhargavan M, Faulkner K, et al. "Radiologic And Nuclear Medicine Studies In The United States And Worldwide: Frequency, Radiation Dose, And Comparison With Other Radiation Sources—1950–2007". *Radiology* 2009;253:520-531.

10. Gemmell, HG, Murray AD, and Sharp PF. *Practical Nuclear Medicine*. New York: Springer-Verlag London Limited, 2005.
11. Petersen H, Holdgaard PC, Madsen PH, et al. "FDG PET/CT In Cancer: Comparison Of Actual Use With Literature-Based Recommendations". *Eur J Nucl Med and Mol Imaging*. 2015;43:695-706.
12. Hamilton DI. *Diagnostic Nuclear Medicine: A Physics Perspective*. Secaucus, NJ: Springer, 2010.
13. Stroobants S, Goeminne J, Seegers M, et al. "18FDG-Positron Emission Tomography For The Early Prediction Of Response In Advanced Soft Tissue Sarcoma Treated With Imatinib Mesylate Glivec®". *Eur J Cancer*. 2003;39:2012-2020.
14. Weber WA, Peterson V, Schmidt B, et al. "Positron Emission Tomography In Non–Small-Cell Lung Cancer: Prediction Of Response To Chemotherapy By Quantitative Assessment Of Glucose Use". *J Clin Onc* 2003;21:2651-2657.
15. Miele E, Spinelli GP, Tomao F, et al. "Positron Emission Tomography PET Radiotracers In Oncology – Utility Of 18F-Fluoro-Deoxy-Glucose FDG-PET In The Management Of Patients With Non-Small-Cell Lung Cancer NSCLC". *Journal of Experimental & Clinical Cancer Research* 2008;27:52.
16. Kitson SL, Cuccurullo V, Ciarmello A, et al. "Clinical applications of Positron Emission Tomography PET imaging in medicine: Oncology, Brain diseases and Cardiology". *Curr Radiopharm*. 2009;2:224.

17. Wahl RL, Jacene H, Kasamon Y, et al. "From RECIST To PERCIST: Evolving Considerations For PET Response Criteria In Solid Tumors". *J Nucl Med*. 2009;50:122S-150S.
18. Guralnik L, Rozenberg R, Frenkel A, et al. "Metabolic PET/CT-Guided Lung Lesion Biopsies: Impact On Diagnostic Accuracy And Rate Of Sampling Error". *J Nucl Med*. 2015;56:518-522.
19. Xia Q, Jianjun L, Cheng W, et al. "Prognostic Significance Of 18FDG PET/CT In Colorectal Cancer Patients With Liver Metastases: A Meta-Analysis". *Cancer Imaging*. 2015;15.
20. Iseki Y, Mizuno H, Futami Y, et al. "Positron Camera For Range Verification Of Heavy-Ion Radiotherapy". *Nucl Instrum Methods Phys Res A* 2003;515:840-849.
21. Enghardt W, Crespo P, Fiedler F, et al. "Charged Hadron Tumour Therapy Monitoring By Means Of PET". *Nucl Instrum Methods Phys Res A*. 2004;525:284-288.
22. Pauwels S, Barone R, Walrand S, et al. "Practical Dosimetry of Peptide Receptor Radionuclide Therapy with 90Y-Labeled Somatostatin Analogs". *J Nucl Med*. 2005;46:92S-98S.
23. Lhommel R, van Elmbt L, Goffette P, et al. "Feasibility Of 90Y TOF PET-Based Dosimetry In Liver Metastasis Therapy Using SIR-Spheres". *Eur J Nucl Med Mol Imaging*. 2010;37:1654-1662.
24. Makris NE, Boellaard R, Visser EP, et al. "Multicenter Harmonization Of 89Zr PET/CT Performance". *J Nucl Med*. 2013;55:264-267.

25. Antunes P, Ginj M, Zhang H, et al. "Are Radiogallium-Labelled DOTA-Conjugated Somatostatin Analogues Superior To Those Labelled With Other Radiometals?". *Euro J Nucl Med and Mol Imaging*. 2007;34:982-993.
26. Soderlund AT, Chaal J, Tjio G, et al. "Beyond 18F-FDG: Characterization Of PET/CT And PET/MR Scanners For A Comprehensive Set Of Positron Emitters Of Growing Application--18F, 11C, 89Zr, 124I, 68Ga, and 90Y". *J Nucl Med*. 2015;56:1285-1291.
27. Weineisen M, Schottelius M, Simecek J, et al. "68Ga- And 177Lu-Labeled PSMA I&T: Optimization Of A PSMA-Targeted Theranostic Concept And First Proof-Of-Concept Human Studies". *J Nucl Med*. 2015;56:1169-1176.
28. Martí-Climent JM, Preto P, Elosua C, et al. "PET Optimization For Improved Assessment And Accurate Quantification Of 90Y-Microsphere Biodistribution After Radioembolization". *Med Physics*. 2014;56.
29. Lopci E, Nanni C, Castellucci P, et al., "Imaging with non-FDG PET tracers: outlook for current clinical applications". *Insights Imaging* 2010;1(NS28):373-385.
30. Buck A, Halter G, Schirrmeister H, et al. "Imaging Proliferation in Lung Tumors with PET: 18F-FLT Versus 18F-FDG" *J Nucl Med*. 44;2003:1426-1431.
31. Clark C, Schneider JA, Bedell BJ, et al. "Use of Florbetapir-PET for Imaging Beta-Amyloid Pathology" *JAMA* 2011;305:275-283.
32. Ortuño JE, Guerra-Gutiérrez P, Rubio JL, et al. "3D-OSEM Iterative Image Reconstruction For High-Resolution PET Using Precalculated System Matrix". *Nucl Instrum Methods Phys Res A* 2006;569:440-444.

33. Dahlbom M. *Physics Of PET And SPECT Imaging*. Boca Raton, FL: CRC Press (Taylor and Francis Group), 2017.
34. Miller M, Zhang J, Binzel K, et al. "Characterization of the Vereos Digital Photon Counting PET System". *J Nucl Med*. 2015;56:434.
35. Daube-Witherspoon ME, Surti S, Perkins A, et al. "The imaging performance of a LaBr₃ based PET scanner". *Phys Med Biol*. 2010;55:45-64.
36. Vandenberghe S and Marsden P. "PET-MRI: a review of challenges and solutions in the development of integrated multimodality imaging". *Phys. Med. Biol*. 2015;60:R115-R154.
37. Moses WW. "Fundamental Limits Of Spatial Resolution In PET". *Nucl Instrum Methods Phys Res A*. 2011;648:S236-S240.
38. Lewellen TK. "Recent Developments In PET Detector Technology". *Phys Med Biol*. 2008;53:R287-R317.
39. Levin CS and Zaidi H. "Current Trends In Preclinical PET System Design". *PET Clinics* 2007;2:125-160.
40. Surti S, Scheuermann R, Werner ME, et al. "Improved Spatial Resolution In PET Scanners Using Sampling Techniques". *IEEE Trans Nucl Sci*. 2009;56:596-601.
41. Cherry, SR, Sorenson JA, and Phelps ME. *Physics in Nuclear Medicine*. Philadelphia, PA: Saunders, 2012.
42. Derenzo SE, Budinger TF, Huesman RH, et al. "Imaging Properties of a Positron Tomograph with 280 BGO Crystals". *J of Comput Assist Tomo*. 1981;5:950.

43. Levin CS and Hoffman EJ. "Calculation Of Positron Range And Its Effect On The Fundamental Limit Of Positron Emission Tomography System Spatial Resolution". *Phys Med Biol.* 44;1999:781-799.
44. Sanchez-Crespo A. "Comparison Of Gallium-68 And Fluorine-18 Imaging Characteristics In Positron Emission Tomography". *Appl Radiat Isot.* 2013;76:55-62.
45. Surti S, Shore AR, and Karp JS. "Design Study Of A Whole-Body PET Scanner With Improved Spatial And Timing Resolution". *IEEE Trans Nucl Sci.* 2013;60:3220-3226.
46. Schmall JP, Karp JS, Werner ME, et al. "Parallax Error In Long-Axial Field-Of-View PET Scanners—A Simulation Study". *Phys Med Biol.* 2016;61:5443-5455.
47. Vandenberghe S, Mikhaylova E, D’Hoe E, et al. "Recent Developments In Time-Of-Flight PET". *Eur J Nucl Med Mol Imaging* 2016;3.
48. Saha G. *Basics Of PET Imaging*. 1st ed. Cham: Springer International Publishing, 2016.
49. Eriksson L, Townsend D, Conti M, et al. "An Investigation Of Sensitivity Limits In PET Scanners". *Nucl Instrum Methods Phys Res A* 2007;580:836-842.
50. Knoll GF. *Radiation Detection and Measurement*. New York: Wiley, 2000.
51. Hutton BF. "Recent Advances In Iterative Reconstruction For Clinical SPECT/PET And CT". *Acta Oncologica* 2011;50:851-858.

52. Gong K, Cherry SR, and Qi J. "On The Assessment Of Spatial Resolution Of PET Systems With Iterative Image Reconstruction". *Phys Med Biol.* 2016;61:N193-N202.
53. Alessio, AM, Stearns CW, Tong S, et al. "Application And Evaluation Of A Measured Spatially Variant System Model For PET Image Reconstruction". *IEEE Trans on Med Imaging.* 2010;29:938-949.
54. Erlandsson K, Buvay I, Pretorius PH, et al. "A Review Of Partial Volume Correction Techniques For Emission Tomography And Their Applications In Neurology, Cardiology And Oncology". *Phys Med Biol.* 2012;57:R119-R159.
55. Rahmim A and Tang J. "Noise Propagation In Resolution Modeled PET Imaging And Its Impact On Detectability". *Phys Med Biol.* 2013;58:6945-6968.
56. Rahmim A, Qi J, and Sossi V. "Resolution Modeling In PET Imaging: Theory, Practice, Benefits, And Pitfalls". *Med Phys.* 2013;40.
57. Tohka J and Anthonin Reilhac. "Deconvolution-Based Partial Volume Correction In Raclopride-PET And Monte Carlo Comparison To MR-Based Method". *NeuroImage.* 2008;39:1570-1584.
58. Tong, SA, Alessio M, and Kinahan PE. "Noise And Signal Properties In PSF-Based Fully 3D PET Image Reconstruction: An Experimental Evaluation". *Phys Med Biol.* 2010;55:1453-1473.
59. Tong S, Alessio AM, and Kinahan PE. "Image Reconstruction For PET/CT Scanners: Past Achievements And Future Challenges". *Imaging in Medicine.* 2010;2:529-545.

60. Gross-Weege N, Schug D, Hallen P, et al. "Maximum Likelihood Positioning Algorithm For High-Resolution PET Scanners". *Med Phys*. 2016;43:3049-3061.
61. Basu S, Zaidi H, Holm S, et al. "Quantitative Techniques In PET-CT Imaging". *Current Medical Imaging Reviews* 2011;7:216-233.
62. Tarantola, G, Zito F, and Gerundini, P. " PET Instrumentation and Reconstruction Algorithms in Whole-Body Applications". *J Nucl Med*. 2003;44:756-769.
63. Kinahan PE and Fletcher JW. "Positron Emission Tomography-Computed Tomography Standardized Uptake Values In Clinical Practice And Assessing Response To Therapy". *Seminars in Ultrasound, CT and MRI* 2010;31:496-505.
64. Laffon E, Burger IA, Lamare F, et. al. "SUVpeak Performance in Lung Cancer- Comparison to Average SUV from the 40 Hottest Voxels" *J Nucl Med*. 2016;55:85-88.
65. Minamimoto R, Barkhodari A, Harshman L, et al. "Prognostic Value Of Quantitative Metabolic Metrics On Baseline Pre-Sunitinib FDG PET/CT In Advanced Renal Cell Carcinoma". *PLOS ONE* 2016;11.
66. Carlier T and Bailly C. "State-Of-The-Art And Recent Advances In Quantification For Therapeutic Follow-Up In Oncology Using PET". *Frontiers in Medicine* 2015;2:18.
67. National Electrical Manufacturers Association: NEMA Standards Publication NU 2–2007: Performance Measurements of Positron Emission Tomographs. *NEMA*. 2007.
68. Soret M, Bacharach SJ, and Buvat I. "Partial-Volume Effect In PET Tumor Imaging". *J Nucl Med*. 2007;48:932–945.

69. Rousset O, Ma Y, and Evans AC. "Correction for partial volume effects in PET: principle and validation". *J Nucl Med*. 1998;39:904-911.
70. Kessler, Ellis JR, and Eden M. "Analysis of Emission Tomographic Scan Data: Limitations Imposed by Resolution and Background". *Journ. Comp. Assist. Tomog*. 1984;83:514-522.
71. Castiglioni I, Rizzo G, Gilardi MC, et al. "Lesion Detectability And Quantification In PET/CT Oncological Studies By Monte Carlo Simulations". *IEEE Trans Nucl Sci*. 2005;52:136-142.
72. Geworski L, Knoop BO, de Cabrejas ML, et. al. "Recovery correction for quantitation in emission tomography: a feasibility study" *Euro Journ. Nucl. Med*. 2000;27:161-169.
73. Rahmim AQ and Sossi V. "Resolution modeling in PET imaging: Theory, practice, benefits, and pitfalls" *Med Phys*. 2013;40.
74. Boellaard R. "Need For Standardization Of 18F-FDG PET/CT For Treatment Response Assessments". *J Nucl Med* 52.Supplement_2 2011;52:93S-100S.
75. Boellaard R, Oyen WJ, Hoekstra CJ, et al. "The Netherlands Protocol For Standardisation And Quantification Of FDG Whole Body PET Studies In Multi-Centre Trials". *Eur J Nucl Med and Mol Imaging* 2008;35:2320-2333.
76. Tomitani T and Brooks RA. " Image Reconstruction and Noise Evaluation in Photon Time-of-Flight Assisted Positron Emission Tomography ". *J Comput Assist Tomo*. 1982;6:652-653.

77. Daube-Witherspoon ME , Surti S, Perkins AE, et al. "Determination Of Accuracy And Precision Of Lesion Uptake Measurements In Human Subjects With Time-Of-Flight PET". *J Nucl Me.d.* 2014;55:602-607.
78. El Fakhri G, Surti S, Trott CM, et al. "Improvement In Lesion Detection With Whole-Body Oncologic Time-Of-Flight PET". *J Nucl Med.* 2011;52:347-353.
79. Kadrmas DJ, Casey ME, Conti M, et al. "Impact Of Time-Of-Flight On PET Tumor Detection". *J Nucl Med.* 2009;50:1315-1323.
80. Karp JS, Surti S, Daube-Witherspoon ME, et al. "Benefit Of Time-Of-Flight In PET: Experimental And Clinical Results". *J Nucl Med.* 2008;49:462-470.
81. Surti S and Karp JS. "Experimental Evaluation Of A Simple Lesion Detection Task With Time-Of-Flight PET". *Phys Med Biol.* 2009;54:1087-1087.
82. Surti S. "Update On Time-Of-Flight PET Imaging". *J Nucl Med.* 2014;56:98-105.
83. Melcher CL "Scintillation Properties for PET". *J Nucl Med.* 2000;41: 1051-1055.
84. van Eijk CWE. "Inorganic scintillators in positron emission tomography". *Radiation Detectors for Medical Applications* 129 2006;12:259-274.
85. van Eijk, CWE. "Inorganic Scintillators In Medical Imaging". *Phys Med Biol.* 2002;47:R85-R106.
86. Humm, JL, Rosenfeld A, Del Guerra A. "From PET Detectors To PET Scanners". *Eur J Nucl Med and Mol Imaging* 2003;30:1574-1597.
87. A. Nassalski, Kapusta M, Batsch T, et al. "Comparative study of scintillators for PET/CT detectors", *IEEE Trans Nucl Sci.* 2007;54:3-10.

88. Rihua M, Wu C, Dai L, et al. "Crystal Growth And Scintillation Properties Of LSO And LYSO Crystals". *Journal of Crystal Growth* 2013;36:97-100.
89. Melcher CL, Manente RA, Peterson CA, et al. "Czochralski Growth Of Rare Earth Oxyorthosilicate Single Crystals". *Journal of Crystal Growth* 1993;128:1001-1005.
90. Brandle CD, Valentino AJ, and Berkstresser GQ. "Czochralski Growth Of Rare-Earth Orthosilicates Ln_2SiO_5 ". *Journal of Crystal Growth* 1986;79:308-315.
91. Laishun Q, Li H, Lu S, et al. "Growth And Characteristics Of LYSO $\text{Lu}_{21-x}\text{Y}_x\text{SiO}_5$:Ce Scintillation Crystals". *Journal of Crystal Growth* 2005;28:518-524.
92. Ronacli E and Cherry S. "Application of Silicon Photomultipliers to Positron Emission Tomography". *Annals of Biomed Eng.* 2009;39:1358-1377.
93. Ito M, Hong SJ, Kwon SI, et al. "Performances of two flat panel multi-anode PMTs for readout from pixelated LGSO crystals". *J Nucl Med.* 2009;50:1533.
94. Pani R, Pellegrini R, Cinti MN, et al. "Factors Affecting Hamamatsu H8500 Flat Panel PMT Calibration For Gamma Ray Imaging". *IEEE Trans Nucl Sci.* 2007;54:438-443.
95. Hamamatsu, Technical Data Sheet "Flat Panel Type Multianode PMT Assembly H8500 Series/H10966 Series", Jul 2011.
96. Jarritt PH and Acton PD. "PET Imaging Using Gamma Camera Systems". *Nucl Med Commun.* 1996;17:758-766.
97. D'Asseler Y, Vandenberghe S, Winter FD, et al. "PET Imaging Using Gamma Cameras". *Computerized Medical Imaging and Graphics.* 2001;25:87-96.

98. Peng H and Levin CS. "Recent Developments In PET Instrumentation". *Curr Pharm Biotechno.* 2010;11:555-571.
99. Boronat M, Marinas C, Frey A, et al. "Physical Limitations To The Spatial Resolution Of Solid-State Detectors". *IEEE Trans Nucl Sci.* 2015;62:381-386.
100. Casey ME and Nutt R. "A multi-crystal two-dimensional BOO detector system for positron emission tomography". *IEEE Trans Nucl Sci.* 1985;NS33:460-463.
101. Karp JS, Daube-Witherspoon ME, Freifelder R, et al. "Performance of a Brain PET Camera Based on Anger-Logic Gadolinium Oxyorthosilicate Detectors". *J Nucl Med.* 2003;44:1340-1349.
102. Surti S, Karp JS, Freifelder R, et al. "Optimizing The Performance Of A PET Detector Using Discrete GSO Crystals On A Continuous Lightguide". *IEEE Trans Nucl Sci.* 2000;47:1030-1036.
103. Surti S, Kuhn A, Werner ME, et al. "Performance of Philips Gemini TF PET/CT Scanner with Special Consideration for Its Time-of-Flight Imaging Capabilities". *J Nucl Med* 2007;43:471-480.
104. Adam, LE, Karp JS, Daube-Witherspoon ME, et al.. "Performance of a Whole-Body PET Scanner Using Curve-Plate NaI(Tl) Detectors". *J Nucl Med.* 2001;42:1821-1830.
105. Li X, Hunter WCJ, Lewellen TK, et al. "Use of Cramer-Rao Lower Bound for Performance Evaluation of Different Monolithic Crystal PET Detector Designs". *IEEE Trans Nucl Sci.* 2012;59:1961-1971.

106. Maas, MC, van der Laan DJ, Schaart DR, et al. "Experimental Characterization Of Monolithic-Crystal Small Animal PET Detectors Read Out By APD Arrays". *IEEE Trans Nucl Sci.* 2006;53:1071-1077.
107. van Dam HT, Seifert S, Vinker R, et al. "A Practical Method For Depth Of Interaction Determination In Monolithic Scintillator PET Detectors". *Phys Med Biol.* 2011;56:4135-4145.
108. Lerche CW, Benlloch JM, Snchez F, et al., "Depth of interaction within continuous crystals from the width of its scintillation light distribution", *IEEE Trans. Nucl. Sci.* Jun. 2005;52:560-572.
109. Wang Y, Wang L, Li D, et al. "Self-Organizing Map Neural Network-Based Depth-Of-Interaction Determination For Continuous Crystal PET Detectors". *IEEE Trans Nucl Sci.* 2015;62:766-772.
110. Lerche CW, Ros A, Herrero V, et al., "Dependency of Energy-, Position- and Depth of Interaction Resolution on Scintillation Crystal Coating and Geometry". *IEEE Trans Nucl Sci.* 2008;55:1344–1351.
111. Joung J, Miyaoka RS, and Lewellen TK. "Cmice: A High Resolution Animal PET Using Continuous LSO With A Statistics Based Positioning Scheme". *Nucl Instrum Methods Phys Res A.* 2002;489:584-598.
112. van Dam HT, Seifert S, Vinke R, et al. "Improved Nearest Neighbor Methods For Gamma Photon Interaction Position Determination In Monolithic Scintillator PET Detectors". *IEEE Trans Nucl Sci.* 2011;58:2139-2147.

113. Borghi G, Tabacchini V, and Schaart D. "Experimental Validation of an Efficient Fan-Beam Calibration Procedure for -Nearest Neighbor Position Estimation in Monolithic Scintillator Detectors". *IEEE Trans Nucl Sci.* 2015;62:57-67.
114. Bruyndonckx P, Léonard S, Tavernier S, et al. "Neural Network-Based Position Estimators for PET Detectors Using Monolithic LSO Blocks". *Trans. Nucl. Sci.* 2004;51:2520-2524.
115. Gray, R M and Macovski A. "Maximum A Posteriori Estimation Of Position In Scintillation Cameras". *IEEE Trans Nucl Sci.* 1976;23:849-852.
116. Miyaoka R, Li X, Lockhart C, et al. "Comparison of Detector Intrinsic Spatial Resolution Characteristics for Sensor on the Surface and Conventional Readout Designs". *IEEE Trans Nucl Sci.* 2010;57:990-997.
117. Marcinowski R, Mollet P, Van Holen R, et al. "Sub-millimetre DOI detector based on monolithic LYSO and digital SiPM for a dedicated small-animal PET system" *Phys. Med. Biol.* 2016;61:2196-2212.
118. Nayar SK, Ikeuchi K, and Kanade T. "Surface Reflection: Physical And Geometrical Perspectives". *IEEE Trans Pattern Anal Mach Intell.* 1991;13:611-634.
119. Levin A and Moissan C. "A more physical approach to model the surface treatment of scintillation counters and its implementation into DETECT". In: *Conference Record of 1996 IEEE Nuclear Science Symposium and Medical Imaging Conference.* 1996:702-706.

120. Li H and Torrance K. " A Practical, Comprehensive Light Reflection Model". *Program of Computer Graphics, Technical Report PCG-05-03*, Cornell University, 2005.
121. Zaidi H. "Relevance Of Accurate Monte Carlo Modeling In Nuclear Medical Imaging". *Med Phys.* 1999;26:574-608.
122. Andreo P. "Monte Carlo Techniques In Medical Radiation Physics". *Phys Med Biol.* 1991;36:861-920.
123. Buvat I and Castiglioni I. " Monte Carlo simulations in SPET and PET". *Q J Nucl Med.* 2002;46:48-61.
124. Surti S, Karp JS, and Muehllehner G. "Image Quality Assessment Of Labr 3 - Based Whole-Body 3D PET Scanners: A Monte Carlo Evaluation". *Phys Med Biol.* 2004;49:4593-4610.
125. Karp JS and Muehllehner G. "Performance a position sensitive scintillation detector". *Phys Med Biol.* 1985;307:643-655.
126. Lay MD and Lyon MJ. "An Experimental And Monte Carlo Investigation Of The R1408 Hamamatsu 8-Inch Photomultiplier Tube And Associated Concentrator To Be Used In The Sudbury Neutrino Observatory". *Nucl Instrum Methods Phys Res A.* 1996;383:495-505.
127. Motta D and Schönert S. "Optical Properties Of Bialkali Photocathodes". *Nucl Instrum Methods Phys Res A.* 2005;539:217-235.
128. Zhang Y et al. "Variation Of Spectral Response For Exponential-Doped Transmission-Mode Gaas Photocathodes In The Preparation Process". *Applied Optics.* 2010;49:3935.

129. Lay MD. "Parameterisation of the angular response of the R1408 Hamamatsu eight-inch photomultiplier tube to be used in the Sudbury Neutrino Observatory". *Nucl. Instrum. Methods Phys. Res. A*. 1996;383:485-494.
130. Janecek M and Moses WW. "Measuring Light Reflectance Of BGO Crystal Surfaces". *IEEE Trans Nucl Sci*. 2008;55:2443-2449.
131. Janecek M and Moses WW. "Simulating Scintillator Light Collection Using Measured Optical Reflectance". *IEEE Trans Nucl Sci*. 2010;57:964-970.
132. Janecek, M. "Reflectivity Spectra For Commonly Used Reflectors". *IEEE Trans Nucl Sci*. 2012;59:490-497.
133. Weidner, Victor R., and Hsia JJ. "Reflection Properties Of Pressed Polytetrafluoroethylene Powder". *J. Opt. Soc. Am*. 1981;71:856.
134. Ling T, Burnett TH, Lewellen TK, et al., "Parametric positioning of a continuous crystal PET detector with depth of interaction decoding", *Phys. Med. Biol*. 2008;53:1843-1863.
135. Etxebeste A, Barrio J, Muoz E, et al., "3D position determination in monolithic crystals coupled to SiPMs for PET", *Phys. Med. Biol.*, 2016;61:3914-3934
136. Llosá G, Barrillon P, Barrio J, et al., "High performance detector head for PET and PET/MR with continuous crystals and SiPMs," *Nucl. Instrum. Methods Phys. Res. A*. 2013;702:3-5.
137. P. Conde, Gonzalez AJ, Gonzalez A, et al., "Analysis of the Statistical Moments of the Scintillation Light Distribution With dSiPMs," *Nucl. Instrum. Methods Phys. Res. A*. 2015;625:1981-1988.

138. Lerche CW, Benlloch JW, Snchez F, et al., "Depth of interaction within continuous crystals from the width of its scintillation light distribution", *IEEE Trans. Nucl. Sci.*, Jun. 2005;52:560-572.
139. Kaul M, Surti S, and Karp JS, "Combining Surface Treatments With Shallow Slots to Improve the Spatial Resolution Performance of Continuous, Thick LYSO Detectors for PET". *Trans. Nucl. Sci.* 2013;60:44-60.
140. Borghi G, Tabacchini V, and Schaart DR. "Towards monolithic scintillator based TOF-PET systems: practical methods for detector calibration and operation". *Phys Med Biol.* 2016;61:4904-4928.
141. Schaart D, van Dam HT, Seifert S, et al. "A Novel, Sipm-Array-Based, Monolithic Scintillator Detector For PET". *Phys Med Biol.* 2009;54:3501-3512
142. Schaart D, van Dam HT, Seifert S, et al. "SiPM-Array Based PET Detectors with Depth-of- Interaction Correction". *IEEE NSS Conf. Rec.* 2008.
143. Zhang H, Zhou R, and Yang C. "A PET Detector Module With Monolithic Crystal, Single End Readout, Sipm Array And High Depth-Of-Interaction Resolution". *Journal of Instrumentation.* 2016;11.
144. Borghi G, Peet BJ, and Schaart DR. "A 32 Mm \times 32 Mm \times 22 Mm Monolithic LYSO:Ce Detector With Dual-Sided Digital Photon Counter Readout For Ultrahigh-Performance TOF-PET And TOF-PET/MRI". *Phys Med Biol.* 2016;61:4929-4949.
145. Miyaoka RS, Xiaoli L, Lockhart C, Macdonald LR, et al. "Design of a High Resolution, Monolithic Crystal, PET/MRI Detector with DOI Positioning

- Capability". In: *Conference Record of 1997 IEEE Nuclear Science Symposium and Medical Imaging Conference*. 2008;4688-4692.
146. Ling TK, Lee K, and Miyaoka RS. "Performance Comparisons Of Continuous Miniature Crystal Element Cmice Detectors". *IEEE Trans Nucl Sci*. 2006;53:2513-2518.
 147. Schaeffer RD. *Fundamentals of Laser Micromachining*. Boca Raton: Taylor & Francis, 2012.
 148. Bryn W, Chase C, and Chang B. "Increased efficiency and performance in laser pump chambers through use of diffuse highly reflective materials". *SPIE Proceedings, Laser Beam Shaping VIII* Vol. 6663 2007.
 149. Zorila A, Rusen L, Straten A, et al. "Measuring The Effective Pulse Duration Of Nanosecond And Femtosecond Laser Pulses For Laser-Induced Damage Experiments". *Optical Engineering* 2013;52.
 150. Dorman C and Matthias S. "Picosecond Micromachining Update". *Laser Technik Journal* 5.4 2008;5:44-47.
 151. Liu J. "Pulse Shaping High-Energy Fiber Lasers". *SPIE Newsroom* 2010.
 152. R. Viskup. "High Energy and Short Pulse Lasers". 2016.
 153. Sabet H, Blackberg L, Uzun-Ozsahin D, et al. "Novel Laser-Processed Csi:Tl Detector For SPECT". *Med Phys*. 43.5 2016;43:2630-2638.
 154. Sabet H, Bhandari Hm Kudrolli H, et al. "A Method For Fabricating High Spatial Resolution Scintillator Arrays". *IEEE Trans Nucl Sci*. 2013;60:1000-1005.

155. Hunter, CJW, Miyaoka RS, Macdonald L, et al. "Light-Sharing Interface For Dmice Detectors Using Sub-Surface Laser Engraving". *IEEE Trans Nucl Sci.* 2015;62: 7-35.
156. Yoshida Eiji, Tashima H, Inadama N, et al. "Intrinsic Spatial Resolution Evaluation Of The X'Tal Cube PET Detector Based On A 3D Crystal Block Segmented By Laser Processing". *Radiological Physics and Technology* 2012;6:21-27.
157. Yoshida E, Somlai-Schweiger I, Tashima H, et al. "Parameter Optimization Of A Digital Photon Counter Coupled To A Four-Layered DOI Crystal Block With Light Sharing". *IEEE Trans Nucl Sci.* 2015;62:748-755.
158. Orita N, Murayama H, Kawai H, et al. "Three-Dimensional Array Of Scintillation Crystals With Proper Reflector Arrangement For A Depth Of Interaction Detector". *IEEE Trans Nucl Sci.* 2005;52:8-14.
159. Uchida H, Sakia T, Yamauchi H, et al. "A Novel Single-Ended Readout Depth-Of-Interaction PET Detector Fabricated Using Sub-Surface Laser Engraving". *Phys Med Biol.* 2016;61:6635-6650.
160. Ogata Y, Ohnishi T, Moriya T, et al. "GPU-based optical propagation simulator of a laser-processed crystal block for the X'tal cube PET detector". *Radiol. Phys. Technol.* 2014;7:35-42.
161. He XD, Torrance KE, Sillion FX, et al. "A Comprehensive Physical Model For Light Reflection". *ACM SIGGRAPH Computer Graphics* 25.4 1991;25:175-186.

162. M. Kaul, "Investigating the Spatial Resolution Characteristics of a Monolithic Scintillator Detector for PET" Ph.D. Diss. University of Pennsylvania, Philadelphia, PA 2013.
163. Buvat I and Castiglioni I. "Monte Carlo simulations in SPET and PET". *Q J Nucl Med.* 46 2002;46:48-61.
164. Abushab, KM, Herraiz JL, Vicente E, et al. "Evaluation Of Penelopet Simulations Of Biograph PET/CT Scanners". *IEEE Trans Nucl Sci.* 2016;63:1367-1374.
165. Blackston D, Habte F, and Hausladen P. "A Comparison of GEANT4 and DETECT2000 for the Simulation of Light Transport in Scintillation.
166. Adam, LE, Karp JS, and Brix G. "Investigation Of Scattered Radiation In 3D Whole-Body Positron Emission Tomography Using Monte Carlo Simulations". *Phys Med Biol.* 1999;44:2879-2895.
167. Popescu LM, Matej S, and Lewitt RM. "Iterative image reconstruction using geometrically ordered subsets with list-mode data". *Conference Record of 2004 IEEE Nuclear Science Symposium and Medical Imaging Conference.* 2004:3536-3540.
168. Matej S and Lewitt RM. "Efficient 3D grids for image reconstruction using spherically-symmetric volume elements". *IEEE Trans Nucl Sci.* 1995;42:1361–1370.
169. Watson CC, "Extension of Single Scalier Simulation to Scalier Correction of Time-of-Flight PET," in *IEEE Nuclear Science Symposium and Medical Imaging Conference*, San Juan, Puerto Rico, 2005:2492-2496.

170. Werner M, Surti S, and Karp JS. "Implementation and Evaluation of a 3D PET Single Scatter Simulation with TOF Modeling". *IEEE NSS Conf. Rec.* 2006: 1768-1773.
171. Palmer, MR, Xuping Z, and Parker JA. "Modeling And Simulation Of Positron Range Effects For High Resolution PET Imaging". *IEEE Trans Nucl Sci.* 2005;52: 391-1395.
172. Tabacchini, V, Surti S, Borghi G, et al. "Improved Image Quality Using Monolithic Scintillator Detectors With Dual-Sided Readout In A Whole-Body TOF-PET Ring: A Simulation Study". *Phys Med Biol.* 2017;62:2018-2032.
173. Panetta JV, Daube-Witherspoon ME, and Karp JS. "Validation of Phantom-Based Harmonization for Patient Harmonization". *Med Phys.* 2017.
174. Shankar LK, Hoffman JM, Bacharach S at al. "Consensus recommendations on the use of positron emission tomography PET and [18F]-2-fluoro-2-deoxy-d glucose FDG as an indicator of therapeutic response in patients involved in National Cancer Institute NCI clinical trials". *J Nucl Med.* 2006;47:1059-1066.
175. Sunderland JJ and Christian PE. "Quantitative PET/CT scanner performance characterization based upon the Society of Nuclear Medicine and Molecular Imaging Clinical Trials Network oncology clinical simulator phantom". *J Nucl Med.* 2015;56:145–52.
176. Kelly MD and Declerck JM. "SUVref: reducing reconstruction-dependent variation in PET SUV". *Eur J Nucl Med Mol Imaging Res.* 2011;1:16.

177. Sunderland J, Kinahan P, Karp JS, et al. “Development and testing of a formalism to identify harmonized and optimized reconstructions for PET/CT in clinical trials”. *J Nucl Med*. 2015;56:563.
178. Lasnon C, Desmonts C, Quak E, et al. “Harmonizing SUVs in multicentre trials when using different generation PET systems: prospective validation in non-small cell lung cancer patients”. *Eur J Nucl Med Mol Imaging*. 2013;40:985–996.
179. Quak E, Leroux PY, Hofman MS, et al. “Harmonizing FDG PET quantification while maintaining optimal lesion detection: prospective multicentre validation in 517 oncology patients”. *Eur J Nucl Med Mol Imaging*. 2015;42:2072-2082.
180. Armstrong IS, Kelly MD, Williams HA, et al. “Impact of point spread function modelling and time of flight on FDG uptake measurements in lung lesions using alternative filtering strategies”. *Eur J Nucl Med Mol Imaging*. 2014;1:99.
181. Richardson WH. “Bayesian-based iterative method of image restoration”. *J Opt Soc of Amer*. 1972;62:55-59.
182. Lucy LB. “An iterative technique for the rectification of observed images”. *The Astron Jour*. 1974;79:745-749.
183. Tohka J and Reilhac A. “Deconvolution-based partial volume correction in Raclopride-PET and Monte Carlo comparison to MR-based method”. *NeuroImage*. 2008;39:1570–1584.
184. Hoetjes NJ, van Velden FH, Hoekstra OS, et al. “Partial volume correction strategies for quantitative FDG PET in oncology”. *Eur J Nucl Med Mol Imaging*. 2010;37:1679–1687.

185. Zhang B, Olivier P, Lorman B, et al. "PET image resolution recovery using PSF-based ML-EM deconvolution with blob-based list-mode TOF reconstruction". *J Nucl Med*. 2011;52S:1-266.
186. Snyder D and Miller M. "The use of sieves to stabilize images produced with the EM algorithm for emission tomography". *IEEE Trans Nucl. Sci*. 1985;32:3864-3872.
187. Jakoby BW, Bercier Y, Conti M, et al. "Physical and clinical performance of the mCT time-of-flight PET/CT scanner." *Phys. Med. Biol*. 2011;568:2375-2389.
188. Kyba CCM, Wiener RI, Newcomer FM, et al. "Evaluation of local PMT triggering electronics for a TOF-PET scanner". *Conference Record of 2008 IEEE Nuclear Science Symposium and Medical Imaging Conference*. 2008;4608-4613.
189. Surti S, Scheuermann J, El Fakhri G, et al. "Impact of time-of-flight PET on whole-body oncologic studies: A human observer lesion detection and localization study". *J Nucl Med*. 2011;52:712-719.
190. Berthon B, Marshall C, Edwards A, et al. "Influence of cold walls on PET image quantification and volume segmentation: a phantom study". *Med Phys*. 2013;40.
191. Smith R, Karp JS, Muehllehner G, et al. "Singles transmission scans performed post-injection for quantitative whole-body PET imaging". *IEEE Trans Nucl Sci*. 1997;44:1329-1335.
192. Son JW, Ko GB, Won JY, et al., "Development and Performance Evaluation of a Time-of-Flight Positron Emission Tomography Detector Based on a High-Quantum-Efficiency Multianode Photomultiplier Tube", *IEEE Trans Nucl. Sci*. 2016;63: 44-51.